PACIFIC EARTHQUAKE ENGINEERING RESEARCH CENTER

Effective Stress Analysis of Liquefaction Sites and Evaluation of Sediment Ejecta Potential

Daniel Hutabarat
Jonathan D. Bray

Department of Civil and Environmental Engineering
University of California, Berkeley

PEER Report No. 2021/03

Pacific Earthquake Engineering Research Center
Headquarters at the University of California, Berkeley
April 2021

PEER 2021/03
April 2021

Effective Stress Analysis of Liquefaction Sites and Evaluation of Sediment Ejecta Potential

Daniel Hutabarat

Jonathan D. Bray

Department of Civil and Environmental Engineering
University of California, Berkeley

PEER Report 2021/03
Pacific Earthquake Engineering Research Center
Headquarters at the University of California, Berkeley

April 2021

ABSTRACT

Sediment ejecta mechanism contributes significantly to the severity of liquefaction-induced ground failure (e.g., excessive land subsidence). Estimating the amount of ejected sediment is a key step to assess the severity of ground failure; however, procedures to quantify it are currently lacking. Sediment ejecta is a post-shaking phenomenon resulting from the migration and redistribution of excess-pore-water-pressure (u_e) generated during earthquake shaking. The dissipation process of residual u_e can trigger high-gradient upward seepage, which can exploit cracks in the upper non-liquefiable crust layer. Once cracks in the crust layer are fully formed and there is sufficient artesian water pressure, the seepage flow can produce artesian flow above the ground surface while ejecting the fluidized sediment to the ground surface. As more sediment is transported to the ground surface, additional ground subsidence is produced.

The characteristics of liquefiable sites that did and did not produce sediment ejecta manifestation after the 2010–2011 Canterbury earthquake sequence in Christchurch, New Zealand, remain unclear. The severity of liquefaction-induced ejecta manifestation for the 2010–2011 Canterbury earthquakes was overestimated or underestimated using liquefaction-induced ground failure indices, such as the Liquefaction Potential Index (LPI) or Liquefaction Severity Number (LSN), at several sites in Christchurch. By capturing the sediment ejecta mechanism, it is possible to have a reliable estimate of ground failure severity and prevent costly or unconservative ground improvement designs in mitigating liquefaction hazards. This research proposes a new way to quantify the quantity of sediment ejecta and hence the severity of post-shaking liquefaction consequences due to sediment ejecta for level ground.

Firstly, dynamic nonlinear effective stress analyses (ESA) are performed to back-analyze two representative level-ground sites where simplified liquefaction triggering procedures indicated liquefaction effects would be severe but either surface manifestations were not observed, or inconsistent amounts of sediment ejecta were observed after the 2010–2011 Canterbury earthquakes. The ESA solves a fully coupled *u-p* formulation using the fast OpenSees finite-element code and robust PM4Sand and PM4Silt constitutive models to model the cyclic behavior of liquefiable materials. The ESA simulation focuses on the influence of the site's impedance contrasts and its profile of vertical hydraulic conductivity (k_v) to estimate the site's potential to produce ejecta. The simulation results show that a thick, clean sand site can develop high-gradient upward seepage that is sustained after strong shaking ends to trigger seepage-induced secondary liquefaction at shallow depths. The upward seepage can flow rapidly within highly permeable deposits without significant restriction from low k_v layers and develop high excess hydraulic head (h_{exc}) at shallow depths to sufficiently produce artesian flow above the surface that produces severe ejecta. Conversely, the stratified silty soil site develops high u_e and h_{exc} in deep isolated liquefiable layers, but the overlying low k_v layers impede the upward water flow, so the h_{exc} at shallow depths is insufficient to produce an artesian flow to transport the fluidized sediment.

The Artesian Flow Potential (AFP) and Ejecta Potential Index (EPI) concepts are formulated to capture the post-shaking hydraulic mechanism. The AFP estimates the required artesian pressure at a specified time step to produce artesian flow above the ground surface, exploit

cracks in the crust layer, and eject the fluidized sediment. The EPI, which is the integral of AFP over time, estimates the severity of sediment ejecta by tracking the duration in which the generated h_{exc} exceeds the critical head required for artesian flow (h_A) at shallow depths. The h_{exc} profile with depth that develops during and after earthquake shaking determines the potential of upward seepage-induced artesian flow to produce severe ejecta. The proposed EPI captures key aspects of the post-shaking hydraulic mechanisms of sediment ejecta manifestation and was formulated to account for the influence of these factors in evaluating the severity of sediment ejecta at liquefiable level-ground sites: (a) liquefaction triggering; (b) dynamic response of the soil system; (c) amount of h_{exc}; (d) potential of upward seepage-induced artesian flow; (e) duration of $h_{exc} > h_A$ (i.e., artesian flow potential); (f) hydraulic conductivity contrasts and (g) advection process. The EPI values computed from the simulations of the two representative sites capture the observed trends of liquefaction manifestations during the Canterbury earthquakes.

The AFP and EPI concepts are then evaluated further by applying them to 44 well-documented liquefaction Christchurch case histories and the Port Island Vertical Array site during the 1995 Kobe earthquake. The calculated LSN, LPI, and EPI values are compared to the observed ejecta manifestation. The computed EPI values correlate well to observed ejecta amount as opposed to LSN and LPI values, which do not. The range of median EPI values of the back-analyzed case histories with None, Minor, Moderate, Severe, and Extreme ejecta severity are 0–1, 11–50, 43–113, 111–259, and 322–421, respectively. The calculated EPI value is influenced by (1) h_{exc} generated during shaking, which is predominantly determined by the location of AFP depth (z_{AFP}), groundwater level, soil relative density, and ground shaking intensity; (2) the earthquake input ground-motion characteristics and the resulting seismic site response, which depends on the properties of and impedance contrast between soil layers; and (3) the advection process, which is governed by the distribution of h_{exc} and the k_v profile of the deposit.

Sensitivity analysis of several parameters that influence computed EPI values are also presented in this report. There are cases where the EPI is insensitive to variables such as input ground motions, hydraulic conductivity, and groundwater level, but there are also cases where the EPI can be sensitive to those variables. However, the results presented in this report prove EPI to be a useful index that correlates well to the ejecta manifestation observed in the field case histories. Sites with severe ejecta have high EPI values, and sites without ejecta have low EPI values. Lastly, recommendations on how to use AFP and EPI for performance-based design in engineering practice are also discussed.

ACKNOWLEDGMENTS

This study was supported by the Pacific Earthquake Engineering Research Center (PEER) through the Transportation Systems Research Program (TSRP – Project #NCTRJ00118) and by the National Science Foundation (NSF) under Grant CMMI-1561932. All opinions, findings, and conclusions or recommendations expressed in this material are those of the authors and do not necessarily reflect the views of the PEER, NSF, or the Regents of University of California. Data compiled by New Zealand and U.S. researchers following the Canterbury earthquake sequence events, which is now available in the New Zealand Geotechnical Database and GEER reports, were essential to this research. Post-earthquake research collaborations with Professor Misko Cubrinovski of the University of Canterbury in Christchurch were of great help with the access to and interpretation of data resulting from the Canterbury earthquake sequence. Data and insights shared by Dr. Sjoerd van Ballegooy of Tonkin + Taylor, Ltd., were also of great help. Discussions with Long Chen and Professor Pedro Arduino of the University of Washington regarding the implementation of PM4Sand and PM4Silt in OpenSees were of great value. Lastly, much of the data used in this research resulted from collaborative post-earthquake reconnaissance efforts of New Zealand researchers at several universities, government organizations, and private companies, and the U.S. NSF-funded Geotechnical Extreme Events Reconnaissance (GEER) Association.

CONTENTS

LIST OF TABLES

LIST OF FIGURES

LIST OF SYMBOLS AND ABBREVIATIONS

Abbreviations

AFP	Artesian Flow Potential
LPI	Liquefaction Potential Index [Iwasaki 1978; 1982]
LPI_{ISH}	Ishihara-inspired Liquefaction Potential Index [Maurer et al. 2015]
LSN	Liquefaction Severity Number [van Ballegooy 2014]
ESA	Effective Stress Analysis
EDP	Engineering Demand Parameter
EPI	Ejecta Potential Index
NZGD	New Zealand Geotechnical Database
SPT	Standard Penetration Test
CPT	Cone Penetrometer Test
CSR	Cyclic Stress Ratio
CSS	Cyclic Simple Shear
CRR	Cyclic Resistance Ratio
GEER	Geotechnical Extreme Event Reconnaissance
GWL	Groundwater Level

Symbols

D_r	Soil relative density
σ'_{vo}	Effective vertical stress
σ_{vo}	Total vertical stress
FS_L	Factor of safety against liquefaction triggering as the ratio of CRR to CSR
G_o	Shear modulus coefficient used in PM4Sand and PM4Silt constitutive models
N-SPT	Measured blowcount from SPT
N_{160}	Corrected blowcount
$N_{c\text{-}liq}$	Required number of cycles to trigger liquefaction
h_{po}	Contraction rate parameter in PM4Sand and PM4Silt constitutive models used to adjust number of cycles to reach liquefaction triggering
K_o	At-rest lateral coefficient pressure
q_t	Corrected tip resistance
q_c	Measured tip resistance
q_{c1Ncs}	Clean-sand equivalent measured tip resistance
i	Hydraulic gradient
I_c	Robertson [2009] Soil Behavior Type Index

I_B	Robertson [2016] Soil Behavior Type Index
k_v	Soil vertical hydraulic conductivity (m/sec)
k_h	Soil horizontal hydraulic conductivity (m/sec)
V_s	Soil shear wave velocity (m/sec)
V_p	Soil compressional wave velocity (m/sec)
u	Solid nodal displacement
p	Fluid nodal pressure
r_d	Depth reduction factor to capture soil nonlinearity
U	Fluid nodal displacement
u_e	Excess-pore-water-pressure generated inside soil skeleton
h_{exc}	Excess hydraulic head (u_e / γ_{water})
h_A	Critical excess head required for artesian flow
z	Depth (m)
z_{GWL}	Depth of groundwater level (m)
z_{AFP}	Artesian Flow Potential depth (m)
ε_v	Soil volumetric strain

1 Introduction

1.1 RESEARCH BACKGROUND

Earthquake-induced soil liquefaction analysis can be distinguished into three main parts: (1) characterization of susceptible material; (2) evaluation of liquefaction triggering during earthquake shaking; and (3) evaluation of post-shaking consequences. The first part deals with various testing methods used to characterize liquefaction susceptibility of earth materials. The second part aims to quantify the cyclic shear stress amplitude (seismic demand) and the cyclic shear resistance of the liquefiable deposit (initial and critical state of the soil) for liquefaction triggering during intense earthquake shaking. Various material characterization and liquefaction triggering evaluation methods have been developed since the 1964 Great Alaska and Niigata earthquakes, and these methods are considerably mature now. For the third part, post-shaking liquefaction consequences such as sediment ejecta-induced ground subsidence contribute significantly to the resulting ground damages; however, the procedures to estimate its severity are currently lacking.

Sediment ejecta contribute significantly to liquefaction-induced ground failures (e.g., excessive subsidence, bearing capacity failures, ground cracks, and building settlement). After earthquake shaking stops, the dissipation process of residual excess-pore-water-pressure (u_e) generated after strong shaking triggers high-gradient seepage flow that can transport the liquefied sediment vertically towards the surface or laterally underneath the ground. The seepage can flow continuously from high to low total hydraulic head in any direction until the hydrostatic condition is reached. The dissipation process of residual u_e can trigger high-gradient upward seepage, which can exploit cracks in the upper non-liquefiable crust layer. Once cracks in the crust layer are fully formed and there is sufficient artesian water pressure, the seepage flow can produce artesian flow above the ground surface while ejecting the fluidized sediment to the ground surface. As more sediment is transported to the ground surface, additional ground subsidence is produced.

Simplified liquefaction triggering procedure and liquefaction ground-failure indices such as Liquefaction Potential Index (LPI) and Liquefaction Severity Number (LSN) are commonly used to estimate the severity of liquefaction-induced ground failures. These procedures are useful to estimate the occurrence of sediment ejecta during the 2010–2011 Canterbury earthquake sequence and other earthquake events. However, they often overestimated or underestimated the amount of sediment ejecta at sites in Christchurch, New Zealand. Hence, the severity of ground failure from the Canterbury earthquakes was often over- or under-estimated [Maurer et al. 2014, van Ballegooy et al. 2014, and van Ballegooy et al. 2015(a), (b)]. The key characteristics of liquefiable sites that will or will not produce severe ejecta amount remain unclear, and analytical procedures to estimate the amount of ejecta are currently lacking.

It is extremely rare to have the opportunity to learn how the same ground and structures responded to several significant earthquakes, such as the Canterbury earthquake sequence that delivered different intensities and durations of strong shaking. The well-documented performance of land and structures in Christchurch, with the extensive suite of ground-motion recordings and the comprehensive subsurface investigation program, provide an exceptional opportunity to advance our understanding of the characteristics of liquefiable sites that will or will not produce severe ejecta amount. Nonlinear dynamic effective stress analysis (ESA) using finite-element codes such as OpenSees and robust constitutive soil models for liquefiable materials such as PM4Sand and PM4Silt is useful to simulate the hydromechanical interaction of liquefaction sites during shaking and the post-shaking redistribution of u_e during advection stage. There is merit in performing a back-analysis study of well-investigated liquefaction case histories in Christchurch to gain insights that can significantly advance the current state of the liquefaction hazard assessment practice.

1.2 PROBLEM STATEMENT

The characteristics of liquefiable sites that did and did not produce sediment ejecta manifestation during the Canterbury earthquake sequence events remain unclear. High-gradient upward seepage developed during the post-shaking advection process may become the key factor that governs ejecta occurrence and its severity. These complex hydraulic processes are not directly captured in the liquefaction-induced ground failure severity indices such as LPI or LSN, which focuses primarily on the amount of liquefaction triggering. Thus, it is not surprising that these indices often mis-estimate ejecta severity. The estimation based on LPI or LSN can potentially lead to overconservative or unconservative liquefaction mitigation designs. Figure 1.1 shows examples of underestimation and overestimation produced by LSN-based procedure in Shirley and Gainsborough district during the 2011 Christchurch earthquake that will be briefly discussed in this chapter.

Figure 1.1 shows the Shirley area (approximately 2.25 km^2) overlaid by maps of observed ejecta amount [Figure 1.1(a)] and estimated ejecta amount [Figure 1.1(b)]. The Shirley area was shaken by peak surface acceleration (PGA) of 0.35–0.45g during the 2011 Christchurch earthquake. The blue area in Figure 1.1(b) was estimated to have no ejecta (LSN < 8 based on Tonkin+Taylor [2013] LSN criteria); however, it produced Minor to Large quantities of ejecta (underestimation), as shown in Figure 1.1(a). Conversely, there are numerous sites in the Gainsborough area (Figure 1.1c-d) where high LSN values were computed (i.e., estimated to produce severe amounts of ejecta); however, there were no sediment ejecta observed during the post-earthquake reconnaissance (which is an overestimation). More than 70% of the Gainsborough area produced None to Minor amount of ejecta [Figure 1.1(c)], but it was estimated to produce Moderate amount of ejecta (LSN > 25). Even LSN values greater than 40 were calculated in many areas without any observed ejecta. The Gainsborough area was shaken by a PGA of 0.35–0.45g during the Christchurch earthquake, which is a similar shaking intensity to that of the Shirley area.

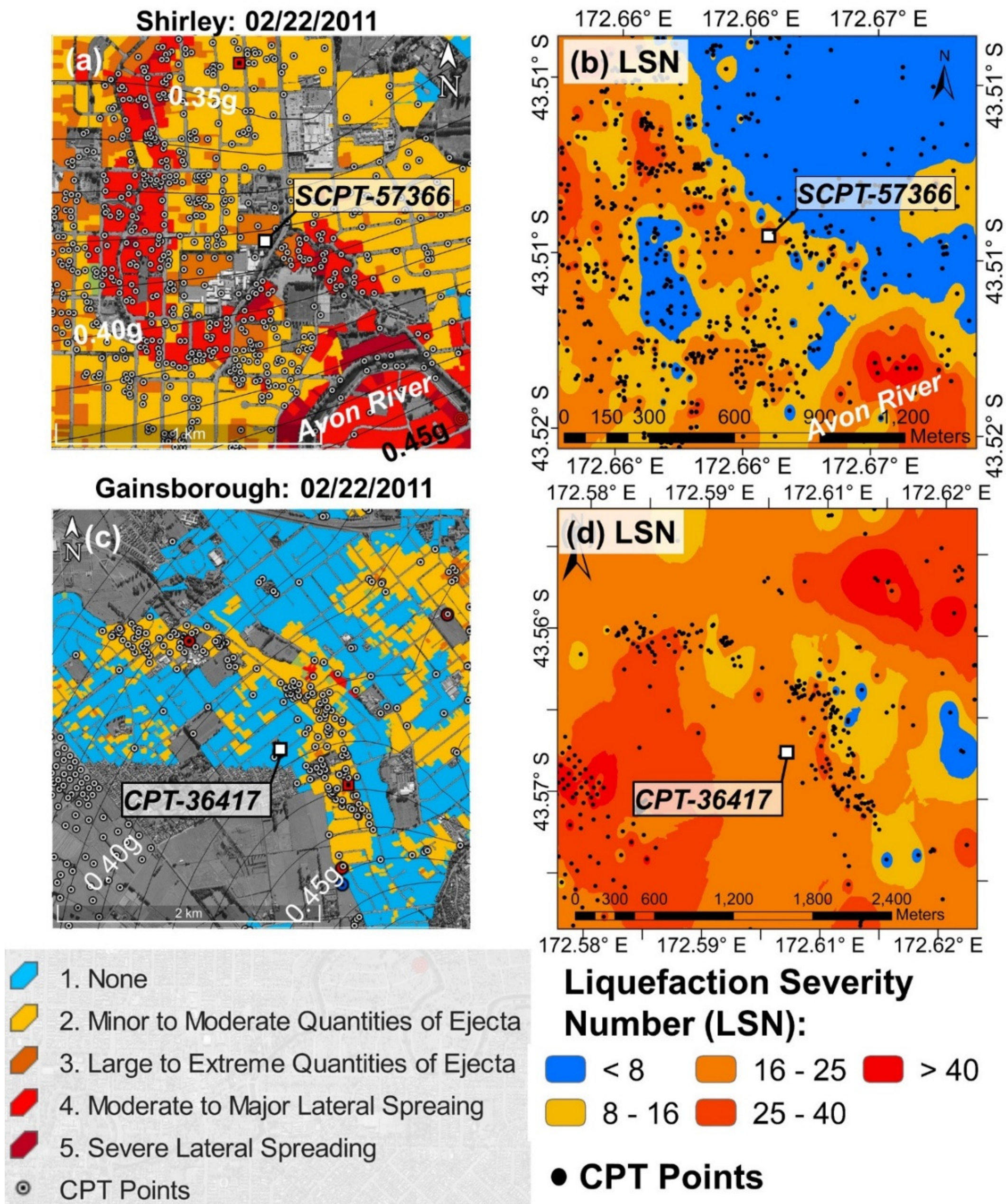

Figure 1.1 **The maps of Shirley (a-b) and Gainsborough areas (c-d) overlaid by observed ejecta manifestation after the 02/22/2011 Christchurch earthquake and calculated LSN value.**

Figure 1.2(a) indicates most areas in Shirley (70% area of the map) are underlain by silty sand to sandy silt materials [i.e., I_c = 2.05–2.60, where I_c is the Robertson [2009] CPT-based soil behavior type index] within the 0.0–3.0 m depth. The average thickness of non-liquefiable crust layer in Shirley site is approximately 3.0 m. The crust layer is then followed by thick, clean sand deposits (I_c = 1.31–1.80) until a depth of 10.0 m [Figure 1.2(b]. Interestingly, the northeast area of the Shirley map produced Minor to Moderate amount of ejecta, although it is underlain by relatively thick deposits consisting of dense sands material ($I_c \leq 1.31$) with a highly permeable crust layer. Similar underestimation cases are also observed in other parts of Christchurch described later in this report. Figure 1.2(c) indicates the soils within the depth of 0.0–3.0 m in Gainsborough consists of silty sand to sandy silt materials (I_c = 2.05-2.60), which is similar to the Shirley area. However, the soil within 3.0–10.0 m depth [Figure 1.2(d)] in most of the Gainsborough area consists of highly stratified deposits of loose liquefiable sand to silty sand and low plasticity silt to silty clay with a mean I_c of 2.05–2.60. The values between CPT points in Figures 1.1(b, d) and 1.2 are interpolated using the standard inverse distance technique using ArcMap 10 software. The maps are reprocessed using raw data published by the New Zealand Geotechnical Database [NZGD 2019]. As shown in Figure 1.2, the geotechnical stratifications of the Shirley and Gainsborough areas are fundamentally different, which may explain their distinct performance during the Christchurch earthquake in producing sediment ejecta.

The distinct layer stratification (i.e., contrasting drainage characteristics and impedance contrast) may determine the post-shaking hydraulic process that governs the direction and rate of seepage in transporting the fluidized sediment. The post-shaking hydraulic process is currently largely ignored in the typical liquefaction evaluations, as it is difficult to be considered using the simplified procedure. Advanced dynamic ESA is useful to understand the soil–water interaction during shaking and post-shaking excess pore water pressure redistribution; it requires additional effort, but the insights obtained from ESA are noteworthy, and it is feasible to perform ESA efficiently with current technologies and knowledge. However, the framework to interpret dynamic simulation results that can assess sediment ejecta potential and its severity is currently lacking. Analytical procedures that capture the post-shaking hydraulic processes of liquefaction sites are required to estimate ejecta potential reliably. Lastly, it is also possible to adopt insights obtained from ESA simulation to develop a more simplified procedure in the future.

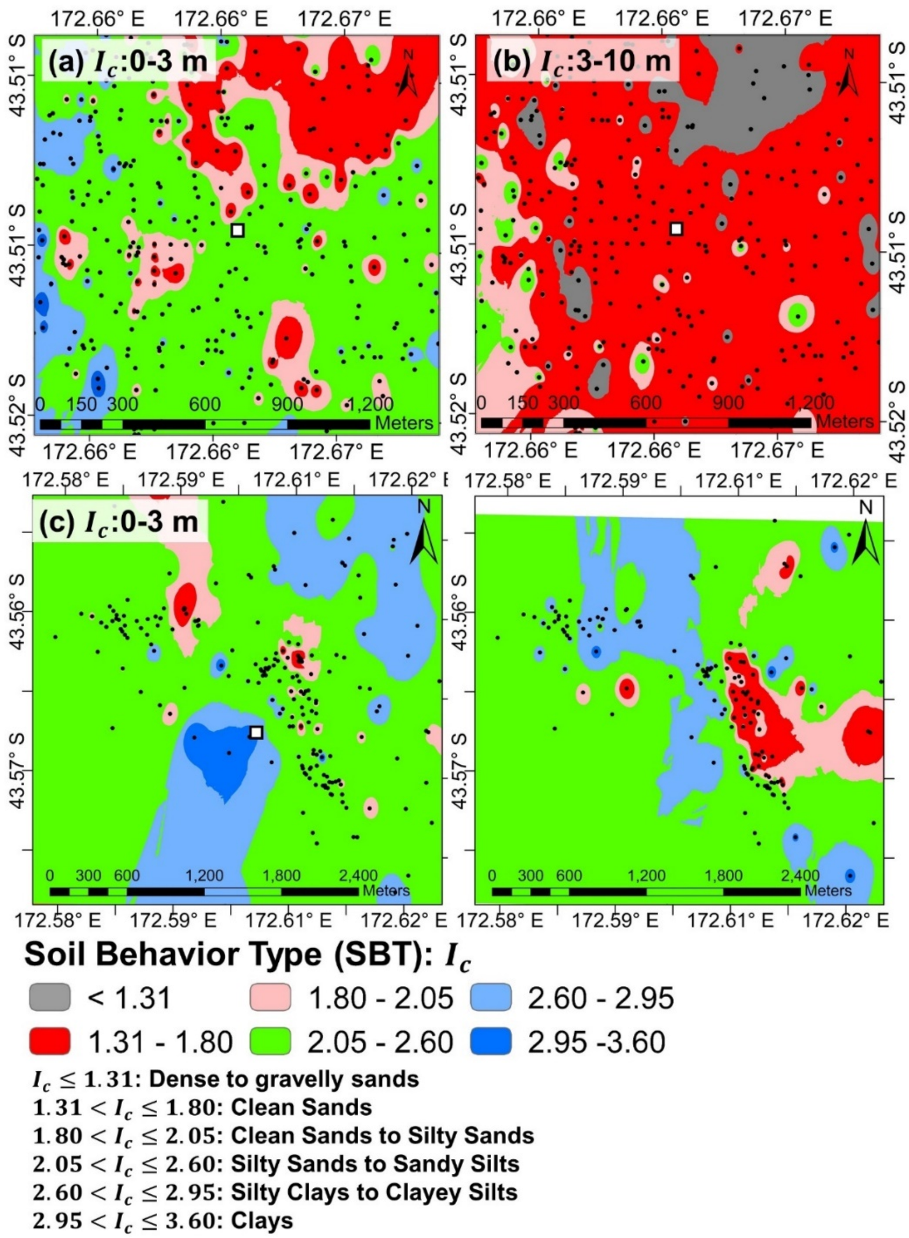

Figure 1.2 **The maps of Shirley (a-b) and Gainsborough areas (c-d) overlaid by the mean values of Robertson [2009] Soil Behavior Type (I_c) within 0.0–3.0 m depth and 3.0–10.0 m depth.**

1.3 RESEARCH OBJECTIVES

To address the problems elaborated previously, the primary objectives of this research are:

1. Identify the key geotechnical characteristics of well-investigated liquefiable sites that produce different amounts of ejecta manifestation after the 2010–2011 Canterbury earthquake sequence across Christchurch, New Zealand;

2. Investigate reasons that cause the simplified liquefaction ground-failure indices to often underestimate or overestimate the amount of sediment ejecta during the Canterbury earthquakes. Insights are gained by simulating the site's hydromechanical interaction and post-shaking advection processes using a nonlinear, fully coupled formulation, dynamic finite-element analysis (OpenSees), and robust constitutive models (PM4Sand and PM4Silt) to model the cyclic response of sand-like, transition, and clay-like soils; and
3. Develop an ESA framework and quantitative ejecta potential index to estimate the severity of sediment ejecta. The framework and indices should be: (a) able to capture the site's hydromechanical response during shaking and post-shaking hydraulic processes that govern ejecta occurrence and its severity (b) sufficiently straightforward for use in engineering practice; and (c) suitable for performance-based design as a reliable engineering demand parameter (EDP).

1.4 ORGANIZATION OF REPORT

The remaining parts of this PEER report are organized into five chapters, as follows:

- Chapter 2 reviews the mechanisms of sediment ejecta and available analytical procedures to estimate liquefaction-induced ejecta manifestation, including the simplified liquefaction ground-failures indices and advanced nonlinear dynamic ESA. The capabilities and limitations of each procedure, the governing equations, numerical model, and constitutive models for liquefiable materials utilized in this study are briefly reviewed.
- Chapter 3 summarizes the 44 well-investigated liquefiable sites that represent diverse soil stratification and ground shaking intensity during the 2010–2011 Canterbury earthquake sequence events. The key geotechnical characteristics that distinguish sites with and without ejecta are discussed. The evaluations of liquefaction-induced ejecta manifestation at these sites are performed using the CPT-based liquefaction triggering procedure and the liquefaction ground-failures indices. The correlation of estimated severity based on computed index values and observed ejecta amount is evaluated using the box-and-whisker framework.
- Chapter 4 presents the application of dynamic ESA to perform liquefaction evaluation and to estimate the severity of sediment ejecta manifestations. The ESA is performed to back-analyze two representative level-ground sites that were overestimated and underestimated using simplified liquefaction procedures after the 2010–2011 Canterbury earthquake sequence events. The former site consists of a stratified silty soil deposit that develops high pore water pressures in isolated sandy soil layers, but the amount and rate of upward seepage are insufficient to produce ejecta. The later site consists of a thick, clean sand site that develops high seepage rates

that are sustained long after strong shaking, ends to produce severe ejecta. This chapter presents the formulation of the Artesian Flow Potential (AFP) concept and the Ejecta Potential Index (EPI) to capture the post-shaking hydraulic mechanism and to estimate ejecta potential quantitatively using ESA.

- Chapter 5 presents the results of dynamic ESA of 45 well-documented liquefaction field case histories that provide insights on the seismic response of sites where simplified procedures indicated liquefaction effects would be severe, but surface manifestations were not observed, or inconsistent amounts of sediment ejecta were observed. The EPI values for each site are computed, and the seismic response characteristics of sites with and without ejecta manifestation are discussed. The results indicate a strong correlation between the estimations based on the EPI and the observed ejecta severity. Sites without ejecta have low EPI values, and sites with severe ejecta have high EPI values.
- Chapter 6 summarizes the analyses performed in this report and the key findings identified in this research.

2 Analytical Procedures for Evaluating Liquefaction-Induced Ejecta Manifestation

2.1 MECHANISM OF SEDIMENT EJECTA

Sediment ejecta (also referred to as a sand boil) is a primary manifestation of soil liquefaction triggering. It results from the dissipation of high residual excess-pore-water-pressure (u_e) and excess hydraulic pressure head ($h_{exc} = u_e / \gamma_{\text{fluid}}$ generated after strong earthquake shaking (e.g., Housner [1958], Ambraseys and Sarma [1969], Lowe [1975], and Seed [1979]). The elevated h_{exc} produces a transient hydraulic gradient that triggers groundwater seepage advecting from high to low total hydraulic head. During the advection process, the seepage can transport the liquefied sediment vertically or laterally (which creates cavities at some locations), on top of which the ground can subside excessively. High-gradient upward water flow with enough artesian water pressure can buoy up the soil particles, inducing heaving (quicksand condition) or hydraulic fracturing of the overlying competent crust layer. Consequently, with sufficient artesian pressure, upward seepage-induced artesian flows above the surface occurs while ejecting the fluidized sediment, which lasts until the system reaches a steady state. The more sediment is transported to the surface, the larger the cavity that is created, which in turn leads to more severe ground failure.

Sediment ejecta appeared several minutes after the beginning of the 1934 Bihar, India, earthquake [Housner 1958]. The time-delay represents the required time for exploiting cracks within the crust layer before the liquefied sediment can be ejected onto the ground surface. The height of the ejection can reach 4–5 ft above the ground surface and produce a large conical-shaped (volcano-like) sediment ejecta (up to 6 m in diameter). Similar descriptions were reported by Ambraseys and Sarma [1969] in several important earthquakes in history (e.g., 1906 San Francisco and 1964 Niigata earthquakes). These researchers proposed closed-form solutions to quantify the magnitude of artesian pressure as a basis to estimate ejecta potential; however, their use in engineering practice is limited. The fundamentals of liquefaction-induced ejecta described in Lowe [1975], Seed [1979], and NRC [1985], NASEM [2016] provide key insights toward the understanding of the sediment ejecta process.

The 1976 Tangshan, China, earthquake is an interesting case history with documentation of sediment ejecta. The New York Times newspaper, on June 11, 1979, reported:

> *"...some sand blows around Tangshan reached a height of 10 feet and continued for several hours. They were so voluminous that irrigation canals were blocked, and farmland was buried."* [Sullivan 1979]

The reporter summarized the field investigations by a team led by the late Professor Housner. There was one village near the coast that settled 3 m and was inundated permanently by the sea [Huixian et al. 2002]. They reported that the ejecta began to appear one minute after the earthquakes and continued for several minutes—eyewitness accounts reported several hours in some cases. Gao et al. [1983] performed a detailed study of a level-ground area in the north of Tangshan city, which is underlain by a sandy clay crust followed by a loose deposit of fine sand with varying thickness with Standard Penetration Test (SPT) *N* values between 5 and 24. The study collected 226 boring logs with the water table shallower than 4 m. Later, the boring logs were analyzed by Ishihara [1985] to construct the boundary curves for identifying surficial liquefaction-induced damages. The Ishihara [1985] plot is commonly used in engineering practice to estimate the likelihood of ejecta occurring based on non-liquefiable crust thickness, liquefiable layer thickness, and PGA of earthquake shaking.

The 1989 Loma Prieta, California, earthquake produced moderate sediment ejecta across the Marina District of San Francisco [Bardet and Kapuskar 1993]. The eyewitness accounts reported that the sand boils appeared two or three minutes after the earthquake. Kawakami [1965] reported a similar ejection time frame following the 1964 Niigata, Japan, earthquake. The largest well-measured sand boils in the Marina District covered about 29 m^2 area with sediment height of 10–20 cm range. The 1995 Kobe, Japan, earthquake is another case history with well-documented reports of sand boils occurring (e.g., Cubrinovski et al. [1996] and Soga [1998]). The Port Island strong-motion station vertical array is a valuable liquefaction case history site that has been studied extensively by numerous researchers. The surrounding strong-motion station was covered by sediment ejecta where 300–400 mm ground subsidence and 150–200 mm of ejected sediment height was observed.

The 2011 Tohoku, Japan, earthquakes and the 2010–2011 Canterbury earthquake sequence events produced extensive documentation of sediment ejecta (e.g., the GEER reports [Ashford et al. 2011 and Cubrinovski et al. 2011] and the New Zealand Geotechnical Database [NZGD 2019]). Observed ejecta severity from none to extreme ejecta are recorded and quantified very well as shown in Figure 2.1. Extreme ejecta amounts were observed on a level-ground area in Kamisu city [Figure 2.1(a)], which is on a natural deposit 11 km away from the bay. The sediment ejecta covered almost the entire area of the city (1000–10,000 m^2) and caused extreme ground failure [Ashford et al. 2011]. The reported ground subsidence was as high as 2 m. Similar phenomena were observed during the 2011 February Christchurch earthquake, where the post-shaking upward seepage caused ground heaving conditions on level-ground areas underlain by thick sand deposits. The upward seepage triggered after the earthquake raised the pre-event groundwater level (GWL) to the ground surface elevation at sites [e.g., Figure 2.1(a-b)]. The ground softened significantly and, in many cases, led to complete loss of bearing capacity (i.e., buoyancy condition or quicksand). Light objects—such as a car—can sink into the ground, but when the sand deposit gains back its strength, it is difficult to pull the object from the ground; see Figure 2.1(b).

(a) (b) (c)

Figure 2.1 **(a) Extreme ejecta manifestation in Kamisu city after the 2011 Tohoku earthquake [Ashford et al. 2011]; (b) A car sunk into liquefied ground where the GWL raised to the surface after the 2011 February Christchurch earthquake [Cubrinovski et al. 2011]; and (c) sediment ejecta process at sites with low k_v crust layer in Christchurch suburb after the 2011 June Christchurch earthquake (source: https://youtu.be/rRVK5NJE2qE).**

The typical pattern of ejected sediment at thick, clean sand sites is usually longitudinal and uniformly distributed. Sediment ejecta mechanism at sites with low-hydraulic conductivity (k_v), cohesive and competent crust layer differs. Instead of heaving, localized upward seepage-induced cracks (e.g., due to hydraulic fracturing and internal erosion) is mobilized in the weakest part of the crust. The low k_v layer confines the high-gradient upward seepage so the GWL cannot rise quickly. Consequently, the high-gradient upward water flow exploits cracks in the crust layer, and with enough artesian pressure, it can produce long-duration artesian flow while transporting a significant amount of liquefied sediment to the ground surface. The ejection process is illustrated in the video recorded by an eyewitness account during the 2011 June Christchurch earthquake shown in Figure 2.1(c). The eyewitness account reported, *"The liquefaction started gushing up about 5 minutes after the quake and was very noisy."* The time delay represents the required time for the upward seepage to mobilize cracks in the entire crust layer. The diameter and the height of the sand boil are estimated to be 7 m and 30 cm, respectively. The size of the sand boil depends on the ejection duration, which is controlled by the amount of the residual u_e that must be dissipated to reach a hydrostatic condition. Numerous cases of buildings experiencing large differential settlements caused by sediment ejecta were also observed and documented in Bray et al. [2014].

Sediment ejecta is a post-shaking hydraulic phenomenon that can be assessed by characterizing important parameters including (1) stratification of soil deposit, i.e., vertical and horizontal hydraulic conductivity, density, and drainage characteristic; (2) thickness and materials of top crust layer; (3) groundwater level; (4) spatial variability; and (5) ground-motion intensity. Case histories documentation since the last 85 years identify key characteristics of sediment ejecta process, including (1) time-delay before ejection started; (2) rise of the GWL to the ground surface; (3) tendency to trigger upward seepage-induced heaving or hydraulic fracturing that depends on the material of crust layer; (4) long ejection duration that lasts several minutes after shaking ceased; and (5) ejection height that could exceed a meter above the surface. Hence, the key aspects for evaluating sediment ejecta potential are to analyze the post-shaking redistribution of residual u_e and h_{exc}, seepage flow direction, and total hydraulic head developed during and after the earthquake.

To better visualize the sediment ejecta process, it is informative to generalize the sediment ejecta process at level-ground sites into several hypothetical soil stratification systems for three time periods (i.e., before shaking, during shaking, and after shaking) as illustrated conceptually in Figure 2.2. The one-dimensional (1D) soil profiles A, B, and C represent sites with thick liquefiable clean sand deposits with different density overlain by high k_v, thin low k_v, and thick low k_v, competent crust layers, respectively. The soil profiles D, E, and F represent sites with partially stratified liquefiable clean sand deposits separated by thin low k_v layer in between, which is overlain by thick low k_v, thin low k_v, and high k_v crust layer, respectively. The soil profiles G, H, and I represent sites with highly stratified deposits of liquefiable sand, silt, and clay with relatively similar thickness. The profile J is similar to profiles A-C; however, site J is visualized to represent sites located adjacent to the sites like site G-I and to represent the influence of spatial variability.

Earthquake shaking generally tends to liquefy the loosest clean sand deposit first (layers with white background color in Figure 2.2) and generate high u_e and h_{exc} at deeper depths, which is the part of the deposit subjected to higher cyclic shear stress. Liquefaction triggering at deeper elevation can reduce the amplitude of cyclic shear stress at a shallower depth in some cases to a level insufficient to liquefy the shallow soil (e.g., Cubrinovski et al. [2019] and Kramer and Greenfield 2019]. The low k_v layers do not liquefy, but they can still generate pore water pressure depending on its plasticity index (PI). Once earthquake shaking stops, the dissipation of residual u_e initiates upward water flow. The upward seepage developed at sites A-C can flow without any restriction from low k_v layers, and site A or J may produce ejecta during shaking where a quicksand condition is expected. With a similar hydraulic gradient with site A (similar arrow thickness), upward seepage-induced hydraulic fracturing processes in the low k_v competent crust layers begin to occur at sites B-C. During the advection stage, the seepage completely cracks the crust layer, wherewith sufficient artesian pressure; it can produce artesian flows that ejects severe to extreme ejecta amount. The surrounding upward seepage can also flow into the localized crack that contributes to a longer ejection process and transport more sediments at the location where the cracks are developed.

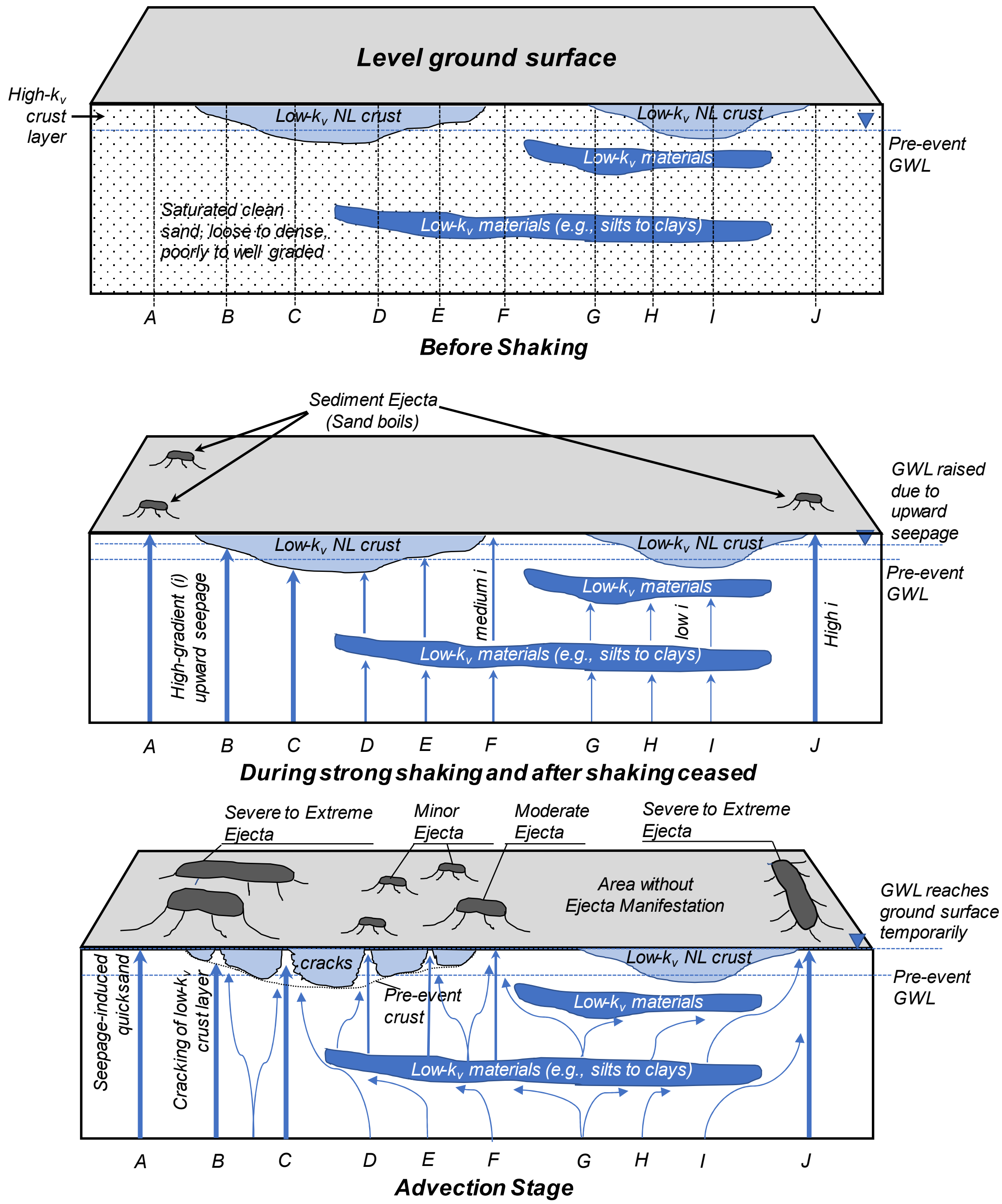

Figure 2.2 **Conceptual illustrations of the process of sediment ejecta in different layer stratification systems (A-J) at level-ground sites. The scale for the quantity of surficial ejecta manifestation is drawn for illustrative purposes only. The horizontal distance is not to scale.**

Earthquake shaking tends to liquefy the loosest sandy soil first located below and above the low k_v layers at sites D-F. The upward seepage developed above the low k_v layer can flow without restriction and start to mobilize cracks in the top crust layer during shaking. However, the upward seepage developed at deeper depth is impeded by the low k_v layer; see Figure 2.2. During the advection stage, the rate of upward seepage developed at sites D-F is lower than sites A-C because the flow contribution from deeper sand deposits is eliminated; thus, less ejecta are expected. The thickness and permeability of the crust layer largely determine the ejecta severity. The upward seepage will also flow towards zones with the lowest hydraulic head where some can flow to nearby localized cracks and contribute to an extended ejection duration. The low k_v layer can sustain high u_e inside their pores after shaking due to its slow dissipation behavior (i.e., low coefficient of consolidation, c_v).

For sites G-I, the highly stratified deposit consists of the interlayered liquefiable clean sand deposit and more than one low k_v layers, as illustrated in Figure 2.2. The earthquake shaking most likely only liquefies the bottom and middle sand deposits. The seismic stress working at the top sand deposit is usually insufficient to liquefy the soils due to soil softening at a deeper liquefied layer. Consequently, upward seepage is developed only at the bottom and middle sand layers, but they cannot flow through the top low k_v layers. The water will flow toward the zone with a lower total head. If there is an adjacent site like site J with a clean sand deposit that dissipates the excess hydraulic head rapidly, the seepage from site G-I can flow laterally (to site J or F), which can extend the ejection duration at site F or J. This post-shaking hydraulic process can produce contrasting amounts of ejecta at adjacent sites, where no ejecta manifestation is observed above the highly stratified profile (site G-I), but severe-to-extreme ejecta is observed above the clean sand site (site J or F). Additionally, at sites like A, F, and J, the upward seepage can raise the GWL to the ground surface quickly and cause heaving, as shown in Figure 2.1(a-b). Conversely, the upward seepage cannot raise the GWL quickly at sites B, C, D, and E; however, it can mobilize localized cracks in the crust layer that will produce typical sand boils, as shown in Figure 2.1(c).

2.2 SIMPLIFIED PROCEDURE

The simplified procedures for evaluating liquefaction triggering of cohesionless soils are derived empirically based on the post-earthquake reconnaissance database. The liquefaction criteria are inferred based on the presence of sand boil or ground cracks at the surface or other indications of liquefaction. The site is inferred to not liquefied if there are no observed sand boil or cracks, etc. regardless of triggering of liquefaction and post-shaking advection mechanism underneath the site. *In situ* penetration testing such as SPT or cone penetrometer test (CPT) are then performed at selected investigated sites to determine the critical and loosest sandy layer and its engineering parameters (e.g., depth, soil properties, and penetration resistance). The penetration resistance is normalized and corrected to account for effects such as fines content and atmospheric and overburden pressure.

Seismic demand in terms of cyclic shear stress ratio (CSR) for each critical layer is then estimated using the procedure proposed by Seed and Idriss [1971] as the function of: (1) total and effective overburden vertical stress (σ_{vo}); (2) best-estimated peak surface acceleration value, (3) earthquake magnitude to represent event duration and loading cycles, and (4) depth reduction factor (r_d) to account for soil column nonlinearity at a deeper depth. The normalized penetration resistance and CSR for each critical layer are then compared on a CSR vs. penetration resistance axes, as illustrated in Figure 2.3(a). The filled and void dots represent investigated sites with and without evidence of sand boils or cracks, respectively. An advanced regression based on deterministic or probabilistic analysis is then performed to construct a boundary line between the filled and the void database, and referred to as the cyclic resistance ratio (CRR) line.

The CRR line represents the maximum CSR value a soil element can resist, at a specified depth and penetration resistance value, against triggering of liquefaction. The factor of safety against liquefaction (FS_L) of soil elements [illustrated by red square dots in Figure 2.3(b)] can be computed by dividing the estimated CRR with the CSR value at each depth. The points plotted above the CRR line indicate that CSR is strong enough to trigger liquefaction at the specified depth, as illustrated in Figure 2.3(a). For the last 50 years, numerous researchers have collected field data to construct more accurate CRR lines by utilizing a different database, *in situ* testing, r_d, normalization procedures, and regression techniques [e.g., Seed and Idriss [1971], Seed and de Alba [1986], Stark and Olson [1995], Suzuki et al. [1995], Robertson and Wride [1998] (RW), [Youd et al. 2001] YEL), Cetin et al. [2004], Moss et al. [2006] (MEL), Idriss and Boulanger [2008], Boulanger and Idriss [2014], Boulanger and Idriss [2016] (BI-16)].

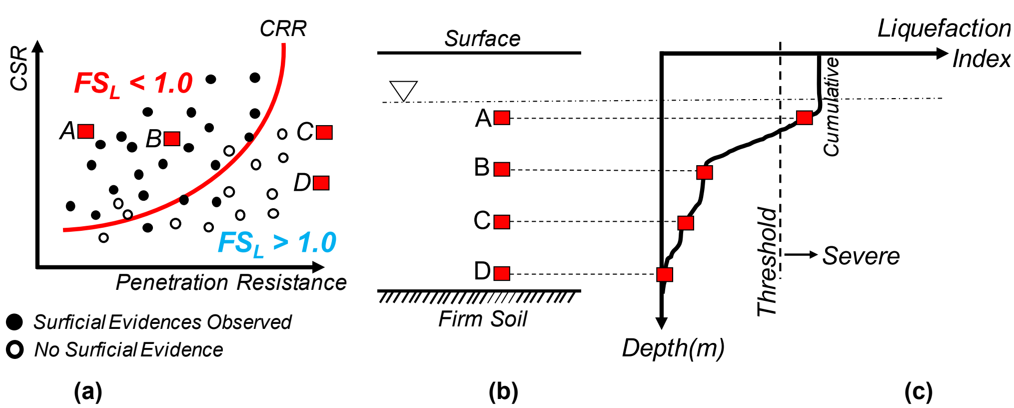

Figure 2.3 **Conceptual illustrative of the simplified procedure for evaluating liquefaction triggering of cohesionless soils at an elevation and liquefaction vulnerability indices for assessing the severity of liquefaction-induced damages.**

Simplified liquefaction triggering procedures (FS_L-based) are reliable if it is used to evaluate triggering of liquefaction at a specified depth although the procedures do not provide an assessment of the severity of liquefaction consequences. Liquefaction-induced ground failure indices [e.g., LPI [Iwasaki et al. 1978 1982] or LSN [van Ballegooy et al. 2014)] are commonly used to estimate ground failure severity. Each index requires FS_L value at each depth as an input to compute the index value through different equations. The LPI equation is based on FS_L at each depth with linear depth function, whereas the LSN equation is based on estimated post-liquefaction volumetric strain and power-law depth function as the weighting factor. The estimated severity of liquefaction manifestations (e.g., Minor, Moderate, Major) are derived empirically by correlating the calculated index values for each investigated case history and the observed surficial manifestation. A site with liquefaction indices exceeding a severe threshold value, as illustrated in Figure 2.3(c), is expected to have a severe liquefaction-induced ground failure. The shallow soil elements illustrated in Figure 2.3(c) (between A and B) are usually the critical layer as they contribute the most (i.e., have the steepest slope) to the total calculated index value.

The Ishihara [1985] boundary curves in Figure 2.4 are derived empirically from case histories of 1976 Tangshan, China, and 1983 Nihonkai, Japan, earthquakes; see Figure 2.4(a). To estimate the likelihood of ejecta occurring, the procedure is based on non-liquefiable crust thickness (H_1), liquefiable layer thickness (H_2), and the PGA of earthquake shaking. Liquefaction-induced ground damage is expected if a case is plotted above the proposed boundary curves in Figure 2.4(b) and vice versa. The boundary curve for 0.2g and 0.4~0.5g cases are derived based on the 1983 Nihon Kai-Chubu and 1976 Tangshan case history, respectively. The definition of H_1 and H_2 are illustrated conceptually in Figure 2.4(c).

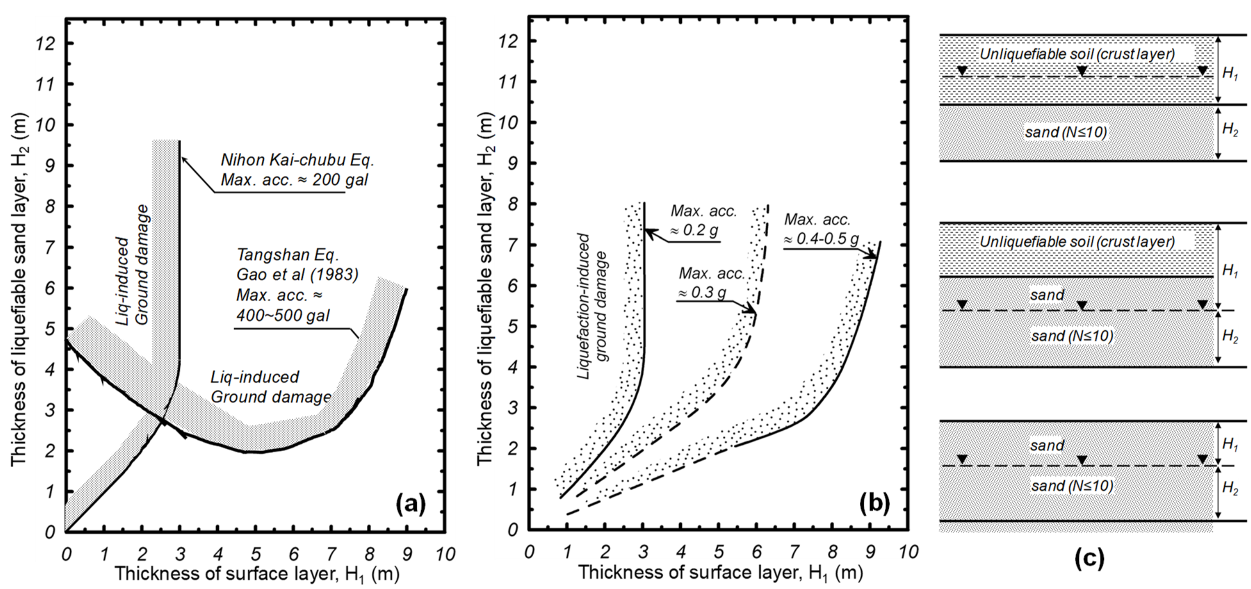

Figure 2.4 **The Ishihara [1985] curves derived from two earthquake events to distinguish liquefied field case histories that did and did not produce observed liquefaction-induced ground damage.**

Gao et al. [1983] reported some cases where liquefaction-induced ground failures are not observed at sites with thin crust layer underlain by a liquefiable sand layer; see Figure 2.4(a). It is highly likely that soil stratification at these sites may have prevented ejecta from occurring. Ishihara [1985] argued that the characterization of the surface layer thickness is probably the main reason for the deficiency. It must be noted that in this figure, the curves are limited to sites with thick deposits of liquefiable sand and does not address stratified soil sites. Moreover, the curves provide only a binary prediction (Yes or No) without providing an estimate of the amount of ejecta.

Towhata et al. [2016] developed a useful liquefaction severity chart by comparing the computed LPI values and H_1 values for cases with and without various levels of liquefaction-induced damage at residential house sites. The chart was developed using 116 borehole data in 14 sites in the South Kanto district of Japan after the 2011 Tohoku earthquake. The LPI is computed using the Japanese Highway Bridge Design Code, and H_1 is estimated using the Ishihara [1985] procedure, but without considering soft clay layers with SPT-N ≤ 2. To improve the evaluation, they reduced the estimated cyclic resistance to consider (a) the long duration of the M_w9.1 Tohoku earthquake and (b) the influence of the age to cyclic resistance of sand deposits. The philosophy of the chart is similar to that of the Ishihara [1985] chart as it compares the liquefaction demand (i.e., using LPI instead of the thickness of the liquefied layer used in Ishihara [1985] chart) and crust resistance represented by H_1.

The FS_L-based simplified procedures (e.g., RW, YEL, MEL, and BI-16) are a practical, useful, and reliable framework for evaluating liquefaction triggering at a specified depth. However, the derived liquefaction indices (e.g., LPI and LSN) often misestimate the quantity of surficial ejecta manifestation, which determines the severity of ground failure [e.g., Toprak and Holzer [2003], Holzer et al. [2006], Maurer et al. [2014], and van Ballegooy [2015a, b]. Conceptually, the simplified procedure evaluates the liquefaction-induced damage by only evaluating the CSR and CRR during earthquake shaking, without directly considering post-shaking mechanisms in the formulation. The procedure is derived based on the presence or absence of surficial manifestations of liquefaction, which is produced by the post-shaking hydraulic mechanism. However, the index formulations do not directly capture the post-shaking hydraulic mechanisms that govern the occurrence of sediment ejecta and its severity. It is not surprising that they struggle to capture a phenomenon as complex as the formation of sediment ejecta. To estimate ejecta amount reliably well, the liquefaction index should capture the post-shaking hydraulic process. The advanced numerical analysis presented in the next section provides a mechanistic and physics-based approach that can capture the soil–fluid interaction during and after shaking that may provide insights for quantifying sediment ejecta potential.

2.3 NONLINEAR EFFECTIVE STRESS ANALYSIS

Early studies (e.g., Housner [1958] and Ambraseys and Sarma [1969]) developed closed-form solutions for computing the distribution of u_e within the soil deposit to quantify the artesian pressure that can blow the liquefied sediment to the ground surface. These researchers suggested that estimating the u_e generated by earthquake shaking is the key step to quantify ejecta potential. Soil can be treated as a porous medium comprised a solid skeleton and voids filled with water, air, or other fluids. Soil is a multiphase material, and its behavior is strongly influenced by the interaction of the solid and fluid phases. Liquefaction is triggered when the increase of pore fluid pressure during seismic excitation causes the solid particles to lose their inter-granular contact and frictional strength. The equation that governs the solid-fluid interaction was first established by Biot [1941] for the consolidation problem—theory of porous media—and extended later for dynamic problems (e.g., Biot [1956], [1962a], and [1962b]). Zienkiewicz and Shiomi [1984] generalized Biot's equations and proposed a solution technique utilizing the finite-element method. The governing equations are distinguished into three general coupled formulations based on the unknown dependent variables that must be solved: (1) *u–p*; (2) *u–U*; and (3) *u–p–U,* where u is the solid displacement, p is the pore fluid pressure, and U is the pore fluid displacement. Hereafter, ESA is defined as a numerical method used to solve the governing coupled equations in which the unknown variables for each formulation are computed simultaneously at each time step.

Figure 2.5 illustrates the ESA framework employed in this research. It is convenient to idealize a level-ground site with saturated liquefiable deposit shaken by earthquake event, $\ddot{u}(t)$, into a 1D or two-dimensional (2D) space where the deposits of nonlinear soil above an elastic half-space are modeled using a constitutive law. The nonlinear soils are treated as saturated porous material consists of solid and fluid, where it can be discretized into smaller element meshes subjected to seismic cyclic shear stress (τ_{xy}) as illustrated in Figure 2.5.

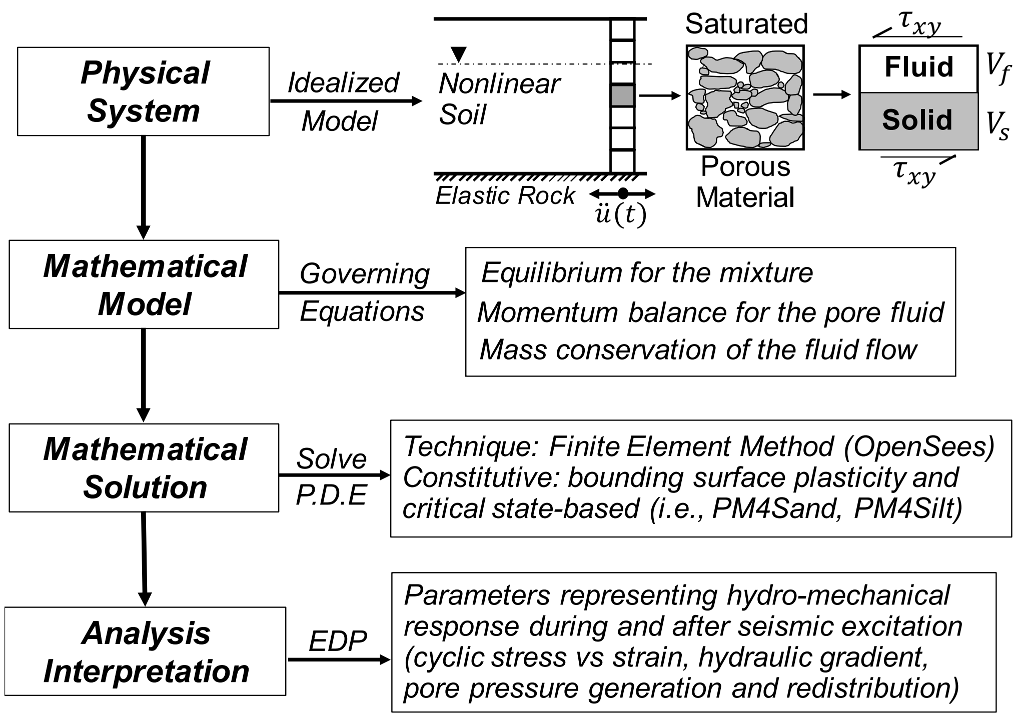

Figure 2.5 Computational frameworks to perform a numerical simulation of soil–water interaction during liquefaction using nonlinear effective stress analysis procedure.

The *u-p* formulation proposed by Zienkiewicz and Shiomi [1984] is selected as the governing equation in which the analysis is carried out to compute *u* of the solid phase and *p* of the fluid phase simultaneously (fully coupled analysis). The first governing equation is the equilibrium or momentum balance equation for the solid–fluid mixture, where the divergence of the internal stresses and acting body forces (due to gravity) equal the external excitation, such as lateral seismic forces. By assuming that the influence of fluid acceleration ($\ddot{U}$) in the system can be neglected, using index notation for tensor calculus, the equation is given by

$$(\sigma'_{ij} + \delta_{ij} p)_{(,j)} - \rho \ddot{u}_i + \rho b_i = 0 \tag{2.1}$$

where σ'_{ij} is the effective stress tensor; δ_{ij} is the Kronecker delta; p is the fluid pore pressure; and ρ is the density of the solid–fluid mixture, which for fully-saturated soil is equal to $\rho = n\rho_f + (1-n)\rho_s$, where n is the porosity and ρ_f and ρ_s are the solid particle and water density, respectively; $\ddot{u}_i$ is the acceleration of the solid part, and b_i is the body force per unit mass (gravity).

The second governing equation ensures the momentum balance of the fluid phase as

$$-p,_i - R_i + \rho_f b_i = 0 \tag{2.2}$$

where R is the viscous drag force acts between soil matrix and pore fluid. According to Darcy's seepage law, it is expressed as $R_i = K_{ij}^{-1}\dot{w}_i$, where K_{ij} is the Darcy permeability tensor, and $\dot{w}_i$ is the fluid velocity relative to the solid phase. The permeability coefficient K in Equation (2.2) is different from the hydraulic conductivity tensor (k_{ij}) usually measured in the laboratory or estimated using *in situ* testing. Their values are related by $K_{ij} = k_{ij} / g\rho_f$, where g is the gravitational acceleration.

The third equation ensures the conservation of mass of the fluid flow in and out of the mixture (the continuity equation), where the flow divergence, $w_{i,i}$ due to volume changes is balanced. The changes are caused by increased volumetric strain $(\dot{\varepsilon}_{ii})$ compression of void fluid due to the fluid pressure increase, compression of solid grains by the fluid pressure increase, and the change in volume due to change in the intergranular effective contact stress [Zienkiewicz and Shiomi 1984]. The mass conservation of fluid flow equation is given as

$$-\dot{w}_{i,i} = \dot{\varepsilon}_{ii} + \frac{1}{Q}\dot{p} \tag{2.3}$$

where the bulk stiffness of the solid-fluid mixture Q is expressed as $1/Q = n/K_f + (\alpha - n)/K_s$; the Biot's coefficient α is 1.0 for typical soil mechanics problem, and K_f and K_s are the bulk moduli of the solid and fluid phases, respectively. Substituting Darcy's viscous drag force equation into Equation (2.2), Equation (2.3) can be expressed as

$$\left[K_{ij}\left(p_{,i} + \rho_f b_i\right)\right]_i + \dot{\varepsilon}_{ii} + \frac{\dot{p}}{Q} = 0 \tag{2.4}$$

Equations (2.1) and (2.4) are the final fully coupled equations based on the *u-p* formulation for the boundary value problems in geomechanics. The strong form of the Equations (2.1) and

(2.4) can be presented in weak form through matrix equations and solved numerically using finite-element discretization via the standard Galerkin method [e.g., Prevost [1985a], Zienkiewicz et al. 1999, Elgamal et al. [2002, 2003], Huang et al. [2004], Pastor et al. [2011], and McGann et al. [2012]. The *u-p* formulation is the most straightforward and most convenient, although it comes with some limitations. The general, mixed *u-p-U* formulation discussed in Jeremic et al. [2008] provides a complete alternative but with a more complex solution. The equations for the mixture can be extended to solve more complex problems such as the temperature and heat balance equation.

The numerical solution to solve the coupled differential equations of Equations (2.1) and (2.4) was implemented by McGann et al. [2012] in OpenSees [McKenna and Fenves 2000]. An efficient low-order quadrilateral element with an hourglass stabilization technique was developed to provide an element that is free from volumetric locking and satisfies the stability for the incompressible-impermeable condition. The quadrilateral element mesh consists of 1 stabilized-single-point (SSP) integration point and four corner nodes of solid displacement and fluid pressure, as shown in Figure 2.6, which requires less computing time. The model can be extended into 2D space by extending it horizontally with little modification on the boundary condition. The constitutive model for each element is discussed in the following section.

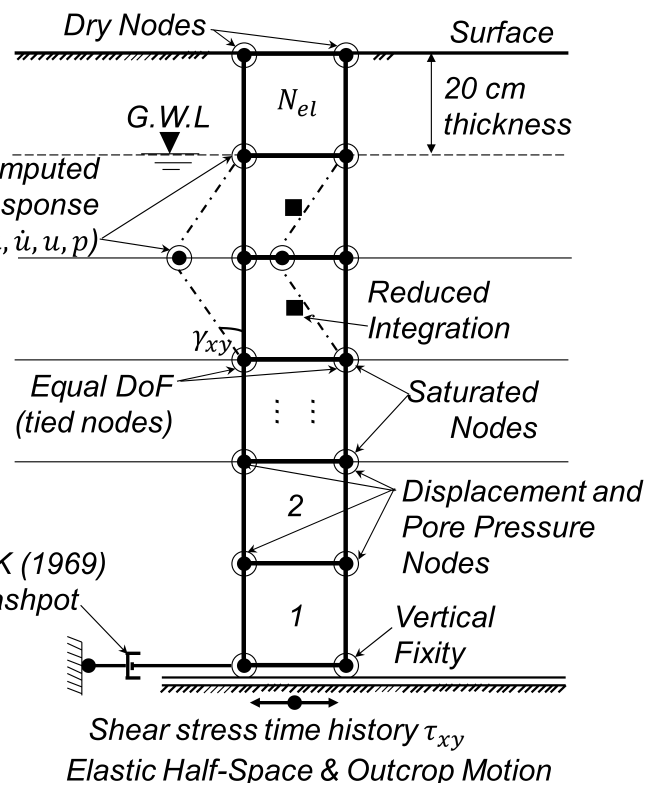

Figure 2.6 **OpenSees finite-element model with SSP quadrilateral element to simulate hydromechanical problems based on *u-p* formulation.**

To represent 1D space and simple shear mechanism, all solid-displacement nodes (u) at the same elevation are tied to move together horizontally. The displacement nodes at the bottom of the model are fixed where the dashpot is attached for the input seismic shear–stress time history, following the Joyner and Chan [1975] procedure. The boundary condition for the pressure nodes is separated based on GWL elevation, where dry nodes have zero p, and p at the saturated nodes are computed. The dynamic analysis is carried out, and parameters that explain the hydromechanical interaction (e.g., shear strain, generated pore pressure) of the problem is interpreted.

Numerous researchers have validated the implementation of advanced dynamic ESA to perform liquefaction simulation by using different numerical formulations and constitutive models (e.g., Zeghal and Elgamal [1994], Cubrinovski et al. [1996], Bonilla et al. [2005], Ziotopoulou et al. [2012], Roten et al. [2014], Gingery et al. [2016], Markham et al. [2016], Kramer et al. [2016], Hutabarat and Bray [2019], and Kramer and Greenfield [2019]). A key aspect of performing reliable simulations is the use of a fully coupled hydromechanical formulation and robust constitutive models for liquefiable materials. The response of liquefiable cohesionless soils under cyclic loading is determined primarily by (1) changes of effective stress tensor (σ'_{ij}); (2) dilatancy behavior (volumetric change caused by shearing deformation); and (3) the initial state (soil fabric, density and mean confining pressure) relative to the critical steady state (no volume changes under constant shearing).

To model these important behaviors, numerous researchers have developed constitutive soil models for liquefiable materials over the last few decades [e.g., Prevost [1985b]; Iai et al. [1992]; Towhata and Ishihara [1995]; Manzari and Dafalias [1997]; Cubrinovski and Ishihara [1998]; Kramer and Arduino [1999]; Li and Dafalias [2002], Yang et al. [2003]; Dafalias and Manzari [2004]; Taiebat and Dafalias [2008]; Beaty and Byrne [2011], Zhang and Wang [2012], Wang et al. [2014], and Boulanger and Ziotopoulou [2017]). In this research, the liquefaction simulations were performed using the McGann [2012] *u-p* formulation, and the PM4Sand and PM4Silt constitutive models that have been implemented into OpenSees*,* which was selected because its implicit formulation allows faster computing time to perform long-duration simulations in this research. The next section reviews the primary parameters and calibrations required to use PM4Sand and PM4Silt constitutive models in numerical simulations.

2.4 REVIEW ON PM4SAND AND PM4SILT CONSTITUTIVE MODELS

2.4.1 PM4Sand

The PM4Sand soil constitutive model [Boulanger and Ziotopoulou 2017] was implemented in OpenSees by Chen [2020]. PM4Sand is formulated based on bounding surface plasticity theory [Manzari and Dafalias 1997] and can account for the effect of soil fabric on the shear-strain accumulation as proposed by Dafalias and Manzari [2004]. PM4Sand is derived based on critical state soil mechanics (CSSM) concept [Been and Jefferies 1985] and follows Bolton [1986] empirical critical state line. PM4Sand is a robust and practical model that was developed specifically for a 2D cyclic simple shear loading condition with a straightforward soil calibration procedure. The model parameters can be estimated from *in situ* testing, such as the CPT. The ESA performed in this report utilizes the PM4Sand model to represent the contractive-dilative response of sand-like material (e.g., non-plastic sandy silts to clean sand).

This section discusses the PM4Sand primary and secondary parameters that influence the modeled cyclic response including, the required number of cycles to reach liquefaction ($N_{c\text{-}liq}$), the shape of the hysteretic loop (cyclic stress vs. strain), rate of shear strain accumulation, pore pressure generation, and stress path. A set of cyclic simple shear (CSS) simulation of one quadrilateral SSP element modeled using the PM4Sand model is performed using OpenSees. The simulation considers a baseline model where each parameter is changed systematically within a realistic range to evaluate its sensitivity. The baseline parameters are:

- Relative density, $D_r = 55\%$
- Confinement, σ'_{vo} = 1 atm
- Shear modulus coefficient, $G_o = 796$ ($N_{160} = 14$)
- Contraction rate parameter, $h_{po} = 1.0$
- At-rest coefficient of lateral pressure, $K_o = 0.5$
- Applied CSR = 0.175
- All secondary parameters are default.

Primary Parameters

The PM4Sand primary parameters are D_r, σ'_{vo}, h_{po}, and G_o. The general trend shown in Figure 2.7 shows that D_r, σ'_{vo}, h_{po} are the most sensitive parameters that determine the required number of cycles to liquefy the soil ($N_{c\text{-}liq}$, using 3% single amplitude shear strain criteria). However, D_r, σ'_{vo}, and G_o are the site (constrained) parameters that can be well-characterized using an *in situ* test. Thus, h_{po} is the only primary parameter for model calibration; Figure 2.8 presents its singular effect on the cyclic response of the soil model. The h_{po} value only influences the $N_{c\text{-}liq}$ and the cyclic rate to reach zero effective stress condition ($r_u = 0.99$), and its influence on the rate of shear-strain accumulation once the liquefaction is triggered is small. The h_{po} value in Figure 2.8 is determined only for capturing the general trend and should not be treated as the limit or range for calibration in engineering practice. The effect of other primary parameters on the modeled soil response can be seen in Appendix E of this report.

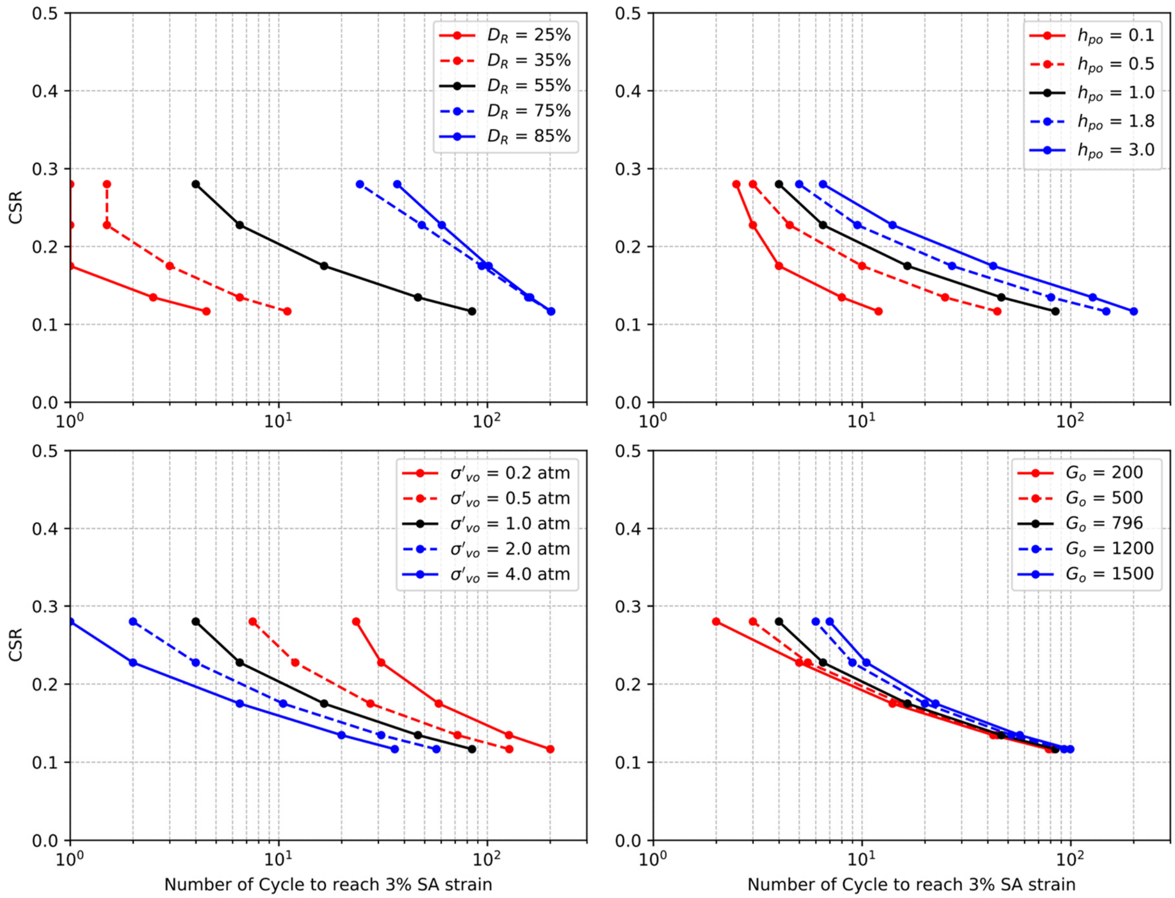

Figure 2.7 **Influence of PM4Sand primary parameters on the cyclic resistance curve and number of cycles to reach 3% single amplitude (SA) strain.**

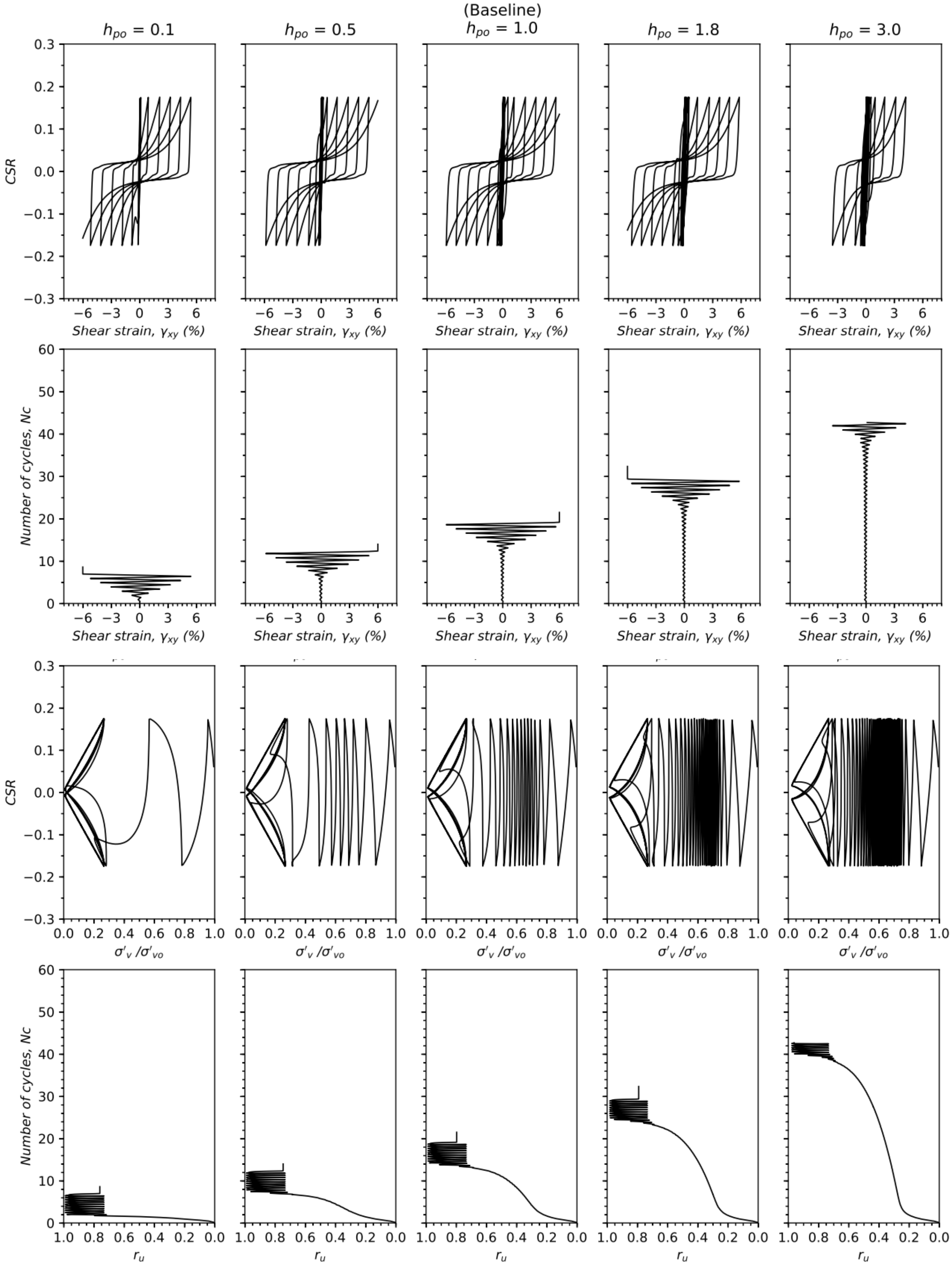

Figure 2.8 Effect of h_{po} parameter on different soil response.

Secondary Parameters

PM4Sand has 21 secondary parameters that can be adjusted to modify the shape of the hysteretic loop, rate of shear strain accumulation, pore pressure generation, and stress path. Pertinent to our study, the four most sensitive single parameters that influence the $N_{c\text{-}liq}$ are the critical state line parameters (R and Q), h_o, and C_{GD}, as shown in Figure 2.9. The effect of the other 17 parameters is relatively minor. However, it must be noted that the calibration procedure may involve more than a single parameter, which can change the overall response. This section only intends to summarize the general trend of the soil response variation modeled by each parameter. The calibration of R and Q parameters determine the position and curvature of Bolton's [1986] critical state line that can determine if advanced cyclic testing is available. However, the default values recommended in Boulanger and Ziotopoulou [2017] are reasonable for the typical uncemented and young-age sand if cyclic testing is not available. The h_o parameter determines the plastic modulus relative to elastic modulus, and its variation has a similar trend to h_{po} parameter. The changes in h_o value are not sensitive to the rate of shear-strain accumulation. The C_{GD} parameter is sensitive to determine the rate of shear-strain accumulation, as shown by the different slope in Figure 2.10. The higher C_{GD} value tends to accelerate the strain accumulation during cyclic loading. The other important parameters are the slope of the bounding surface and phase-transformation line that controls the contractive-dilative transformation response, which is controlled by n^b and n^d parameters; see Appendix E.

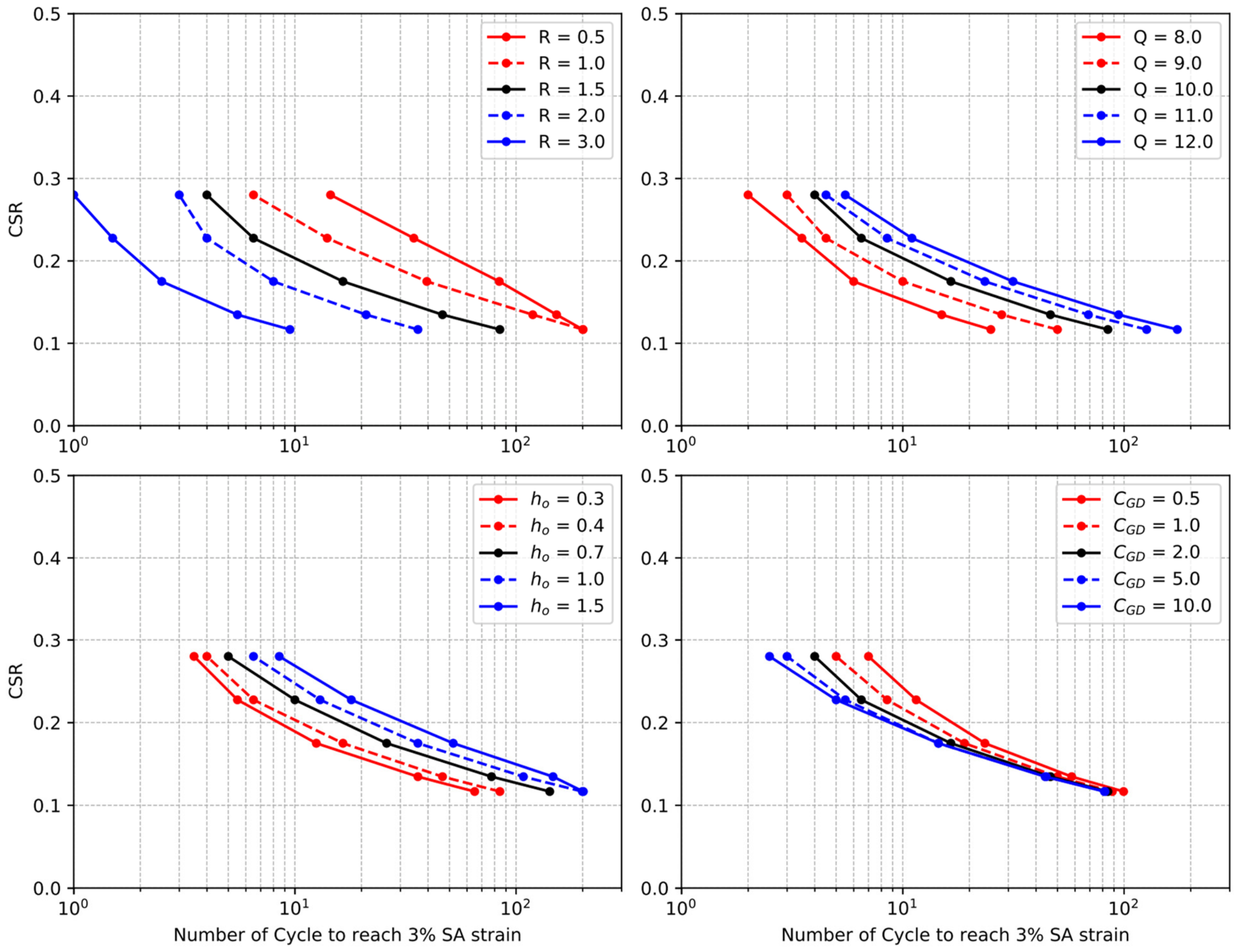

Figure 2.9 **Influence of some of the PM4Sand secondary parameters on the cyclic resistance curve and number of cycles to reach 3% single amplitude (SA) strain on modeled soil response**

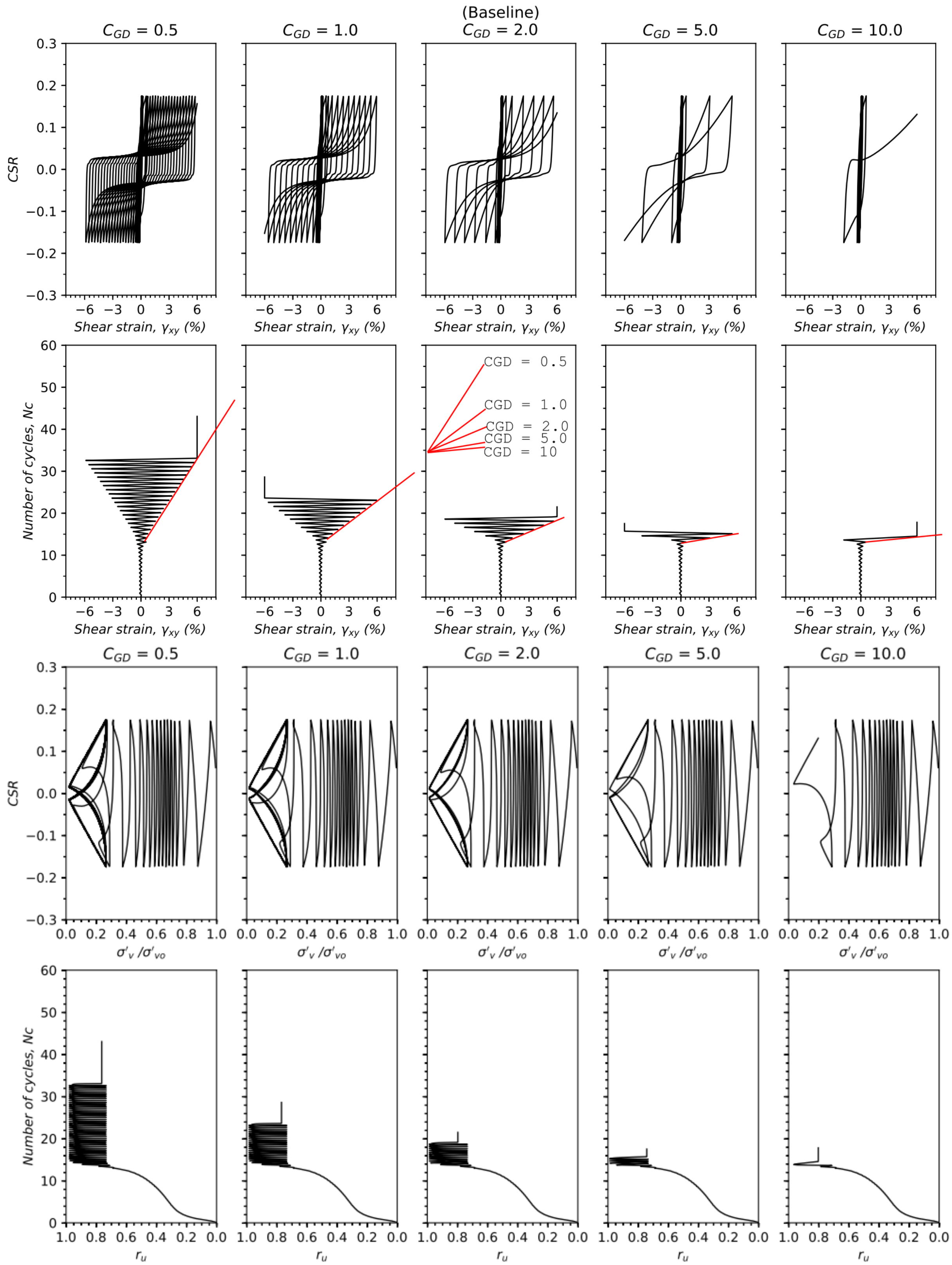

Figure 2.10 Effect of C_{GD} parameter on the rate of shear strain accumulation

Calibration

In this research, the calibration of PM4Sand parameters aims to produce key behaviors including (1) reasonable $N_{c\text{-}liq}$ corresponds to a CSR level; (2) rate of shear strain accumulation before and after liquefaction is triggered; and (3) how abrupt the soil transforms from contractive to dilative behavior during shearing. It is important to capture the dilation pulses phenomenon, which is usually observed in the surface acceleration time history of liquefied sites. Once the initial state of the soil is characterized (i.e., D_R, G_o, σ'_{vo}, and K_o, the *CSL* position on D_R vs. mean confining pressure axis), the h_{po} is calibrated to adjust the number of cycles required to match a target curve. *In situ*-based target curves are used for soils without advanced laboratory testing. The rate of shear strain accumulation can be adjusted if there is available data where the C_{GD} parameter is one effective parameter to calibrate. All the remaining secondary parameters are set to default values as the sensitivity caused by them are considerably minor (see Appendix D).

2.4.2 PM4Silt

The PM4Silt soil constitutive model was implemented in OpenSees by Chen [2020]. PM4Silt is formulated using a similar framework to PM4Sand. The transition fine-grained soils (e.g., low-plasticity silts to clays) are also susceptible to stiffness degradation due to elevated pore pressure during cyclic loading. Transition soils are partially drained materials [Schneider et al. 2008; Robertson 2016], which exhibits partial behavior of sand-like and clay-like materials. The response of transition soils under cyclic loading is primarily determined by its consistency expressed by its Atterberg's limits. The transition soils with higher Plasticity Index (PI) behave like clay-like materials in which cohesive forces exist between soil particles under zero confining stress conditions (e.g., liquefaction). Cyclic triaxial test results of soils with the low and medium PI show that the PI value influences the shape of the hysteretic loop under cyclic shearing in which the soil with higher PI have a fatter hysteretic loop (less dilative) and vice versa (e.g., Boulanger et al. [1998]; Polito and Martin [2001], Sancio [2003], Bray and Sancio [2006], Donahue [2007], Dahl et al. [2014], Price et al. [2017], and Beyzaei et al. [2018b]). The cyclic behavior of transition and clay-like soils under cyclic simple shear loading in this study are modeled using the PM4Silt model [Boulanger and Ziotopoulou 2018].

This section discusses the PM4Silt primary and secondary parameters that influence the modeled cyclic response, such as the rate of shear strain accumulation, size of the hysteretic loop, pore pressure generation, and stress path. A set of CSS simulations of one quadrilateral SSP element modeled using the PM4Silt model was performed using OpenSees. The simulation considered a baseline model where each parameter is changed systematically within a realistic range to evaluate its sensitivity. The baseline parameters are:

- Undrained shear strength ratio, $S_u / \sigma'_{vo} = 0.25$
- Confinement, $\sigma'_{vo} = 1$ atm
- Shear modulus coefficient, $G_o = 600$
- Contraction rate parameter, $h_{po} = 10.0$

- Applied CSR = 0.7 S_u / σ'_{vo}
- All secondary parameters are default.

Primary Parameters

The PM4Silt primary parameters are S_u/σ'_{vo} (or simply S_u), h_{po}, and G_o. Similar to PM4Sand, the h_{po} parameter is the predominant parameter that controls the number of cycles required to reach a 3% single-amplitude strain. The S_u/σ'_{vo} is the most important parameter that controls the stress vs. strain, and whether the modeled soil will behave as a contractive or dilative material. The S_u/σ'_{vo} is analogous with relative density parameter in PM4Sand models since the S_u/σ'_{vo} governs the initial state of the soil relative to the critical state line. The effect of h_{po} parameter on the cyclic response of the soil is given in Figure 2.11. PM4Silt tends to produce a gentler slope of CSR vs. $N_{c\text{-}liq}$ relationship, which is consistent with laboratory test summarized in Boulanger and Ziotopoulou [2018]. The variation of G_o is relatively minor to the overall response that can be seen in Appendix D. Thus, S_u/σ'_{vo} and h_{po} are the key parameters that must be well-characterized to perform a reliable analysis.

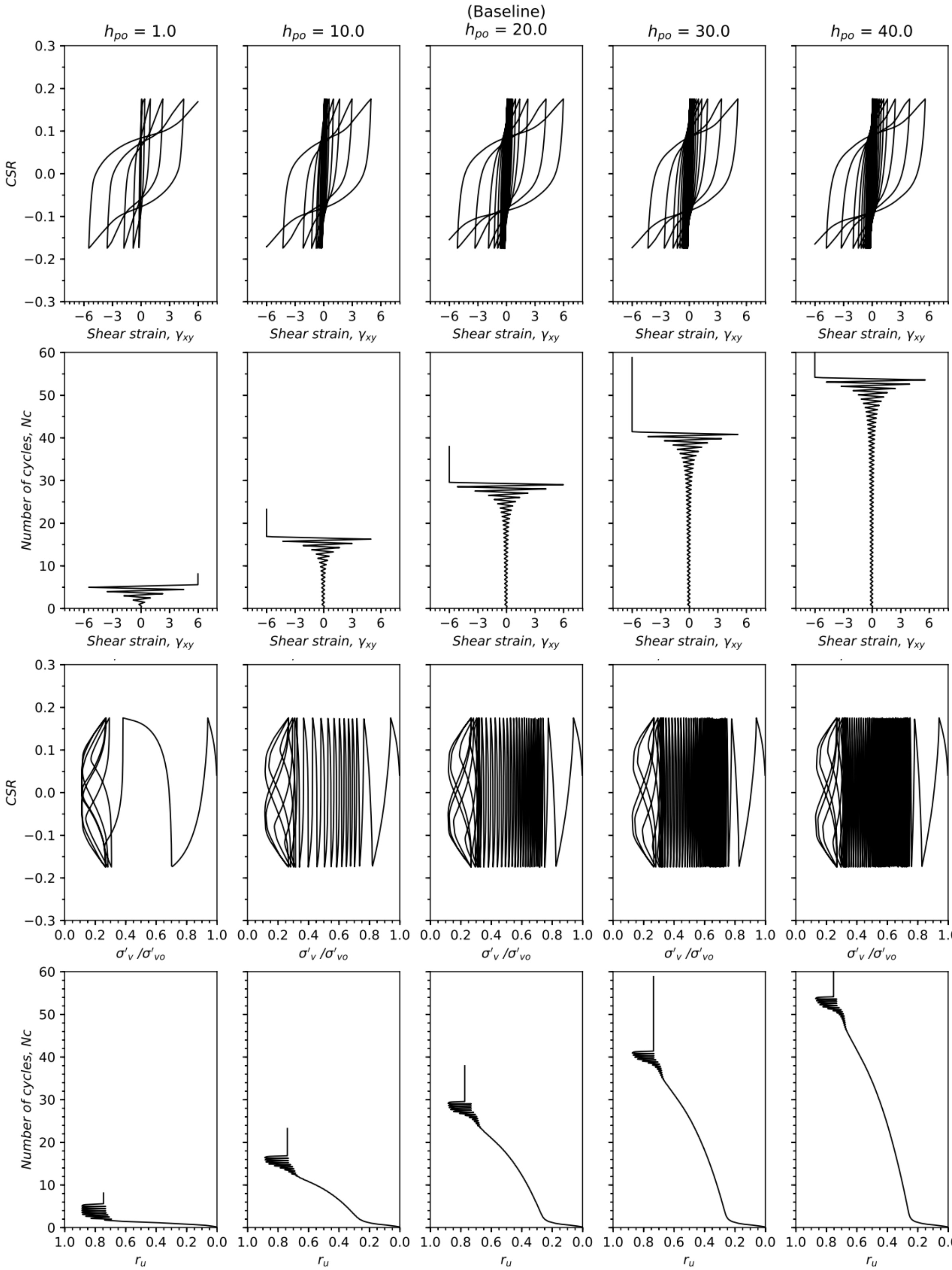

Figure 2.11 Effect of h_{po} parameter on the cyclic response of a PM4Silt soil element.

Secondary Parameters

The secondary parameters of PM4Silt can be adjusted to calibrate the shape of the hysteretic loop, rate of shear strain accumulation, pore pressure generation, and stress path. The four most sensitive parameters that influence soil cyclic response the most are $r_{u\text{-}max}$, A_{do}, C_{GD}, h_o. The $r_{u\text{-}max}$ parameter determines the dilatancy behavior of the modeled soil that controls the size of the hysteretic loop, as shown in Figure 2.12. The $r_{u\text{-}max}$ parameter distinguishes the soil with clay-like behavior ($r_{u\text{-}max}$ < 0.7) from dilative transition-soil ($r_{u\text{-}max}$ > 0.9). Clay-like soils (soils with high PI values) behave as pure contractive materials during cyclic loading but still can accumulate high shear strain and moderate u_e. Soils with lower PI values have more tendency to transform from contractive to dilative phase, and this behavior can be modeled by adjusting the $r_{u\text{-}max}$ parameter. The $r_{u\text{-}max}$ parameter of low-plasticity transition soil (e.g., silty soil with PI < 12 based on Bray and Sancio [2006]} is set to 0.90, as presented later in Chapter 4. The A_{do}, C_{GD}, and h_o parameters are associated with the rate of shear-strain accumulation. These parameters can be calibrated if cyclic testing is available; otherwise, the default value is recommended. The bounding surface parameter ($n^{b,\ wet}$) is important for adjusting the strain hardening or softening response during monotonic loading. The influence of other parameters can be seen in Appendix E.

Calibration

In this research, the calibration of PM4Silt parameters aims to produce key behaviors including:

1. the shape and size of hysteretic stress vs. strain loop under cyclic loading (i.e., the response of clay-like or transition soils);
4. rate of shear strain accumulation before and after liquefaction is triggered; and
5. maximum pore pressure ratio ($r_{u\text{-}max}$).

Once the initial state of the soil is characterized (i.e., S_u/σ'_{vo}, G_o, and $r_{u\text{-}max}$ based on PI data), the h_{po} is calibrated to adjust the number of cycles required to match a target curve. Boulanger and Ziotopoulou [2018] suggested that a peak shear strain of 3% might be caused by 10–30 uniform loading cycles at a CSR = 0.7 S_u/σ'_{vo} or 30–100 uniform loading cycles at a CSR = 0.55 S_u/σ'_{vo}. The rate of shear strain accumulation can be adjusted if there is available data, where the A_{do}, C_{GD}, and h_o parameters are the sensitive parameter; however, default values still produce reasonable behavior. From our study, the remaining secondary parameters have a relatively minor effect on the modeled cyclic response (e.g., see plots like Figure 2.9 and 2.10 for other parameters in Appendix E).

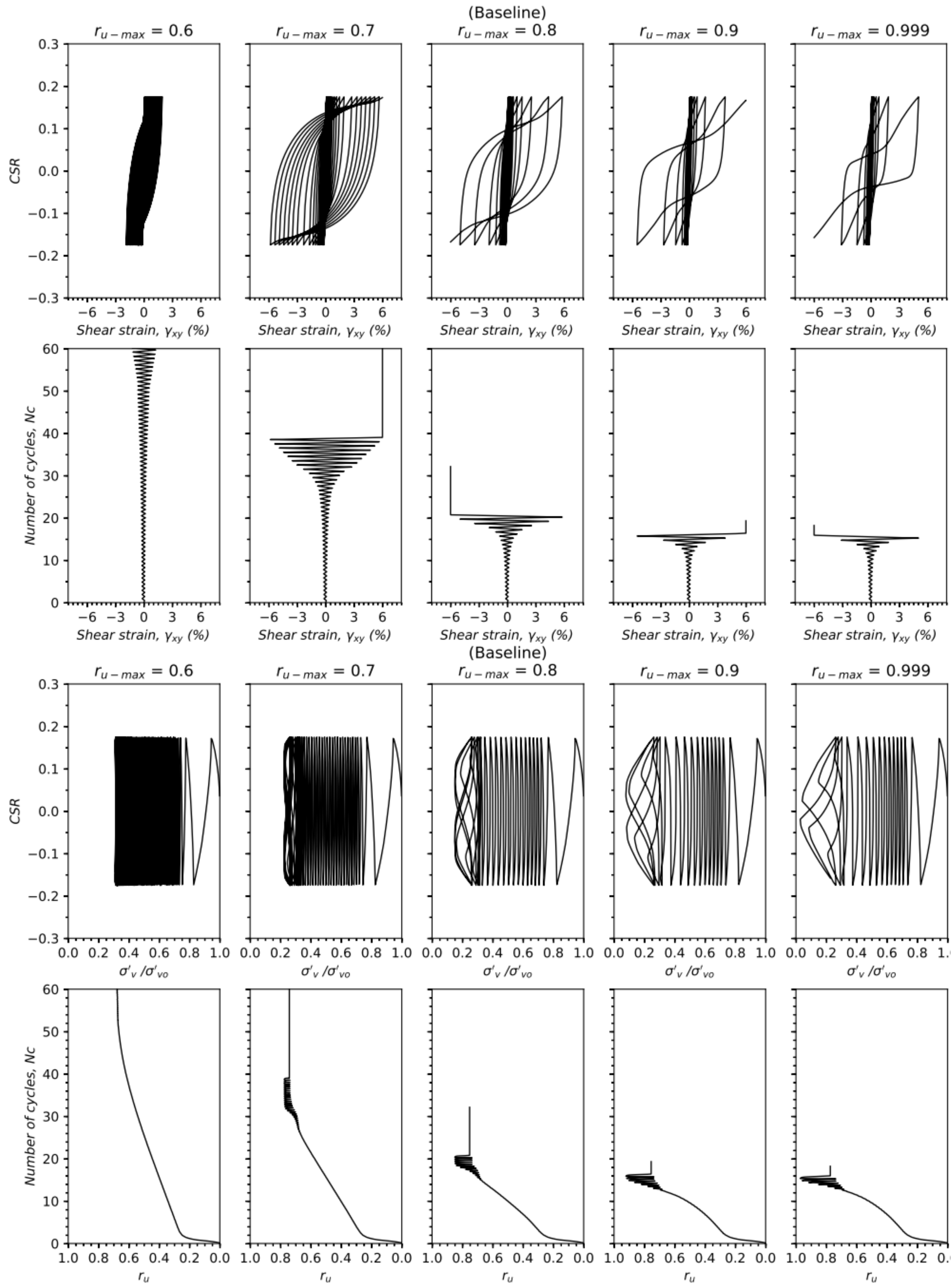

Figure 2.12 Effect of $r_{u\text{-}max}$ parameter on the cyclic response of a PM4Silt soil element.

3 Christchurch Liquefaction Case Histories

3.1 THE 55 LIQUEFACTION SITES PROJECT

The Canterbury earthquake sequence events produced numerous well-documented liquefaction case histories with different amounts of sediment ejecta (e.g., van Ballegooy et al. [2014] and Green et al. [2014]). The LSN-based and LPI-based procedures tended to overestimate or underestimate the likelihood and severity of liquefaction-induced ground failure caused by the Canterbury earthquakes. For example, they produced excessive overestimation at numerous silty soil sites in the southwestern part of Christchurch after the Canterbury earthquake sequence events (e.g., Tonkin + Taylor [2013] and Maurer et al. [2014]). To investigate the cause of these overestimations, researchers from the University of Canterbury, University of California, Berkeley, University of Texas at Austin, and Tonkin + Taylor selected 55 Christchurch sites that represent various soil stratification and ground shaking intensity. The 55 sites produced different amounts of sediment ejecta ranges from none to extreme amount of sediment ejecta manifestations. They noted excessive overestimation based on the liquefaction indices (high LPI or LSN values) at numerous highly stratified soil sites where no evidence of sediment ejecta was observed (e.g., Beyzaei et al. [2018a, b], and Cubrinovski et al. [2019]). The goal of this investigation is to identify reasons that cause the overestimation since all 55 sites contain soil deposit that is judged to liquefies during the Canterbury earthquake sequence events.

Detailed field reconnaissance was carried out by Tonkin + Taylor using data including field inspection, high-quality aerial photographs, ground subsidence estimation based on pre- and post-event LiDAR measurement, and extensive *in situ* (e.g., borehole, CPT, compression and shear wave velocity measurement, V_p and V_s) and laboratory testing (e.g., soil properties and advanced cyclic triaxial testing). The severity of sediment ejecta for each site was classified based on the total area covered by sediment ejecta relative to the total area under assessment, which is within 20-m radius from a CPT investigation point. Table 3.1 summarizes the severity criteria used in this research, as reported by Tonkin + Taylor [van Ballegooy, *Personal Communication*, 2018]. Table 3.1 also provides the best-estimate ejecta induced settlement. The typical aerial photographs of observed ejecta are shown later in this report.

Table 3.1 Criteria to classify observed ejecta manifestation.

Observed ejecta manifestation	Area within 20-m Radius covered by ejecta (%)	Best estimate ejecta-induced settlement (mm)
None	0	0
Minor	< 5	< 50
Moderate	5-20	50 – 100
Severe	20-50	100 – 300
Extreme	> 50	> 300

The relative location of all 55 investigated sites with the geological map of Christchurch region [Brown and Weber 1992] is shown in Figure 3.1. They are deliberately selected to represent various ground-motion intensity level from four different earthquakes (2010 Darfield, 2011 February and June 2011, and 2011 December events) around the city of Christchurch, layer stratification (i.e., which consists of thick sand deposits and partially-to-highly stratified sand, silt, and clay deposits), and different amount of observed surficial ejecta manifestation (i.e., None to Extreme ejecta). There are 11 sites (see black circles in Figure 3.1) located near the Avon River with observed lateral spreading evidence, which are excluded in this research. Thus, the other 44 sites (see blue and red square in Figure 3.1) are the focus of this research: they are located away from the river and can be classified as free-field, level-ground sites (there are nearby light structures such as one-two story residential housing at some sites). All 44 sites have extensive subsurface information (e.g., geophysics measurement, borehole, CPT, GWL monitoring, and laboratory testing) and post-earthquake seismic performance assessments. The detail of the soil profile, CPT-based liquefaction assessment, and observed ejecta severity for each site are summarized in Appendix A.

As noted previously, excessive overestimations were observed at highly stratified soil sites. To evaluate these field case histories, it is useful to divide the 44 level-ground sites into two groups:

1. Sites containing thick, clean sand deposits where there are approximately 4.5 m thickness of continuous sand-like and high k_v soil below the GWL until a depth of 10 m as depicted in Figures 3.1 and 3.2; and

6. Sites containing partially-to-highly stratified sand-like, transition, and clay-like soil layers where there is no continuous sand-like soil with thickness greater than 5 m below the GWL until a depth of 10 m as shown in Figures 3.1 and 3.3

The Robertson [2016] Soil Behavior Type (SBT) I_B classification system is used to classify the sand-like, transition, and clay-like soil, indicated by the colored background in Figures 3.2–3.3. The severity of surficial liquefaction-induced ejecta manifestation observed at each site after the 2010 M_w7.1 Darfield, 2011 M_w6.2 Christchurch, 2011 M_w5.6 and 6.0 June, and 2011 M_w5.8 and 5.9 December earthquakes are represented by four letters below the site's name in Figures 3.2–3.3. Figures 3.4 and 3.5 show the seismic performance of the 44 sites relative to the surrounding area after the Darfield and Christchurch earthquakes, respectively.

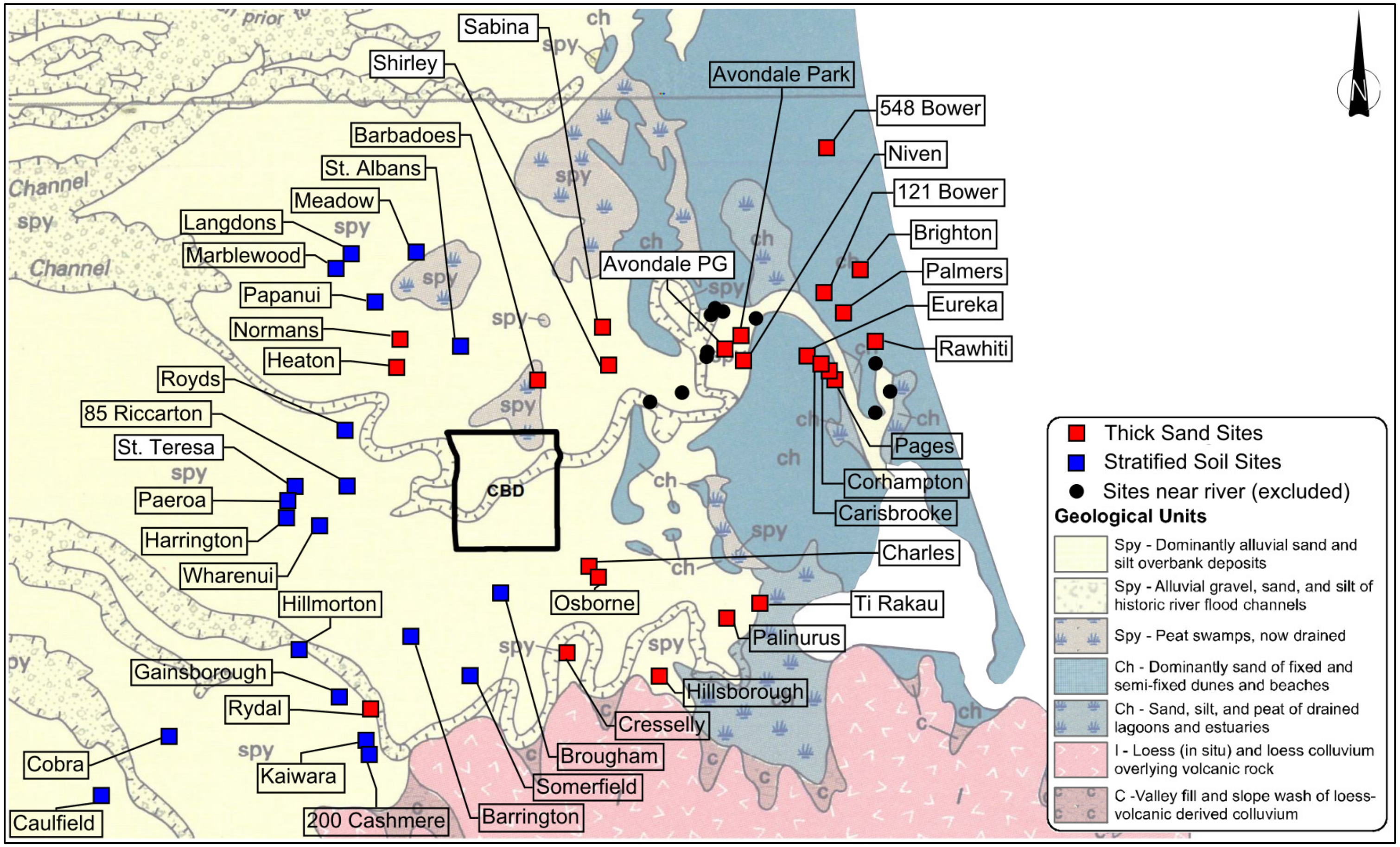

Figure 3.1 **Geological mapping of Christchurch, New Zealand (Brown and Weber [1992], Institute of Geological and Nuclear Science) and the location of 55 well-investigated liquefaction case history (24 thick, clean sand sites, 20 stratified soil sites, and 11 near river sites). (after van Ballegooy, *Personnel Communication* [2018]).**

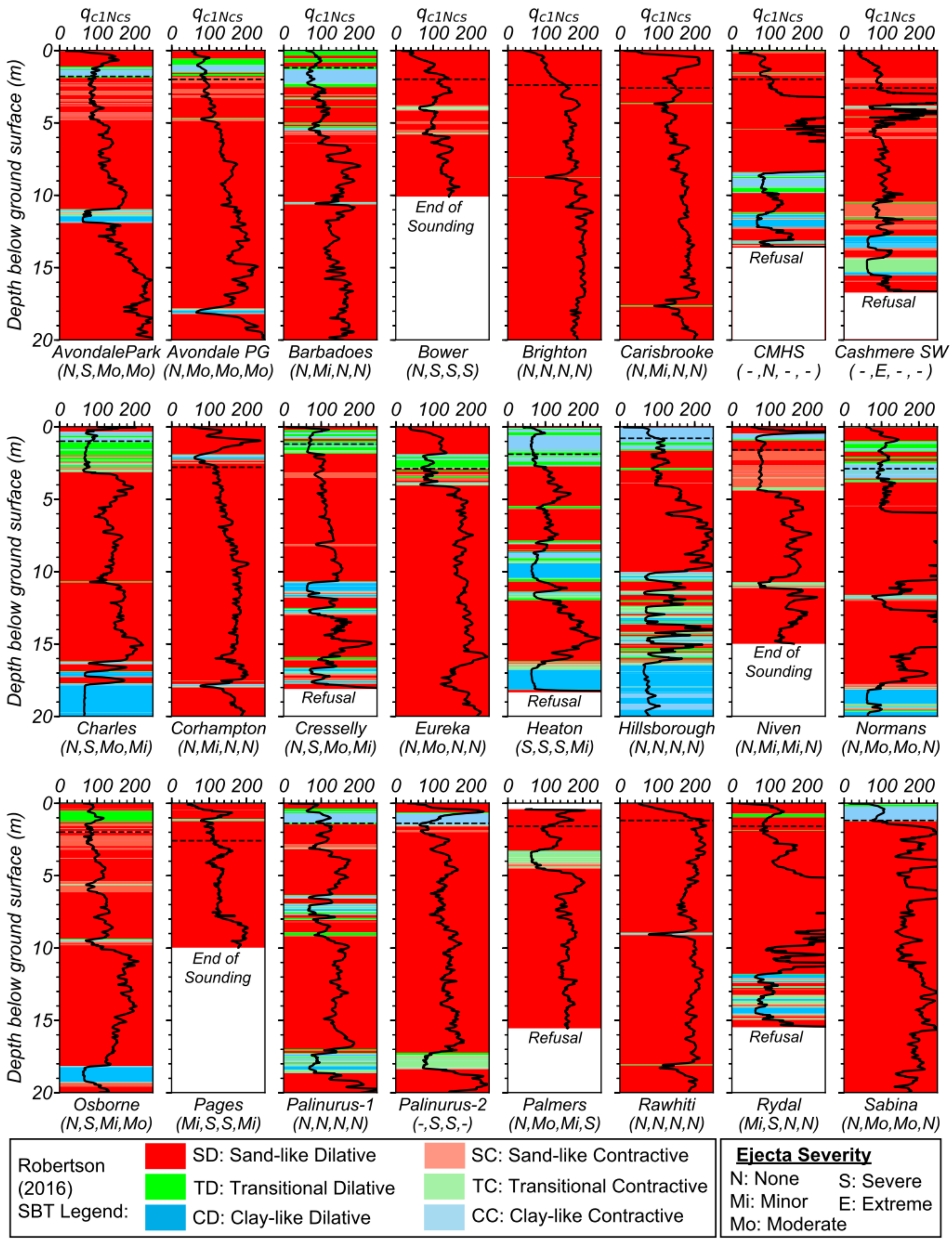

Figure 3.2 **Profile of q_{c1Ncs} of sites in the thick sand group (continued in Figure 3.3) and observed ejecta severity (4 letters below site's name are the sequence of DAR, CHC, JUN, and DEC earthquakes, respectively).**

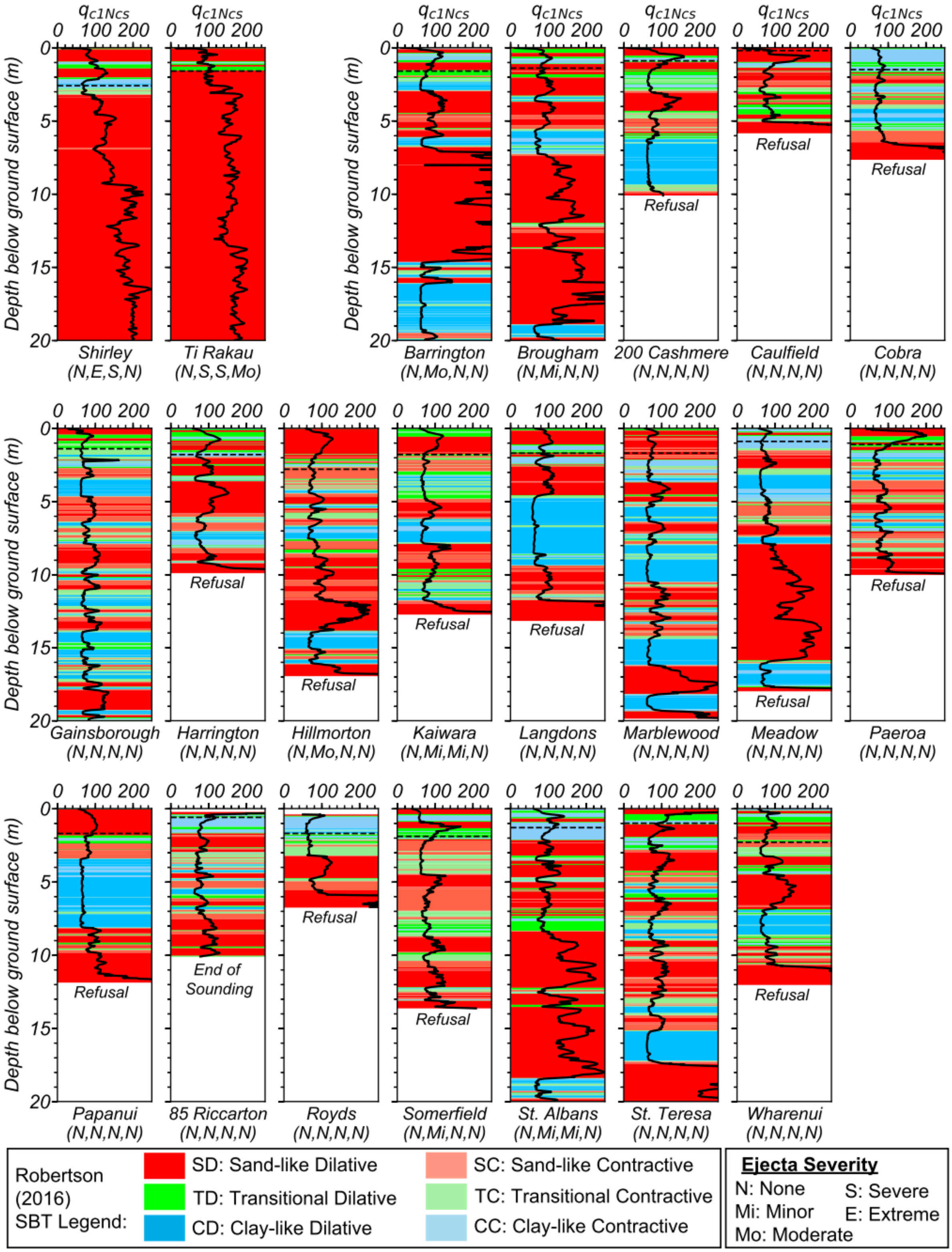

Figure 3.3 **Profile of q_{c1Ncs} of sites in the partially-to-highly stratified group (from left to right start from Barrington) and observed surficial ejecta severity. Note that Shirley and Ti Rakau plots are from thick sand sites group continued from Figure 6.2.**

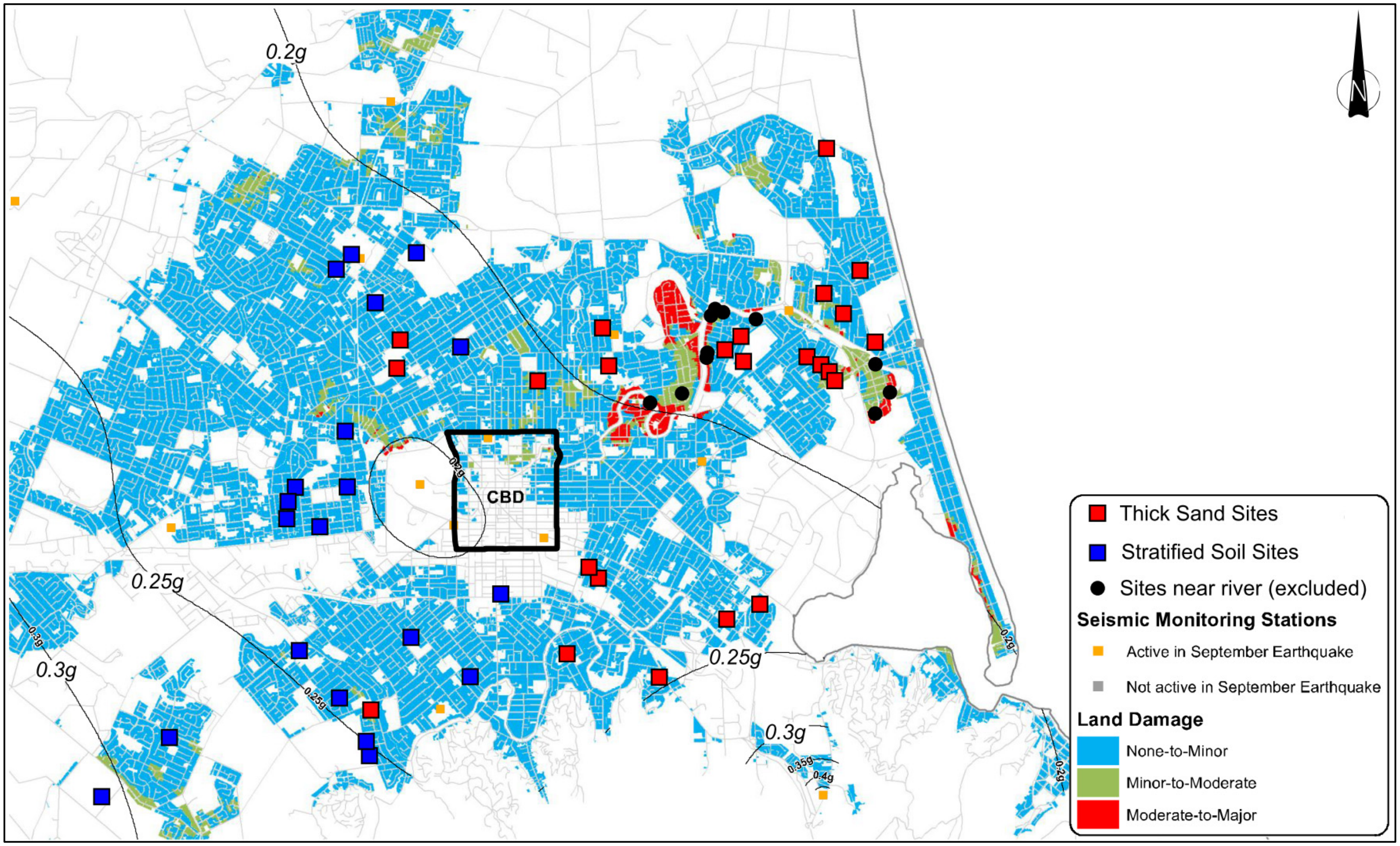

Figure 3.4 **Contour map of estimated surface peak acceleration and observed land damages after the M_w7.1 2010 Darfield earthquake relative to the location of 55 sites. (Modified after van Ballegooy, *Personnel Communication* [2018]).**

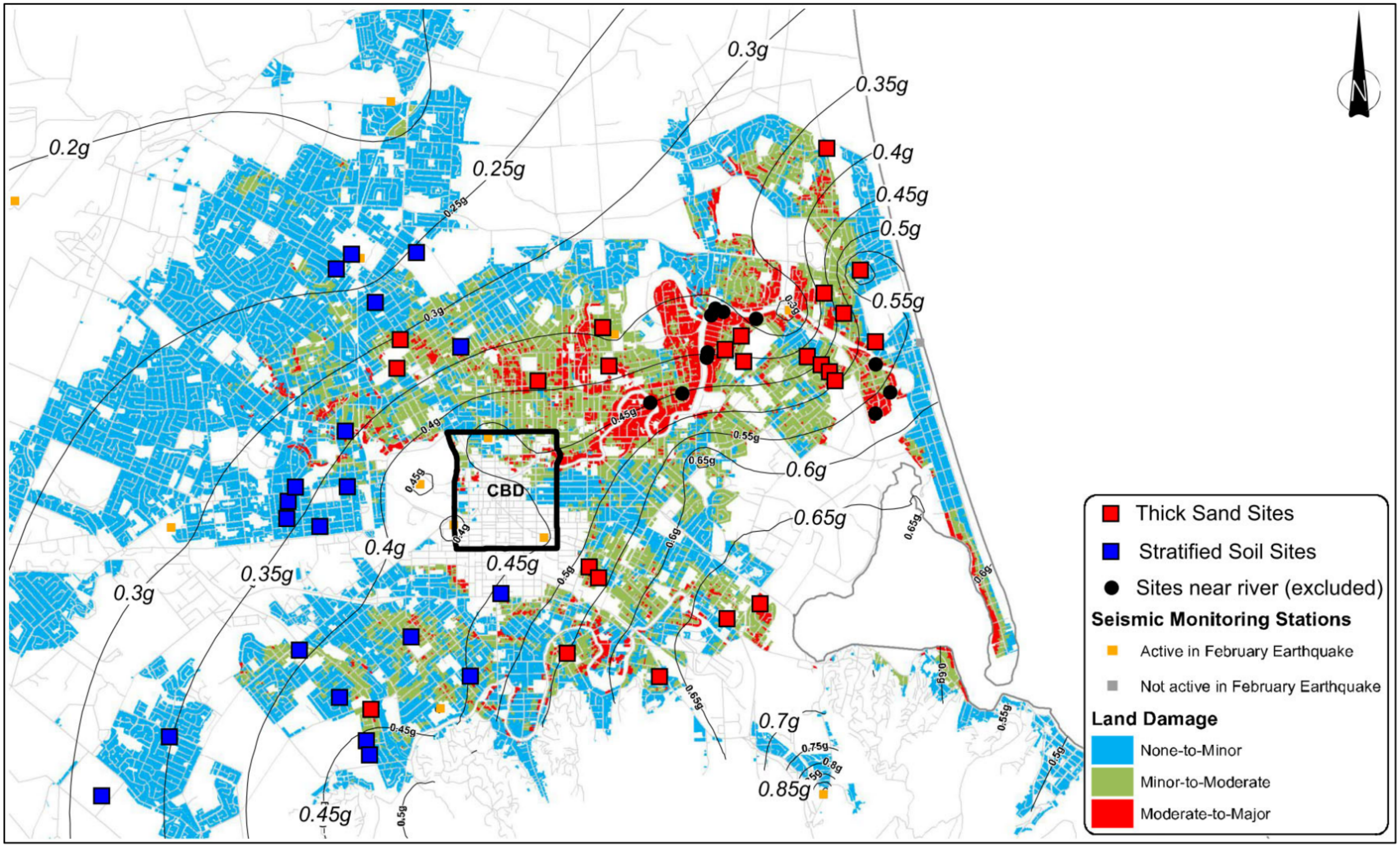

Figure 3.5 **Contour map of estimated surface peak acceleration and observed land damages after the M_w6.2 2011 February Christchurch earthquake relative to the location of 55 sites. (after van Ballegooy, *Personnel Communication* [2018]).**

3.2 CPT-BASED LIQUEFACTION ASSESSMENT

To investigate the typical trend on the underestimation and overestimation of liquefaction field cases histories, CPT-Based liquefaction back-assessments of all 44 sites are performed. Three liquefaction ground-failures indices were considered in this research, including:

- *Liquefaction Severity Number*, LSN (van Ballegooy et al. [2014])

$$\text{LSN} = 1000 \int \frac{\varepsilon_v}{z} dz \tag{3.1}$$

where ε_v = volumetric strain calculated using the Zhang et al. [2002] procedure, and z = depth > 0. The LSN criteria (Tonkin &Taylor [2013]) were used where 0 < LSN <10, 10 ≤ LSN < 20, 20 ≤ LSN < 30, 30 ≤ LSN < 40, and LSN ≥ 40 corresponds to None, Minor, Moderate, Severe, and Extreme amount of ejecta manifestation.

- *Liquefaction Potential Index*, LPI [Iwasaki 1978; 1982]

$$\text{LPI} = \int_0^{20\text{m}} F_1 (10 - 0.5z)\, dz \tag{3.2}$$

where $F_1 = 1 - FS_L$ for $FS_L < 1.0$; $F_1 = 0$ for $FS_L \geq 1.0$, and z is the depth below ground surface (m). The severity criteria used for LPI in this research followed that recommended by Maurer et al. [2014], which are LPI < 4, 4 ≤ LPI < 8, 8 ≤ LPI < 15, LPI ≥ 15 correspond to None, Minor/Marginal, Moderate, and Severe liquefaction manifestation, respectively.

- *Ishihara-inspired Liquefaction Potential Index*, LPI_{ISH} [Maurer et al. 2015]

$$\text{LPI}_{\text{ISH}} = \int_{H_1}^{20m} F(FS_L) \frac{25.56}{z} dz \tag{3.3}$$

where

$$F(FS_L) = \begin{cases} 1 - FS_L, \text{ if } FS_L \leq 1 \cap H_1 m(FS_L) \leq 3 \\ 0, \text{otherwise} \end{cases} \tag{3.4}$$

$$m(FS) = \exp\left[\frac{5}{25.56(1 - FS_L)}\right] - 1 \tag{3.5}$$

The severity criteria used for LPI_{ISH} is from Maurer et al. [2014], which are $\text{LPI}_{\text{ISH}} < 8$, $8 \leq \text{LPI}_{\text{ISH}} < 15$, $\text{LPI}_{\text{ISH}} \geq 15$ correspond to None-to-minor, Moderate, and Severe liquefaction manifestation, respectively.

Figures 3.2–3.5 indicate that thick sand sites generally produced more sediment ejecta than partially-to-highly stratified soil sites. Using the criteria of Table 3.1, the sites in the partially-to-highly stratified group produced 74 None (93%), 4 Minor (5%), and 2 Moderate (2%) cases out of 80 case histories during the four Canterbury earthquake sequence events. In contrast, the sites in the thick sand group produced 47 None (49%), 13 Minor (13%), 15 Moderate (16%), 19 Severe (20%), and 2 Extreme (2%) cases out of 96 cases histories. The geographical locations of all sites are dispersed across Christchurch, and they are shaken by similar ground shaking intensity. The general characteristics of the liquefiable soil (e.g., I_B, and q_{c1Ncs}) in the two site groups are similar, which is consistent with the findings of Cubrinovski et al. [2019]. The q_{c1Ncs} value of liquefiable sand-like soils (red background) at the top 10-m depth at most sites in both of the two groups ranges from 80–130, which is judged to liquefy during the Canterbury earthquakes. The different layer stratification of the two site groups is the primary reason for the different performances of the two groups in producing ejecta.

Liquefaction triggering back-analysis of all 44 sites shaken by four different Canterbury earthquake sequence events (176 total scenarios) was performed using the Boulanger and Idriss [2016] CPT-based procedure (BI-16). The baseline analysis used the fines content fitting parameter (C_{FC}) of 0.13 as recommended in Maurer et al. [2019] to produce a more consistent fines-content estimation for Christchurch soil database. The probability of liquefaction (P_L) of 50% is selected for the baseline back-analysis to remove the conservative bias in conventional liquefaction triggering analyses where P_L = 15%. The FS_L of cohesionless soil (I_c < 2.6) at each depth is then computed to calculate the LPI, LSN, and LPI_{ISH} values. The GWL for each scenario is estimated from the GWL model depicted in Figure 3.6 in addition to site-specific *P*-wave velocity measurements and nearby well recordings. The PGA values are estimated using the 50% values of Bradley [2013] model as illustrated by contour maps in Figures 3.4–3.5 for Darfield and Christchurch earthquakes.

Figures 3.7 and 3.8 provide an example of the CPT-based liquefaction triggering analysis of Shirley (underestimation) and Gainsborough (overestimation) using SCPT-57366 (thick, clean sand deposit) and CPT-36417 (highly stratified deposit) data, respectively, as highlighted in Figure 1.1. Figure 3.7 indicates that all indices estimated that None-to-Minor ejecta manifestation should occur, but the Extreme ejecta amounts were observed at the Shirley site; see Figure 3.7(a). Based on the FS_L-based assessment in Figure 3.7(b), the Christchurch earthquake liquefies only some of the layers below the GWL to a depth of 8 m. The LSN formulation considers the influence of soil layers with FS_L higher than 1.0 through volumetric strain estimation based on Zhang et al. [2002]; however, it seems that the influences of such layers were considerably underestimated. LPI and LPI_{ISH} formulations only consider soil layers with FS_L less than 1.0 to contribute to ejecta production. The upward seepage triggered by high generation of u_e is ignored by the three indices, which may explain why they mis-estimated the extreme amount of ejecta produced at the Shirley site.

Figure 3.8 indicates all indices estimated that severe liquefaction manifestation should occur at Gainsborough for the 2011 Christchurch earthquake, but there were no ejecta observed at the site [Figure 3.8(a)] even though it was shaken with a high PGA (close rupture distance). Based on FS_L-based assessment in Figure 3.8, the Christchurch earthquakes should have triggered liquefaction in almost all the liquefiable materials (I_c < 2.6) at the Gainsborough site. The I_c profile indicates that almost all liquefied layers are isolated between non-liquefiable, low k_v layers consisting of silt to clayey silt soil. Although the residual u_e remained high after the shaking stopped, the water inside the liquefied layer may not have flowed towards the ground surface to produce ejecta because the overlying low k_v layer impeded the flow. Note that all indices assessed the liquefaction consequences without considering any post-shaking hydraulic mechanisms. The presence of low k_v layers that isolate all liquefied layers may explain why the site did not produce ejecta. Additionally, deep liquefaction (e.g., at 12.0–13.0 m and 17.5–19.0 m) induces high shear strain (high damping) that may isolate most of the propagated seismic energy and reduce the amplitude of CSR at shallow depths, so that liquefaction may not trigger within the shallow cohesionless soil layer. The ESA simulations presented in Chapters 4 and 5 provide insights that shed light on these mechanisms.

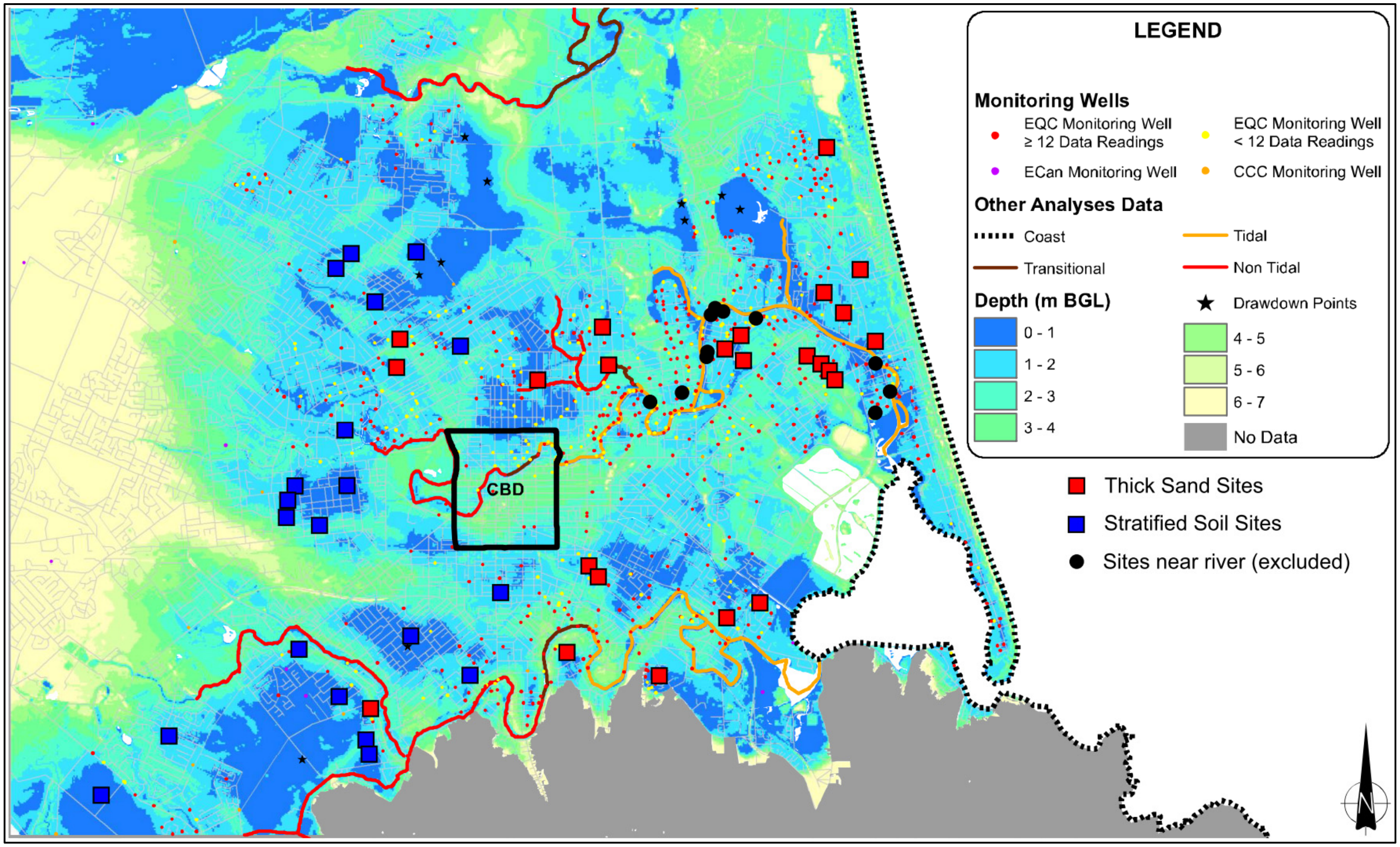

Figure 3.6 **Median depth to groundwater level during the 2010–2011 Canterbury earthquakes and the location of 55 sites. See Figure 2.11 for names of each site. (Modified after Tonkin + Taylor, van Ballegooy, *Personnel Communication* [2018]).**

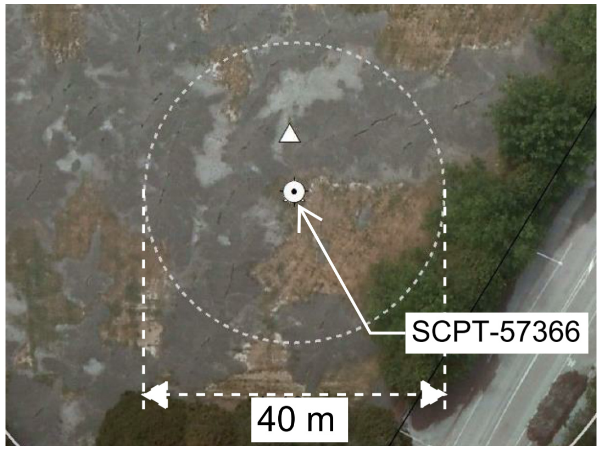

(a) Aerial photograph of Shirley site (-43.51040, 172.66199). (Capture date: 02/24/2011)

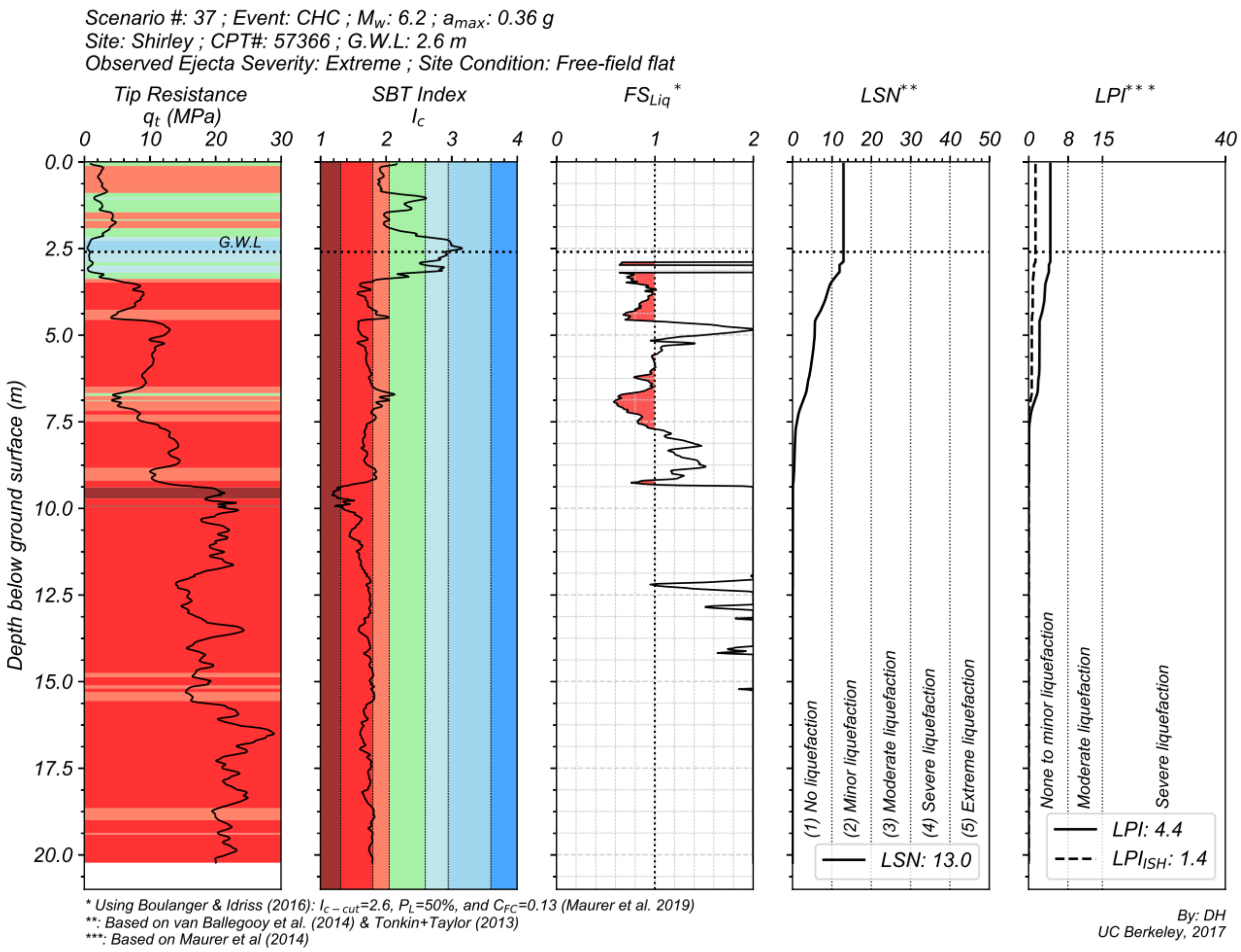

(b) SCPT-57366 interpreted soil profile and summary of CPT-based analysis

Figure 3.7 **Example of underestimation observed in at a thick, clean sand site in Shirley where none to minor liquefaction was estimated but produced Extreme ejecta (80% area within the 20-m radius of white circle were covered by ejected material)**

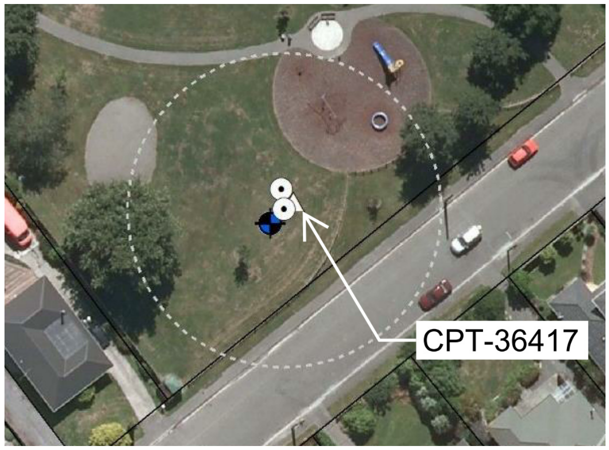

(a) Aerial photograph of Gainsborough site (-43.56362, 172.60191). (Capture date: 02/24/2011)

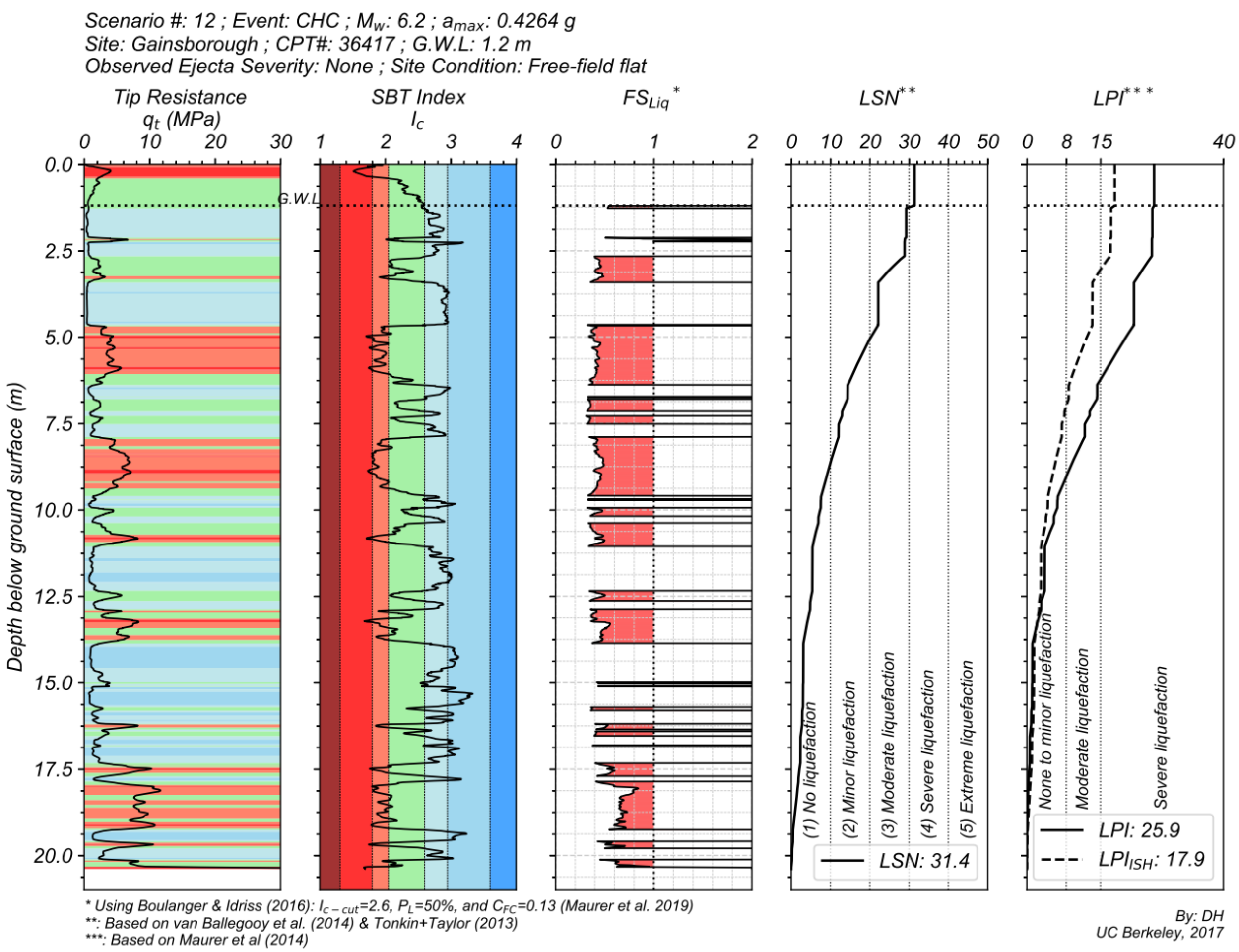

(b) CPT-36417 interpreted soil profile and summary of CPT-based analysis

Figure 3.8 Example of underestimation observed at a highly stratified soil site in Gainsborough where Severe liquefaction manifestation was estimated but no ejecta were observed in the field (None criteria).

To assess some of the uncertainty involved in the calculation, two P_L (15% and 50%) and C_{FC} (0.0 and 0.13) values were considered. P_L of 15% and C_{FC} of 0.0 are the default value of the BI-16 procedure to produce a conservative design in practice. Figure 3.9 shows the box-and-whisker plot for each computed index associated with each observed ejecta amount from 176 scenarios considered herein. Figure 3.9 indicates estimation trends based on LPI, LSN, or LPI_{ISH} that did not correlate well to the observed ejecta amount for all calculations using four different pairs of C_{FC} and P_L. For instance, the median value of all indices for the "Moderate" severity group is lower than the "Minor" group. It is possible for the median value of the "None" group is similar or even higher than the "Severe" group. Furthermore, there are cases where Severe ejecta is estimated (e.g., cases with LSN = 30, LPI = 15, LPI_{ISH} = 15), but the observed ejecta is None (overestimation). Conversely, None to Minor ejecta are estimated (e.g., cases with LSN = 10, LPI = 5, LPI_{ISH} = 5) but Severe ejecta were observed in the field (underestimation). The analysis shown in Figure 3.9 indicates that LPI-, LSN-, or LPI_{ISH}-based estimation do not produce reliable estimates of ejecta amounts for 176 scenarios analyzed herein.

A similar analysis is performed by only considering the thick sand sites group, as shown in Figure 3.10; the trend in the results is improved. The computed median value for each liquefaction index tends to increase as the observed ejecta becomes more severe. The median value of all indices for the None criterion are lower than the median value of cases with observed ejecta manifestation, which is consistent with the findings of other researchers who found LPI, LSN, or LPI_{ISH} estimate ejecta occurrence (Yes/No) reliably well at thick, clean sand sites (e.g., Maurer et al. [2014] and van Ballegooy et al. [2015a, b]). However, misestimations of ejecta amounts are still observed for numerous cases, which is not surprising because the liquefaction indices neglect the post-shaking hydraulic process that may control the amount of sediment ejecta.

Figure 3.10 also indicates that sites with a LSN of 20, LPI of 8, or LPI_{ISH} of 8 are likely to produce ejecta amounts ranging from None to Extreme (i.e., the estimation trend does not converge). For example, for conservative engineering design (P_L = 15%) and Christchurch soil (C_{FC} = 0.13), Figure 3.10 indicates that there are approximately 30%, 50%, 40%, and 50% of the sites with None, Minor, Moderate, or Severe amount of ejecta, respectively, with LSN = 20, even though there is 1 Extreme case (Shirley in Figure 3.7) with LSN =18 in this dataset. The LSN sensitivity analysis in Chapter 4 shows that the variation of other calculation parameters cannot explain the Extreme ejecta amount observed at the Shirley site.

The stratified soil sites did not produce cases more than Moderate ejecta; see Figure 3.11. More than 25% of stratified soil sites with no ejecta have LSN, LPI, and LPI values higher than 20, 10, and 10, respectively, indicating overestimation. There are even cases where the LSNs are higher than 50 dues to shallow GWL, but no sediment ejecta were observed in the field. LSN is highly sensitive to minor variations in the shallow GWL that can significantly influence the liquefaction assessment. Additionally, more than approximately 75% of stratified soil sites with Minor ejecta have LSN, LPI, and LPI values higher than 20, 15, and 10, respectively, also indicating overestimation. Figure 3.11 indicates that current simplified liquefaction indices do not produce reliable estimates of sediment ejecta at stratified soil sites. Note that researchers such as Beyzaei et al. [2018a,b] and Cubrinovski et al. [2019] identified other contributing factors for why overestimation occurred at stratified soil sites, including depositional processes, permeability contrasts in the highly stratified soil deposit, partial saturation of the shallow soil below the groundwater table, and dynamic response effects due to liquefaction of deeper soil layers.

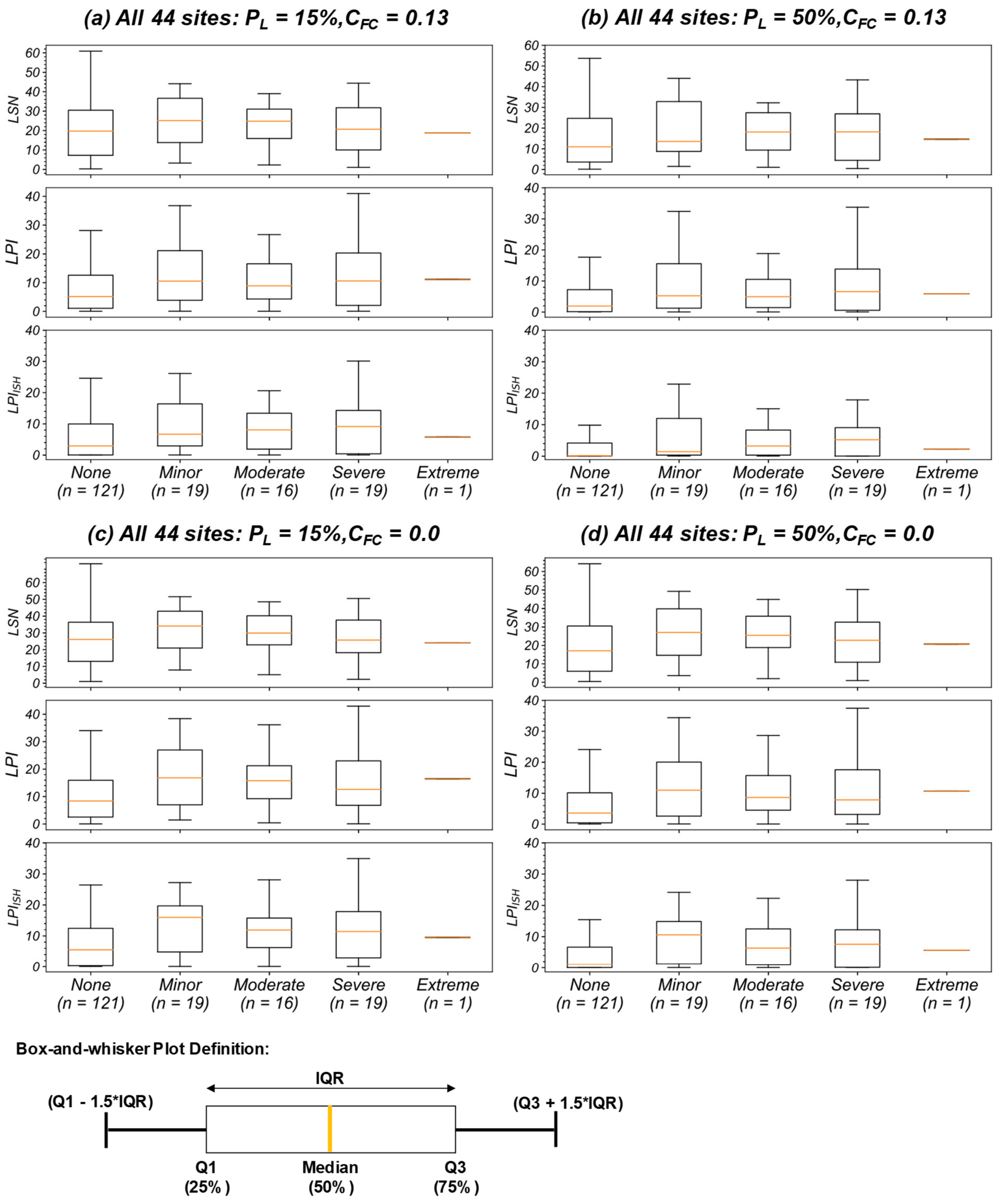

Figure 3.9 **Box-and-Whisker plot showing the distribution of LSN, LPI, and LPI_{ISH} values at all 44 sites shaken by four different Canterbury earthquakes sequence resulting 176 liquefaction case histories scenarios.**

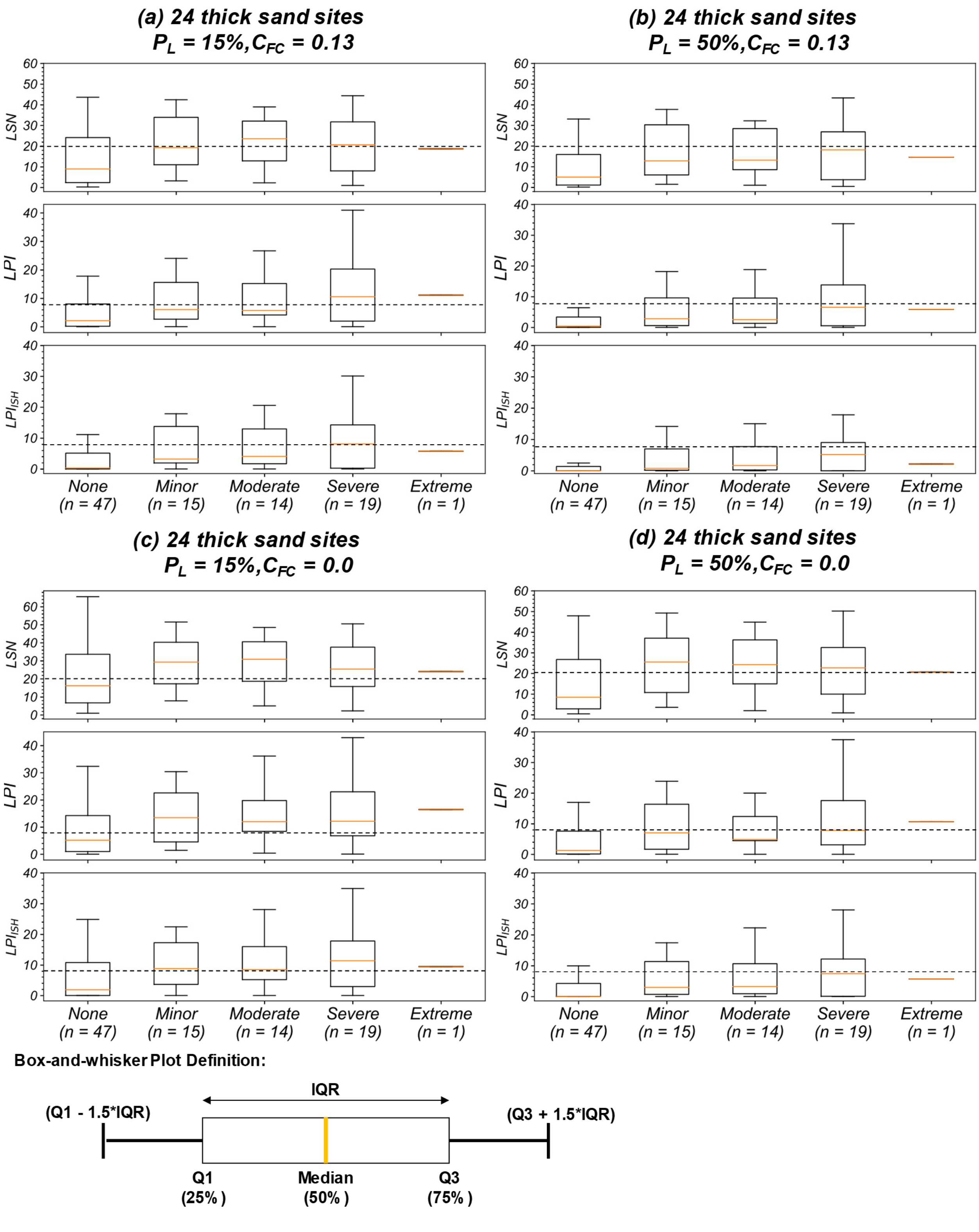

Figure 3.10 Box-and-Whisker plot showing the distribution of LSN, LPI, and LPI_{ISH} values of thick, clean sand sites shaken by four different Canterbury earthquakes sequence resulting 96 liquefaction case histories scenarios.

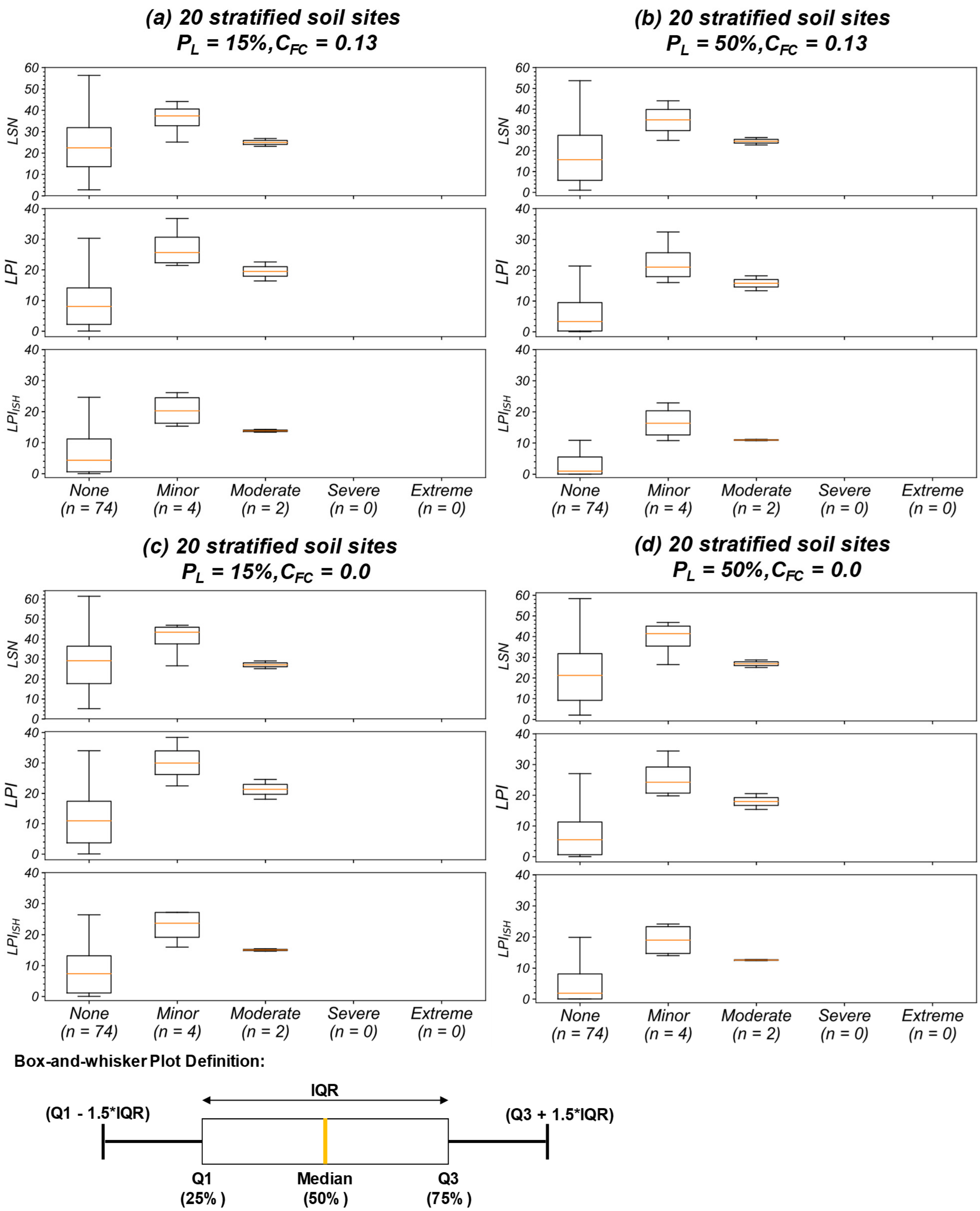

Figure 3.11 Box-and-Whisker plot showing the distribution of LSN, LPI, and LPI_{ISH} values of highly to partially stratified soil sites shaken by four different Canterbury earthquakes sequence resulting 80 liquefaction case histories scenarios.

To evaluate the influence of non-liquefiable crust layer thickness (H_1), all computed liquefaction indices are compared with H_1 of each site, as summarized in Figure 12. The zones of B1, B2, B3, and C in Figures 3.12(a-b) are the zones proposed by Towhata et al. [2016] that represent cases with low-to-high probability to produce severe liquefaction damage. For thick sand sites, LPI tends to produce reasonable ejecta estimation where most of the None-Minor and Moderate-Severe cases are located in the Zone B1-B3 and C, respectively. However, there are a lot of Moderate-Severe cases are plotted in Zone B3 (underestimation), and many None-Minor cases are in Zone C (overestimation). There is also one Extreme case (i.e., red dot for case of Shirley site after 2011 Christchurch earthquake with a LPI = 6 and H_1 = 3.2) that is plotted in the boundary of Zones B1, B2, B3, and C. The horizontal and vertical lines of the chart may cause misinterpretations. Additional transition zones may be helpful. Numerical simulations discussed in Chapter 4 confirmed the underestimation of Shirley site. More importantly, the overestimation is apparent for the sites in the stratified soil group, where numerous None-Minor cases have high LPI and are plotted in Zone C even with small H_1.

The performance of LPI_{ISH} and LSN are relatively similar to LPI in estimating the ejecta amount for the sites in the thick sand group; see Figures 3.12(c) and 3.12(e). Some of the apparent underestimation and overestimation cases at thick sand sites are also observed. The case of Shirley site after 2011 Christchurch earthquake is also plotted in the None and Minor zone in the LPI_{ISH} and LSN chart, respectively (see Appendix A for the numbers). The overestimation cases at stratified soil sites are also apparent [Figure 3.12(d) and 3.12(f)], where there are cases with LPI_{ISH} and LSN values greater than 8 and 30, respectively, but produced no ejecta manifestation.

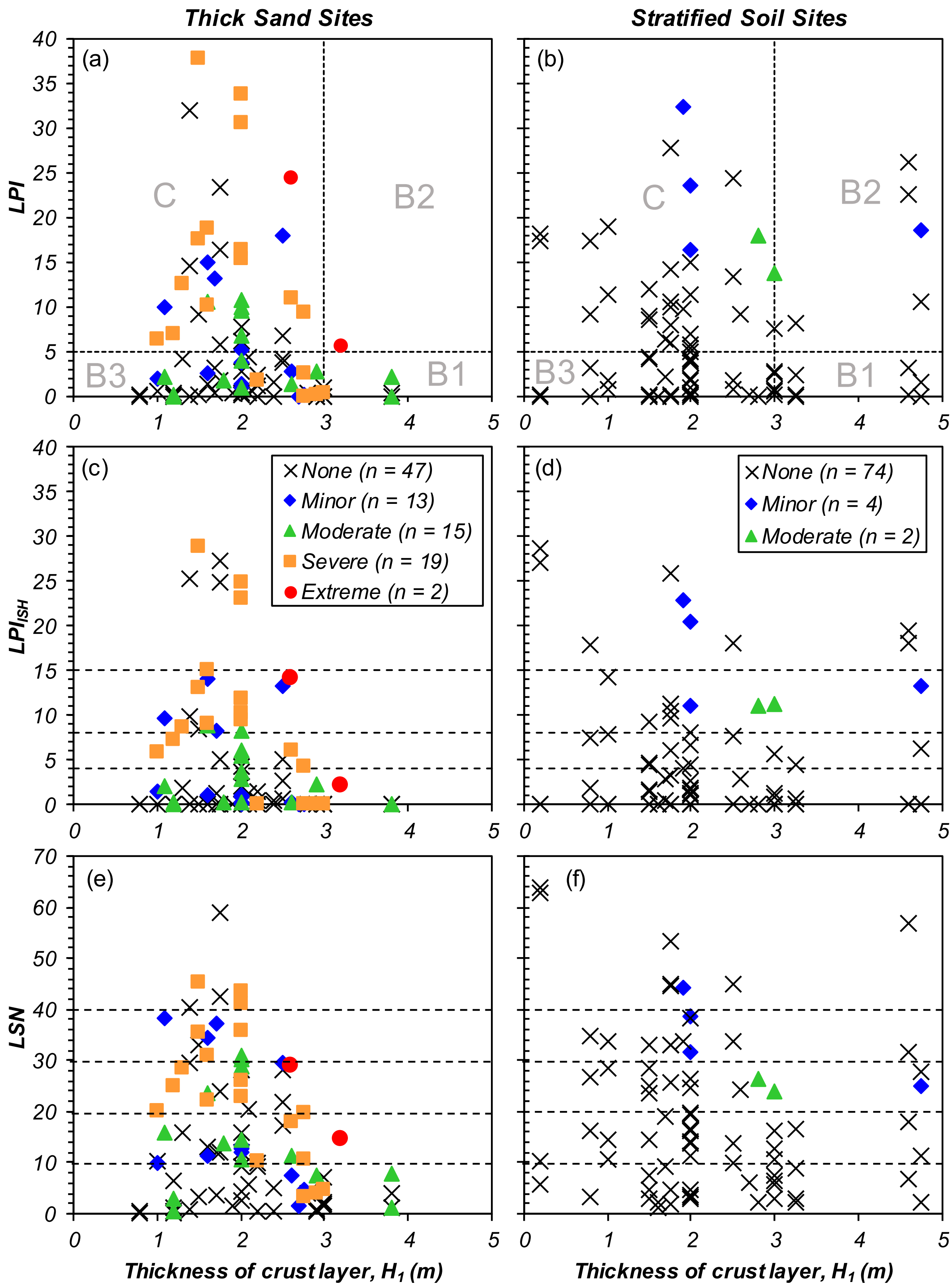

Figure 3.12 Distribution of all liquefaction-induced ground failure indices of 176 liquefaction field case histories compared against H_1.

3.3 SUMMARY

This chapter summarizes simplified analytical procedures to assess liquefaction hazard at 44 Christchurch sites using LSN-, LPI-, LPI_{ISH}-based procedures. Some key points obtained in this chapter are summarized below:

- Based on the analysis of 704 scenarios (i.e., 44 sites shaken by 4 Canterbury earthquake sequence events analyzed using 4 C_{FC}-P_L pairs), the LSN-, LPI-, LPI_{ISH}-based estimation did not produce reliable estimates of the amount of sediment ejecta. High indices values are observed at sites without sediment ejecta, and sites with low liquefaction indices value produced severe sediment ejecta.
- The estimation trend for the thick sand site improves after separating the partially-to-highly stratified soil sites and thick sand sites into two groups.
- The partially-to-highly stratified soil sites produced only moderate ejecta when intensely shaken, whereas thick sand sites could produce extreme amounts of sediment ejecta when shaken at a similar intensity.
- There is no significant difference in q_{c1Ncs} values of the liquefiable materials below the GWL for the sites in the two groups. However, their layer stratification differs significantly, which may be a key factor in distinguishing their capability to produce sediment ejecta.
- The LSN-, LPI-, LPI_{ISH}-based estimations tend to underestimate the ejecta amount at thick, clean sand sites, which may be due to the indices did not consider the intensity of post-shaking upward seepage that occurs during the advection process. Additionally, though liquefaction may not be triggered at certain depths, significant excess pore pressure can still be generated, which may induce upward seepage and produce ejecta.
- The LSN-, LPI-, LPI_{ISH}-based estimations tend to overestimate ejecta amounts at partially-to-highly stratified soil sites. These simplified liquefaction indices do not consider the contributing effects of site impedance and permeability contrasts that can prevent liquefaction triggering at shallow depths and influence post-shaking redistribution of excess hydraulic head, respectively.

These issues will be explored through the examination of the results of the nonlinear ESA presented in the following chapters.

4 Effective Stress Analysis of Liquefiable Sites to Estimate the Severity of Sediment Ejecta

4.1 INTRODUCTION

Sediment ejecta contribute significantly to liquefaction-induced damage. There are numerous examples of infrastructure damage in Christchurch, New Zealand, during the 2010–2011 Canterbury earthquake sequence due to severe ejecta manifestation (e.g., van Ballegooy et al. [2014]). There are also numerous cases of sites where current procedures indicate liquefaction manifestation should have occurred but did not (e.g., Beyzaei et al. [2018a, b]). Several researchers have explored the misestimations of liquefaction manifestation observed in Christchurch during the Canterbury earthquakes (e.g., Maurer et al. [2014], van Ballegooy et al. [2015a, b], and Cubrinovski et al. [2019]). Liquefaction-induced ground failure, which includes ejecta, is typically evaluated with simplified liquefaction ground-failure indices. Quantitative methods to estimate the amount of ejecta likely to develop at a site are not currently available. Dynamic effective stress analysis (ESA) is performed in this report to investigate the inconsistencies between estimates of ground failure from widely used liquefaction indices and the observations in Christchurch.

Dynamic ESA is performed to back-analyze two liquefiable level-ground sites that represent two commonly observed cases in Christchurch. Extreme manifestation of sediment ejecta was observed at the Shirley Intermediate School (Shirley) site, but the simplified procedures estimate minor-to-moderate liquefaction manifestation during the 2011 Christchurch earthquake (i.e., a typical underestimation case). The Shirley site profile consists of thick, continuous, highly permeable, liquefiable, clean sand. Conversely, sediment ejecta were not observed at the St. Teresa School (St. Teresa) site during the Canterbury earthquake sequence, yet liquefaction procedures estimate major-to-severe liquefaction manifestation for the major earthquakes of the sequence (i.e., a typical overestimation case). The St. Teresa site profile is a highly stratified soil deposit consisting of thin, interbedded liquefiable silt, silty sand, and sand layers with significant hydraulic conductivity contrasts.

This chapter first describes the physical process of upward seepage-induced artesian flow that produces sediment ejecta at sites where liquefaction is triggered. Ejecta Potential Index (EPI) is then introduced as a liquefaction severity index to estimate the amount of sediment ejecta by utilizing dynamic nonlinear ESA. The EPI is formulated to quantify the potential of artesian flow by computing the magnitude of excess hydraulic head at each depth and time-step interval. The simulation results indicate that the EPI can capture the post-shaking mechanism of liquefaction-induced ejecta and produce severity estimates consistent with field observations. Lastly, the study's key findings are shared.

4.2 PREVIOUS STUDIES

Early studies (e.g., Housner [1958], Ambraseys and Sarma [1969], Lowe [1975], and Seed [1979]) postulated sediment ejecta are produced by the dissipation process of excess pore water pressure (u_e) generated during shaking. Housner [1958] noted sediment ejecta often initiated several minutes after the earthquake shaking ceased. Ambraseys and Sarma [1969] reported that the ground started to crack 2 to 3 minutes after the beginning of the 1964 M_w7.6 Niigata earthquake near the end of ground shaking, and water began to flow a minute or two later and continued to flow for nearly 20 minutes. The water flow rose 1.5 m above the ground surface while ejecting the fluidized sediment. The sediment was later identified as material from a layer 4.5 m to 6.0 m deep. Similar observations were observed after many earthquakes (e.g., Ambraseys and Sarma [1969], including the 1989 Loma Prieta earthquake (e.g., Bardet and Kapuskar [1993]) and the 2010–2011 Canterbury earthquakes (e.g., *https://youtu.be/rRVK5NJE2qE*). Some studies developed closed-form solutions of the advection equation to quantify the magnitude of what they termed the water-jet pressure, without providing an estimate of the amount of ejecta. However, these studies do suggest the amount of ejecta likely depends on the magnitude of residual u_e that must be dissipated to reach a steady-state condition. Seed [1979] noted that:

> *"…once the cyclic stress applications stop, if they return to a zero stress condition, there will be a residual pore water pressure in the soil equal to the overburden pressure, and this will inevitably lead to an upward flow of water in the soil that could have deleterious consequences for overlying layers.*"

Ishihara [1985] developed a widely used empirical chart that identifies when liquefaction-induced ground failure may occur based on the non-liquefiable crust thickness, liquefiable layer thickness, and the PGA of earthquake shaking. The case histories were limited to sites with a non-liquefiable crust overlying a continuous liquefiable sand deposit. The chart is not suitable for interbedded liquefiable soil layers with significant hydraulic conductivity contrasts (e.g., the St. Teresa site). The chart also does not estimate the severity of liquefaction-induced ground failure. The LPI and LSN were developed to estimate the severity of surficial liquefaction manifestation. The LPI is an empirical method based on a linear depth-weighted factor of safety against liquefaction (FS_L) computation using the simplified liquefaction triggering analysis [Iwasaki et al. 1978; 1982] and is defined as

$$\text{LPI} = \int_0^{20m} F_1 W(z)\,dz \tag{4.1}$$

where $W(z)$ is equal to $10 - 0.5z$; F_1 equals $1 - FS_L$ for $FS_L < 1.0$; F_1 equals 0 for $FS_L \geq 1.0$, and z is the depth below ground surface (m). The LSN takes advantage of the Ishihara and Yoshimine [1992] post-liquefaction volumetric strain (ε_v) relationships as a function of FS_L and the soil's relative density (D_r), emphasizing shallow liquefaction with an inversely proportional depth-weighing factor [van Ballegooy et al. 2014] and is defined as

$$\text{LSN} = 1000 \int \frac{\varepsilon_v}{z} \, dz \tag{4.2}$$

where ε_v is the volumetric strain and z is the depth > 0. The LSN criteria were developed by comparing results from over 11,000 cone penetration tests (CPTs) to the severity of surficial liquefaction manifestations observed in residential areas in Christchurch [Tonkin + Taylor 2013].

The LPI, LSN, and other liquefaction-induced ground failure indices are useful guides for estimating the severity of liquefaction manifestations. However, a site with a specific LPI or LSN value can manifest a wide range of land damage. For example, Christchurch sites with LSN = 20 were observed to have land damage classified from "*No observed ground cracking or ejected material* " to "*Large quantities of ejected material* " [van Ballegooy et al. 2014]. There are also numerous cases with highly interbedded silty soil deposits where ground failure indices indicate a high likelihood of liquefaction manifestations, yet none were observed; for example, Beyzaei et al. [2018a, b] and Cubrinovski et al. [2019] analyzed two soil profiles with different stratification using dynamic ESA and stressed the importance of evaluating the interaction of different liquefiable layers to capture the system response of the soil deposit. These and other researchers identified several contributing factors to why liquefaction ground failure indices might produce inconsistent estimations, including the omission of capturing the advection process, hydraulic conductivity contrasts, and dynamic response characteristics. The simplified liquefaction indices neglect the hydraulic mechanisms of the sediment ejecta phenomenon. They do not consider the influence of an elevated hydraulic gradient that can trigger upward seepage-induced artesian flow, which can exploit cracks in the overlying crust and transport liquefied sediment to the ground surface well after earthquake shaking stops. There is merit in investigating if ESA can provide insight into when ejecta may occur and how much ejecta may occur for different ground conditions.

4.3 LIQUEFACTION OBSERVATIONS AND REPRESENTATIVE SITES IN CHRISTCHURCH

Based on field observations and CPT soundings at more than 1200 sites, Maurer et al. [2014] created LPI prediction error maps for the Canterbury earthquakes. The LPI error map for the 2011 Christchurch event shown in Figure 4.1 identifies many areas where LPI yields reliable liquefaction assessments, i.e., "accurate prediction," "slight-to-moderate underprediction," and "slight-to-moderate overprediction." However, there are large areas, particularly in southwest Christchurch, with "moderate-to-excessive overprediction." There are swamp areas in southwest Christchurch with highly stratified silty soil deposits that are resistant to manifesting liquefaction at the ground surface (e.g., Beyzaei et al. [2018a, b]). Figure 4.1 also shows the projected rupture plane of the three largest earthquakes of the Canterbury earthquake sequence: the 4 September 2010 M_w7.1 Darfield (DAR), 22 February 2011 M_w6.2 Christchurch (CHC), and 13 June 2011 M_w6.0 and M_w5.6 June (JUN) events, which are the focus of this study. The June events were separated by only 80 minutes, so they are recharacterized as one larger M_w6.2 event to consider the combined influence of the first smaller event generating excess pore water pressure.

Two representative sites are selected in this study to examine key aspects of liquefaction manifestation in Christchurch. The Shirley site (-43.5104°, 172.6620°) is a soccer field at a free-field, level ground area in northeast Christchurch about 600 m away from the Avon river. It is in an area classified as "slight-to-moderate underprediction" by Maurer et al. (2014) and represents an underestimation case history. The St. Teresa site (-43.5299°, 172.5921°) is a car parking lot at a free-field, level-ground area in southwestern Christchurch (the nearest structure is 20 m away). The ground conditions and liquefaction manifestations of the St. Teresa site are consistent with sites classified as "severe-to-excessive overprediction" by Maurer et al. [2014] and represent an overestimation case history.

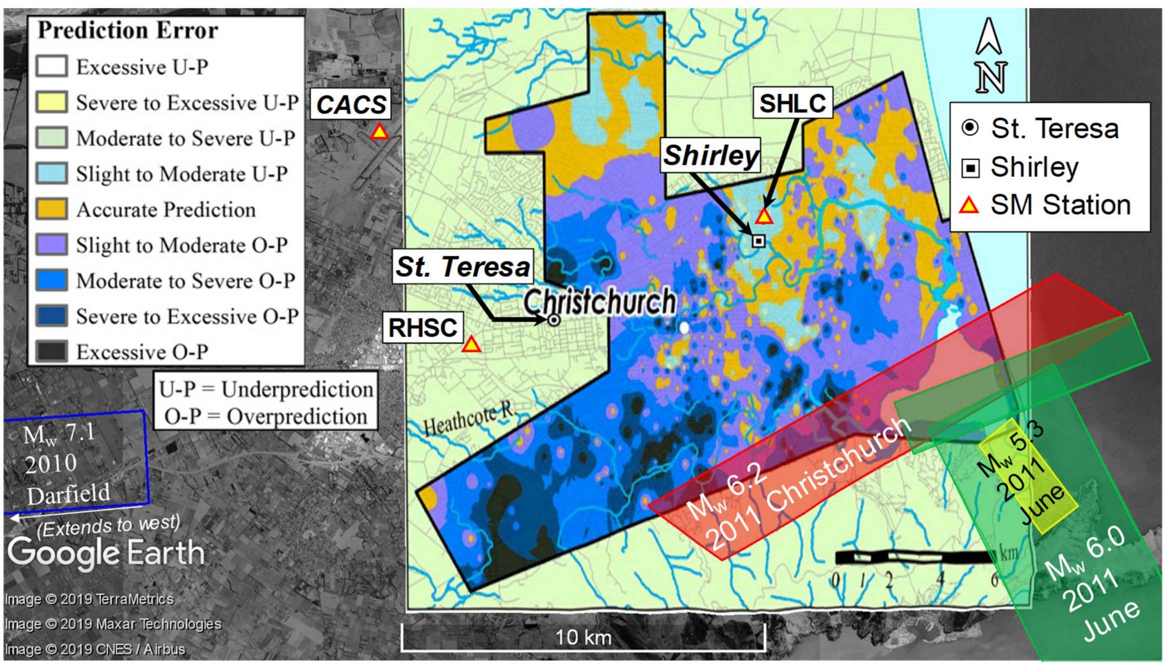

Figure 4.1 **Location of Shirley and St. Teresa sites, and nearby strong motion (SM) stations (SHLC, RHSC, and CACS); projection of finite-fault planes of three Canterbury earthquakes [Bradley 2012; Bradley and Cubrinovski 2011; and Bradley 2016] with the Maurer et al. [2014] prediction error map for the 22 February 2011 M_w6.2 Christchurch event as base map.**

The aerial photographs of the Shirley site captured soon after each earthquake are shown in Figure 4.2(a-c). Different amounts of sediment ejecta are observed for each event. Sediment ejecta quantity is categorized herein by the total area covered by ejecta relative to the total area within 20 m of a central reference point (SCPT-57366 / BH-57258 is shown as a white circle in Figure 4.2.). The ejecta quantity is divided into five categories: 0%, 0-5%, 5-20%, 20–50%, and 50100% of assessment area covered by ejecta, which corresponds to the liquefaction severity classifications of None, Minor, Moderate, Severe, and Extreme, respectively. Liquefaction manifestations at the Shirley site are classified as None, Extreme, and Severe for the Darfield, Christchurch, and June events, respectively. Post-event reconnaissance and high-quality aerial photographs [Figure 4.2(d-f)] at the St. Teresa site show no sediment ejecta manifestations were observed after all earthquakes, so its classification is None for all events.

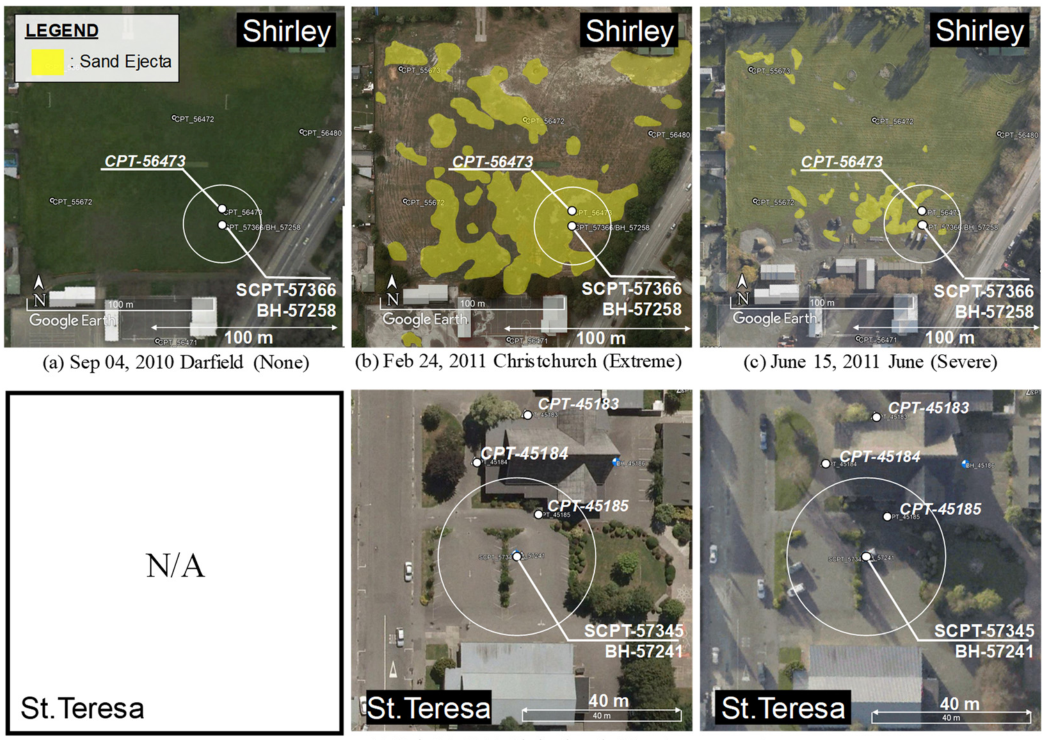

(a) Sep 04, 2010 Darfield (None) (b) Feb 24, 2011 Christchurch (Extreme) (c) June 15, 2011 June (Severe)

(d) Sep 04, 2010 Darfield (None) (e) Feb 24, 2011 Christchurch (None) (f) June 15, 2011 June (None)

Figure 4.2 Aerial photographs after each earthquake and the severity criteria of each observed manifestation. Assessment area shown by 40-m diameter circle centered on SCPT-57366 and SCPT-57345 for Shirley and St. Teresa sites, respectively (data from the New Zealand Geotechnical Database).

4.4 LIQUEFACTION ASSESSMENT

4.4.1 Thick, Clean Sand Site (Shirley)

Fluvial processes produced thick continuous fine clean sand layers at the Shirley site [Brown and Weeber 1992], as shown in Figure 4.3:

- boring log and fines content (FC)
- corrected tip resistance (q_t) of reference and nearby CPTs
- I_c with Robertson [2009] SBT$_n$ zones (6a: clean sand, 6b: sand mixture)
- layer stratification based on SBT$_n$ zones; (e) comparison of normalized ($M_{7.5}$, 1 atm) CSR of each earthquake and CRR computed based on BI-16 with P_L = 50% and C_{FC} = 0.13; solid and dashed line represent SCPT-57366 and CPT-56473, respectively
- computed LSN with Tonkin + Taylor [2013] severity criteria
- shear (red) and longitudinal (black) wave velocity data with depth of GWL for each event

There is a 50-cm-thick brown organic silt fill followed by the Springston formation of non-plastic, yellowish-brown sandy silt to silt (ML) down to a depth of 3.4 m. The Christchurch formation starts at a depth of 3.4 m as a dark gray, uniformly graded, very fine to fine, clean sand that extends to a depth of about 21 m with a thin gravel layer (GW) and is followed by silty clay (CL) and the dense Riccarton Gravel unit. In addition to the cone penetration tests (CPT) and exploratory borings at the Shirley site, CPT-580 (located 150 m east of the Shirley site) is used to extend the profile from 21 m to 27 m depth. The predominant clean uniform sand layers at the Shirley site have a corrected CPT tip resistance (q_t) of generally 5–15 MPa for SP-1 (3.4–9.2 m) and 15–25 MPa for SP-2 (9.2–21 m). The sand layers typically have soil behavior type (SBT) index (I_c) values of 1.3–1.8 and 1.8–2.05 [red and light-red colors in Figure 4.3(d)], respectively, which correspond to clean sand and silty sand behavior types [Robertson 2009]. Based on nearby piezometer readings at the Shirley site, the groundwater level (GWL) is estimated to be at a depth of 2.8 m, 2.6 m, and 2.2 m for the Darfield, Christchurch, and June events, respectively. These values are consistent with the *P*-wave velocity (V_p) measurement at the Shirley site.

The estimated median surface PGA based on Bradley [2013] is 0.19*g*, 0.38*g*, and 0.25*g* for the Darfield, Christchurch, and June events, respectively. Utilizing SCPT-57366 (solid line) and CPT-56473 (dashed line) data and the Boulanger and Idriss [2016] CPT-based liquefaction triggering analysis (referred herein as BI16), the $M_{7.5}$-1 atmosphere (atm) cyclic stress ratio (CSR) and cyclic resistance ratio (CRR) for each earthquake are compared in Figure 4.3(e) and the resulting LSN profiles are shown in Figure 4.3(f). The shallower fluvial sand unit (SP-1) is judged to be the critical layer (e.g., it contributes the most to the calculated LSN value) that can liquefy and develop significant excess pore water pressure to produce sediment ejecta on the ground surface during an earthquake. The LSN is calculated to be 3, 15, and 6 for both SCPT-57366 and CPT-56473 for the Darfield, Christchurch, and June events, respectively, using the mean values summarized in Table 4.1. A LSN value of 15 underestimates the extreme sediment ejecta observed for the Christchurch event and also underestimates the severe liquefaction observed for the June event. However, the lack of liquefaction manifestations is consistent with the low LSN value of 3 calculated for the Darfield event.

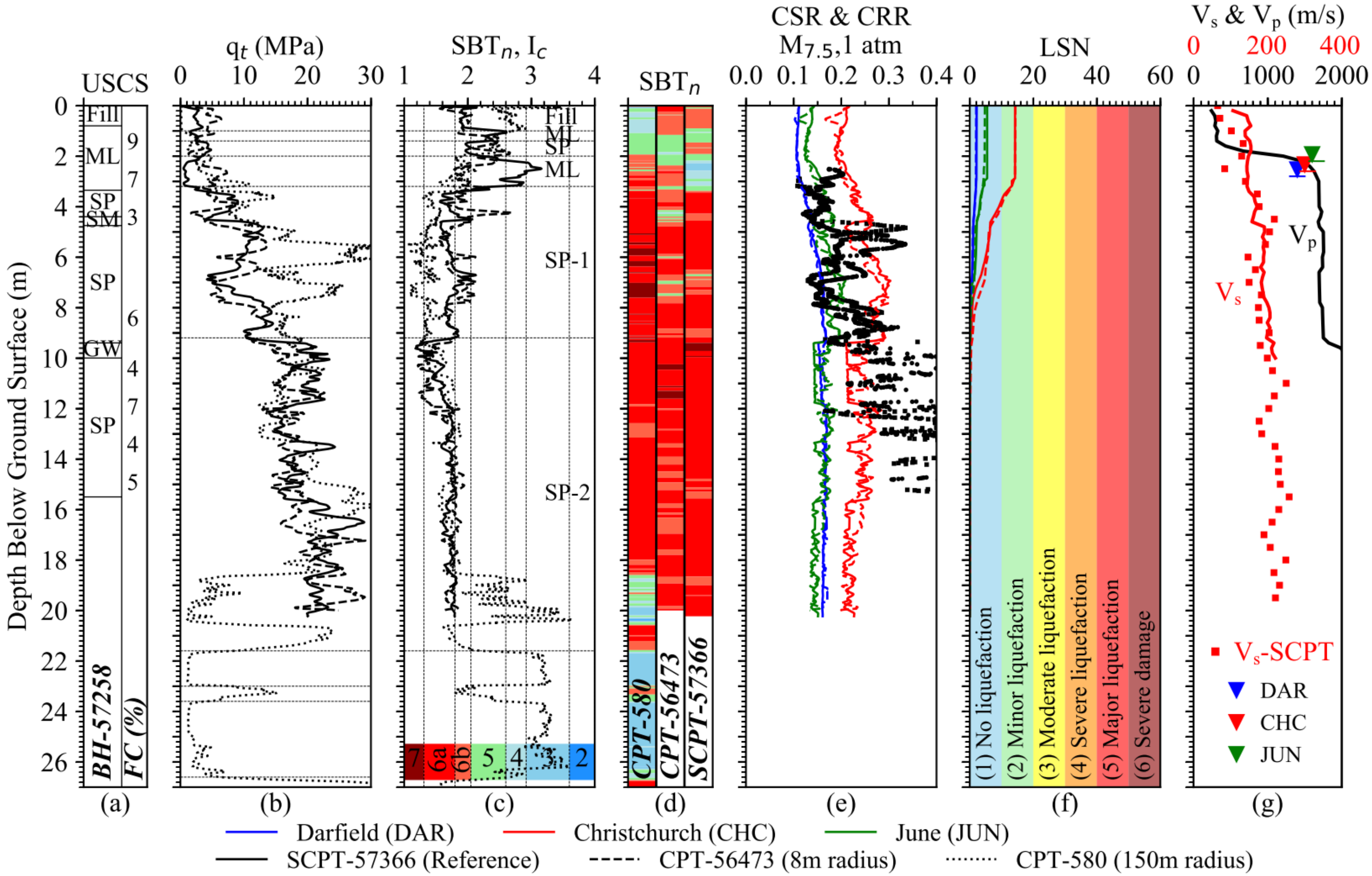

Figure 4.3 Shirley site subsurface information.

4.4.2 Highly Stratified Site (St. Teresa)

The St. Teresa site is an interbedded deposit of silt, silty sand, and sand located in the Riccarton swamp area [Beyzaei et al. 2018b]. The depositional process produced highly stratified, thin soil layers (Figure 4.4) that are judged to be the primary reason why surficial ejecta manifestation was not produced. The Springston formation consists of soft to firm low-plasticity silts (ML) with some thin layers (0.5–1.2 m thickness) of loose, fine to medium, silty (SM) to uniformly graded sands (SP) until a depth of 15.2 m, which is followed by silty clay (CL) and then the dense Riccarton Gravel unit. The ML, SM, and SP layers have q_t of generally 0.8–1.2 MPa, 1–5 MPa, and 7–9 MPa, respectively. The I_c values for the ML, SM, and SP layers are generally 2.6–3.0, 2.0–2.6, and 1.6–2.0, respectively. The colored SBT profiles [Figure 4.4(d)] from nearby CPTs (i.e., within 50 m) show the highly stratified soil deposit at St. Teresa, which differs significantly from the Shirley site; see Figure 4.3(d). The interbedded deposit at the St. Teresa site is a typical soil profile in southwestern Christchurch, where mostly None or Minor ejecta manifestations were observed. The GWL is at 1.0-m depth during all earthquakes based on a nearby piezometer observation and V_p data measured 5 m away from the reference point. The V_p data indicate the soil at 2.5–5 m depth is not fully saturated; however, adjusting its CRR due to a lack of full saturation (e.g., increasing CRR by 20% based on Tsukamoto et al. [2002]) does not affect the results presented later in this chapter.

The estimated median surface PGA based on Bradley [2013] is 0.29*g*, 0.36*g*, and 0.17*g* for the Darfield, Christchurch, and June events, respectively. Utilizing SCPT-57345 (solid line) and CPT-45185 (dashed line) data and the BI16 procedure, the results of liquefaction triggering analysis are summarized in Figure 4.4(e-f) (using the same format described previously). The analysis estimated seismic demand greater than the cyclic resistance of the soil layers, especially for the Darfield and Christchurch events. Figure 4.4(e) denotes all layers with I_c < 2.6 are susceptible to liquefaction due to low CRR values. The low-plasticity ML soil between 1–9 m is classified as susceptible to liquefaction using the Bray and Sancio [2006] criteria. Moreover, the results of cyclic triaxial test of similar soil samples taken at nearby sites (Site 23 in Beyzaei et al. [2018a]) indicate the soil likely liquefied in the Darfield and Christchurch events. The liquefiable silt, silty sand, and sand from 1–5 m depth contribute most to the calculated LSN value (designated as the critical layer). The LSNs were calculated (for CPT-57345 and CPT-45185 using mean values in Table 4.1) to be 44–49, 46–51, and 14–17 for the Darfield, Christchurch, and June event, respectively. The high LSN values of 44 to 51 overestimated excessively the observed lack of ejecta manifestation at the site for the Darfield and Christchurch events. The LSN values of 14–17 were also inconsistent with the field observations of no ejecta for the June event.

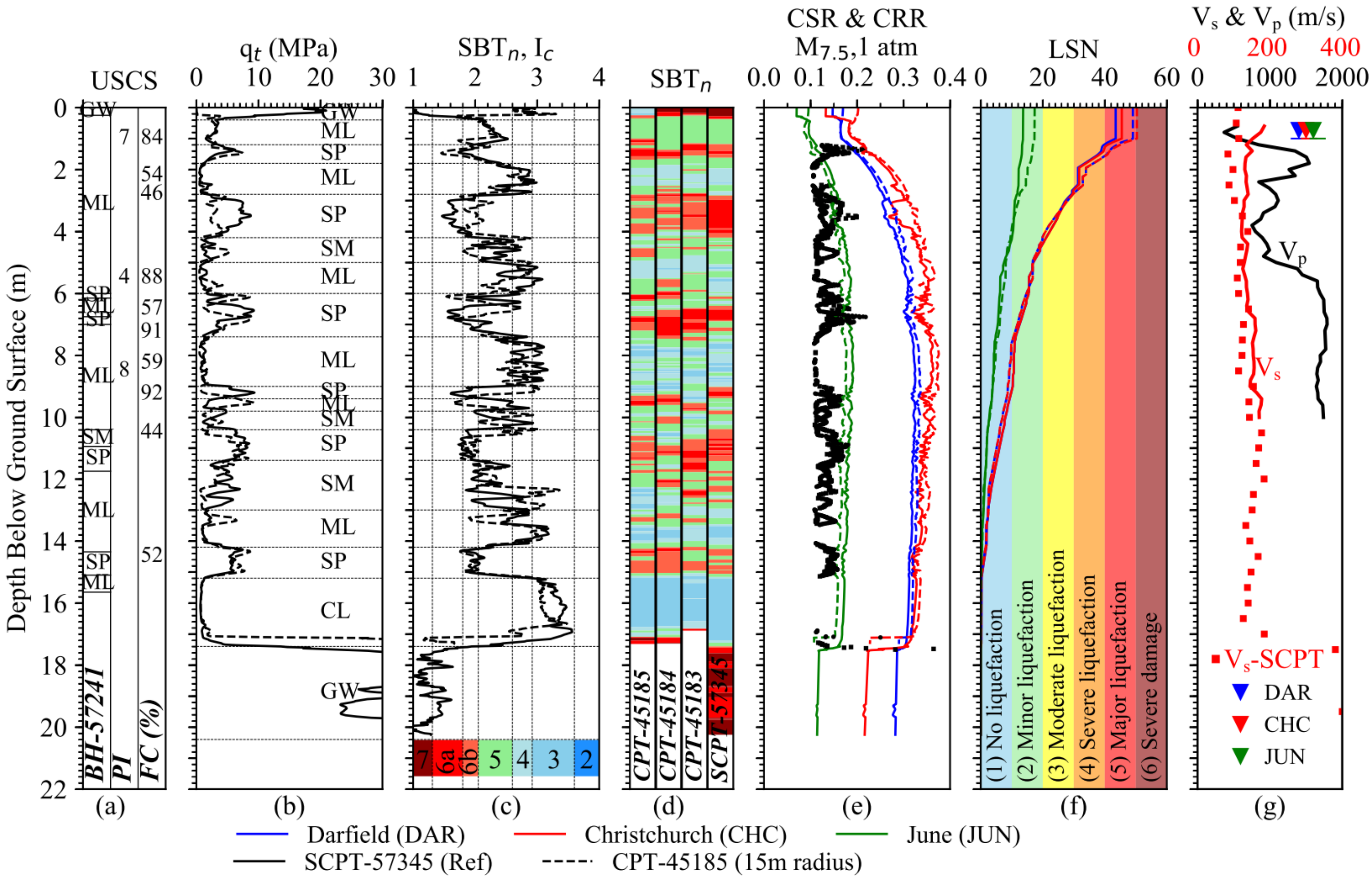

Figure 4.4 St. Teresa site subsurface information using the same format as Figure 4.3.

4.4.3 Sensitivity Analysis

Sensitivity analyses of the LSN computations are performed using the parameters listed in Table 4.1 to quantify the possible range of liquefaction manifestations. Key seismic demand (surface PGA and M_w), site characteristics (q_{t1Ncs} and GWL), and triggering procedure [probability of liquefaction (P_L), $I_{c\text{-}cutoff}$, and fines content correction (C_{FC})] parameters are varied as noted in Table 4.1. The LSN calculations are performed to develop tornado plots by varying each parameter systematically across its range of uncertainty while keeping all other parameters at their baseline mean value (μ). The resulting tornado plots with the observed land damage noted are shown in Figure 4.5.

The LSN-based procedure underestimates the observed ejecta severity at the Shirley site after the Christchurch and June events (with high-intensity shaking at the site). The procedure estimates Minor liquefaction manifestation, whereas the observation was Extreme after the Christchurch event, indicating significant underestimation. The tornado plots in Figure 4.5 indicate LSN is most sensitive to q_{t1Ncs}. The value of q_{t1Ncs} needs to be decreased by more than 25% to produce LSN values consistent with the Extreme category. However, q_{t1Ncs} is unlikely to deviate that much from what was measured with the CPTs. The LSN also underestimates the field observations for the June event considering reasonable variations of the parameters. However, LSN estimates observations reasonably for the Darfield event (with low intensity shaking).

Table 4.1 Parameters used in sensitivity analysis of LSN estimation.

Parameter	Earthquake	Shirley (Mean)	Shirley (Range)	St.Teresa (Mean)	St.Teresa (Range)
Surface PGA (g) (1)	Darfield	0.19	0.13–0.25	0.29	0.20–0.38
	Christchurch	0.38	0.26–0.50	0.36	0.25–0.50
	June	0.25	0.17–0.33	0.17	0.12–0.22
GWL (m) (2)	Darfield	2.80	2.30–3.30	1.00	0.50–1.50
	Christchurch	2.60	2.10–3.10	1.00	0.50–1.50
	June	2.20	1.70–2.70	1.00	0.50–1.50
M_w(3)	Darfield	7.10	7.00–7.20	7.10	7.00–7.20
	Christchurch	6.20	6.10–6.30	6.20	6.10–6.30
	June	6.20	6.10–6.30	6.20	6.10–6.30
P_L (%) (4)	All events	50	15–85	50	15–85
C_{FC} (5)	All events	0.13	-0.14–0.37	0.13	-0.14–0.37
$I_{c\text{-cutoff}}$	All events	2.60	2.40–2.80	2.60	2.40–2.80
q_{t1Ncs}	All events	varies	μ ± 25%	varies	μ ± 25%

*1 Surface PGA is estimated using Bradley [2013] with mean and range values set as 50th and 16th–84th percentiles value, respectively.

2 Mean GWL is from the piezometer measurement and the range values are $\pm$ 50 cm.

3 Mean M_w is that of each event with June extended due to foreshock; range set as $\pm$ 0.1.

4 Probability of liquefaction (P_L) is 50% for base case with the range of 15% to 85% probability.

5 Mean and range values of C_{FC} are based on Maurer et al. [2019].

6 Geomean q_{t1Ncs} is from the CPT data; its range of $\pm$25% is from Phoon and Kulhawy [1999].

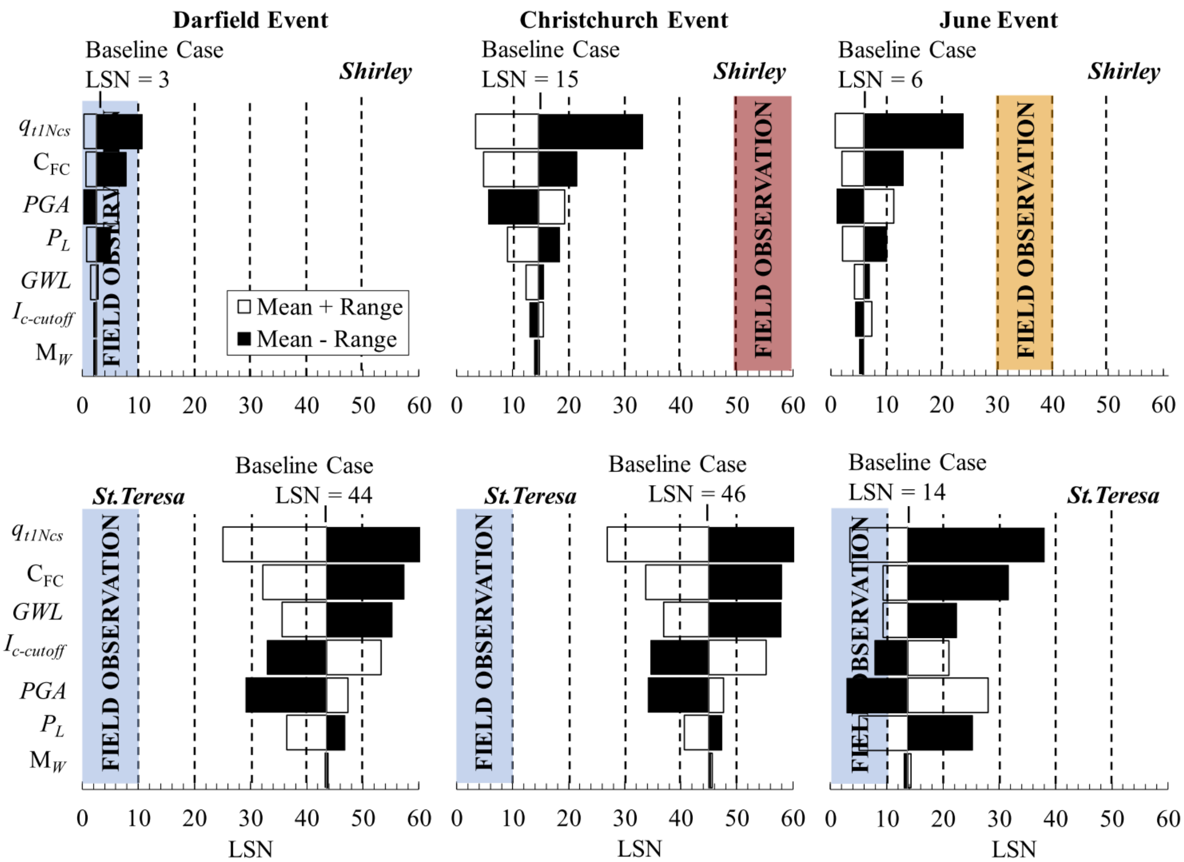

Figure 4.5 **Sensitivity results using parameters listed in Table 4.1 summarizing most sensitive parameters to LSN value at Shirley site (SCPT-57366: 20.2 m) and St. Teresa site (SCPT-57345: 20.2 m) for each event using the BI-16 procedure.**

The LSN-based procedure overestimates the ejecta severity at the St. Teresa site after the Darfield and Christchurch events (with high-intensity shaking). The LSN estimates Major liquefaction manifestation, whereas the observation is None, indicating excessive overestimation. The tornado plots also indicate that q_{t1Ncs} is the most sensitive parameter to the computed LSN. In contrast to the Shirley site, the value of q_{t1Ncs} needs to be increased by more than 25% to produce LSN values consistent with the None category (Figure 4.5), which is unlikely. However, reasonable variations in the parameters can make the LSN values consistent with observations for the June event (with low intensity shaking).

The tornado plots indicate C_{FC} is the second most sensitive parameter to the computation of the LSN. The use of the Christchurch soil-specific C_{FC} value of 0.13 [Maurer et al. 2019] does not resolve the misestimations of LSN at the two sites. An unrealistically high value of $C_{FC} = 0.5$ is required to resolve the misestimation of the LSN at the St. Teresa site [Boulanger et al. 2018]. Figure 4.5 indicates varying the other parameters over reasonable ranges does not resolve the misestimation of LSN for these sites. The tornado plots show that LSN tends to produce misestimations at the sites undergoing high-intensity shaking (i.e., short rupture-to-site distance, R_{rup}), but the LSN produces reasonable estimations for low-intensity shaking.

4.5 EFFECTIVE STRESS ANALYSIS

4.5.1 Input Ground Motion

There are no acceleration-time histories recorded on bedrock in Christchurch for the Canterbury earthquakes. Hence, input rock motions were developed through deconvolution of recorded surface motions at stiff soil sites with nearly linear responses. Markham et al. [2016] deconvolved the recorded surface motion at the RHSC and CACS strong motion stations (shown in Figure 4.1) to produce outcrop motions at the top of Riccarton Gravel formation (15.9 m deep at RHSC and 6.0 m deep at CACS), which serve as the viscoelastic half-space in analysis with its shear-wave velocity (V_s) of 430 m/sec [Wotherspoon et al. 2015]. The Markham et al. [2016] deconvolved outcrop motions were scaled linearly herein to match the Bradley [2013] 5%-damped elastic acceleration response spectra estimated at the Shirley and St. Teresa sites using the R_{rup} and Riccarton Gravel V_s for each site with the M_w of each earthquake.

Seismic response analyses of strong-motion sites throughout Christchurch using the deconvolved RHSC fault-normal horizontal recording produced results generally consistent with those recorded at the sites (e.g., Markham et al. [2016]). because the RHSC station is closer to the St. Teresa and Shirley sites, it is used as the baseline input motion. Additional analyses were performed with horizontal components at different orientations of the deconvolved RHSC and CACS motions to evaluate the sensitivity of the results to the input motions (i.e., fault-normal, fault-parallel, maximum, and median components of motions). The uncertainty in the input ground motion due to its inherent variability is a limitation of this study and other studies of site response in Christchurch for the Canterbury earthquakes.

4.5.2 Soil Constitutive Model and Response

The soil dilatancy response (i.e., contractive or dilative) and the drainage characteristics (i.e., vertical hydraulic conductivity, k_v) are important aspects to simulate the hydro-mechanical response of liquefiable sites. Based on the Robertson [2016] modified SBT$_n$ index (I_B) [Figure 4.6(a)], the SP-1 unit at the Shirley site is classified as dilative sand-like materials (concentrated data points in SD zone). The SP-1 unit is susceptible to pore water pressure generation, cyclic mobility, and shear-strain accumulation depending on the amplitude and duration of the earthquake shaking. The liquefiable interbedded deposits of the St. Teresa site in its upper 10 m consist of sand-like, transition, and clay-like materials. The data points are scattered across different SBT zones, which require modeling thin layers of contrasting contractive and dilative responses with varying k_v of the SP, SM, and ML units at St. Teresa.

The sand-like materials at the Shirley (SP-1 and SP-2) and St. Teresa (SP and SM) sites were modeled using the PM4Sand constitutive model [Boulanger and Ziotopoulou 2017]. PM4Sand model can simulate the contractive-dilative response of sand-like material based on bounding surface plasticity and the critical state concept. The SP units are generally dilative with relatively high values of k_v due to their higher D_r and coarser particle size. The SM units generally exhibited contractive sand-like responses with lower k_v values than the SP units. The ML units at

St. Teresa are modeled using the PM4Silt constitutive model [Boulanger and Ziotopoulou 2018] by setting the maximum pore pressure ratio (r_{u-max}) to 0.9 to enable the triggering of liquefaction (referred herein as PM4Silt-Liq). The cyclic triaxial test results of similar ML soil performed by Beyzaei et al. [2018a] reported $r_u \approx 0.9$. The r_{u-max} parameter of the PM4Silt model was used in this study to distinguish silt-like response—in which liquefaction is possible—from clay-like response—which is not susceptible to liquefaction. The clay-like material (CL) at the Shirley and St. Teresa sites were modeled using the PM4Silt model with the default r_{u-max} value, which is typically less than 0.8 (referred herein as PM4Silt-Clay).

Sediment ejecta develop in part due to the post-shaking advection process in which hydraulic conductivity contrasts govern (i.e., profile of k_v vs depth). The Shirley site is underlain by a thick, continuous sand deposit with estimated high k_v values without significant restrictions to water flow; see Figure 4.6(b). The u_{exc} dissipation process within the thick SP-1 and SP-2 units occurs simultaneously and induces high-gradient upward seepage that may increase the u_{exc} at shallower depths after shaking stops. Conversely, the St. Teresa site is highly stratified with alternating layers of significantly different hydraulic conductivities (i.e., k_v values from 10^{-9} to 10^{-3} m/sec). The u_{exc} dissipation process within the highly stratified thin soil layers occurs largely independently due to the large differences of their k_v values. The u_{exc} generated in isolated layers is not able to produce significant upward seepage during or shortly after earthquake shaking because the low k_v ML units impede the upward flow. The ESA performed in this study captures the dissipation of u_{exc} and hydraulic gradient developed in the soil profile through solving the Biot's saturated porous medium (solid–fluid) equations numerically with a fully coupled formulation, where k_v is the key input parameter.

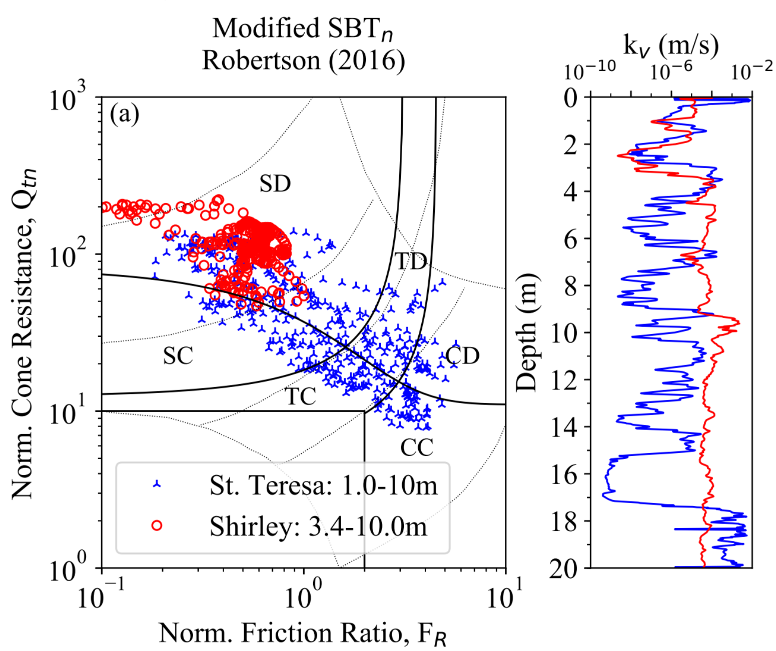

Figure 4.6 **(a) Interpreted soil behavior based on CPT measurement from the bottom of non-liquefiable crust layer until a depth of 10 m at each site; and (b) CPT-based coefficient of consolidation estimate using Robertson and Cabal [2015].**

4.5.3 Soil Parameters and Calibration

The soil constitutive model parameters are estimated primarily using the CPT data. The Robertson [2016] I_B is used to assign the PM4Sand model to the sand-like units ($I_B > 32$), PM4Silt-Liq ($r_{u\text{-}max}$=0.9) to the transitional silt-like units ($22 < I_B < 32$), and PM4Silt-Clay (default $r_{u\text{-}max}$) to the clay-like units ($I_B < 22$), as shown in Figure 4.7(a-b). The Riccarton Gravel is modeled as a viscoelastic material. The most important input soil parameters for the ESA are summarized in Figure 4.7(c-f). Measured V_s data is available at shallower elevations and the McGann et al. [2015] CPT-V_s correlation is used for deeper units. The D_r for SP and SM units are estimated using the Idriss and Boulanger [2008], Kulhawy and Mayne [1990], and Jamiolkowski et al. [2001] correlations with weights of 0.4, 0.3, and 0.3, respectively. The undrained shear strength ratio (S_u/σ'_{vo}) for ML and CL units is estimated using a cone bearing factor (N_{kt}) of 14. The k_v values are estimated using the Robertson and Cabal [2015] correlation for hydraulic conductivity.

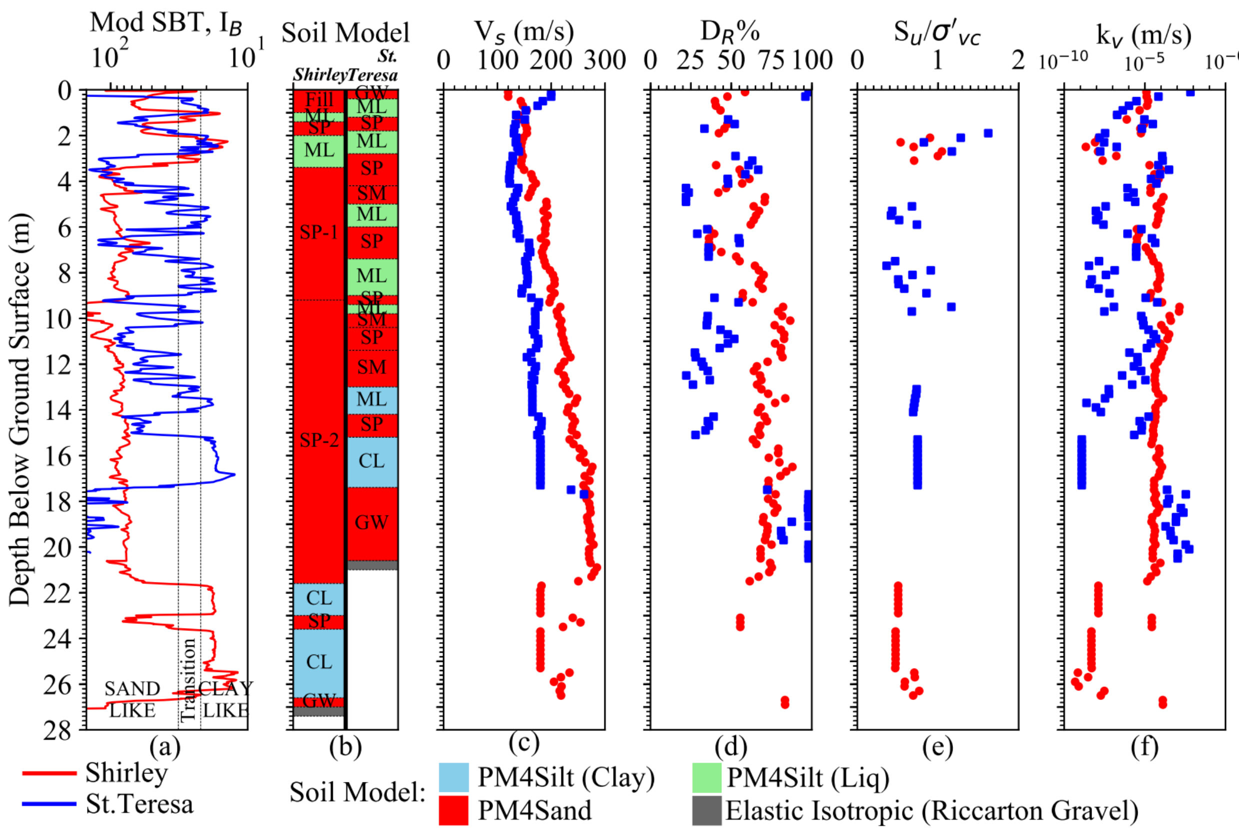

Figure 4.7 I_B**-based soil models and primary parameters used in analyses of the Shirley (Red) and St. Teresa (Blue) sites.**

The calibration of the PM4Sand and PM4Silt-Liq models was performed through undrained cyclic simple shear (CSS) test simulations of a single four-node quadrilateral element in OpenSees [McKenna and Fenves 2000]. The calibrated parameters for each site are listed in Tables 4.2 and 4.3. The calibration process included establishing the following:

- the slope of bounding surface (n_b) and critical state (Φ_{cv})lines in the *p-q* space
- the curvature of critical state line in the mean σ'_{vo}-D_r space
- the h_{po} primary parameter (PM4Sand and PM4Silt) to produce 3% single-amplitude shear strain in 15 cycles

The cyclic testing of Christchurch SP and SM soil by Taylor [2015] and Markham [2015] constrained the first two calibrations, and BI16 15%-85% P_L CRR curves constrained the h_{po} parameter. Figure 4.8 shows examples of the cyclic response of three key soil units at the Shirley and St. Teresa sites. The different stress-strain and contractive-dilative responses of the PM4Silt-Liq [Figure 4.8(b), 8e] and PM4Silt-Clay [Figure 4.8(c) and 8f] models are due to different $r_{u\text{-}max}$ values. Figure 4.9 shows the simulated CSR of the sand-like soils at Shirley and St. Teresa to reach 3% single amplitude shear strain calibrated to the BI-16 q_{t1Ncs} lines. The calibration is performed so that the simulated CSR vs. N_c line is between the BI-16 of 15% and 85% P_L lines.

Table 4.2 Constitutive model parameters for Shirley site.

Parameter	Fill / SM	ML (Low PI)	SP-1	SP-2	CL (Medium PI)
Model	PM4Sand	PM4Silt-Liq	PM4Sand	PM4Sand	PM4Silt-Clay
γ (kN/m^3)	18.0	18.0	18.0 - 19.3	18.4 - 19.6	18.0
Mean q_{t1Ncs}	100	70	100-120	150-175	--
h_{po}	2.0	2.0	3.2-10.2	2.0	1.2
n_b	1.4	--	1.4	1.4	--
e_{max}	1.0	--	1.0	1.0	--
e_{min}	0.6	--	0.6	0.6	--
R	1.0	--	1.0	1.0	--
Q	8.0	--	8.0	8.0	--
φ'_{cv}	35	Default	35	35	25
r_{u_max}	--	Default	--	--	Default

*Unit weight (γ): Robertson [2010] correlation; q_{c1Ncs}: BI-16; contraction rate parameter, h_{po}: calibrated to BI-16 liquefaction resistance curve; PM4Sand secondary parameters: n_b, e_{max}, e_{min}, and ϕ_{cv} are based on Taylor [2015] and critical state line parameters R and Q are based on Markham [2015]; PM4Silt secondary parameters: $r_{u\text{-}max}$ is based on Beyzaei et al. [2018a] and for CL soil is based on Boulanger and Ziotopoulou [2018]. Other parameters set to Boulanger and Ziotopoulou [2017; 2018a] default values.

Table 4.3 Constitutive model parameters for St. Teresa site.

Model	PM4Silt-Liq	PM4Sand	PM4Sand	PM4Silt-Clay	Model
γ (kN/m^3)	18.0	18.0	18.5	18.0	γ (kN/m^3)
Mean q_{t1Ncs}	70	80	120	--	Mean q_{t1Ncs}
h_{po}	2.0–3.0	15.0–20.0	2.0	1.2	h_{po}
n_b	--	1.4	1.4	--	n_b
$e_{\max}$	--	1.0	1.0	--	$e_{\max}$
$e_{\min}$	--	0.6	0.6	--	$e_{\min}$
R	--	1.0	1.0	--	R
Q	--	8.0	8.0	--	Q
ϕ'_{cv}	Default	33	35	25	ϕ'_{cv}
$r_{u\_\max}$	0.90	N/A	N/A	Default	$r_{u\_\max}$

* Parameters are estimated as described in Table 4.2.

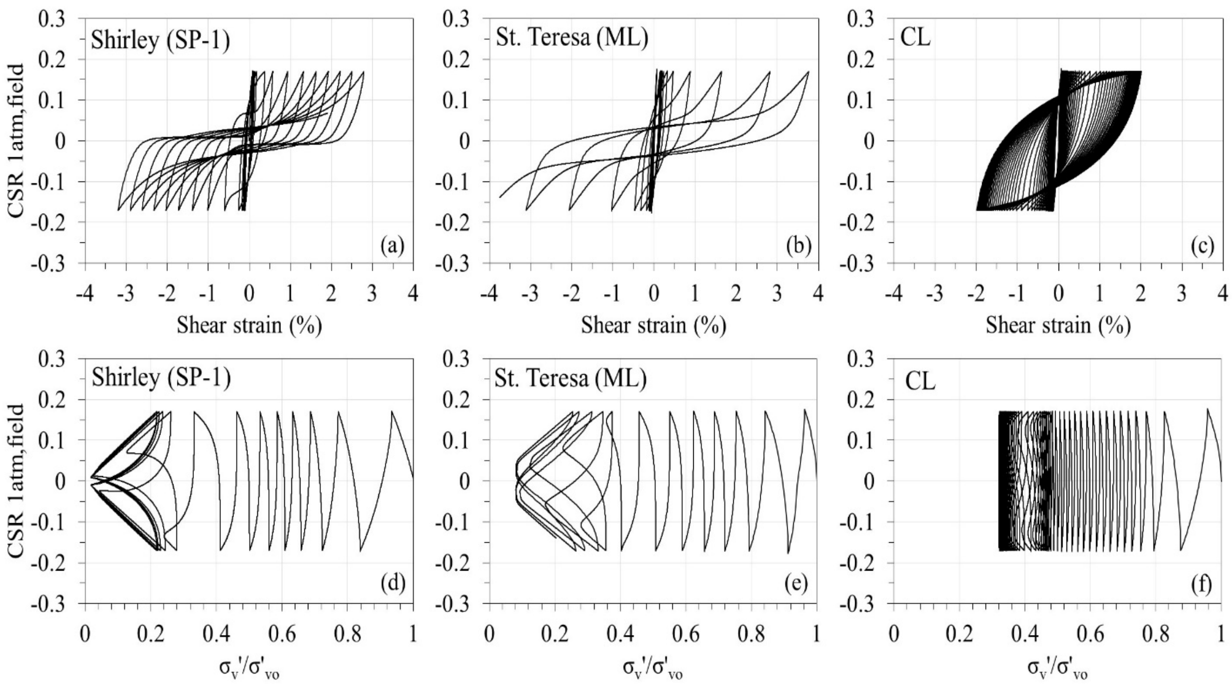

Figure 4.8 Cyclic stress-strain response of: (a) and (d) sand-like (PM4Sand) SP-1 unit at depth of 4.5 m at Shirley site, (b) and (e) transition (PM4Silt-Liq) ML soil at depth of 5.5 m at St. Teresa site, and (c) and (f) typical clay-like (PM4Silt-Clay) deep CL soil at Shirley and St. Teresa site.

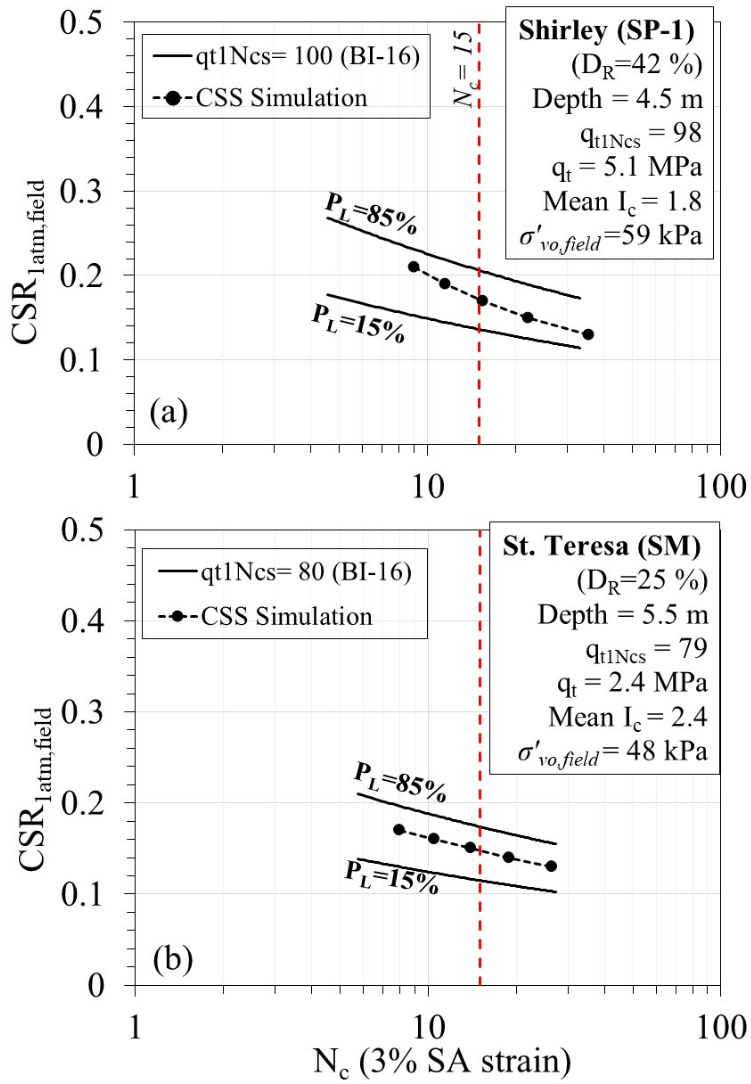

Figure 4.9 Simulated CSR vs N_c (number of cycles) of sand-like soil with 3% single amplitude shear-strain criteria: (a) SP-1 at Shirley site and (b) SM soil at St. Teresa.

4.5.4 Finite Element Model

The dynamic nonlinear ESA is performed using OpenSees with an implicit solver. The ESA utilizes a 2D plane strain four-node quadrilateral element [McGann et al. 2012] to solve the solid-fluid equilibrium and mass balance governing equations of the saturated porous medium (Biot's theory) following the Zienkiewicz and Shiomi [1984] *u-p* formulation (*u*: displacement of solid phase, *p*: fluid pore pressure). The four-node quadrilateral element employs a stabilized single integration-point with an hourglass control technique to avoid mesh locking with faster computing time compared to using a full integration scheme. The nodal displacement of the solid phase and the fluid pore pressure are solved at the corner nodes of each element, and stress and strain are computed at a single point at the center of each element.

Nodes at the same elevation are attached to displace together to represent a 1D column of soil. The base of the model is fixed against vertical movement. The boundary condition for pore pressure is set to be zero pore pressure for dry nodes and free for saturated nodes. The Lysmer and Kuhlemeyer [1969] dashpot is used at the base of the model where the input shear-stress time history is applied to model the viscoelastic base (i.e., dense Riccarton Gravel layer) with the dashpot coefficient computed based on Mejia and Dawson [2006]. The height of each quadrilateral element is 20 cm so it can resolve seismic waves with frequency of at least 50 Hz (i.e., assuming the soil may soften during liquefaction with an equivalent stiffness of about V_s = 80 m/sec). The construction of the damping matrix is based on the full Rayleigh damping formulation. The critical damping ratio is set to 2% at the natural frequency and at the fifth modal frequency of the soil column [Kwok et al. 2007]. The time-step selected for the analysis is 10^{-3} sec for the initial 180 sec during the dynamic simulation and changed to 10^{-1} sec afterward to speed up computation during the advection simulation.

4.5.5 ESA Validation

The ESA is validated by comparing the computed surface motions to nearby recorded ground motions. The SHLC SMS site is located within a similar geological formation 580 m away to the north of the Shirley site; see Figure 4.1. However, CPT-626 (53 m away from SHLC SMS) indicates that the shallower soil of the SHLC site (until a depth of 9.0 m) is denser than the Shirley site, so the site profiles are adjusted accordingly. The results for the Shirley site are shown in Figure 4.10. The response of the soil deposit displays limited nonlinearity during the Darfield earthquake [i.e., its natural period remains about the same, Figure 4.10(a)]. Amplification at most spectral periods (T) occurs due to its limited nonlinear response. The computed ground-surface acceleration time history and its response spectrum are in an excellent agreement with those of the recorded motions [Figure 10(a) (d), and (g)], indicating the amplitude, frequency content, and duration of the recorded motion are captured well. The ESA does not indicate liquefaction triggering, which is consistent with the field observation of no evidence of ejecta at the Shirley and SHLC SMS sites after the Darfield event [New Zealand Geotechnical Database; Wotherspoon et al. 2015].

The Shirley and SHLC SMS sites experienced significant nonlinearity during the intense Christchurch earthquake due to liquefaction. Wotherspoon et al. [2015] reported minor-to-moderate liquefaction at SHLC SMS for this event. The computed acceleration response spectrum indicates deamplification of spectral values at short periods [$T < 0.5$ sec, Figure 4.10(b)], which is due to a liquefaction-induced loss of stiffness of SP-1 unit, which restricts the propagation of the high-frequency component of the input motion. However, amplification at longer periods (0.5 sec $< T <$ 2.0 sec) still occurs because the system can propagate the low-frequency component of the input motion during liquefaction. The computed ground-surface acceleration time history and its response spectrum capture reasonably well those of the recorded motions considering the different densities of the upper soil deposit as well as other different characteristics of the SHLC SMS and Shirley sites. Importantly, the model captures dilation spikes in the computed ground surface motion [Figure 4.10(h)] due to its ability to capture phase transformation in the soil response. The computed and recorded acceleration response spectra differ more significantly for the June 2011 earthquake [Figure 4.10(c)] because liquefaction was not observed at the SHLC SMS site, but severe ejecta manifestation was observed at the Shirley site after the June event. Liquefaction is captured in the simulation as indicated by the dilation spikes in the acceleration time history [Figure 4.10(i)] as well as high calculated r_u values (not shown). Based on these results, the ESA employed in this study is judged to simulate the effects of liquefaction on seismic site response.

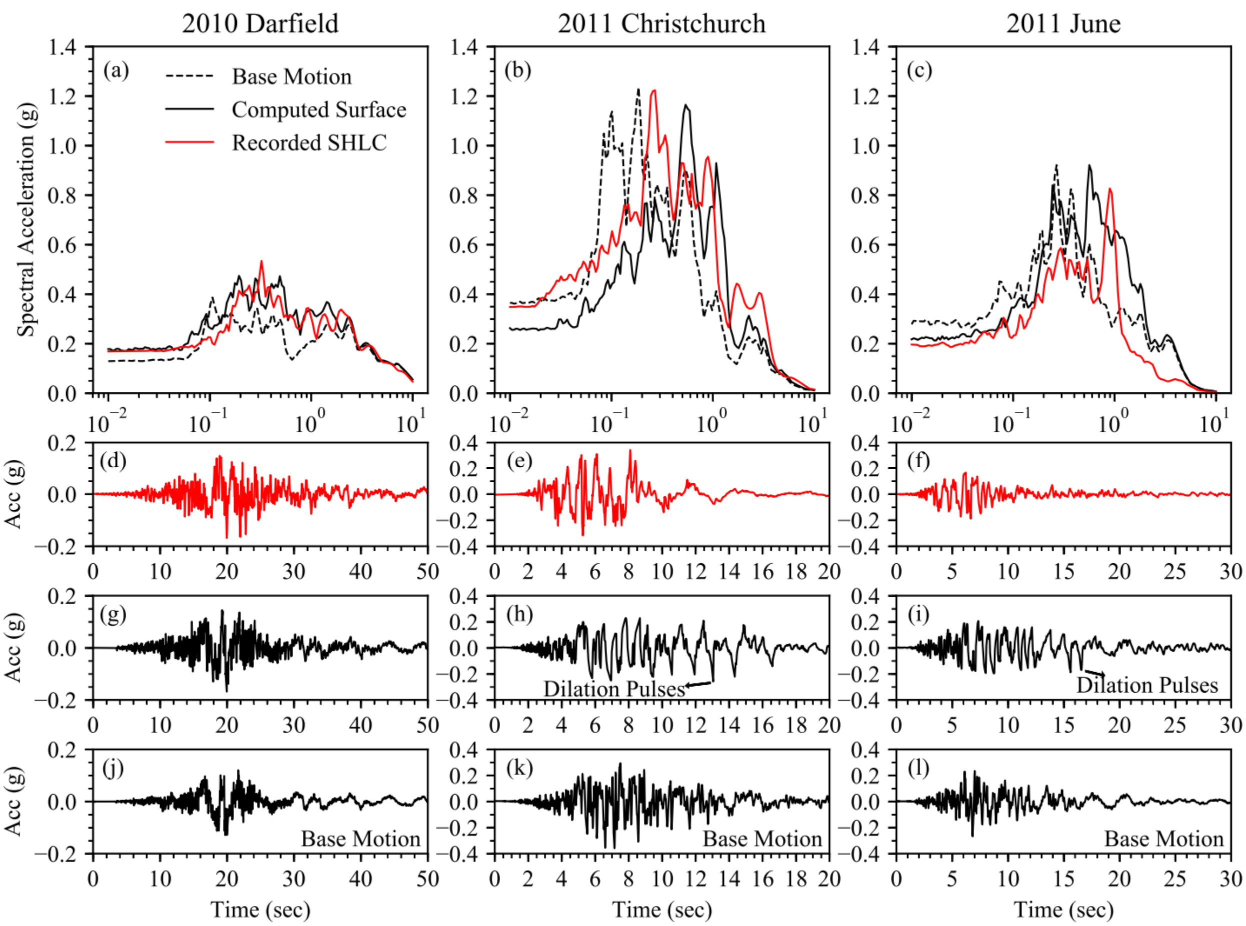

Figure 4.10 **(a-c) Computed 5%-damped spectral acceleration spectra and their (g-i) computed surface acceleration-time histories at Shirley site compared to (a-f) fault-normal recorded motions at SHLC SM station for each event; and (j-l) input base motions for analyses.**

4.6 FORMULATION OF EJECTA POTENTIAL INDEX

4.6.1 Artesian Flow Potential (AFP)

Sediment ejecta develop in part due to the post-shaking advection process in which variations in the hydraulic conductivity of the soil layers play an integral role. The Shirley site has a thick, clean sand deposit with consistently high k_v values, whereas the St. Teresa site is highly stratified with alternating layers of significantly different k_v values. In addition to the variation of k_v values in the soil profile, the total hydraulic head (h_T) that develops during and after earthquake shaking plays a significant role in the hydraulic response of the soil deposit (i.e., upward seepage and creation of ejecta). Figure 4.11(a) shows a soil profile typical of liquefiable sites with observed ejecta manifestation after the Canterbury earthquakes. The site has an upper low k_v crust layer (H_1) followed by a continuous high k_v clean sand deposit (H_2 + H_3), where its upper soil is a loose liquefiable layer (H_2), and its deeper soil has a higher relative density (H_3). Although the H_3 layer may not liquefy, it can generate a significant amount of u_{exc} during earthquake shaking. By assuming that kinetic energy is neglected due to relatively low water flow velocity, h_T is defined as $h_T = h_Z + h_{Po} + h_{exc}$ [Figure 4.11(a), (b)], where h_Z is the elevation head measured from a datum, h_{Po} is the hydrostatic pressure head, and h_{exc} is the excess pressure head due to elevated u_{exc} (i.e., $h_{exc} = u_{exc}/\gamma_w$). Under the initial steady-state hydrostatic condition, the total hydraulic head is defined as $h_{To} = h_Z + h_{Po}$, where the total head difference throughout the soil profile is zero (i.e., no flow).

During earthquake shaking, h_{exc} increases as pore water pressure is generated due to the nearly undrained cyclic loading of the saturated contractive soil. The maximum h_{exc} is the initial vertical effective stress converted to hydraulic head (σ'_{vo}/γ_w) at a depth of interest. For instance, when liquefaction occurs at point B during shaking [Figure 4.11(b), at $t = t_m$), the generated h_{exc} reaches the $\max h_{exc} = \sigma'_{vo}/\gamma_w$ line. After shaking ends ($t > t_m$), the h_{exc} gradually decreases and eventually returns to zero (i.e., the initial hydrostatic condition). At any time, the average secant hydraulic gradient between point B and the initial phreatic surface at the bottom of the crust layer (where $h_p = h_{exc} = 0$) is

$$i = \frac{\Delta h_{exc}}{\Delta z} = \frac{\left[\Delta h_{exc(B)} - h_{exc(crust)}\right]}{(z_B - z_{crust})} \tag{4.3}$$

where Δh_{exc} is the excess head difference between point B and the bottom of the crust, and Δz is the vertical distance between the two points. The higher h_T due to positive h_{exc} in the liquefiable soil initiates upward seepage where its velocity depends on the k_v of the soil (assuming Darcy's law). With the loss of effective stress due to liquefaction and sufficient hydraulic gradient, the upward seepage can initiate artesian flow that exploits cracks in the low k_v crust layer (e.g., through hydraulic fracturing and internal erosion), form a flow channel, and produce sediment ejecta; see Figure 4.11(a). Upward seepage can transport water with sediment ejecta to the ground surface if the generated h_{exc} is high enough to produce artesian flow.

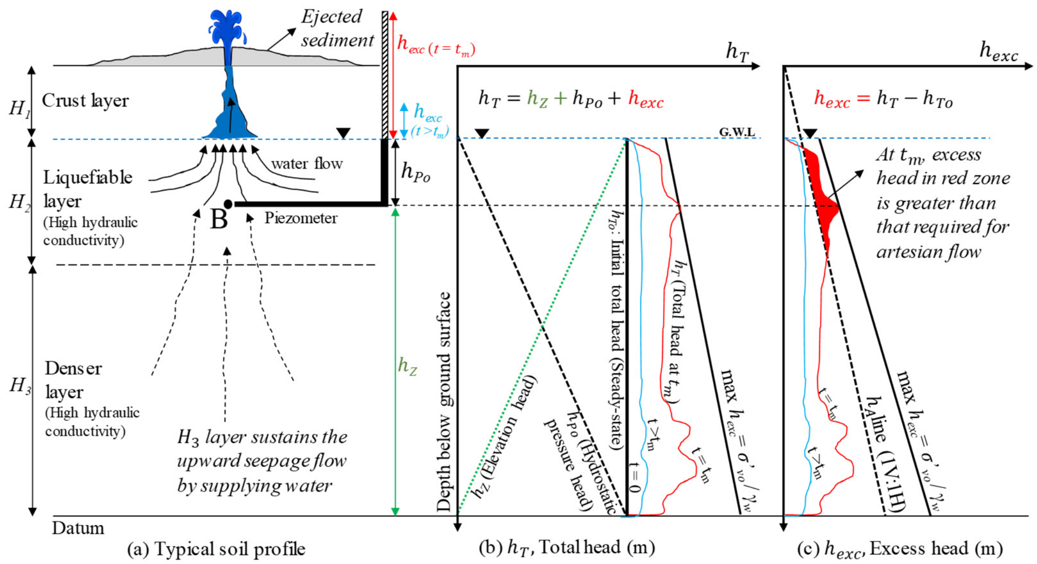

Figure 4.11 Schematic of hydraulic conditions at a site that manifested significant ejecta with definition of excess head (h_{exc}).

Two conditions must be met to produce artesian flows that eject the liquefied sediment, where (1) the total hydraulic head (h_Z + h_{Po} + h_{exc}) is higher than the ground surface and; (2) the soil reaches an adequately low effective stress (σ'_{vo}) where the generated h_{exc} is sufficient to exploit cracks in the crust layer and form a flow channel (e.g., through hydraulic fracturing and internal erosion). As illustrated by the red line in Figure 4.11c, when shaking-induced liquefaction is triggered at point B (at $t = t_m$), the h_{exc} reaches its maximum h_{exc} value ($\sigma'_{vo} = 0$) and produces high artesian pressure. At $t = t_m$, the first condition is met if the h_{exc} is greater than the crust layer thickness (H_1); however, the artesian pressure may not be sufficient to erode the entire crust layer and produce artesian flow above ground surface. To meet the second condition, the h_{exc} at shallow depths must exceed the artesian excess head (h_A) value, as illustrated by the black-dashed h_A line in Figure 4.11(c). The highlighted red zone in Figure 4.11(c) represents the soil layer that generates significant amounts of h_{exc} to produce artesian flow and erodes the crust layer.

The excess hydraulic head required to eject the liquefied sediment to the ground surface is equivalent to the magnitude of h_{exc} that exceeds the artesian excess head (h_A) value. The generated artesian fluid pressure developed during earthquake shaking represents the hydraulic demand to produce ejecta. In this report, the Artesian Flow Potential (AFP) is proposed as an index that quantifies the hydraulic demand for artesian flow at a specified time, given as

$$\mathrm{AFP}(m^3) = \int_{Z_o}^{Z_{\mathrm{GWL}}} (h_{exc} - h_A)^2 \, dz \begin{cases} \text{when } h_{exc} > h_A \\ 0, \text{otherwise} \end{cases} \tag{4.4}$$

where z is depth; z_{GWL} is the depth to groundwater table; z_o equals 10.0 m (the upper 10 m of the profile is assumed to provide most of the demand); and h_A is the required h_{exc} to initiate artesian flow. At each depth, the h_A value required to cause the artesian condition is represented in the soil profile as a line sloping down 1H:1V from the ground surface. The shaded area [with $h_{exc} > h_A$ in

Figure 4.11(c)] represents the zone where enough artesian pressure is developed to eject fluidized sediment. The thicker this zone and the longer the process is sustained after earthquake shaking, the more quantity of fluidized sediment that will be ejected and the more severe the resulting ground failure. The square term in Equation (4.4) emphasizes the relative importance of having $h_{exc} > h_A$, and it gives AFP the dimension of volume (m^3). The AFP quantifies the thickness of the liquefied layer and magnitude of h_{exc} to produce artesian flow.

In most cases, the H_3 layer sustains the h_{exc} at the shallower elevation by supplying water during the u_{exc} dissipation process; see Figure 4.11(a). The dynamic nonlinear ESA performed herein computes the u_{exc} time history to calculate the time history of AFP during and after earthquake shaking. If h_{exc} never exceeds h_A, AFP = 0 and artesian flow and ejecta are not expected. This can occur when high excess pore water pressures are not generated during earthquake shaking or the excess hydraulic head never exceeds the amount required to initiate artesian flow. When AFP > 0, artesian flow and ejecta are possible if liquefaction is triggered.

4.6.2 Ejecta Potential Index (EPI)

The AFP concept is developed to capture the post-shaking water flow and measure the required artesian pressure (i.e., hydraulic demand), represented by h_{exc}, to produce artesian flows that eject the liquefied sediment. The AFP index identifies discrete points in time when $h_{exc} > h_A$. However, field observation suggests that the longer the artesian flow exists, the more ejected sediment is transported to the ground surface. The duration of the condition when $h_{exc} > h_A$ is also a key factor to consider in evaluating the potential of artesian flow and ejecta, because the longer the artesian condition exists, the greater the amount of sediment that will be ejected. This aspect is equivalent to the thickness of the red shaded zone in Figure 4.11(b-c) and the duration of $h_{exc} > h_A$ condition during and after earthquake shaking. The longer $h_{exc} > h_A$ condition is sustained, the more liquefied sediment that will be ejected and the more severe the resulting ground failure. Therefore, the time history of AFP is integrated over time to capture the important influence of duration to define the EPI as

$$\text{EPI}(m^3.s) = \int_{t_o}^{t_f} \int_{Z_o}^{Z_{GWL}} (h_{exc} - h_{i_{cr}})^2 \, dz \, dt \tag{4.5}$$

where t_o is the initial time when the input acceleration reaches 0.05g, and t_f = 150 sec. The t_f of 150 sec is assumed based on multiple observations that the typical time of the crust non-liquefiable layer started to crack is approximately 2 to 3 minutes (150 sec on average) after the beginning of earthquake shaking from shallow crustal earthquakes (e.g., Ambraseys and Sarma [1969], Bardet and Kapuskar [1989], and Kawakami [1965]. The ejecta starting time of 2–3 minutes is also consistent with eyewitness accounts during the Canterbury earthquakes. Furthermore, the simulations performed in this study are not realistic after the non-liquefiable crust cracks significantly due to its dramatic change of hydraulic conductivity and its effect on the system response of the soil profile after cracking.

Such a complex physical process cannot be simulated using the ESA continuum framework employed in this study. Therefore, as an index, EPI is formulated to evaluate the hydro-mechanical response of liquefiable sites for the first 150 sec as a basis to estimate the hydraulic demand for artesian flow that in turn drives the initiation of sediment ejecta after liquefaction is triggered. Varying the value of t_f from 120–180 sec had a minor effect on the computed EPI values of these sites that were shaken by shallow crustal earthquakes of short-to-moderate duration, and it had no impact on the relative values of EPI. The 150 sec of simulation are also computationally efficient for developing an index of the hydraulic demand for artesian flow. The length of the simulation and t_f value used in Equation (4.5) should be extended for low-intensity, long-duration subduction zone earthquake shaking that triggers liquefaction near the end of the record.

4.6.3 Interpretation of ESA Results

The results of computed soil displacement and h_{exc} profile with depth for each time step are attached in the animation video as the electronic supplement of this report. Figure 4.12(a-d) summarizes the key results of the back-analysis of the Shirley site during each of the three primary Canterbury earthquakes. High shear strain ($\gamma > 3\%$) is generated from a depth of 6.0–7.2 m due to the Christchurch earthquake [Figure 4.12(a)], indicating shaking-induced liquefaction at that depth in the sand layer with the lowest D_r. Liquefaction triggering from ground shaking (using the $\gamma >$ 3% criterion) is focused in this 1.2-m thickness of soil in the ESA; whereas the simplified procedure estimates a much greater thickness of sand liquefied; see Figure 4.3(e). The system response of the entire soil deposit is captured in the ESA, where the severe loss of stiffness of the weakest soil layer found from 6.0–7.2 m in depth reduces the seismic demand on upper layers. Consequently, the ESA estimates lower seismic demand and lower shaking-induced shear strain in the soil found at a depth of 3.4–6.0 m.

The shear strain generated during earthquake shaking (i.e., 0 sec < t < 30 sec of the simulation) is only one aspect of the Shirley site response because high $r_{u\text{-}max}$ values are also calculated at depth of about 3 m; see Figure 4.12(b). The advection of post-shaking residual u_{exc} can produce upward seepage and cause deleterious consequences for overlying layers [Seed 1979]. Consequently, the soil system develops high excess pressure head within the depth of 3.5–5.0 m [higher than h_A value, see Figure 4.12(c)] due to pore water migration after the shaking ceased (i.e., t > 30 sec) as shown in Figure 4.12(d) at t = 180 sec. In fact, $h_{exc} = \sigma'_{vo}/\gamma_w$ at 180 sec, which signifies this soil liquefied after earthquake shaking ended due to secondary liquefaction from upward seepage. The value of h_{exc} at t =16.3 sec (during strong shaking) is much less than the excess hydraulic head required to trigger liquefaction from a depth of 3.5–6.0 m; see Figure 4.12(d).

After shaking ceases, h_{exc} at 6.0–7.2 m (liquefied layer) starts to decrease rapidly (high k_v soil profile) resulting in upward seepage (i.e., $h_{exc} > h_A$) that increases the h_{exc} over the depth of 3.5–5.0 m to the point where it also exceeds h_A; see Figure 4.12(d). The $h_{exc} > h_A$ condition in this soil layer was sustained until t = 10,000 sec of the simulation. In reality, the artesian-induced upward seepage would exploit cracks in the crust thus dramatically increasing its effective hydraulic conductivity. This study focused on the impacts of the seismic demands and resulting hydraulic demands of this problem and did not consider the influence of the changing resistance of the crust to water flow because of the difficulties in capturing this effect. However, important insights are provided through extending the duration of the simulation to capture part of the advection process.

Similar results are shown in Figure 4.12(a-c) for the June event but at lower amplitudes due to its weaker ground shaking. The computed h_{exc} is not sufficient to initiate artesian flow (i.e., $h_{exc} < h_A$) for the Darfield earthquake; thus, ejecta were not expected for this event, which is consistent with field observations. Sediment ejecta were expected for the Christchurch and June events because liquefaction was triggered, and there were sufficient duration and thickness of layers with the $h_{exc} > h_A$, which is consistent with field observations for these events. The u_{exc} dissipation within the continuous SP-1 and SP-2 units occurs simultaneously, and water flows relatively easily and quickly towards the upper layers that initially had lower h_{exc}. The SP-2 unit sustained the high h_{exc} in SP-1 after the shaking ceased by supplying upward water flow. High-exit hydraulic gradients ($i_e >> 1$) were calculated in the simulations near the bottom of the nonliquefiable crust, indicating that internal erosion at the bottom of the crust layer was likely. The simulation video (provided as the electronic supplement) is useful to visualize the advection process over time.

Figure 4.12(e-h) summarizes the key results of the back-analysis of the St. Teresa site during each of the three primary Canterbury earthquakes. High shear strains ($\gamma > 3\%$) were generated from depths of 6.0–7.4 m (SP) and 12.0–13.0 m (SM) due to the Christchurch earthquake [Figure 4.12(e)], indicating shaking-induced liquefaction at those depths. Liquefaction triggering from ground shaking (using the $\gamma > 3\%$ criterion) was focused in these two layers in the ESA, whereas the simplified procedure estimated a much greater thickness of liquefied layers; see Figure 4.4(e). The ESA captured the system response of the entire interbedded deposit, where the severe loss of stiffness of the weaker soil layers found at depths of 6.0–7.4 m and 12.0–13.0 m reduced the seismic demand on upper layers. Consequently, the ESA estimated lower seismic demand and lower shaking-induced shear strain in the soil found at depths shallower than 6.0 m. The seismic demand reduction due to shear strain concentration may explain why liquefaction did not trigger at shallower elevations; however, it did not give enough insights on the hydraulic mechanism why ejecta were not produced at the St. Teresa site.

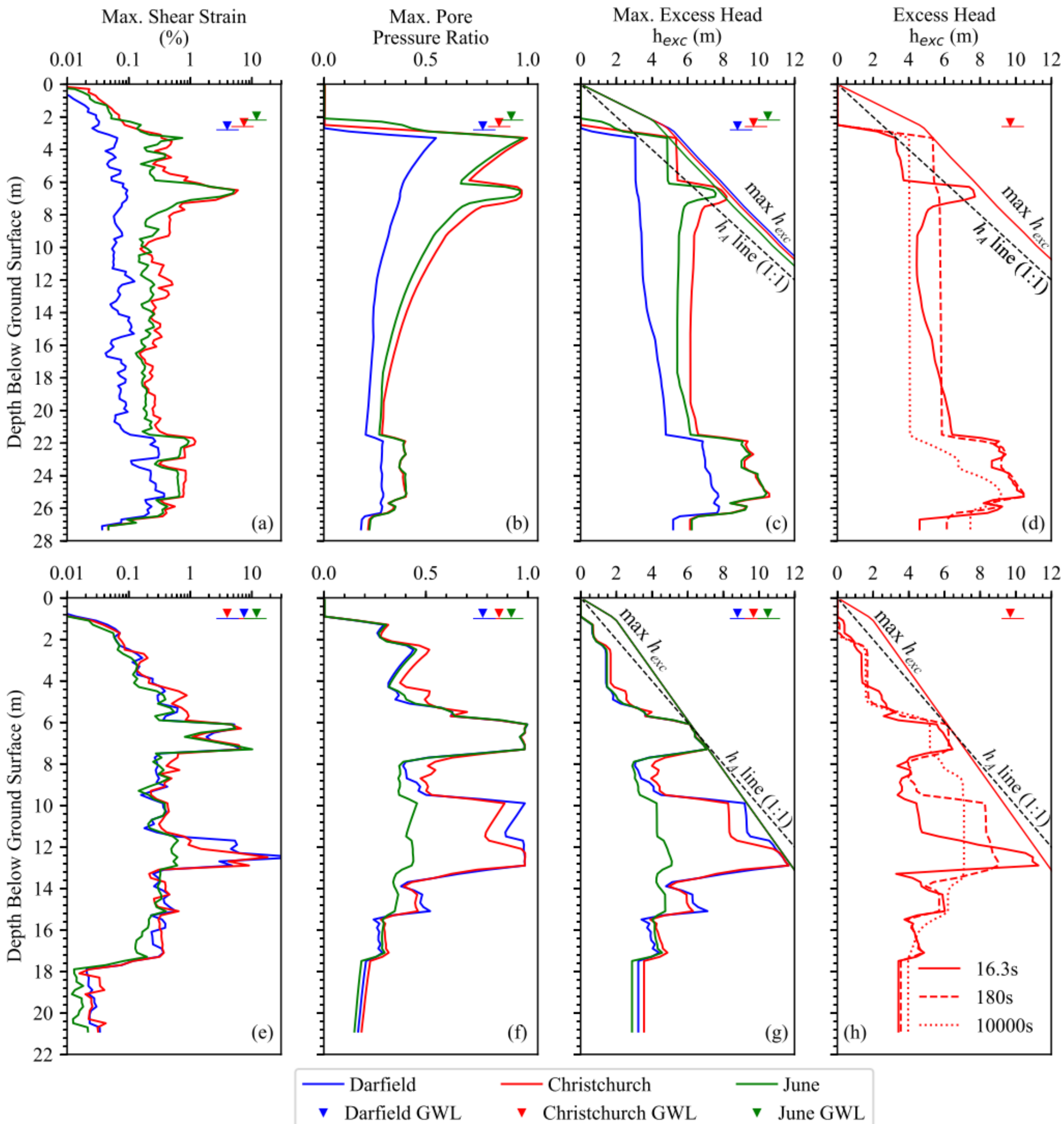

Figure 4.12 **Summary of analytical results for (a-d) Shirley and (e-h) St. Teresa sites: (a) and (e) maximum shear strain; (b) and (f) maximum pore pressure ratio; (c) and (g) maximum excess head relative to σ'_{vo} condition (colored lines for each event and h_A line); (d) and (h) excess head during strong shaking (16.3 sec) and after shaking (180 sec and 10000 sec) for Christchurch event.**

More of the St. Teresa's interbedded deposit is susceptible to liquefaction than the Shirley site due to its shallower GWL (lower σ'_{vo}), which produces a thicker liquefied layer with the simplified liquefaction triggering procedures. However, the lower σ'_{vo} reduces the maximum amount of generated residual u_{exc}, resulting in h_{exc} being lower than the critical h_A value at depths below 6.0 m; see Figure 4.12(g), whereby no $h_{exc} > h_A$ condition developed for the 10,000 sec of simulation, indicating AFP is always zero. A shallow GWL does increases the potential for triggering liquefaction (σ'_{vo} =0) at a depth of interest, but it does not necessarily increase the potential of producing ejecta. This is consistent with some of the cases of the 1976 Tangshan, China, earthquake case history reported by Ishihara [1985]; ground failure was not observed at sites with a very shallow GWL (i.e., very thin crust) overlying a thick liquefiable layer. Upward water seepage occurs with the development of excess water pressures in the liquefiable layer, but they are not sufficient to produce artesian flow and ejecta.

The advection process within the interbedded St. Teresa deposit does not occur simultaneously due to hydraulic conductivity contrasts that inhibit the upward seepage flow toward ground surface. Figure 4.12(f-h) indicates secondary liquefaction occurred at the depth of 9.6–11.6 m, as shown in Figure 4.12(h) (at t = 180 sec), due to upward seepage flowing from the underlying SM unit, at the depth of 12.0–13.0 m, which is liquefied during shaking. However, upward flow into the ML unit is impeded due to its significantly lower hydraulic conductivity; thus, secondary liquefaction did not occur in the ML unit. The generated h_{exc} in the SP and SM units at depth of 6.0–7.8 m triggered liquefaction but it did not generate sufficient upward flow into the shallower soil unit above the depth of 6.0 m [as indicated in Figure 4.12(h)] due to the low hydraulic conductivity of the overlying ML layer at 5.0–6.0 m. Secondary liquefaction at shallow depths, which occurred at the Shirley site, did not occur at the St. Teresa site. As a result, the magnitude of the h_{exc} at the potentially critical layers between 1.0–6.0 m depth never exceeded the h_A line, so the AFP remained zero. There is insufficient artesian pressure to produce ejecta. Similar results are shown in Figure 4.12(e-g) for the Darfield and June event but at lower amplitudes due to their weaker ground shaking. The ML layer impedes the upward seepage that could have produced secondary liquefaction at shallower depths. Thus, ejecta were not expected for these events, which is consistent with field observations. The calculated hydraulic gradients near the bottom of the nonliquefiable crust at the St. Teresa site are significantly lower than at the Shirley site, indicating that internal erosion was unlikely.

Figure 4.13 illustrates how AFP concept is used to interpret the post-shaking hydraulic process obtained from ESA simulations of a thick, clean sand deposit at Shirley site [left soil column in Figure 4.13(a)] and highly stratified silty soil deposit at St. Teresa site [right soil column in Figure 4.13(a)]. Soil layers highlighted in red and blue are high-k_v (clean sand) and low k_v (silt) layers, respectively. The light red soil layers consist of silty sand with lower k_v values than SP soil. The Shirley site's simulation results demonstrated that liquefaction is first triggered (at t = 15.7 sec) within the loosest sand layer (depth of 6–8 m) that influences the seismic demand in other layers due to the dynamic site response. High h_{exc} were generated at these depths when liquefaction was triggered, as illustrated by the red curve in Figure 4.13(b). The dissipation of h_{exc} within the liquefied layer triggers high-gradient upward seepage, which increases the h_{exc} at shallow depths (depth of 3–5 m) after the shaking stop (at t = 180 sec) as illustrated in Figure 4.13(c). The simulation showed that the artesian pressures at 3-5 m developed after the shaking are higher than the h_A line. Using Equation (4.4), the computed AFP value (area of red zone) at t = 15.7 sec and t = 180 sec are 1.2 m^3 and 3.6 m^3, respectively. The plot of AFP-time history of Shirley site is shown in Figure 4.13(d), where the AFP value at the two time steps shown in Figure 4.13(b-c) are highlighted by white dots. The simulation shows that during the 2011 Christchurch earthquake [Figure 4.13(e)] the AFP value increases to its highest value after the shaking stop.

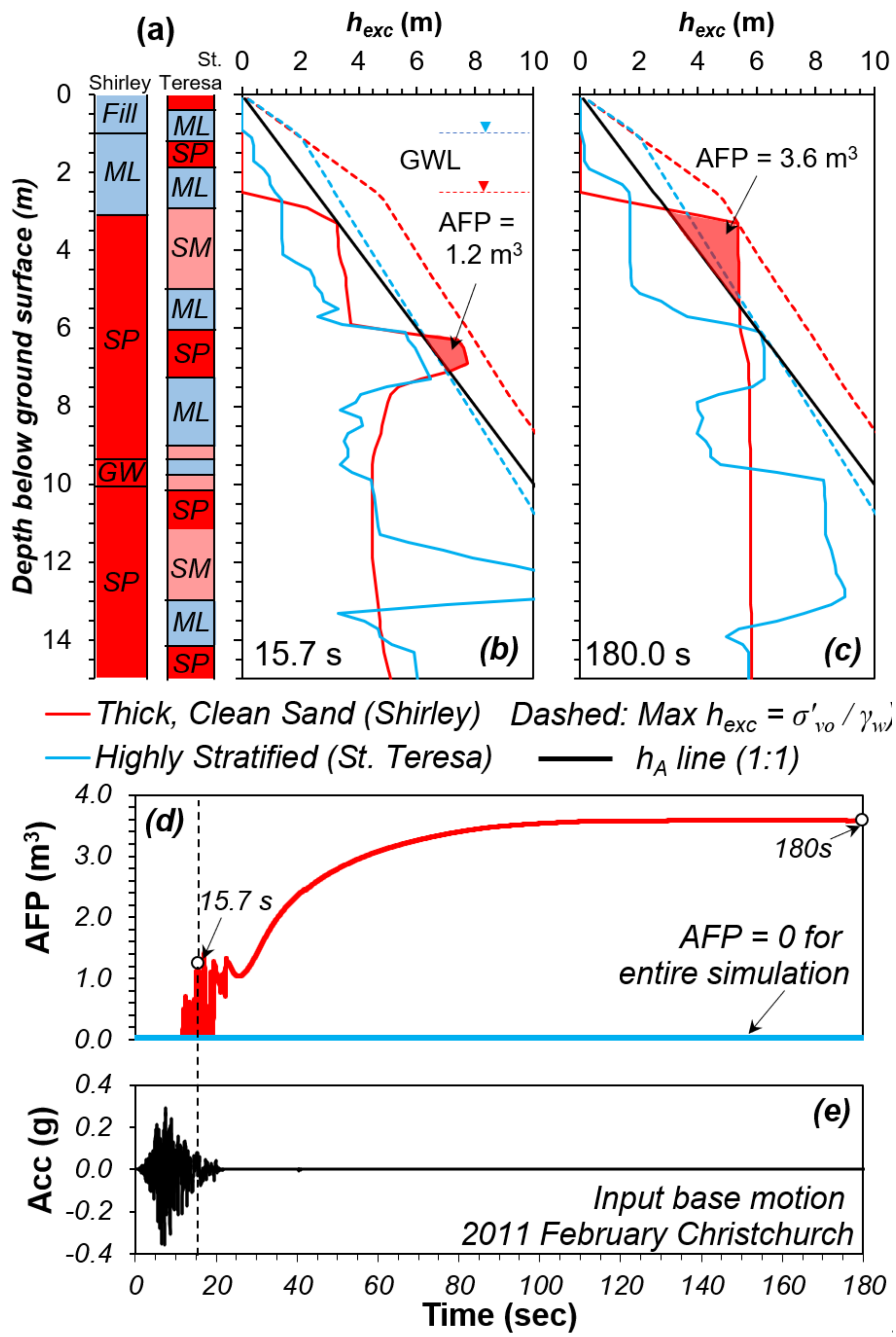

Figure 4.13 **(a) borehole profiles of a thick, clean sand (Shirley–left column) site and highly stratified (St. Teresa–right column) site; (b) profiles of computed h_{exc} during shaking (t = 15.7 sec); (c) after shaking (t = 180 sec), area in which $h_{exc} > h_A$ (red shaded zone) represents AFP at a point in time; (d) AFP-time histories; and (e) input base motion.**

For highly stratified soil deposit [St. Teresa in Figure 4.13(a), right column], the simulation also indicates that liquefaction was triggered at the loosest sand layers, and high h_{exc} is developed in these layers during strong shaking. However, the liquefied layers are isolated between low k_v layers that develop lower h_{exc}. The post-shaking hydraulic response of a highly stratified soil deposit is governed by its heterogeneous k_v-profile. For instance, the low k_v layer at depths of 5.0-6.0 m impedes upward water flow so that the h_{exc} at depths of 1.0-5.0 m remains low during and after the earthquake, as illustrated by the blue lines in Figures 4.13(b) and 4.13(c). The artesian pressures developed in the shallow depths are insufficient to develop cracks in the crust layer and produce artesian flows that eject the liquefied sediment. Therefore, the computed AFP for the entire simulation for St. Teresa site is always zero (i.e., h_{exc} within the profile never exceeds its h_A value). Moreover, the simulation indicates that the shallow soil does not liquefy during shaking because the deeper, weaker liquefied layer reduces the cyclic shear stress amplitude at shallow depths.

The AFP time histories shown in Figure 4.14 illustrate some key aspects of the earthquake shaking-induced generation of high excess water pressures and the migration of high excess water pressures after shaking stops for all earthquake event studied herein. The AFP values of the Shirley site during Christchurch and June events increased after the shaking stopped. They reached their highest value at t > 60 sec, indicating a thicker zone with $h_{exc} > h_A$ after shaking ceased. Conversely, the AFP remained at zero for the other simulations, regardless of the duration of the computation due to h_{exc} never exceeding h_A.

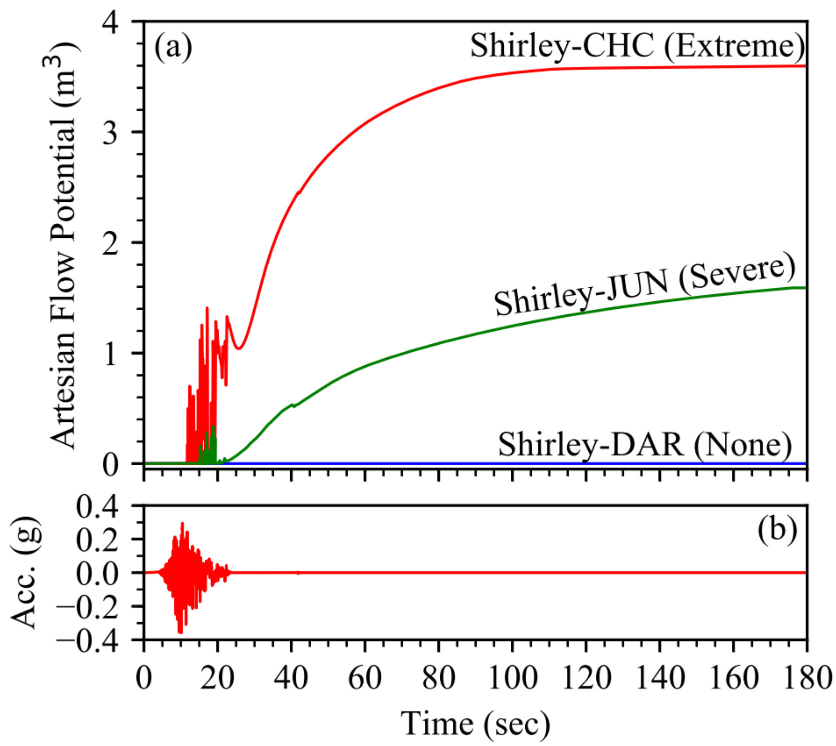

Figure 4.14 **(a) The AFP time histories at Shirley site for three Canterbury earthquakes with the (b) input acceleration time history at Shirley site for the Christchurch event. All AFP-time histories at St. Teresa site had zero values.**

The observations of sediment ejecta are provided in Table 4.4 with the corresponding computed LSN and EPI values [using Equation (4.5)]. The LSN does not correspond well to the observed liquefaction manifestation for most of these case histories. Conversely, the EPI does correspond well to the field observations of liquefaction ejecta. Only two cases (i.e., the Shirley site for the Christchurch and June events) have non-zero EPI values, and they are the only two cases where sediment ejecta were observed following the Canterbury earthquakes. The other four cases (i.e., the Shirley site for the Darfield event and the St. Teresa site for all Canterbury earthquakes) produced EPI = 0, which is consistent with the field observations of no sediment ejecta observed for these case histories. The results indicate that the h_A (1V:1H) line distinguishes sites with and without sediment ejecta manifestation well. The consistency of the computed EPI values with the field observations provided in Table 4.4 show promise in developing EPI as an index to estimate sediment ejecta. More work is required before EPI can be used in engineering practice. Accordingly, the robustness of EPI is being evaluated using a larger set of field case histories.

Table 4.4 Observed liquefaction manifestation with LSN and EPI values.

Earthquake	Site	Observed manifestation	LSN[1] (estimation)	EPI[2] (m^3sec)
Darfield	Shirley	None	3 (None)	0
	St. Teresa	None	44 (Extreme)	0
Christchurch	Shirley	Extreme	15 (Minor)	405
	St. Teresa	None	46 (Extreme)	0
June	Shirley	Severe	6 (None)	133
	St. Teresa	None	14 (None)	0

* [1] LSN calculated using mean parameters listed in Table 4.1.
[2] EPI calculated using calibrated parameters listed in Tables 4.2 and 4.3.

4.7 DISCUSSION

Several reasonable assumptions of the ground motions should be used to develop a reliable estimate of EPI for a thick, clean sand site (i.e., the Shirley site) for an earthquake. Simulations using the suite of eight input ground motions discussed previously produced consistent results in terms of identifying the soil layers that liquefied and the calculated excess hydraulic head profile, and they calculated EPI values within 16% of the mean value, except for one motion. The deconvolved fault-normal CACS input ground motion produced a seismic response at the Shirley site that triggered liquefaction initially at a different depth than the other motions, so its excess hydraulic head profile differed sufficiently to calculate an EPI value 50% lower the mean of the other motions. Performing analyses with several input motions can identify typical responses and potentially atypical responses to consider in the evaluation. At sites such as the St. Teresa site where the potential for ejecta is low because of significant layer stratification that impedes upward seepage after ground shaking stops, the results were insensitive to the input ground motion and EPI was always zero.

The AFP concept was derived to quantify the potential of a system to produce artesian flow. It was not developed to simulate the full complexity of sediment fluid flow, which requires modeling details on hydraulic fracturing and internal erosion of the crust layer. AFP is an index of the seismic and hydraulic demand intended to correlate with the likelihood of sediment being transported from the liquefied layer to the ground surface. Additionally, the EPI is formulated to account for the influence of these factors in evaluating the severity of sediment ejecta at liquefiable level-ground sites:

- liquefaction triggering
- input ground motion and the resulting dynamic response of the soil system
- amount of h_{exc}
- potential of upward seepage-induced artesian flow
- duration of $h_{exc} > h_A$ (i.e., artesian flow potential)
- hydraulic conductivity contrasts
- advection process

The integrity of the crust layer (i.e., strength and defects) is not accounted for in the EPI formulation. Alternative EPI formulations that included a term that characterized the integrity of the non-liquefiable crust through a weighted average of the strength and thickness of the layers in the crust did not produce enhanced insights. The authors also computed the integral of the generated AFP (demand) divided by the average shear strength of its overlying materials (resistance) at each elevation interval, as a proxy of hydraulic fracturing and internal erosion processes. However, this alternative EPI did not provide improved results and made the calculation more complex. Other EPI formulations with different weightings of the hydraulic demand or EPI formations that attempted to capture the cracking of the crust layer and fractured water flow did not provide improved insights and were also overly complex. In particular, the cracking process of the crust layer is a complex physical process that should consider the path of water flow within the crust layer, strength of crust material, defects in the crust, fracture mechanics, and fractured water flow, which is beyond the capability of the numerical technique utilized in this study. Advanced numerical analysis (e.g., coupled CFD-DEM or MPM) would be required to model cracking and internal erosion of the crust layer. However, the application of these techniques to soil liquefaction and ejecta formation are not yet verified. It must be noted that modeling the development of cracks in the crust are beyond the capability of conventional numerical analyses used in engineering practice. Evaluating the potential of upward seepage-induced artesian flow with ESA using validated constitutive models captures key features of liquefaction triggering and the generation of excess pore water pressures that produces sediment ejecta. Currently, ESA represents a reasonable path forward.

The primary goal of the development of EPI is to advance the liquefaction hazard assessment by accounting for the key aspects described previously. Despite its robustness, the ESA performed in this study has several limitations including:

- employed 1D site response analysis assumption (e.g., infinite horizontal layering, upward wave propagation)
- assumed 1D seepage
- considered only shallow soil column (up to 30 m)
- other limitations inherent in continuum finite element analyses.

Obviously, the robustness of the calculated EPI value can be no better than the robustness of the ESA used to estimate it. The EPI could be used as an EDP in performance-based design by considering a wide range of scenarios (e.g., input motions, spatial variability, uncertainty in model parameters, and different constitutive models) using the parallel processing capabilities of OpenSees. The EPI could also be utilized for bi-directional shaking simulations through computing the u_{exc} time history.

Laboratory cyclic test data were used in conjunction with field CPT data in this study to estimate PM4Sand and PM4Silt secondary parameters. Sensitivity analyses indicate the influence of the secondary parameters is relatively minor to the computed EPI value if the CRR line is calibrated with the h_{po} parameter to match the field-based CRR curve. Thus, the PM4Sand and PM4Silt primary parameters can be developed using CPT data focusing on I_B, q_{t1ncs}, and k_v correlations, default secondary parameters can be used, and the h_{po} parameter can be selected to match the target CRR. Doing so will compute EPI values consistent with the field observations for the cases studied. Additional work is warranted to investigate the robustness of the EPI for more case histories; this work is being undertaken.

4.8 CONCLUSION

The severity of the liquefaction manifestation was not captured well at several sites shaken by the Canterbury earthquakes using simplified liquefaction ground-failure indices (e.g., LSN and LPI). The misestimation of sediment ejecta at these sites cannot be explained by the uncertainty of the parameters used to characterize the sites. To gain insight into this problem, dynamic ESA was performed to simulate the hydro-mechanical response of liquefiable deposits at two sites representative of underestimated and overestimated case histories (i.e., the Shirley site and St. Teresa site, respectively). The investigation of key factors contributing to the large amounts of sediment ejecta produced at the Shirley site for the Christchurch and June earthquakes and lack of ejecta observed at the Shirley site for the Darfield event and at the St. Teresa site for all earthquakes led to the development of two indices of the hydraulic demand to produce artesian flow. The Artesian Flow Potential (AFP) and the integral of AFP over time (called the Ejecta Potential Index, EPI) show promise for capturing the observed trends in liquefaction manifestations at these two sites.

High hydraulic gradients develop through the crust at the Shirley site during the intense Christchurch earthquake due to the relatively large u_{exc} developed in its underlying thick deposits of liquefiable, clean sand. High-gradient upward seepage in the Shirley soil profile produced significant secondary liquefaction during this event. Consequently, a high EPI value was calculated for the Christchurch earthquake, which produced extreme ejecta at the Shirley site. A lower EPI value was calculated at the Shirley site for the June event, which was consistent with the severe ejecta observed at the site. The EPI = 0 at the Shirley site for the Darfield event, which is consistent with the observation of no ejecta. Conversely, the highly stratified soil layers with contrasting values of hydraulic conductivity at the St. Teresa site only developed high excess pore water pressures and trigger liquefaction in a few isolated layers. The amount of artesian pressure and rate of upward seepage were insufficient to cause secondary liquefaction in shallow soil layers that could produce ejecta at the ground surface. The calculated EPI values of zero at the St. Teresa site for all three of the primary Canterbury earthquakes was consistent with the lack of ejecta observed at this site.

Simplified liquefaction triggering procedures and hence the liquefaction indices that are based on them, miss key features of the seismic site response and post-shaking hydraulic conditions of liquefiable sites. It is not surprising that they struggle to capture a phenomenon as complex as the formation of sediment ejecta. Liquefaction indices neglect the post-shaking upward water flow process that is a key mechanism for producing ejecta after the earthquake shaking ceases. Sediment ejecta is largely a post-shaking phenomenon driven by the advection process due to residual u_{exc}. These procedures only consider the cyclic demand and cyclic resistance during the strong shaking, which was useful for triggering analysis, but cannot capture the post-shaking hydraulic mechanism of sediment ejecta. The ESA captures the system response of a thick, clean sand deposit and highly stratified silt and sand deposit, where the severe loss of stiffness of the weakest soil layer reduces the seismic demand on upper layers. Consequently, ESA estimates lower seismic demand and lower shaking-induced shear strain in the soil at shallow depths. However, evaluating only the dynamic response of the soil system during the shaking is not adequate to evaluate the hydraulic mechanism of sediment ejecta. The post-shaking advection process should also be simulated to evaluate the amount and distribution of residual u_{exc} after the shaking stops, which can develop high-gradient upward seepage that transports ejecta to the ground surface.

The EPI is formulated to evaluate the hydro-mechanical response of liquefiable sites to estimate the severity of sediment ejecta for use in performance-based earthquake engineering and to account for the hydraulic processes, drainage contrast, post-shaking advection stage, and duration of the $h_{exc} > h_A$ condition. Although dynamic ESA requires more effort, ESA can be employed in engineering practice using a standardized finite-element model (i.e., OpenSees script) and robust constitutive models with standardized calibration of soil parameters (e.g., PM4Sand and PM4Silt). The ESA can provide important insights in the development of the profile of h_{exc} and its influence on the production of sediment ejecta that simplified methods do not capture. An ESA captures the following key features:

1. the reduction in the seismic demand on soil layers overlying deeper layers that liquefy first and soften;
2. the generation of dilation pulses due to a temporary increase of stiffness (i.e., phase transformation) and;
3. the lengthening of the site's natural period due to stiffness degradation.

At the Shirley site, the upward seepage initiated from shaking-induced liquefied layer flows freely through the high-k_v clean sand deposit and causes secondary liquefaction within the shallow sand layers below the groundwater table. The secondary liquefaction initiates the $h_{exc} > h_A$ condition in the shallow sand unit that produces high artesian pressure to eject the fluidized sediment. The deeper, denser sand layer sustains the $h_{exc} > h_A$ condition by supplying upward flow during the advection process. Conversely, at the St. Teresa site, upward seepage occurred due to the generation of excess pore water pressures in the sand and silty sand units, but the upward seepage was insufficient to produce significant flow through the overlying low k_v silt layer, which prevented secondary liquefaction of shallower soil layers. Hence, ejecta were not produced. Ongoing work is evaluating the robustness of the EPI with a larger set of case histories.

5 Seismic Response Characteristics of Liquefiable Sites with and without Sediment Ejecta Manifestation

5.1 INTRODUCTION

The ESA results of a thick, clean sand deposit at the Shirley site performed in Chapter 4 has demonstrated significant increases of u_e and h_{exc} at shallow depths due to high-gradient upward seepage developed during the redistribution process of u_e within the entire soil profile after the shaking ceases. Intense upward water flow can trigger post-shaking secondary liquefaction in soil layers that did not liquefy during strong shaking [Seed 1979]. The simulation result suggests these post-shaking processes are responsible for extreme ejecta manifestations observed at the Shirley site, which were not captured by simplified liquefaction indices that may yield to underestimation. Conversely, researchers observed numerous highly stratified sites such as St. Teresa site with high LPI and LSN values (i.e., severe to extreme ejecta should have occurred) that did not produce any sediment ejecta manifestations during major Canterbury earthquakes (i.e., excessive overestimation). The ESA results of highly stratified silty soil deposit at St. Teresa site in Chapter 4 demonstrated that intermediate low-vertical hydraulic conductivity (k_v) layers could impede the upward water flow from underlying liquefied layers, which prevents the generation of high h_{exc} in the shallow depths. The simulation performed in Chapter 4 stresses the importance of layer stratification in governing the generation of h_{exc} during and after shaking at shallow depths that significantly influence sediment ejecta production.

Chapter 4 discusses in length the concepts of AFP and EPI to estimate ejecta severity using a 1D, fully coupled dynamic nonlinear ESA with robust constitutive models for liquefiable materials that can capture pore water pressure generation and migration within the soil deposit. This chapter aims to evaluate the AFP and EPI concepts by examining its capabilities using a larger field case history suite. The physical processes of sediment ejecta, current procedures to estimate ejecta severity, and the definition of AFP and EPI are first reviewed. The key geotechnical characteristics, seismic demand, and observed ejecta manifestation of 45 well-documented liquefaction case histories are then presented. The insights obtained from back-analyses results are presented, and the correlation between median EPI values and observed ejecta severity of all case histories are examined. Several key variables that influence interpretations of ESA results and calculated EPI values due to the variability of input ground motions are also explored.

5.2 CHARACTERISTICS OF LIQUEFACTION EJECTA CASES HISTORIES

5.2.1 Christchurch Sites

Figure 5.1 shows the relative location of sites that did (red circle) and did not (blue circle) produce sediment ejecta manifestations after the 2010–2011 Canterbury earthquakes. There are 20 free-field, level-ground sites analyzed in this chapter selected from 55 well-documented Christchurch sites investigated by Cubrinovski et al. [2019]. The selected sites are at least 500 m away from a river, have no evidence of lateral spreading, have high-resolution post-event aerial photographs, and have detailed subsurface information until the top of the dense Riccarton Gravel (shear-wave velocity, V_s of 400–450 m/sec). The projection of finite-fault planes of three main Canterbury earthquakes: 4 September 2010 M_w7.1 Darfield (Blue), 22 February 2011 M_w6.2 Christchurch (Red), and 13 June 2011 M_w6.0 (Green) events are also shown in Figure 5.1. There was a M_w5.3 precursor event, which occurred 80 minutes before the mainshock of the 2011 June event. To account for the smaller earthquake that preceded the mainshock in generating pore pressure, the two events are treated as one event with the higher M_w (i.e., 6.2) when performing the simplified and dynamic analyses to represent the combined duration effect on elevated excess pore pressure. The combination of 20 sites and two or three earthquakes produces 44 case histories from the Canterbury earthquakes. The key parameters of Canterbury liquefaction case histories to perform the analysis are summarized in Table 5.1.

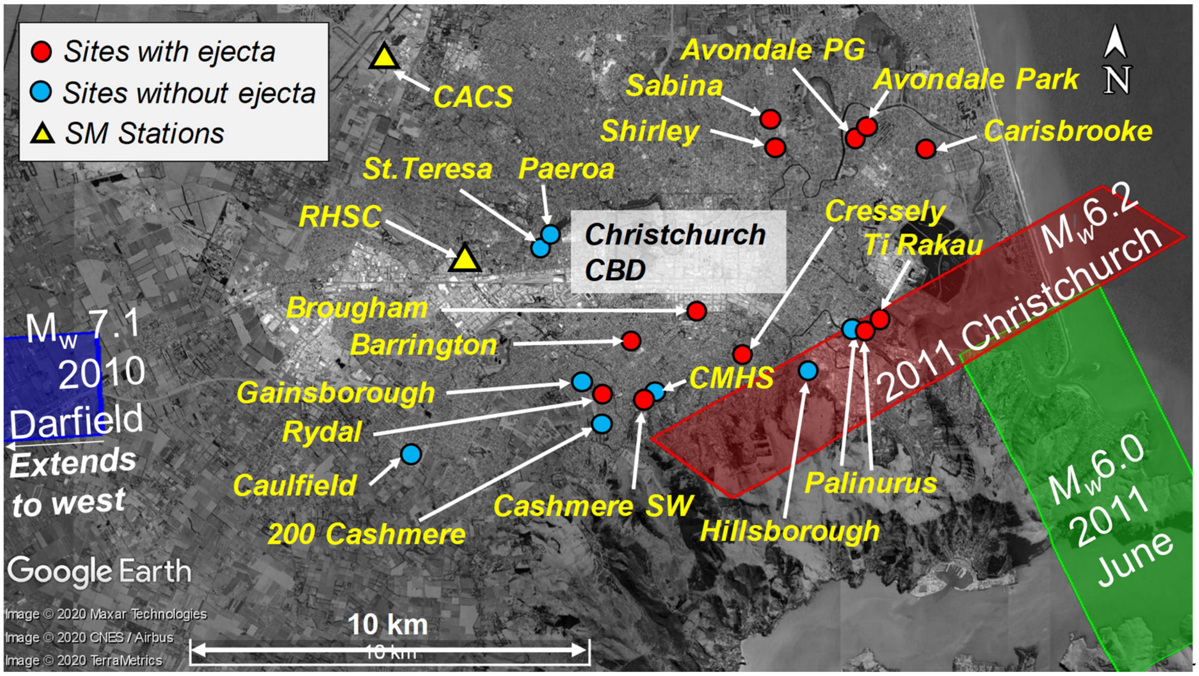

Figure 5.1 **Location of CACS and RHSC strong-motion (SM) stations and well-investigated level-ground sites in Christchurch relative to the projection of finite-fault planes of 2010 Darfield (the entire fault plane extends to west), 2011 Christchurch, and 2011 June earthquakes based on Bradley [2012], Bradley and Cubrinovski [2011], and Bradley [2016], respectively.**

Table 5.1 Summary of the case histories.

#	Site	Lat. (o)	Long. (o)	Event (Mw)	R_{rup} (km)	PGA (g)[1]	H_{soil} (m)[2]	CPT [3]	GWL (m) [4]
1	St. Teresa	-43.52987	172.59213	DAR (7.1)	12.3	0.22	21.0	57345	1.0
2	St. Teresa	-43.52987	172.59213	CHC (6.2)	5.7	0.34	21.0	57345	1.0
3	St. Teresa	-43.52987	172.59213	JUN (6.0)	9.7	0.17	21.0	57345	1.0
4	200 Cashmere	-43.57261	172.60810	DAR (7.1)	13.2	0.25	10.6	36421	0.8
5	200 Cashmere	-43.57261	172.60810	JUN (6.0)	8.5	0.19	10.6	36421	0.8
6	200 Cashmere	-43.57261	172.60810	CHC (6.2)	1.8	0.46	10.6	36421	0.8
7	Caulfield	-43.57970	172.54865	CHC (6.2)	6.3	0.32	7.0	36419	0.2
8	Caulfield	-43.57970	172.54865	DAR (7.1)	7.7	0.31	7.0	36419	0.2
9	Caulfield	-43.57970	172.54865	JUN (6.0)	13.5	0.13	7.0	36419	0.6
10	Gainsborough	-43.56362	172.60191	DAR (7.1)	12.1	0.25	20.4	36417	0.6
11	Gainsborough	-43.56362	172.60191	JUN (6.0)	8.5	0.18	20.4	36417	1.0
12	Gainsborough	-43.56362	172.60191	CHC (6.2)	2.8	0.43	20.4	36417	1.2
13	Hillsborough	-43.56064	172.67310	DAR (7.1)	18.0	0.25	23.4	57365	0.8
14	Hillsborough	-43.56064	172.67310	JUN (6.0)	4.0	0.36	23.4	57365	0.4
15	Hillsborough	-43.56064	172.67310	CHC (6.2)	0.5	0.63	23.4	57365	0.8
16	Paeroa	-43.53211	172.59050	DAR (7.1)	12.1	0.22	10.6	36418	1.0
17	Paeroa	-43.53211	172.59050	JUN (6.0)	9.5	0.17	10.6	36418	1.0
18	Barrington	-43.55403	172.61754	DAR (7.1)	13.5	0.23	20.6	37818	1.6
19	Barrington	-43.55403	172.61754	JUN (6.0)	7.4	0.20	20.6	37818	1.6
20	Shirley	-43.51040	172.66199	DAR (7.1)	18.3	0.19	27.0	57366	2.8
21	Palinurus_1	-43.55132	172.68822	CHC (6.2)	0.5	0.68	22.4	57360	1.4
22	Palinurus_1	-43.55132	172.68822	JUN (6.0)	1.9	0.42	22.4	57360	1.4
23	CMHS	-43.56561	172.62417	CHC (6.2)	1.4	0.45	24.0	72541	2.0
24	Paeroa	-43.53211	172.59050	CHC (6.2)	5.5	0.34	10.6	36418	1.0
25	Carisbrooke	-43.51081	172.70994	CHC (6.2)	2.8	0.46	33.2	57347	2.6
26	Brougham St.	-43.54724	172.63751	CHC (6.2)	2.9	0.46	23.4	57355	1.4
27	Rydal	-43.56580	172.60849	DAR (7.1)	12.7	0.25	15.8	62763	1.6
28	Avondale PG	-43.50810	172.68719	JUN (6.0)	5.2	0.26	33.2	57354	2.0
29	Cresselly	-43.55676	172.65220	JUN (6.0)	4.7	0.29	18.6	57353	1.2
30	Barrington	-43.55403	172.61754	CHC (6.2)	3.0	0.42	20.6	37818	1.6
31	Avondale PG	-43.50810	172.68719	CHC (6.2)	3.9	0.40	33.2	57354	2.0
32	Sabina	-43.50434	172.66066	CHC (6.2)	5.3	0.34	27.4	57346	1.2
33	Avondale Park	-43.50549	172.69076	JUN (6.0)	5.4	0.25	33.4	57342	1.2
34	Sabina	-43.50434	172.66066	JUN (6.0)	6.5	0.20	27.4	57346	1.0
35	Palinurus_2	-43.55142	172.68914	CHC (6.2)	0.5	0.68	22.4	62761	1.4
36	Ti Rakau	-43.54882	172.69537	JUN (6.0)	1.2	0.43	23.0	57341	1.2
37	Palinurus_2	-43.55142	172.68914	JUN (6.0)	1.9	0.42	22.4	62761	1.4
38	Shirley	-43.51040	172.66199	JUN (6.0)	5.9	0.22	27.0	57366	2.2
39	Ti Rakau	-43.54882	172.69537	CHC (6.2)	0.5	0.68	23.0	57341	1.6
40	Cresselly	-43.55676	172.65220	CHC (6.2)	1.1	0.55	18.6	57353	1.8
41	Rydal	-43.56580	172.60849	CHC (6.2)	2.2	0.44	15.8	62763	1.6
42	Avondale Park	-43.50549	172.69076	CHC (6.2)	4.0	0.37	33.0	57342	1.8
43	Port Island	34.67338	135.20576	Kobe (6.9)	2.7	0.72	32.0	C96*	3.0
44	Cashmere SW	-43.56669	172.62202	CHC (6.2)	1.4	0.45	24.0	33758	2.6
45	Shirley	-43.51040	172.66199	CHC (6.2)	4.7	0.38	27.0	57366	2.6

Note: #: Case History, CHC: 2011 Christchurch EQ, DAR: 2010 Darfield EQ, Kobe: 1995 Kobe EQ, JUN: 2011 June EQ, R_{rup}: rupture distance. C96*: Based on SPT blow counts from Cubrinovski et al. [1996].

[1] Median value of PGA at surface elevation used for simplified liquefaction evaluation based on Bradley [2013], as published in NZGD website.
[2] Height of the soil column modeled in the analysis (H).
[3] CPT reference number from New Zealand Geotechnical Database (NZGD).
[4] Best-estimated GWL during the earthquake event obtained from V_p measurement or nearby well records.

The severity criteria of ejecta manifestation in Table 3.1 are based on the total area covered by ejecta relative to the total area under assessment, which is within 20 m of a cone penetration test (CPT) for each site. Tonkin + Taylor [van Ballegooy, Personal Communication, 2018] provided best estimate ejecta-induced ground subsidence obtained using pre- and post-event Light and Detection Ranging (LiDAR) measurements; see Table 3.1. The severity classification for each case history is consistent with the field inspection performed by Tonkin + Taylor engineers. Figure 5.2 shows representative aerial photographs from five Christchurch sites for each category (None to Extreme).

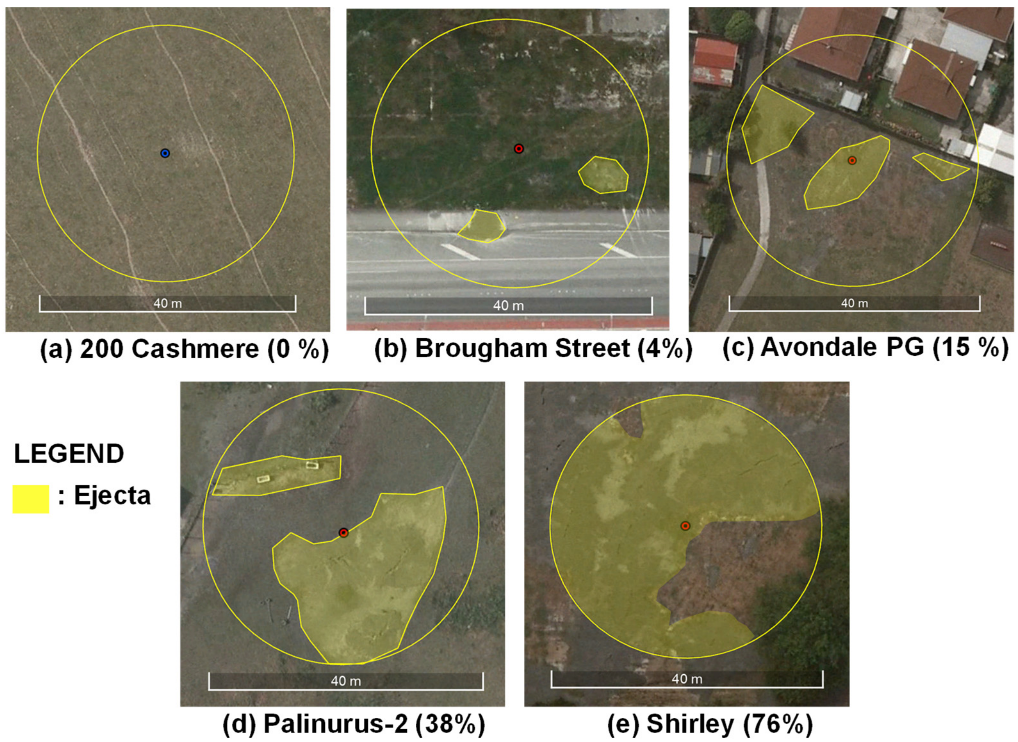

Figure 5.2 **Aerial photographs taken after 2011 Christchurch earthquake showing liquefaction severity based on the percentage of area covered by sediment ejecta within a 20-m radius of site location: (a) None, (b) Minor, (c) Moderate, (d) Severe, and (e) Extreme. Source: New Zealand Geotechnical Database (www.nzgd.org.nz).**

Subsurface information for each site includes seismic and conventional CPT with pore pressure measurement, V_p and V_s measurement using direct-push cross-hole technique, disturbed samples for a particle size distribution test, and Atterberg's limit testing, and undisturbed sampling for cyclic triaxial testing. All data are available on the New Zealand Geotechnical Database (NZGD) website. Figure 5.3 summarizes the profile of stress-normalized, equivalent clean sand tip resistance (q_{c1Ncs}) based on Boulanger and Idriss [2016], and Robertson [2016] soil behavior type (SBT) index (I_B) of the 20 Christchurch sites. They are grouped by the severity of liquefaction observed at the site after the intense Christchurch earthquake. The soil layer zones labeled as A, B and C for each site in Figure 5.3, and the definition of z_{AFP} is discussed later in this chapter.

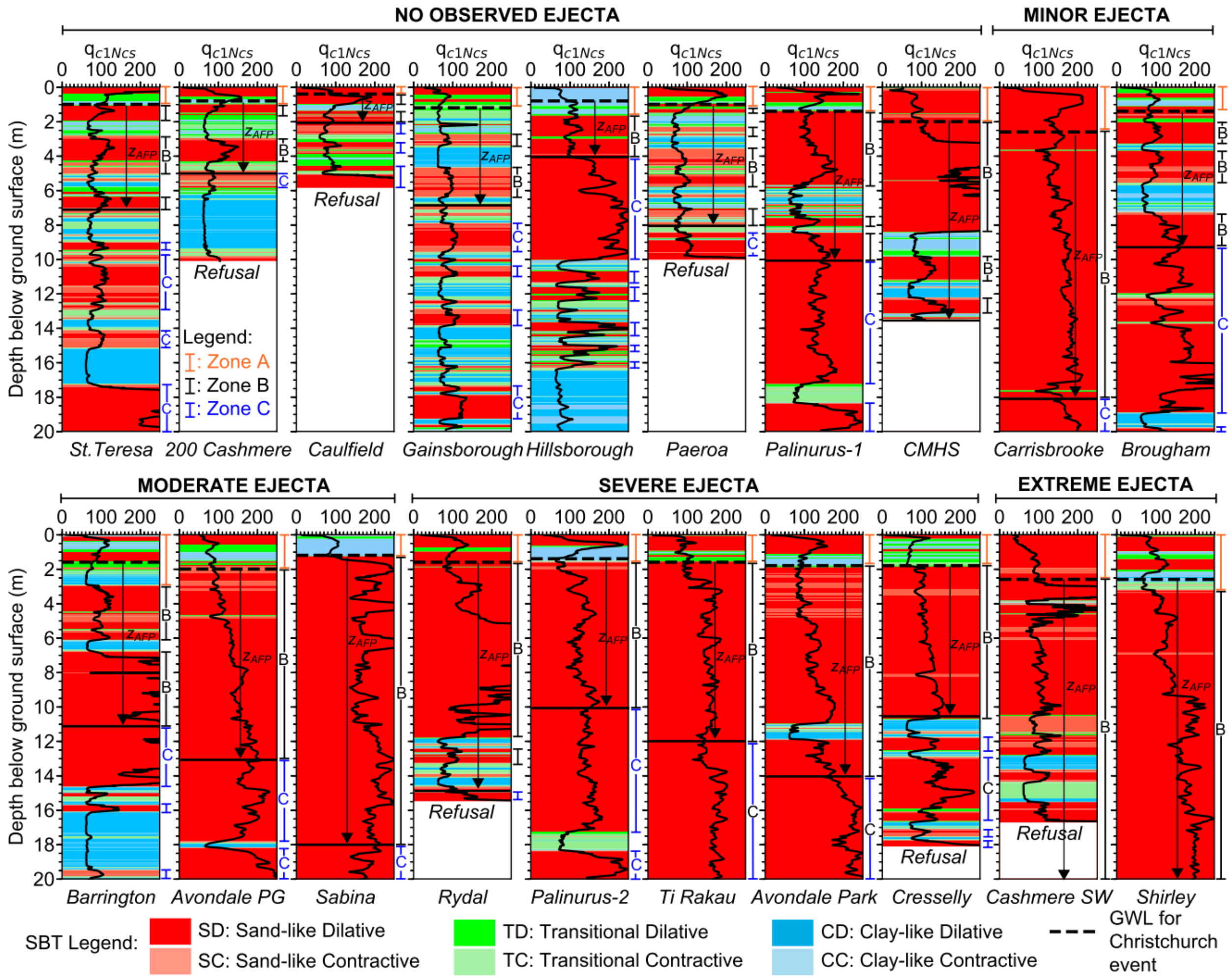

Figure 5.3 **Normalized clean-sand equivalent measured tip resistance (q_{c1Ncs}) of 20 sites in Christchurch with different amounts of ejecta manifestation after Christchurch event. The Robertson [2016] Soil Behavior Type (SBT) Index, I_B is plotted as background color. All axes are at same scale. The thickness of each Zones A, B, C are highlighted by vertical lines with different colors on the right side of each soil profile plot. The Artesian Flow Potential depth (z_{AFP}) is highlighted by black solid horizontal line.**

The I_B color profiles in Figure 5.3 show distinct layering of the highly stratified deposits of sand-like, transition, and clay-like soil at sites without ejecta manifestation (with the exception of the Hillsborough, Palinurus-1, and CMHS sites, which require ESA to explain as discussed later in this chapter). These sites generally have contrasting layers of soil with different responses and drainage characteristics. The range of q_{c1Ncs} of the liquefiable sand-like soils are 80–120. The transition soils are characterized as nonplastic to low-plasticity silt that may experience significant loss of stiffness. Cyclic triaxial test results show the pore pressure ratio (r_u) can reach 0.9 in this soil [Beyzaei et al. 2018b]. Most of the sites without ejecta manifestations have a thin crust layer and a shallow GWL that result in high LPI and LSN values (i.e., excessive overestimation), because the sand-like and transition soil layers at all depths with $q_{c1Ncs} < 100$ and Robertson [2009]

SBT, $I_c < 2.6$, are estimated to liquefy for the Christchurch earthquake. The ESA results discussed later show liquefaction did not occur at shallow depths due to significant liquefaction and soil softening occurring in deeper layers, and low k_v layers impeded upward seepage that could produce secondary liquefaction.

The sites with observed ejecta manifestations in Figure 5.3 generally consist of thick, highly permeable, dilative sand-like material with limited thin clay-like soil layers (low k_v and non-liquefiable). The typical range of q_{c1Ncs} values of sand-like soils are 100–250, with increasing density at deeper depths. The sand-like soil is the typical Christchurch-formation dark gray sand that forms a uniformly graded, very fine to fine, alluvial clean sand deposit (fines content, FC < 10%) because of the depositional process. The non-liquefiable crust layer consists of permeable or impermeable materials. Some sites have relatively deeper GWL compared to the highly stratified sites without ejecta, which may generate higher h_{exc}, thus increasing EPI values.

5.2.2 Port Island Vertical Array

The well-documented Port Island Array (PIVA) site shaken by the M_w6.9 Kobe, Japan, earthquake is added to the Canterbury cases listed in Table 5.1 (Case #43). The PIVA site consists of five distinct soil layers to a depth of 83.0 m [Cubrinovski et al. 1996; Elgamal 1996]. The first layer is 18.0 m of reclaimed fill consisting of loose, gravelly sand with standardized penetration test (SPT) corrected blow counts [$(N_1)_{60}$] of 3 to 15, followed by original seabed material consisting of soft alluvial Holocene clay with undrained shear strength (s_u) of 50–60 kPa to a depth of 27.0 m. It is followed by Pleistocene gravelly sand [$(N_1)_{60} = 25$] to 60.0 m, and then diluvial clay deposits to 83.0 m. The reclaimed fill materials consist of a thick, sand-like layer with a similar density to the Christchurch sites with severe and extreme ejecta manifestation. The GWL during the 1995 M_w6.9 Kobe earthquake was estimated to be 3.0 m. The PIVA is one of the most studied liquefied sites, with recorded motions at the ground surface, 16.0 m, 32.0 m, and 83.0 m depths in north–south and east–west direction. The maximum PGAs recorded at these depths are 0.43*g*, 0.63*g*, 0.72*g*, and 0.66*g*, respectively. The earthquake shaking lasted for about 20 sec and liquefied all loose reclaimed fill and produced sediment ejecta that covered almost the entire area within the radius of 20 m [Cubrinovski et al. 1996]. The ground surface subsided about 300–400 mm. The site was covered with about 150–200-mm-thick ejecta, which classifies it as extreme liquefaction severity based on Table 3.1 used herein.

5.3 EFFECTIVE STRESS ANALYSIS

5.3.1 Analysis Model and Input Motions

Dynamic ESA was performed to back-analyze each case history using the open-source, nonlinear, OpenSees with an implicit solver [McKenna and Fenves 2000]. The detailed numerical analysis frameworks (e.g., fully coupled formulation, solid-fluid elements, mesh resolution, and boundary condition) are described in Chapter 4. There were no acceleration-time histories recorded on outcropping bedrock in Christchurch during the 2010–2011 Canterbury earthquakes. Thus, deconvolution of surficial recorded motions was performed to the top of the Riccarton gravel unit to generate input motions. Markham et al. [2016] identified two strong-motion stations (CACS and RHSC stations shown in Figure 5.1) that responded in a relatively linear manner for all earthquakes. Markham et al. [2016] produced a suite of CACS and RHSC deconvolved motions, which consisted of fault-normal and fault-parallel components. The simulations performed in this chapter utilized the fault-parallel and normal component, maximum component (RotD100), and median component (RotD50) to assess the variability of the input ground motions to the results. The Top-of-Riccarton Gravel motions were then adjusted using an event-calibrated ground-motion model based on the differing distance of each site relative to the RHSC station or the CACS station and the differing V_s values of the Riccarton Gravel due to its differing depths at each site to get the best estimate of the likely ground motions at each site for each earthquake. The detailed input motions for each case history are shown in Appendix B.

For the PIVA site, the ESA simulation only modeled the top 32 m soil column because the seismic response of soil below 32 m indicated a linear response [Elgamal et al. 1996]. The horizontal motions recorded at 32 m is used as a "within motion" applied to a rigid base. To consider the ground motion variability, the North-South, East-West, maximum, and minimum rotated components were also simulated. A total of 356 of 1D-Dynamic nonlinear ESA simulations are performed from a combination of eight input motions to 44 Christchurch case histories (i.e., 352 simulations for the Canterbury earthquakes) and four PIVA simulations during the Kobe earthquake. Appendix B of this report shows the AFP-time histories for each case history simulation performed in this research.

5.3.2 Soil Model

The sand-like materials in Figure 5.3 consist of loose to medium-dense silty sand to sand (SP or SM). These materials are modeled using the PM4Sand constitutive model [Boulanger and Ziotopoulou 2017] with parameters listed in Table 5.2. PM4Sand is an effective stress model based on the critical state concept and bounding surface plasticity theory that can simulate the contractive-dilative response under cyclic shearing conditions. The soil primary response characteristics (i.e., dilatancy and strain accumulation [Seed 1979]) are based on its SBT zone (i.e., contractive or dilative behavior), relative density, and the number of cycles required to reach liquefaction represented by the PM4Sand contraction rate parameter (h_{po}). The baseline k_v values for all soil units are estimated using the Robertson and Cabal [2015] CPT correlation.

The transition soils in Figure 5.3 consist of sandy silt to clayey silt (ML) with zero to low plasticity index value (PI). These soils are modeled using the PM4Silt constitutive model [Boulanger and Ziotopoulou 2018], as summarized in Table 5.2. The maximum pore pressure ratio ($r_{u\text{-}max}$) for the transition soil with PI ≤ 12 (i.e., using the Bray and Sancio [2006] criteria) is set to 0.9 based on cyclic triaxial test results [Beyzaei et al. 2018b]. The transition soil with PI > 12 and the contractive clay-like materials, which are distinguished based on the SBT, are modeled using PM4Silt with default $r_{u\text{-}max}$ values. The methodology for developing and calibrating the model parameters for each soil unit is explained in Chapter 4.

Table 5.2 **Representative parameters of primary soil units used in the analyses of case histories.**

Parameter	Medium SP/SM	Loose SP/SM	ML (PI≤12)	ML (PI>12)	CL (Cohesive)
Soil Model	PM4Sand	PM4Sand	PM4Silt-Liq	PM4Silt	PM4Silt-Clay
Color	Red	Red	Green	Blue	Blue
SBT[1]	SD	SC	TD	TC-CD	CC
Response[2]	Cyclic Mobility	Flow-Liquefaction	Cyclic Mobility	N/A	N/A
D_R (%)	40-70	20–40	N/A	N/A	N/A
q_t (MPa)	>10	2–10	1–2	1–2	0.5–1
q_{c1Ncs}	>85	70–85	N/A	N/A	N/A
I_c	1.8-2.4	1.8–2.6	2.6–2.8	2.8–3	>3.0
I_B	>80	32–80	27–32	22–27	<22
S_u (kPa)	N/A	N/A	$(q_t - \sigma'_{vo})/14$	$(q_t - \sigma'_{vo})/14$	$(q_t - \sigma'_{vo})/14$
h_{po}	2.0–7.0	18–23	2.0–5.0	10	1.2
ϕ'_{cv} (degree)	35	33	33	33	25
r_{u_max}	N/A	N/A	0.90	Default	Default

* Note: [1]SBT: SD: Sand-like dilative, SC: Sand-like contractive, TD: Transitional dilative, TC: Transitional contractive, CC: Clay-like contractive (from Robertson 2016); [2]Cyclic Mobility and Flow-Liquefaction (from Seed [1979]).

5.3.3 Simulation Results

The LPI and LSN values listed in Table 5.3 are calculated using the Boulanger and Idriss [2016] CPT-based liquefaction triggering procedure. The estimated ejecta manifestation using the LSN criteria [Tonkin + Taylor 2013] matched the post-event observation in only 11 of the 45 case histories. Sensitivity analyses of LSN calculations of the representative Shirley clean sand site and St. Teresa stratified silty soil site found adjusting input parameters (e.g., q_{c1Ncs}, I_c, C_{FC}, GWL, PGA) did not resolve the misestimation problem; see Figure 4.5. As mentioned previously, LPI and LSN depend on liquefaction triggering procedures that do not directly capture the post-shaking hydraulic process, which only can be captured using dynamic ESA.

Tables 5.1 and 5.2 summarize the baseline site's parameters used in the dynamic ESA. The baseline site parameters and all associated input ground motions shown in Appendix B are used to calculate EPI median values for each case history, as listed in Table 5.3. As summarized in Table 5.3, the trend of EPI median values correlates very well with observed ejecta severity, where sites with more severe ejecta tend to have higher median EPI value and vice versa. The ranges of median EPI values for sites with none, minor, moderate, severe, and extreme ejecta manifestation are 0–1, 11–50, 43–113, 111–259, and 322–421, respectively. Sensitivity analyses to assess the influence of several key site's parameters on computed EPI values are presented later in this chapter.

The AFP-time history for each representative site group based on their severity criteria are shown in Figure 5.4, which are the simulation results from the fault-normal component of RHSC deconvolved input motions selected as the representative response. The AFP-time histories of all 356 simulations are given in Appendix B of this report shows a similar trend with Figure 5.4. EPI is equivalent to the total area below the AFP-time history. Cases with more severe ejecta have higher artesian pressures (i.e., higher AFP and consequently higher EPI) that must be dissipated to reach steady state. The change in AFP value after strong shaking describes the artesian pressure generation at shallow depths due to upward seepage, the process of secondary liquefaction, and indicates the potential to produce artesian flow that can exploit cracks in the low k_v crust layer. The low k_v crust layer initially impedes the artesian flow; eventually, the high-pressure artesian flow starts to exploit cracks within the crust layer (e.g., through hydraulic fracturing, ground oscillation, existing defects, and internal erosion). Once the cracks in the crust layer are completely developed, the artesian flow will eject the liquefied sediment to the ground surface.

Table 5.3 **Summary of estimation of surficial liquefaction manifestation based on LPI and LSN values compared to field observation and proposed EPI.**

#	LPI[1]	LSN[1]	Est. [2]	Obs.[3]	Median EPI ($m^3.s$)	EPI- based Est.
1	23	44	Extreme	None	0	None
2	26	46	Extreme	None	0	None
3	2	14	Minor	None	0	None
4	9	27	Moderate	None	0	None
5	3	16	Minor	None	0	None
6	17	35	Severe	None	0	None
7	17	63	Extreme	None	0	None
8	18	64	Extreme	None	0	None
9	0	7	None	None	0	None
10	22	56	Extreme	None	0	None
11	4	19	Minor	None	0	None
12	26	31	Severe	None	0	None
13	6	23	Moderate	None	0	None
14	17	59	Extreme	None	0	None
15	24	42	Extreme	None	0	None
16	12	28	Moderate	None	0	None
17	2	16	Minor	None	0	None
18	4	15	Minor	None	0	None
19	1	7	None	None	0	None
20	0	3	None	None	0	None
21	32	40	Extreme	None	0	None
22	14	29	Moderate	None	0	None
23	6	12	Minor	None	1	None
24	19	33	Severe	None	0	None
25	3	8	None	Minor	11	Minor
26	23	38	Severe	Minor	25	Minor
27	2	10	Minor	Minor	50	Moderate
28	1	10	Minor	Moderate	43	Moderate
29	11	32	Severe	Moderate	63	Moderate
30	14	24	Moderate	Moderate*	80	Moderate
31	10	28	Moderate	Moderate	73	Moderate
32	0	2	None	Moderate*	113	Severe
33	7	29	Moderate	Moderate	97	Moderate
34	0	0	None	Moderate*	99	Moderate
35	37	45	Extreme	Severe	122	Severe
36	7	25	Moderate	Severe	111	Severe
37	17	35	Severe	Severe	119	Severe
38	1	6	None	Severe	160	Severe

39	19	31	Severe	Severe	172	Severe
40	34	43	Extreme	Severe*	190	Severe
41	10	22	Moderate	Severe	259	Severe
42	16	36	Severe	Severe	255	Severe
43	31	45[4]	Extreme	Extreme	322	Extreme
44	25	29	Moderate	Extreme	333	Extreme
45	6	15	Minor	Extreme	421	Extreme

*Determined based on judgement since the field observation indicates the severity is at the boundary between two criteria.

[1]Computed using BI16 with 50% P_L and Maurer et al. [2019] C_{FC} value and Bradley [2013] 50% PGA.

[2]Estimation based on Tonkin + Taylor [2013].

[3]Field observation with severity criteria defined in Table 5.2.

[4]Computed based on N-SPT data with SPT-CPT correlation of q_{cpt} = 6 N-SPT.

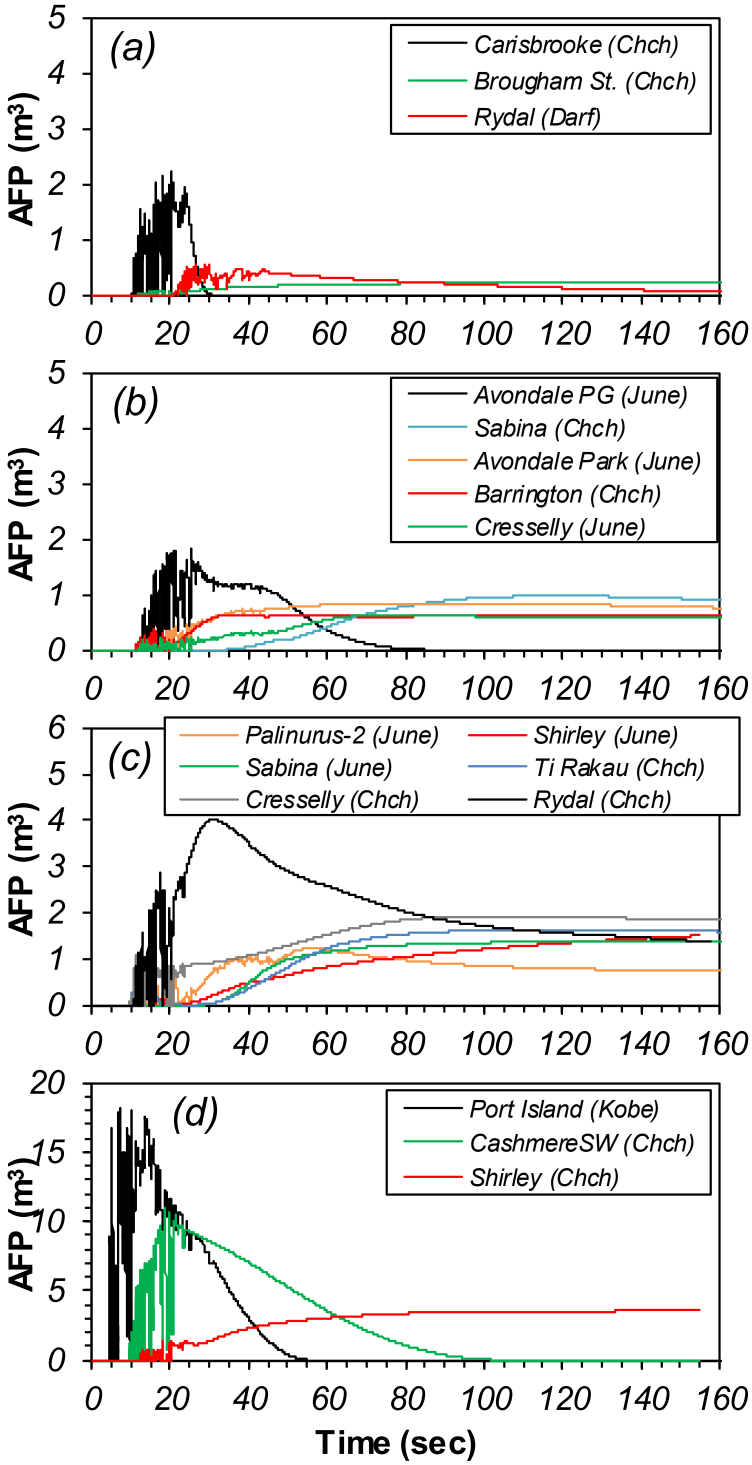

Figure 5.4 **AFP-time histories computed based on baseline parameters and the fault-normal component of RHSC deconvolved input motions for sites with: (a) Minor, (b) Moderate, (c) Severe, and (d) Extreme ejecta manifestations. The AFP-scale is increased for cases with Extreme manifestation. The shaking for CHC, JUN, DAR, and Kobe events in the simulation ended after 25 sec, 30 sec, 50 sec, and 30 sec, respectively.**

Case histories without ejecta had negligible values of AFP for the entire 160 sec of simulation; see Appendix B for each case history. Cases with minor ejecta in Figure 5.4(a) (e.g., the case history pairs of the Rydal-DAR and Brougham Street-CHC) had AFP values less than 0.5 m^3 during and after strong shaking due to weak shaking intensity and thin layers experiencing the $h_{exc} > h_A$ condition. The simulation shows the Carisbrooke site developed higher AFP values during strong shaking, but the h_{exc} dissipated rapidly after shaking ceased due to high k_v values. The permeable crust of the Carisbrooke site allowed upward water flow to raise the GWL uniformly without confining the artesian flow, which may not delay the ejection process after shaking stops. The ground might soften during this process, allowing any objects to settle into it, but the process lasts only briefly.

The AFP values for cases with moderate ejecta ranges from 0.5–2.0 m^3 during and after the earthquake shaking. The Avondale PG site during the JUN 2011 event developed the highest AFP value during strong shaking, but it decreased rapidly after strong shaking due to the high k_v values of the thick sand deposit. The results suggest cracking of the crust layer may have started during shaking if enough artesian pressure was generated. The ESA results indicate the process did not last long after shaking stopped; therefore, only moderate ejecta were produced. Many of the cases shown in Figure 5.4(b) developed AFP lower than 0.5 m^3 during shaking, which increased to higher than 0.5 m^3 well after the shaking had stopped. Similar mechanisms were observed at the case histories with severe ejecta, but these cases produced larger AFP values and, consequently, high EPI values. The maximum AFP values at the cases shown in Figure 5.4(c) with severe ejecta reach more than 4.0 m^3. Moreover, Figure 5.4(c) shows AFP values greater than 1.0 m^3 are sustained over 150 sec after strong shaking starts on all cases except the Palinurus-2-JUN case. The variation of AFP time histories for sites due to various input ground motions are shown in Appendix B, which showing a similar trend of advection behavior.

The AFP values for cases with extreme ejecta shown in Figure 5.4(d) are significantly higher than the other sites. The GWLs are deeper than 2.6 m, which means the system can generate higher h_{exc} and higher artesian pressures when liquefaction is triggered within the profile due to the higher initial vertical effective stress. The PIVA site developed an AFP value greater than 10 m^3 because the loose reclaimed fill materials liquefied extensively at depths of 4.0–15.0 m after being shaken intensely (input PGA = 0.72*g*). Although the advection process ends quickly due to the high k_v value of the fill, the hydraulic demand was sufficient to transport a large amount of sediment and produced extreme ground failure at this site. The hydraulic process of the Cashmere southwest (SW)-CHC case is like the PIVA site in that a thick, loose sand deposit was estimated to liquefy during earthquake shaking. The input PGA at Cashmere SW during the Christchurch earthquake was high (0.45*g*), but its relatively thinner liquefied deposit and shallower GWL produced a lower AFP value. The ESA results of the Shirley-CHC case indicate a thinner liquefied layer compared to the other two extreme ground failure case histories studied herein. However, the long duration of the $h_{exc}>h_A$ condition due to upward seepage-induced artesian flow produced an extreme amount of ejecta. The Shirley crust layer is a low k_v layer that confined artesian flow and caused localized internal erosion, allowing the concentrated sediment flow from surrounding areas that contributed to the extreme ejecta. Consequently, an AFP value greater than 3.5 m^3 was sustained long after shaking ended.

5.3.4 EPI-based Severity Estimation

The trend of median EPI values computed for each case history correlates well to the observed ejecta severity. Sites without ejecta had negligible median EPI values, and sites with severe or extreme ejecta had high median EPI values. Figure 5.5 shows how the severity of liquefaction ejecta increases from one category (defined in Table 3.1) to a higher category as the median EPI values listed in Table 5.3 increase systematically. All EPI values computed from 356 simulations and the variability of the results due to different input motions are shown in Figure 5.5. The threshold median EPI values for each category of observed ejecta manifestation are refined based on the distribution of data shown in Figure 5.5 to develop EPI ranges for estimating ejecta severity. Based on the results, the proposed threshold median values for cases with none, minor, moderate, severe, and extreme ejecta severity are EPI ≤ 10, 10 < EPI ≤ 50, 50 < EPI ≤ 100, 100 < EPI ≤ 300, and EPI > 300, respectively. Using these threshold values, the EPI-based estimation on ejecta severity for all 45 case histories shown in Table 4 correlates well to the observed severity.

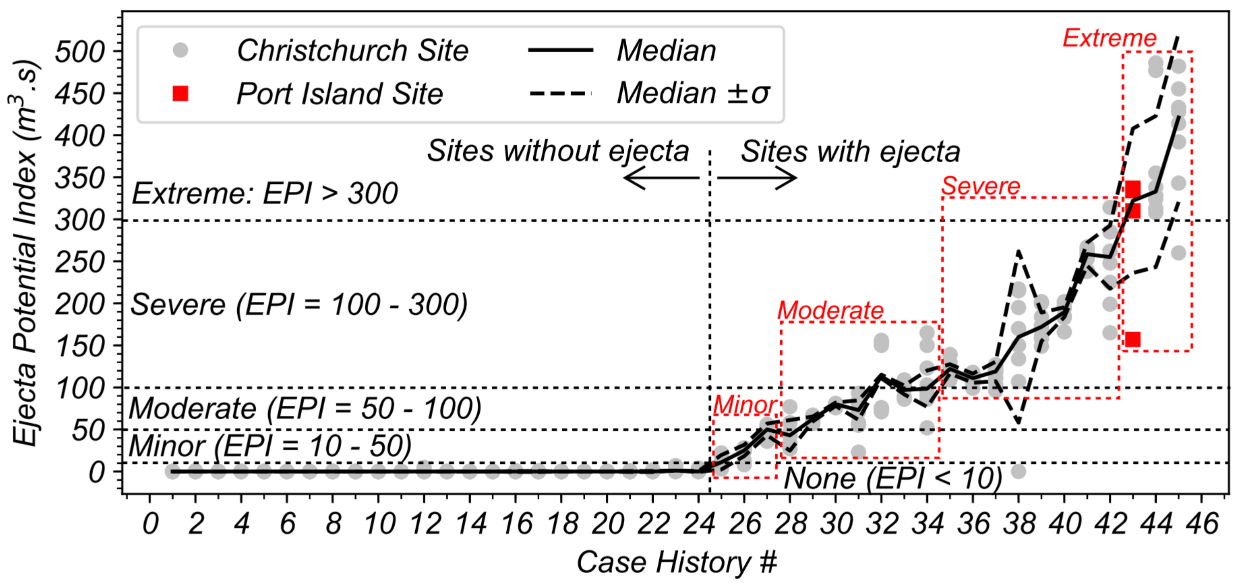

Figure 5.5 **Computed EPI values based on best-estimate soil parameters and ground motion intensity for case histories described in Table 5.1.**

5.4 SEISMIC RESPONSE CHARACTERISTICS OF LIQUEFIABLE SITES

5.4.1 Insights from Analysis of Adjacent Sites Regarding Layer Stratification

Dynamic ESA is performed to back-analyze adjacent sites that produced contrasting amounts of ejecta manifestation at Palinurus Road [Figure 5.6(a)] and Cashmere High School [Figure 5.7(a)}. The CPTs of Palinurus-1 (no ejecta) and Palinurus-2 (severe ejecta) are 70 m apart and show similar soil density [Figure 5.8(a)] and behavior [Figure 5.8(b)] except at a depth of 6.0–8.0 m. The LSN values for the CPTs at Palinurus Road for the Christchurch event are 30–44, indicating severe ejecta is expected. Contrasting k_v values are observed at the 6.0–8.0 m depth between the two sites; see Figure 5.8(c). Examining the Palinurus road cross section shown in Figure 5.6(b), the area at Palinurus Road without ejecta is underlain by a 1.0–3.0-m thick low k_v soil layer at 6.0–9.0 m depth. The area with ejecta does not contain this low k_v soil layer. The simulation results indicate the Christchurch earthquake liquefied much of the soil profile at Palinurus-1 and Palinurus-2 sites, which generated high h_{exc}; see Figure 5.8(d). The simulation of Palinurus-1 site shows that deep liquefaction occurred first at 14–16 m depth, which reduced the cyclic shear stress (CSR) at shallow depths. Hence, the soil at 2–6 m did not liquefy during shaking, and h_{exc} never exceeded h_A over this depth (i.e., AFP = 0) because the low k_v layer at 6-8 m impedes the upward seepage from the deep liquefied layer. The simulation of Palinurus-2 indicates that the CSR is distributed uniformly throughout the soil profile, which liquefied the soil at the 6–8 m depth and then the shallower soil. Water flowed upward freely through the high-k_v soil and h_{exc} exceeded h_A within the depth of 2–4 m [Figure 5.8(d)], which resulted in a high artesian pressure (i.e., high AFP) over a sustained period to produce severe ejecta. It is likely that water also flowed laterally from the deeper liquefied layer at Palinurus-1 to supply additional water to sustain the artesian flow that produces severe ejecta manifestation at Palinurus-2, as illustrated conceptually in Figure 5.6(b) by the blue dashed arrows.

At Cashmere High School [Figure 5.7(b)], the area without ejecta (CMHS site) is underlain by 2–5-m thick dense gravelly sand at 3–9 m depth, which is underlain by 2–4-m-thick low k_v soil at 7–9 m depth. The LSN is 11–26, which indicates minor-to-moderate ejecta are expected (an overestimation). The adjacent area with ejecta (Cashmere SW site) is underlain by thick deposit of loose high-k_v soils until a depth of 13 m. The adjacent Cashmere sites consist of generally sand-like soil [Figure 5.8(f)] with different density [Figure 5.8(e)] in their upper 8 m, followed by deeper deposits of significantly different k_v values; see Figure 5.8(g)]. The simulation of CMHS site (see electronic supplement) indicates Christchurch earthquake liquefied the sand-like soil and generated high h_{exc} at depths of 10–12 m at the CMHS site [Figure 5.8(h)], which reduced the CSR acting on dense gravelly sand at depths of 3–8 m, so it did not liquefy. Additionally, the low k_v soil at 8–10 m depth impeded the upward seepage from the underlying liquefied layer and prevented h_{exc} from exceeding h_A at shallow depths (i.e., AFP = 0). Thus, no ejecta were expected at the CMHS site, which it is consistent with field observations. Conversely, the simulation of the Cashmere SW site indicates that the loose sand-like materials at a depth from 5–13 m [Figure 5.8(e)] were liquefied and generated high h_{exc} during the Christchurch earthquake. With such high artesian pressure [Figure 5.8(h)] and without low k_v layers [Figures 5.7(b) and 5.8(g)] that restrict the upward seepage from the liquefied sand, high-gradient upward water flow can produce artesian flows that eject extreme amount of liquefied sediment to the ground surface, which is represented by high AFP values during and after earthquake shaking.

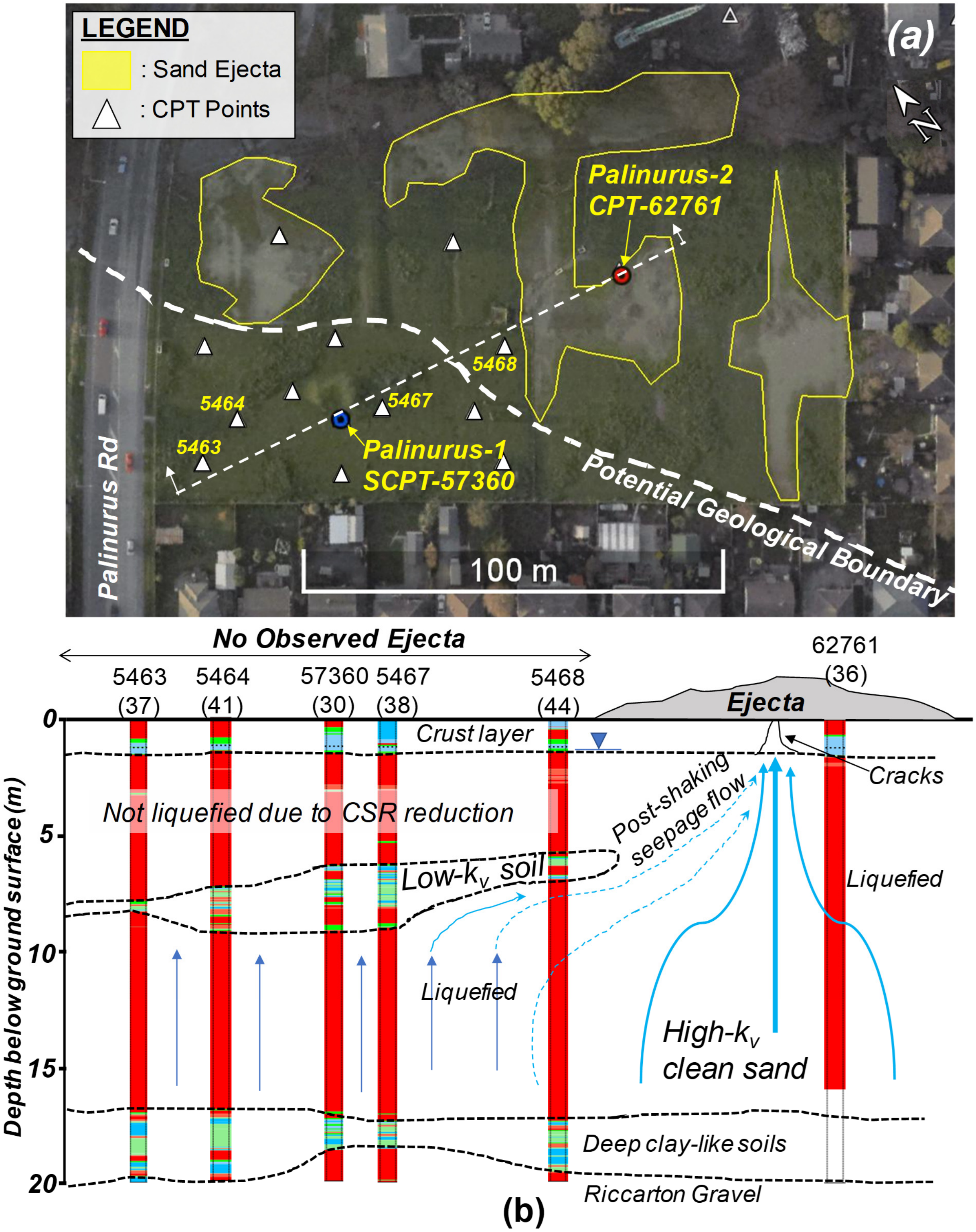

Figure 5.6 (a) Aerial photographs of Palinurus-1 and Palinurus-2 sites showing contrasting amounts of sediment ejecta; and (b) cross sections at Palinurus Road sites. The 4–6-digit number denotes the CPT designation, and the number inside parenthesis is the LSN for the Christchurch event.

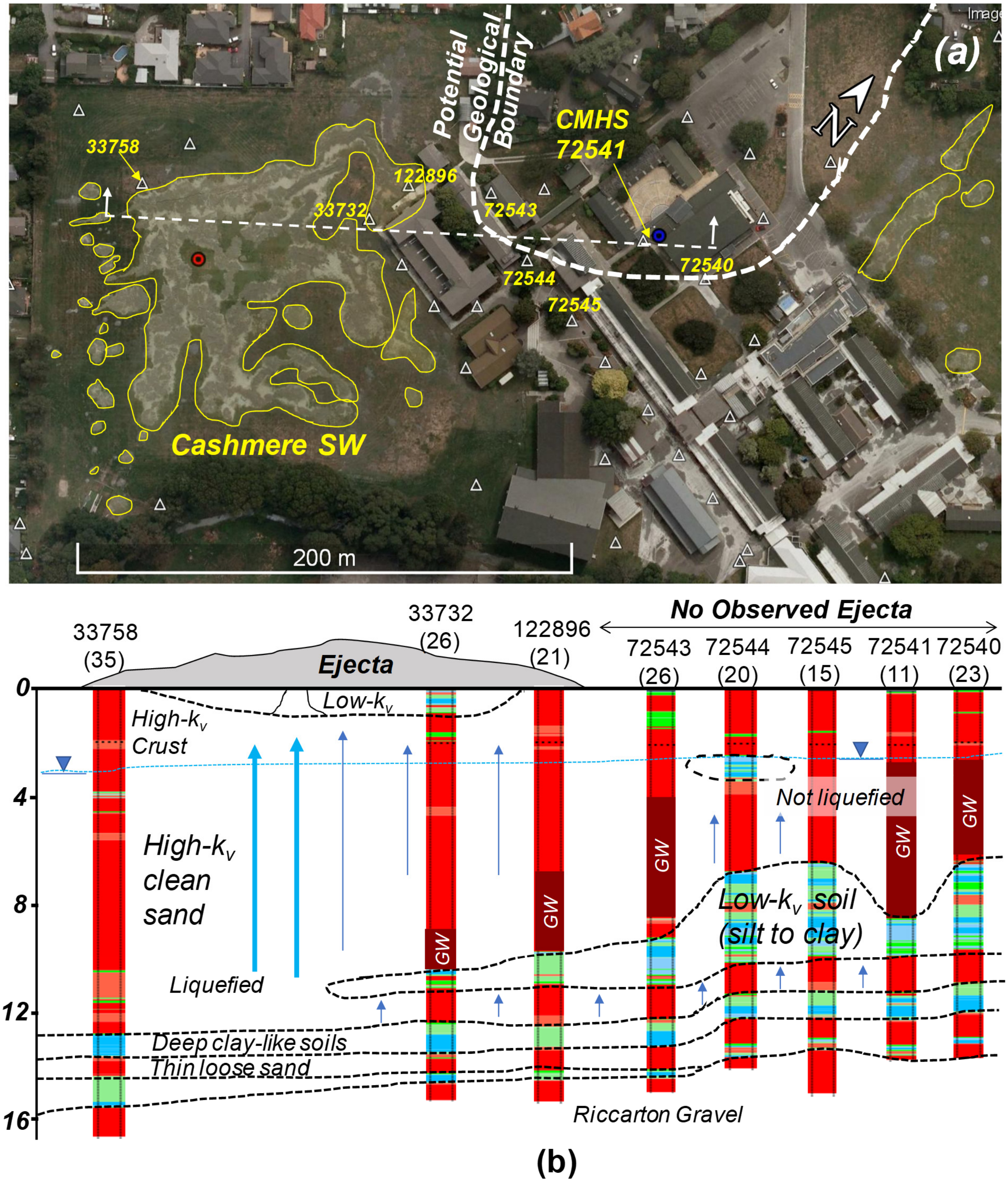

Figure 5.7 (a) Aerial photographs of CMHS SMS and Cashmere SW sites showing contrasting amounts of sediment ejecta; and (b) cross sections of Cashmere High School. The 4–6-digit number denotes the CPT designation, and the number inside parenthesis is the LSN for Christchurch event.

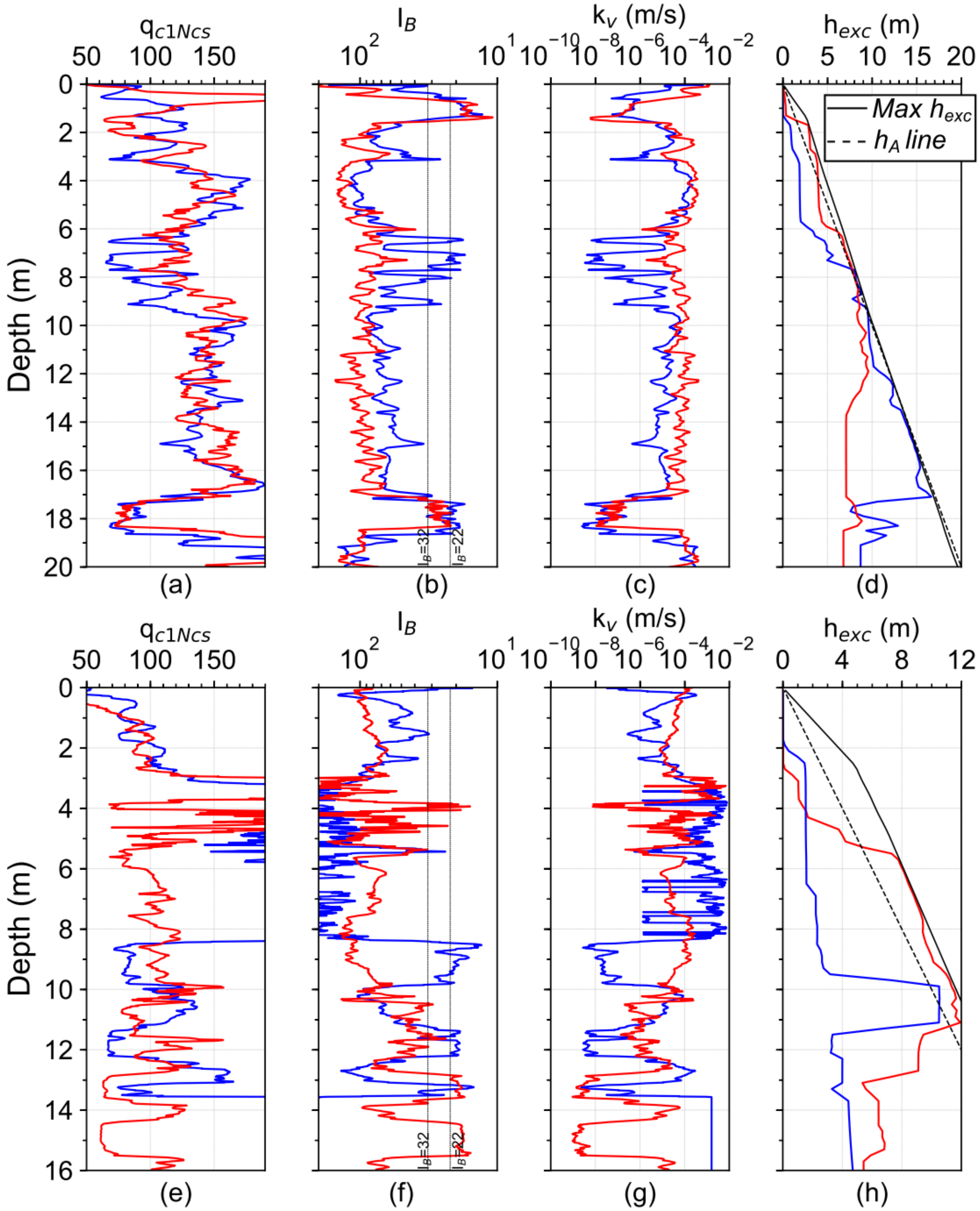

Figure 5.8 **Computed responses of two adjacent sites with contrasting amounts of ejecta: (a-d) Palinurus sites (Blue: Palinurus-1 with no ejecta; Red: Palinurus-2 with ejecta), and (e-h) Cashmere High School sites (Blue: CMHS SMS with no ejecta; Red: Cashmere SW with ejecta).**

5.4.2 Generalized Site Response

The liquefiable layers below the GWL where h_{exc} can exceed h_A (i.e., the zone where the maxh_{exc} line is located to the right of the h_A line as illustrated in Figures 5.9–5.11) can trigger high-gradient upward seepage and produce high artesian pressures that can exploit cracks in crust layer and eject the liquefied sediment. This zone extends from the GWL to the depth where h_{exc} cannot exceed h_A (the AFP depth, z_{AFP}), which is a function of the GWL, σ'_{vo} , and h_A. The z_{AFP} for each case history is identified in Figure 5.3. The z_{AFP} extends deeper as the σ'_{vo} increases due to a deeper GWL, heavier soil, or surcharge load, or as the assumed h_A line slope becomes steeper than 1V:1H. Although soil layers below z_{AFP} can generate significant h_{exc} that triggers upward seepage even if they do not liquefy, the amount is insufficient to produce artesian flows that can erode the upper crust layer (i.e., the maximum h_{exc} is less than h_A). Therefore, z_{AFP} distinguishes the depth at which soil layers above it can directly produce high-pressure artesian flows that may produce ejecta and those soil layers below it that can supply water to sustain longer artesian flow potential in layers above z_{AFP} .

The generalized responses of the case histories analyzed in this study are grouped based on ejecta severity (i.e., None, Minor–Moderate, and Severe–Extreme) and illustrated conceptually in Figures 5.9–5.11. As explained below, it is informative to categorize layers within a soil deposit into three zones as illustrated conceptually by Zones A, B, and C in Figures 5.9–5.11 to assess the potential of liquefiable sites for producing ejecta:

- Zone A is the non-liquefiable crust that may comprise cohesive, competent material (e.g., fill consists of silt and clay) or erodible, permeable material (e.g., fine clean sand). The clay-like crust layer may confine the upward seepage from the underlying liquefied layer and prevent the rise of the GWL; consequently, localized cracks can develop at the weakest part of the crust. The fluid flow will then concentrate through the cracks that develop in the crust and transport sediment to the ground surface until the hydraulic system reaches a steady state, which can last tens of minutes. Conversely, the upward seepage can easily raise the GWL to the ground surface at a site with a permeable and highly erodible crust layer. When there is sufficient artesian pressure, a significant amount of liquefied sediment can also be ejected to the ground surface during and after shaking. When the upward seepage buoys the entire soil particles, light objects (e.g., a car) can sink into the low strength crust due to the loss of effective stress and frictional forces. This process lasts briefly as the excess water pressures dissipate rapidly, and the sand layer regains its original shear strength.
- Zone B is below Zone A and above the z_{AFP} that comprises cohesionless liquefiable soil layers that can generate high h_{exc} during shaking, which may produce high-pressure artesian flow. In some cases, the soil layers in Zone B may not liquefy during earthquake shaking. Instead, h_{exc} remains less than h_A until high-gradient upward seepage from deeper layers supplies enough

water to develop the artesian flow ($h_{exc} > h_A$), which may cause secondary liquefaction, mobilize cracks in upper crust layer, and produce ejecta. Thus, earthquake shaking can either trigger liquefaction in one or more layers in Zone B and produce ejecta directly because $h_{exc} > h_A$, or if the seismic demand is insufficient to liquefy soil layers in Zone B, they only produce ejecta due to secondary liquefaction resulting from the generation of artesian water pressures ($h_{exc} > h_A$) due to upward seepage. Zone B layers must be sufficiently thick and continuous with high k_v values to produce severe ejecta. For example, Zone B liquefiable soil layers of the St. Teresa or Gainsborough sites shown in Figure 5.3 are isolated by low k_v soil layers that reduced the upward seepage-induced artesian flow potential; thus, ejecta were not expected.

- Zone C is below the z_{AFP}. High k_v liquefiable soil layers in Zone C can generate significant h_{exc} that triggers upward seepage and supplies water to Zone B. Although Zone C soil layers may liquefy, they cannot produce ejecta directly because h_{exc} never exceeds h_A; see Figure 5.9. They can generate significant u_e due to the high σ'_{vo} and trigger upward seepage even if liquefaction is not triggered; see Figure 5.11. If layers in Zone C liquefy, they can reduce the CSR developed in shallow layers in Zone B and limit the generation of h_{exc} and ejecta production. Thus, the Zone C soil layers can supply water to Zone B which enhances ejecta production or limit the seismic demand in shallower soil layers which decreases ejecta production. Zones B and C must be connected hydraulically to produce severe ejecta. For example, Zones B and C of the Palinurus-2 and Ti Rakau sites are connected hydraulically so that the large upward seepage developed during shaking in Zone C can flow freely up into Zone B and produce ejecta.

Therefore, the location of primary and secondary liquefaction triggering relative to z_{AFP} and the continuity of Zones B and C are key characteristics that distinguish sites that produce different ejecta amount as discussed below.

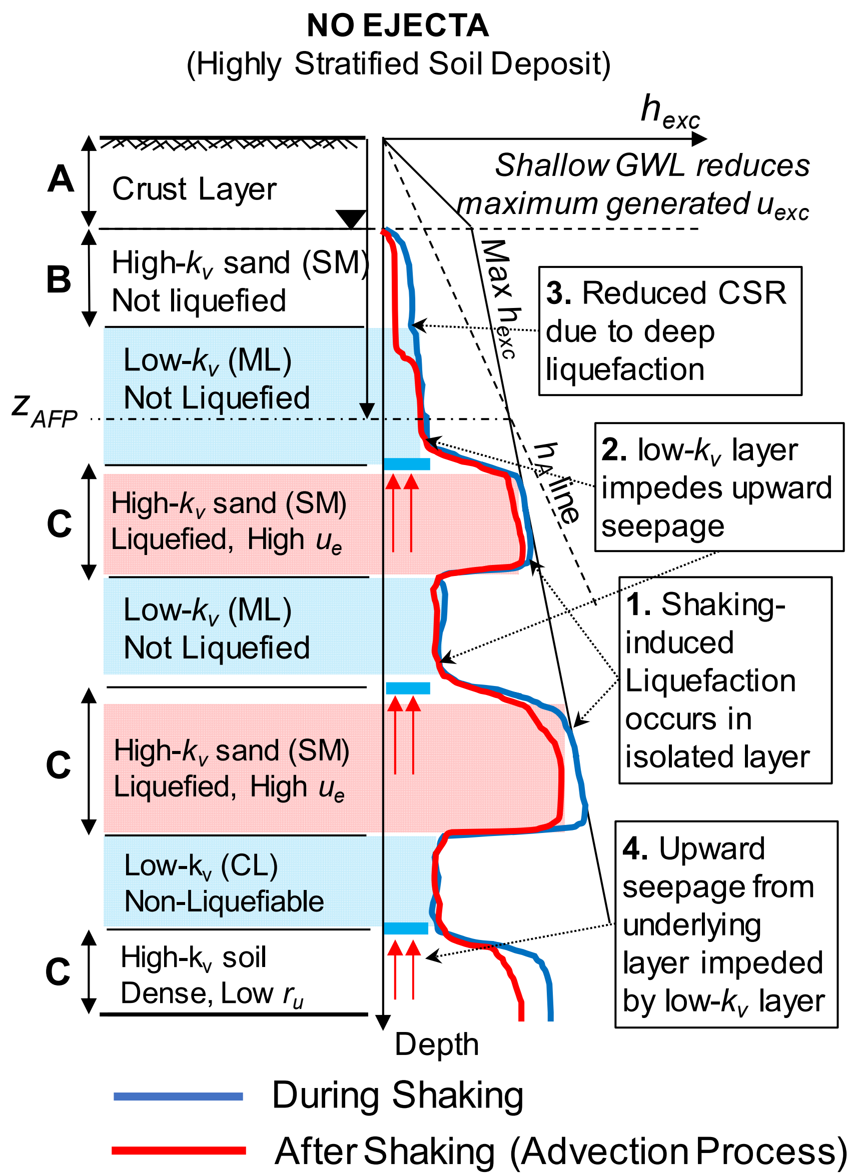

Figure 5.9 **Schematic of highly stratified soil deposit response at sites where liquefaction triggering was calculated but ejecta were not observed.**

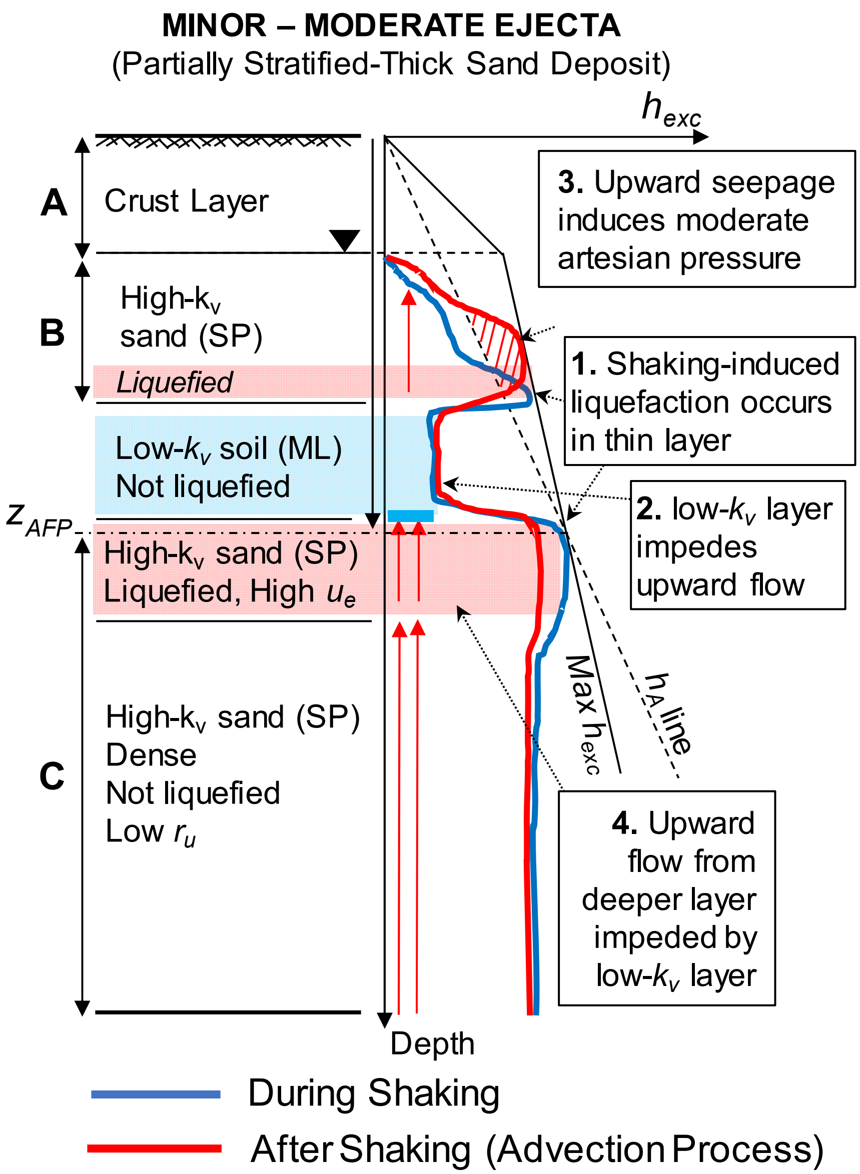

Figure 5.10 **Schematic of partially stratified soil deposit response at sites where minor-to-moderate amounts of ejecta were observed.**

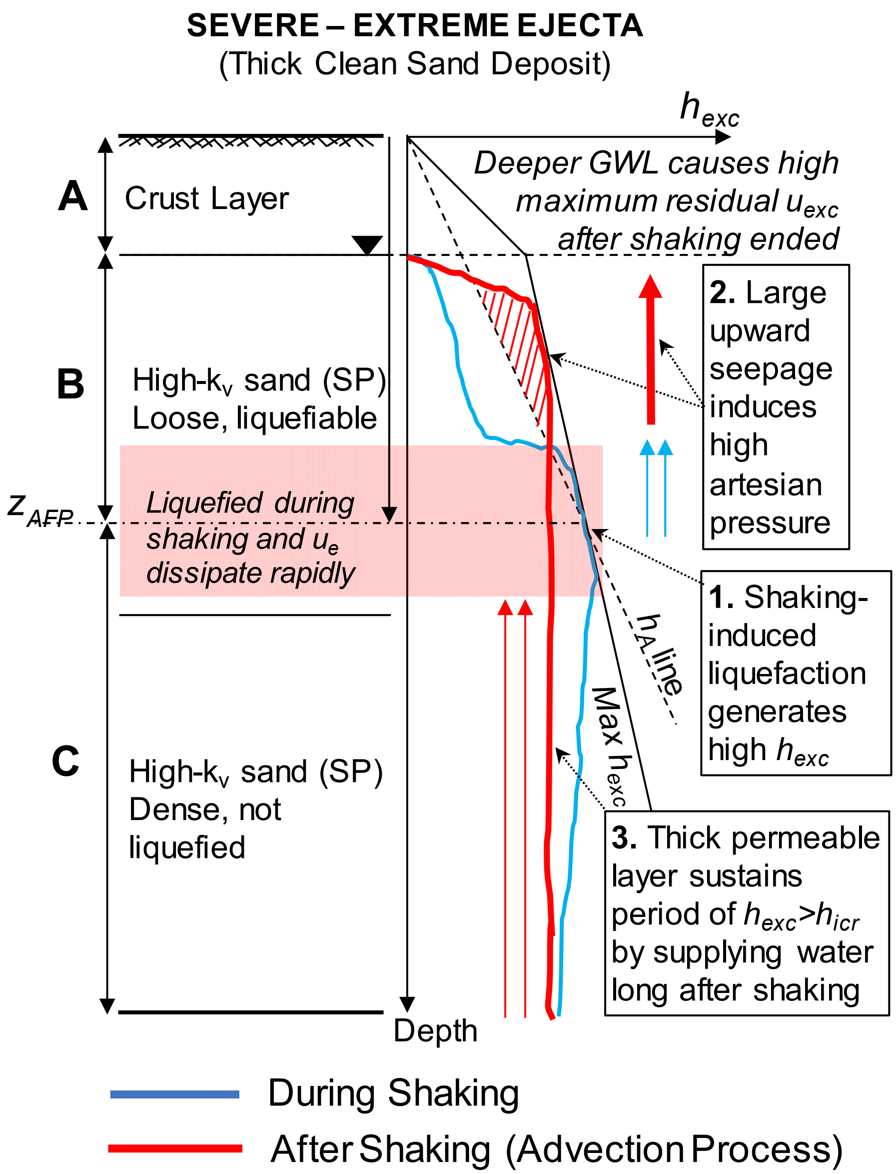

Figure 5.11 **Schematic of thick soil deposit response at sites where severe-to-extreme amounts of ejecta were observed.**

5.4.3 Sites with No Observed Ejecta

Most sites without ejecta manifestation consist of highly stratified deposits of thin, liquefiable sand-like soil layers; low-plasticity silt layers susceptible to liquefaction; and low-permeability clay-like soil layers; see Figures 5.5 and 5.11. Although these sites may have increased liquefaction susceptibility due to the lower σ'_{vo} resulting from their shallow GWL, they cannot produce ejecta because h_{exc} cannot exceed h_A due to the limited σ'_{vo} from the shallow GWL. Zone B is relatively shallow (with a small z_{AFP}). If triggered, shaking-induced liquefaction typically occurs first in deeper, isolated loose sand-like soil layers in Zone C (Figures 5.5 and 5.11), which develop high h_{exc} and initiate upward seepage. Liquefaction may also occur within the silt layers. However, water flows slowly within any liquefied low k_v silt layers and flows even more slowly through overlying low k_v clay-like layers during the advection stage. Therefore, the h_{exc} developed above the z_{AFP} never exceeds the h_A either during or after shaking (i.e., AFP ≈ 0), as illustrated in Figure 5.9. After shaking, the h_{exc} within the soil profile remains high (see Figure 5.9) until seepage dissipates the residual u_e to return to the hydrostatic condition. This can occur through horizontal flow in addition to vertical flow. The ground will remain stable for a free-field site; however, lateral movement could occur if there is a significant driving horizontal or gravitational shear stress in a liquefied sand layer, or vertical movement could occur if a heavy building loses support for its foundation.

5.4.4 Sites with Minor-Moderate Sediment Ejecta

Sites with minor-to-moderate ejecta manifestation consist of partially stratified deposits of thick, liquefiable sand-like and nonplastic to low-plasticity transition soils (susceptible to liquefaction). Initially, earthquake shaking liquefies the loosest layers in Zones B and C (e.g., as shown in Figure 5.10, this was often part of Zone C and a thinner layer in Zone B in Christchurch). High h_{exc} generated in Zone C initiate upward seepage but the overlying low k_v soil layer restricts the flow of water, which minimizes secondary liquefaction in Zone B; see Figures 5.3 and 5.10. The liquefied layer of Zone B can produce moderate upward seepage and artesian pressure ($h_{exc} > h_A$ condition) to transport the liquefied sediment, e.g., the Barrington site, see Figure 5.3. However, the ejection duration is relatively short and only transports minor-to-moderate liquefied sediment to the ground surface because the supply of water from the underlying layer is limited due to the thin liquefied layer. The volume of ejecta is determined by the layer thickness above the z_{AFP} that experiences $h_{exc} > h_A$. The dissipation of h_{exc} within the system is faster (i.e., higher k_v) than a highly stratified site. Ground instability may occur during this short period of time. Some sites may consist of a thick deposit of clean sand without low k_v layers and only produce minor-to-moderate ejecta such as Carisbrooke or Sabina; see Figure 5.3. For these cases, the amplitude of CSR and soil density control the amount of artesian pressure generated at the sites. If Zone A consists of permeable material, upward seepage can flow uniformly and not produce ejecta (no localized and concentrated flow), although the ground may lose bearing support.

5.4.5 Sites with Severe-Extreme Sediment Ejecta

Sites with severe-to-extreme ejecta manifestation consist of thick, continuous clean sand; see Figures 5.5 and 5.13. The maximum generated h_{exc} at these sites may be relatively higher due to higher σ'_{vo} from a deeper GWL. Earthquake shaking initially liquefies the loosest parts of Zones B and C and generates high h_{exc}, which depends on the dynamic response of the site and the amplitude of the CSR. The dissipation of h_{exc} occurs rapidly in clean sand deposits that initiate large upward seepage without restriction from a low k_v layer. As illustrated in Figure 5.11, the high-gradient upward seepage can increase or sustain high h_{exc} in the upper part of Zone B that cause secondary liquefaction after shaking stops. The upward seepage erodes soil within the crust layer, creates a flow channel, and produces artesian flow while ejecting the liquefied sediment. High h_{exc} developed in the denser sand layers in Zone C also produces significant upward seepage that supplies water to sustain the $h_{exc} > h_A$ condition in Zone B. The longer duration of the $h_{exc} > h_A$ condition in Zone B, the more ejecta will be produced.

5.5 IMPORTANT PARAMETERS INFLUENCING EPI

5.5.1 Hydraulic Conductivity

The sensitivity of the EPI to variations of the k_v values used in the ESA was investigated by multiplying baseline k_v values as follows: $0.1k_v$, $0.316k_v$, $3.16k_v$, and $10k_v$. Figure 5.12 shows the variation of the EPI due to the change in k_v values of representative sites from each ejecta severity category. There is a k_v profile that produces the peak EPI value, with the EPI decreasing for profiles with lower or higher k_v values. Although there can be significant variation in the computed EPI when k_v varies over two orders of magnitude, the peak EPI value for each case does not differ much from the EPI calculated using the baseline k_v values. The EPI values for sites with more severe ejecta are more sensitive to variations of the k_v values. However, EPI values are greater than zero for these cases, indicating ejecta are still expected, which is consistent with field observations. For instance, the range of ejecta estimation at the Shirley site based on criteria in Figure 5.5 are moderate-to-extreme using values within a factor of 10 of the baseline k_v values. Similarly, EPI values for highly stratified sites (e.g., Gainsborough and St. Teresa) are not sensitive to a variation of k_v values. The EPI values are always zero for these sites, indicating no ejecta are expected, which is consistent with field observations.

As shown with the AFP-time histories in Figure 5.13, the AFP does not vary significantly as a function of differing k_v profiles during earthquake shaking. Instead, k_v governs the post-shaking hydraulic processes that produces different AFP values after shaking ends, which in turn, leads to different EPI values. After shaking stops, water flowing easily through high k_v soil causes shallow soil layers to be more vulnerable to secondary liquefaction. Conversely, low k_v soil layers delay upward seepage and reduce the chance of secondary liquefaction.

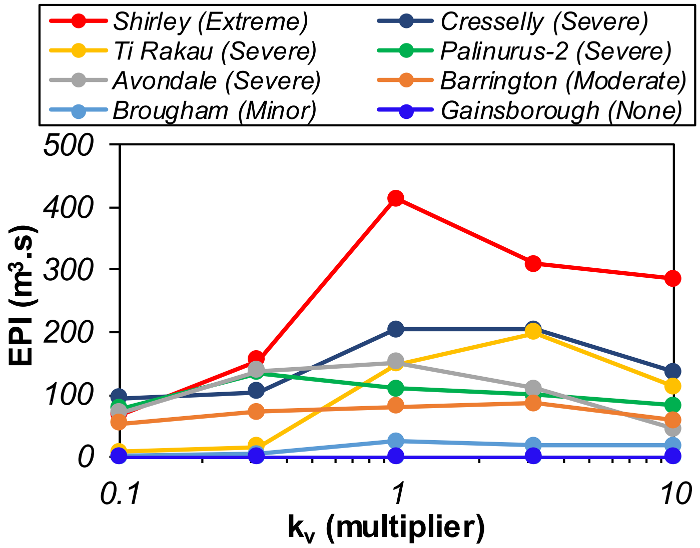

Figure 5.12 **Influence of variations in hydraulic conductivity on computed EPI values for sites with different manifestations.**

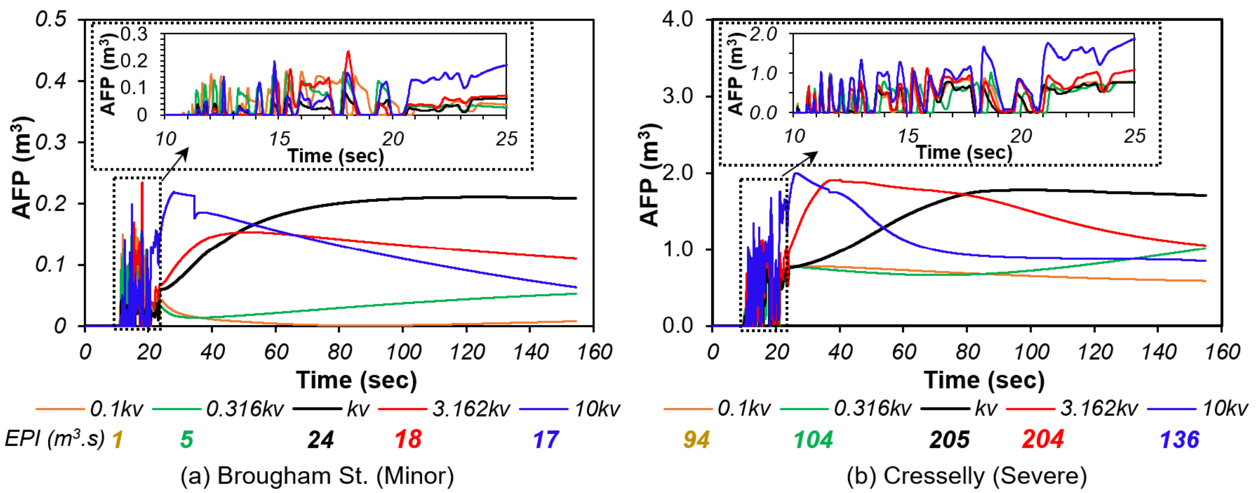

Figure 5.13 **Influence of hydraulic conductivity on time history of AFP during and after shaking.**

5.5.2 Groundwater Level

The sensitivity of EPI to variations of the GWL is investigated by increasing and decreasing the baseline GWL by 40 cm in the analyses of several representative sites. The influence of the variations in the depth to groundwater on EPI are depicted in Figure 5.14. The EPI value for sites without ejecta manifestation (e.g., St. Teresa and Gainsborough) are always zero; see Figure 5.14. The change of GWL might increase or decrease the thickness of the liquefied layer, but the low k_v layer still prevents secondary liquefaction from occurring at shallow depths. Several sites with ejecta have a peak EPI value with decreasing EPI at higher or lower GWL; see Figure 5.14. A deeper GWL increases the maximum residual h_{exc} that increases the EPI value when the $h_{exc} > h_A$

condition happens. When the GWL becomes deeper and increases the site resistance due to a higher σ'_{vo}, the earthquake shaking liquefies the thinner layers, which reduces the EPI. A GWL that balances these effects will produce a peak EPI value. For some sites with ejecta, the EPI increases systematically as the GWL lowers. A slightly deeper GWL can produce a zero EPI value (e.g., the Ti Rakau site) because a deeper GWL may increase the cyclic resistance of soils at shallower elevations, which generates a lower h_{exc} that is insufficient to cause secondary liquefaction. Although the EPI calculated for some sites is sensitive to GWL changes, the resulting EPI values remain in a similar ejecta severity category (e.g., the EPI values of the Shirley and Cashmere SW sites shown in Figure 5.14 are in the range of severe-to-extreme ejecta depicted in Figure 5.5).

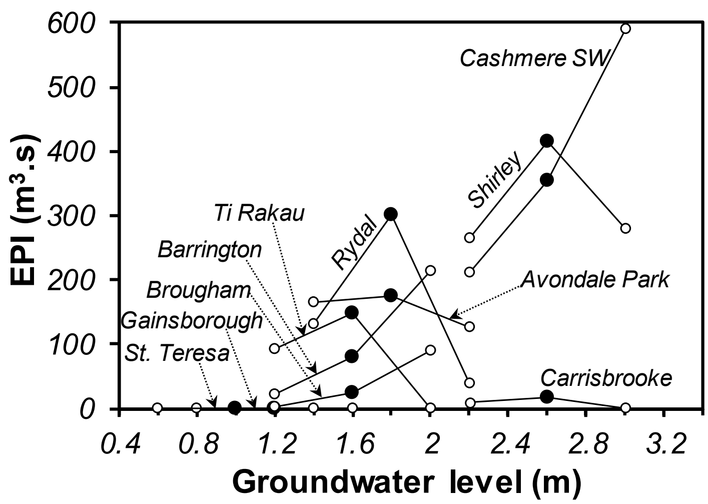

Figure 5.14 **Influence of variations of groundwater depth on computed EPI value. Filled dots are baseline cases.**

5.5.3 Ground-Motion Intensity Level

The sensitivity of EPI to variations in the intensity of the earthquake ground shaking is evaluated by scaling the baseline PGA of the input base motion by factors of 0.6 and 1.6 to represent approximately 16th and 84th percentile values. The results of the sensitivity study are depicted in Figure 5.15. The EPI values for sites without ejecta manifestation (i.e., Gainsborough, Hillsborough, and St. Teresa in Figure 5.15) remain zero for all three intensities of earthquake shaking. Increasing earthquake shaking by a factor of 1.6 does not trigger liquefaction in the shallow soil because the liquefaction of deeper soil units significantly reduces the intensity of the ground shaking in the shallow layers. Moreover, low k_v layers between liquefiable layers prevent secondary liquefaction from occurring, which confirms that layer stratification is the primary reason ejecta are not observed at these sites.

Sites in Figure 5.15 with ejecta (i.e., Shirley, Cresselly, Avondale PG, Barrington, and Brougham) are insensitive to increasing the input motion PGA beyond the baseline PGA value for the Christchurch earthquake because those ground motions are already sufficiently intense to liquefy a thick deposit of clean sand at those sites. The residual h_{exc} developed in the liquefied layers remains the same at the stronger shaking intensity, because it is bounded by the σ'_{vo} at each depth. Thus, EPI does not increase significantly for these cases for higher PGA ground motions; see Figure 5.15. However, the EPI decreases at lower intensities of input ground motion in most cases because either liquefaction is not triggered at the reduced level of earthquake shaking or it is greatly reduced. Thus, the trends in the EPI are consistent with trends in the liquefaction index LSN, which increases rapidly from a low value at low PGA to a higher value at a PGA level that triggers liquefaction, which does not increase significantly as PGA continues to increase [van Ballegooy et al. 2014]. The EPI follows this brittle response of soil to liquefaction.

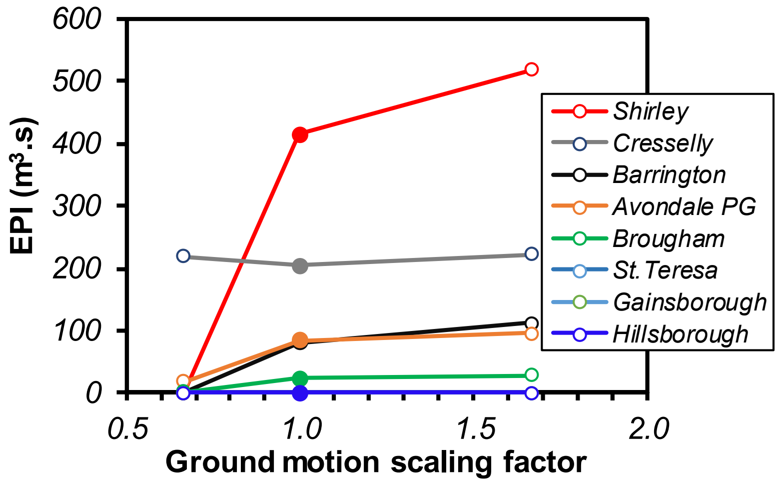

Figure 5.15 **Influence of PGA on computed EPI values at several sites for the 2011 Christchurch earthquake. Filled dots are baseline cases.**

5.6 DISCUSSION

Similar to the results from previous studies of the system response of liquefiable sites (e.g., Cubrinovski et al. [2019]), dynamic ESA provides insights not possible using simplified liquefaction procedures. The EPI is a useful index derived from the results of the ESA for estimating the potential severity of liquefaction ejecta at a site shaken by a design earthquake ground motion. The AFP and EPI are useful concepts in interpreting the potential seismic performance of level-ground sites with various layer stratifications (e.g., interbedded deposit of sand, transition, and clay soil; partially stratified, clean sand and silt deposit; and thick, clean sand deposit). Importantly, the AFP and EPI capture the post-shaking upward seepage mechanism that largely governs the occurrence of sediment ejecta. The EPI can be used as an EDP in performance-based design in which various scenarios of site variables, ground-motion intensity, and soil properties are simulated.

The thin-layer effect may significantly influence the CPT tip resistance measurement of a soil layer thinner than 0.5 m. However, most of the critical layers at sites studied in this research have a thickness more than 1.0 m, making the thin-layer effect less significant. Beyzaei et al. [2020] used the smaller CPT cone size to study the effect and found that the relative influence is small. We have performed analysis using parameters derived from inverse-CPT measurement (i.e., Boulanger and DeJong [2018]) of the studied sites and found the results are not significantly different.

The EPI can distinguish sites with and without ejecta manifestation, as shown in Figure 5.5. There are numerous cases when the results of ESA and the corresponding calculation of the EPI are insensitive to reasonable variations in the input parameters. For example, the variation of k_v, GWL, and ground-motion intensity do not change the calculated zero EPI value for highly stratified sites, thereby affirming that layer stratification is the primary reason why surficial ejecta were not produced at these sites for the Canterbury earthquakes. The contrasting dynamic responses and post-shaking hydraulic responses of adjacent sites with different layer stratifications (i.e., Palinurus Road sites and Cashmere High School sites) can produce contrasting ejecta manifestations. These important differences can be captured by dynamic ESA using the AFP and EPI concepts. The simulations capture the hydromechanical response of these sites, and the computed EPI values correlate well to the observed ejecta manifestations. There are cases when EPI is sensitive to variables such as k_v and GWL. However, even when the EPI was shown to be sensitive to variations in the input parameters, the resulting range of EPI values typically fell within a range of liquefaction ejecta severity categories that produced consistent assessments of ground performance. The EPI value of a site is limited to a peak value regardless of shaking intensity because there is a maximum thickness of the liquefied layer and the amount of generated h_{exc} (equivalent to the effective overburden stress).

The EPI has been developed to estimate ejecta severity by capturing soil stratification, the site dynamic response, artesian flow potential, and the post-shaking hydraulic processes. The EPI-based empirical severity criteria in this study were derived using primarily CPT data to characterize the soil parameters required in the dynamic ESA using the PM4Sand and PM4Silt soil models. Consequently, the liquefaction assessment and dynamic ESA employed to estimate EPI in this study are based on the CPT correlations, soil model calibration, and numerical simulations described in Chapter 4. To use the EPI severity criteria depicted in Figure 5.5, the analyst should use the Robertson and Cabal [2015] relation to estimate the baseline k_v values to be consistent with the methodology used in this study. Additionally, use of the PM4Sand and PM4Silt models will lead to results more consistent with the results of this study. For high-risk projects, a comprehensive sensitivity analyses that considers reasonable variations of site and large set of input ground motions and modeling parameters are recommended to produce the likely range of median EPI values.

Based on post-earthquake reconnaissance reports, we assumed large cracks that significantly changed water flow would not occur during the first 150 sec of simulation (i.e., 2.5 minutes) following the start of the earthquake. Thus, the non-liquefiable crust layer still confines the upward flow from the underneath liquefiable system. Using this assumption, we quantify the artesian pressure (due to h_{exc}) to produce artesian flows that would carry liquefied sediment to the ground surface when a crack formed. The severity of sediment ejecta is correlated to median EPI value as it captures the history of hydraulic ejecta demand (h_{exc} profile) to produce artesian flow (AFP). The goal of this ESA study is to stress that post-shaking water flow is important, and ESA can be used to quantify the hydraulic ejecta demand through an index (EPI) that correlates well to the ejecta severity observed in the field.

Quantifying ejecta-induced ground failure is a difficult task and can be sensitive to several variables. The critical part of this task is to assess whether upward seepage-induced secondary liquefaction above the z_{AFP} depth is triggered or not. Dynamic ESA is superior to a simplified procedure because it can capture the hydromechanical interaction of liquefiable sites during and after shaking. Moreover, the computation time is relatively fast; for example, 160 sec of OpenSees simulation (Δt = 0.001 sec) of a 33-m deep soil column with 20 × 20 cm mesh resolution required about 670 sec of computation time using a standard personal computer. Additional effort is required to perform the dynamic ESA to calculate the EPI, but the insights gained are noteworthy. Two-dimensional simulation can provide a more accurate evaluation that captures horizontal flow; however, the analysis requires additional effort to characterize the model and is more computationally expensive. One-dimensional analysis is efficient and effectively captures key post-shaking mechanisms. By combining multiple 1D ESAs of columns within a 2D cross section of a site, one can identify the area where ejecta may be produced and may require ground improvement.

5.7 CONCLUSION

Simplified liquefaction ground-failure indices (e.g., LPI and LSN) underestimated or overestimated the ejecta severity at several sites in Christchurch during the Canterbury earthquakes. Moreover, they do not provide an estimate of the amount of ejecta. To advance understanding, the seismic response characteristics of liquefiable sites that did or did not produce ejecta are investigated through dynamic nonlinear ESA. An ESA is required because simplified liquefaction ground-failure indices do not directly capture the seismic response characteristics and the post-shaking hydraulic processes that govern the occurrence of ejecta and its severity. The concepts of AFP and EPI provide valuable insights. The computed EPI values correlate well to ejecta manifestations observed at 44 well-investigated liquefiable case histories in Christchurch and the Port Island site. Case histories without ejecta have negligible EPI values, and sites with more severe ejecta have higher EPI values. The EPI-based criteria developed in this study can be used to estimate the severity of sediment ejecta at a site for a prescribed earthquake loading. Performing ESA requires more effort and additional work is required to confirm the applicability of the proposed EPI criteria for worldwide use, but the concepts proposed in this report provide valuable insights.

The key factors that control the occurrence and severity of sediment ejecta are:

1. depth of shaking-induced liquefaction and upward seepage-induced secondary liquefaction relative to z_{AFP};
2. hydraulic continuity of zones B and C liquefiable soil layers (i.e., k_v profile), and
3. the Zone A crust layer characteristics.

Sites without ejecta are distinguished by liquefiable soil layers in zones B and C that are separated by non-liquefiable, low k_v materials. The upward seepage flow from a deep liquefied layer is impeded by an overlying low k_v layer; thus, h_{exc} remains low in Zone B, and secondary liquefaction is not triggered. The EPI value is negligible because h_{exc} never exceeds h_A or $h_{exc} > h_A$ occurs only for a moment. Consequently, there is not enough artesian water pressure to transport the liquefied sediment to the ground surface. The location and thickness of the low k_v layer contribute significantly to preventing the accumulation of the artesian water pressure required to produce ejecta. Conversely, the liquefiable layers in Zones B or C are hydraulically connected without intermediate low k_v soil layers at sites with ejecta manifestation. Liquefaction of soil layers in zones B and C produce high u_e and hence high h_{exc} that initiate intense upward seepage, which increases the h_{exc} in shallow soil layers above z_{AFP}, which in turn sustains liquefaction in Zone B soil layers that liquefied or produces secondary liquefaction in Zone B soil layers. For these cases, the EPI is high. If the $h_{exc} > h_A$ condition lasts for a long period of time while accumulating high artesian water pressures, severe cases of ejecta can occur. The observed ejecta severity for sites with ejecta manifestations increase as the thickness of Zone B and duration of the $h_{exc}>h_A$ condition increase. The EPI captures these aspects of the problem.

The calculated EPI value is influenced by the following:

1. h_{exc} generated during shaking, which is predominantly determined by location of z_{AFP} and GWL, soil density, and ground shaking intensity;
2. Site dynamic response, which depends on the properties of and impedance contrast between soil layers and whether liquefaction in Zone C reduces the seismic demand in shallower layers; and
3. The advection process, which is governed by the distribution of h_{exc} and the k_v profile of the deposit.

Dynamic ESA using the AFP concept and EPI can distinguish the seismic response characteristics of liquefiable sites that produce None, Minor–Moderate, and Severe–Extreme ejecta manifestations; see Figure 5.5. The critical parts of performing an ESA to estimate ejecta severity are:

1. Evaluating the influence of layer stratification on the seismic site response during earthquake shaking (i.e., impedance contrast) where it can reduce the amplitude of CSR at shallow elevation due to deep liquefaction, which prevents shaking-induced liquefaction within the soil above z_{AFP}; and
2. Evaluating the post-shaking hydraulic process that is governed by the site k_v-profile during which the large upward seepage can increase the h_{exc} within the soil above the z_{AFP} and sustain the $h_{exc} > h_A$ condition (i.e., post-shaking secondary liquefaction) that lengthens the duration of sediment ejecta process.

Whereas sediment ejecta are derived from soil layers in Zone B that undergo primary or secondary liquefaction, the mechanical and hydraulic responses of soil layers in Zone C also contribute greatly. Whether Zone C soil layers liquefy or not, they must be hydraulically connected to soil layers in Zone B to supply the water that produces and sustains $h_{exc} > h_A$ to create Severe-to-Extreme ejecta manifestation.

6 Conclusions

6.1 SUMMARY

Estimating sediment ejecta amount is necessary to develop a more quantitative assessment of the severity of the liquefaction-induced ground failure. The more liquefied sediment erupted to the ground surface, the more severe the resulting ground failure (e.g., excessive ground subsidence or deformation) and its resulting adverse impacts on engineered systems. This research employed simplified evaluation procedures and advanced nonlinear dynamic effective stress analysis (ESA) to assess liquefaction-induced ejecta potential of well-investigated liquefaction case histories. The ESA was performed to investigate the dynamic response of liquefiable sites and soil–water hydromechanical interaction during and after shaking ends. The research led to the development of the concepts of the Artesian Flow Potential (AFP) and the Ejecta Potential Index (EPI) as new ways to capture the post-shaking hydraulic process that governs ejecta occurrence and its severity.

First, this PEER-funded research project back-analyzed 44 well-investigated liquefaction field case histories using state-of-the-practice CPT-based simplified liquefaction triggering procedures. The seismic performance of free-field, level-ground sites undergoing four major Canterbury, New Zealand, earthquakes (i.e., the 2010 M_w7.1 Darfield, 2011 M_w6.2 Christchurch, 2011 M_w6.0 June, and 2011 M_w5.9 December events) were investigated. This study analyzed a total of 176 case histories (i.e., 44 sites undergoing four earthquakes) with varying amounts of ejecta. Of these 176 case histories, there are 121 cases with no surface manifestations of liquefaction, 17 cases with minor liquefaction ejecta, 17 cases with moderate ejecta, 19 cases with severe ejecta, and 2 cases with extreme ejecta. One goal of this project was to identify the geotechnical characteristics of sites that did and did not produce ejecta. All of the sties studied contain liquefiable materials with a similar characteristic (e.g., q_{c1Ncs} and depth), and all sites were shaken by similar intensities of ground shaking for each earthquake. To evaluate the influence of layer stratification on ejecta production., the 44 sites were divided into two groups: (1) 24 sites with *a thick sand deposit,* and (2) 20 sites with *a partially-to-highly stratified silty soil deposit.* The sites with thick sand deposits produced relatively more ejecta than the sites with stratified silty soil deposits. The values of LSN, LPI, and LPI_{ISH} for each site were compared against observed ejecta manifestation. The results show that these indices did not correlate well to the observed ejecta amounts. For instance, there are several cases where the LSN, LPI, and LPI_{ISH} values were high, but no ejecta was observed.

Secondly, nonlinear dynamic ESA was performed to evaluate the influence of soil layer stratification of the two representative sites in producing ejecta. The Shirley and St. Teresa sites were selected to represent the thick, clean sand and partially-to-highly stratified soil deposits, respectively. The LSN sensitivity analysis using a tornado diagram framework indicated that the underestimation and overestimation of the sediment ejecta amount at Shirley and St. Teresa sites, respectively, cannot be explained by the uncertainty of the parameters used to characterize the sites. The nonlinear dynamic ESA was set up to simulate the hydromechanical response of the two sites using the finite-element code OpenSees. Using its implicit formulation, OpenSees can perform long-duration simulations relatively quickly without requiring very small time steps.

The robust PM4Sand and PM4Silt constitutive models were utilized to model the contractive-dilative behavior of liquefiable sand-like, intermediate, and clay-like soil. The CPT results were used primarily to assign the soil parameters for the constitutive model and to calibrate the model parameters to produce reasonable cyclic behavior. The results of the ESA simulation of the sites were compared with the recorded motions at nearby strong-motion stations to validate the ESA framework used in this research. The computed ground motions compare favorably with the recorded motions. The detailed examination of these sites enabled the development of the AFP and EPI concepts. They were applied to these two sites to estimate ejecta potential by tracking the duration in which the excess hydraulic head exceeded the critical head required for artesian flow. The EPI captured key aspects of the post-shaking hydraulic processes. The EPI values computed from the simulations of the two sites are consistent with the observed ejecta amount for these two sites for all major Canterbury earthquakes.

Thirdly, the performance of AFP and EPI for identifying liquefaction case histories that did and did not produce sediment ejecta manifestation were examined using a larger suite of case histories. The seismic performance of 45 well-documented liquefaction field case histories (i.e., 44 Christchurch cases and the Port Island site in Japan) were simulated using nonlinear dynamic ESA. The LSN, LPI, and EPI values for each case were computed and compared to the observed ejecta manifestation. The computed EPI values correlated well to the observed ejecta amounts as opposed to LSN and LPI, which did not. Cases with severe ejecta had high EPI values, and cases without ejecta had low EPI values. The analysis also explained the possible mechanisms involved in two adjacent liquefiable sites that produced different amounts of ejecta. Furthermore, the generalized concept of seismic response characteristics of liquefiable sites that produce None, Minor-to-Moderate, and Severe-to-Extreme ejecta were established. A sensitivity analysis of key parameters (i.e., PGA, k_v, and GWL) was performed to evaluate their influence on the variation of EPI. The results indicate that although these parameters are insensitive to EPI values at highly stratified sites, the EPI at thick sand sites can be sensitive to these parameters. Note: the resulting range of EPI values typically fell within a range of liquefaction ejecta severity categories that produced consistent performance assessments of the ground.

The findings of this research elucidate the role of post-shaking hydraulic mechanism in producing sediment ejecta, which is a critical aspect in evaluating liquefaction consequences. This research has identified the key hydromechanical characteristics of liquefiable sites that did and did not produce ejecta. The AFP and EPI capture the post-shaking upward seepage mechanism that largely governs the severity of sediment ejecta, which is ignored in the formulation of LPI, LPI_{ISH}, or LSN. The EPI could be used as EDPs in a performance-based design in which various scenarios of site variables, ground-motion intensity, and soil properties are simulated. Performing nonlinear dynamic ESA is superior to evaluating a site with the CPT-based simplified procedure; thus, it should be used in practice to perform liquefaction hazard assessments for high-risk projects.

6.2 FINDINGS

This research develops new ways to estimate the severity of liquefaction-induced sediment ejecta for level-ground conditions. Key findings from the research are:

- Sediment ejecta is a post-shaking hydraulic phenomenon resulting from the migration and redistribution of excess-pore-water-pressure (u_e) generated during earthquake shaking. The dissipation process of residual u_e can trigger high-gradient upward seepage that can mobilize cracks in the crust layer. With sufficient artesian water pressure, the seepage can eject the liquefied sediment onto the ground surface. The site k_v-profile largely determines the amount of ejecta that can be produced once a high hydraulic gradient is achieved.
- The material of the non-liquefiable crust layer influences the pattern of surficial ejecta manifestation where localized cracks or ground heaving conditions tend to occur at sites with impermeable (e.g., competent cohesive layer) or permeable crusts (e.g., fine clean sand), respectively.
- Of the 176 of well-investigated liquefaction field case histories investigated, 96 thick sand site cases with at least 4 m thickness of sand-like materials within the top 10 m of its profile produced 47 cases with no ejecta, 13 cases with minor ejecta, 15 cases with moderate ejecta, 19 cases with severe ejecta, and 2 cases with extreme ejecta. Conversely, the remaining 80 partially-to-highly stratified silty site cases produced 74 cases with no ejecta, 4 cases with minor ejecta, 2 cases with moderate ejecta, and no cases with severe or extreme ejecta. Thus, soil stratigraphy greatly affects the occurrence and quantity of sediment ejecta.
- The LSN, LPI, and LPI_{ISH} do not correlate well to the observed ejecta severity in the field case histories analyzed herein. Using C_{FC} = 0.13 and P_L = 50% as the recommended values, there are approximately 30%, 50%, 50%, 50%, and 25% of the case histories with None, Minor, Moderate, Severe, and Extreme amounts of ejecta, respectively, that have a LSN = 20 (i.e., the trend does not converge). There are cases with LSN values as high as 50 that did not produce ejecta. The trends of these liquefaction ground-damage indices did not vary considering different values of the C_{FC} and P_L parameters. These liquefaction indices did estimate ejecta occurrence (i.e., Yes/No type of assessment, not an estimation of ejecta amount) reliably well at thick, clean sand sites but did not estimate it well at stratified silty

sites. LSN, LPI, and LPI_{ISH} tend to produce excessive overestimation of ejecta amount at partially-to-highly stratified silty soil sites.

- The q_{c1Ncs} of the liquefiable sand-like soil between the two groups are similar, ranging from 80–120, and they are observed within the depth of 3–20 m depth. The Robertson [2009] SBT of the liquefiable materials is also similar (I_c = 1.8–2.0). However, the continuity of the sand-like soil in the two sites groups differs. The loose sand-like soils at partially-to-highly stratified soil sites are isolated between low k_v soils, whereas the sand-like soil at thick sand sites is relatively continuous. Other contributing factors that explain why overestimation occurred at stratified soil sites include depositional processes, permeability contrasts in the highly stratified soil deposit, partial saturation of the shallow soil below the groundwater table, and dynamic response effects due to liquefaction of deeper soil layers [Beyzaei et al. 2018; Cubrinovski et al. 2019].
- The LSN may underestimate the amount of ejected sediment at the thick sand sites. A sizeable area in Shirley district has a LSN < 8 (i.e., estimated to produce no ejecta) but produced Minor-to-Severe ejecta quantities after shaken by an estimated surficial PGA of 0.35–0.45g during the 2011 Christchurch earthquake (underestimation). The top 3 m of the Shirley profile (i.e., its non-liquefiable crust) consists of sandy to silty materials (I_c = 2.05–2.60) with low k_v value, which is then followed by the homogenous deposit of high k_v, loose to dense sand (I_c = 1.31–1.80) until the depth of 20 m.
- The LSN may overestimate the amount of ejected sediment at highly stratified sites. There are many areas in the Gainsborough district with LSN > 25 (estimated to produce at least a moderate ejecta amount) where no ejecta was observed during post-event reconnaissance. The top 3 m of their soil profiles are like the material encountered in Shirley district. However, the soil deposit below the crust comprised a highly stratified (interbedded) deposit of loose clean sand, loose silty sand, and low-plasticity silt material with I_c ranging from 1.8–2.6.
- The LSN, LPI, and LPI_{ISH} mis-estimate the ejecta amount because they did not consider the post-shaking hydraulic process that governs ejecta production and its severity. Consequently, LSN, LPI, and LPI_{ISH} often overestimate the ejecta amount because they do not capture the influence of a site's k_v profile. Although liquefaction is triggered and the residual u_e - remained high after the shaking stopped, if the liquefied layers are isolated between non-liquefiable low k_v layers, the water cannot flow freely towards the ground surface to produce ejecta. These indices also ignore the effect of liquefaction triggering at a deeper depth that may reduce the seismic demand to trigger liquefaction (i.e., h_{exc} remains low) at shallow depths. The simplified liquefaction triggering (FS_L-based) procedure is derived only to

evaluate liquefaction triggering at a specified depth. The FS_L-based procedure is reasonably accurate to evaluate the seismic demand (CSR) and site resistance (CRR) during earthquake shaking. However, sediment ejecta is a post-shaking hydraulic phenomenon, and the formulation of current liquefaction indices cannot directly capture the upward seepage-induced artesian flow, which is the key mechanism that governs ejecta production after the earthquake shaking ceases. Thus, it is not surprising that LSN, LPI, or LPI_{ISH} cannot estimate reliably the ejecta amount.

- Adjustment of several LSN calculation parameters (e.g., q_{c1Ncs}, GWL, C_{FC}, P_L, and PGA) within a reasonable range (evaluated using the tornado diagram approach) did not explain the underestimations and overestimations at the Shirley and St. Teresa sites.
- Nonlinear dynamic ESA of a thick sand site (e.g., Shirley) can identify the layer that liquefies first (which then influences the site's dynamic response) and generates a significant amount of u_e (which governs the post-shaking hydraulic gradient that produces seepage) during strong shaking. Dynamic ESA can simulate the post-shaking redistribution of residual u_e, which is important to evaluate the potential of intense upward seepage that can erode the overlying crust layer. Rapid u_e dissipation within the high c_v soil triggers high-gradient upward seepage within the soil profile to produce significant secondary liquefaction and accumulate high artesian pressure. These post-shaking hydraulic processes are responsible for the extreme ejecta amount observed at the Shirley site. The ESA simulation of the Shirley site during the intense Christchurch earthquake successfully captures this mechanism. The simplified procedure cannot capture this complex post-shaking mechanism and underestimates its consequences.
- Nonlinear dynamic ESA of partially-to-highly stratified sites (e.g., St. Teresa) can capture the influence of site impedance contrast (different stiffness) and contrasts in the k_v-profile within a highly stratified layer of sand, silt, and clay soil. It can also capture the severe loss of stiffness in a weak deeper soil layer that reduces the seismic demand at a shallower depth. The post-shaking simulation of St. Teresa sites shows that upward seepage-induced secondary liquefaction did not occur within the shallow soil as the shallow h_{exc} remains low. The upward seepage occurred due to the generation of u_e in the isolated sand and silty sand layer, but it was insufficient to produce significant flow through the overlying low k_v silt layer, which prevented secondary liquefaction of shallower soil layers. The simplified procedure cannot capture this complex mechanism and tends to overestimate the amount of ejected sediment, as observed in many partially-to-highly stratified sites analyzed in this research.
- Soil layer stratification greatly affects the post-shaking hydraulic mechanism that governs the rate of seepage developed after the shaking

ends. Both Shirley and St. Teresa sites contain liquefiable sand-like materials with q_{c1Ncs} < 100, but their continuity, k_v, and c_v-profile are different. The Shirley site is a thick, continuous sand deposit with estimated high k_v values without significant restrictions to water flow. The u_e within the clean sand units dissipates simultaneously (i.e., rapid water flow through a high hydraulic conductivity deposit), which induces intense upward seepage that can exploit cracks in the crust layer. The St. Teresa site is highly stratified with alternating layers of significantly different hydraulic conductivities (i.e., k_v values from 10^{-9} to 10^{-3} m/sec). The u_e dissipation process within the highly stratified thin soil layers occurs mostly independently due to the significant differences of their k_v values. The u_e generated in isolated layers is not able to produce significant vertical water flow during or shortly after earthquake shaking due to the low hydraulic conductivities of the ML units. The delayed u_e dissipation process reduces the intensity of upward flow; consequently, the upward seepage developed in an isolated liquefied layer is impeded by the overlying low k_v layer.

- The Robertson [2016] SBT*n* index (I_B) is useful in discriminating between sand-like units (I_B > 32) in which PM4Sand is employed, intermediate silt-like units (22 < I_B < 32) in which PM4Silt-Liq ($r_{u\text{-}max}$ = 0.9) is employed, and clay-like units (IB < I_B) in which PM4Silt-Clay (default $r_{u\text{-}max}$) is employed. The calibration framework presented herein proves to be successful in producing reasonable hydromechanical responses consistent with field observations. The calibration presented in this study is considered practical to be implemented in engineering practice. A major part of calibration is to adjust the required number of cycles to reach liquefaction estimated using recommended liquefaction triggering lines.
- The AFP quantifies the required artesian pressure to produce high-pressure artesian flow above the ground surface at a specified time step. The AFP measures the magnitude of artesian pressure (i.e., hydraulic demand), represented by h_{exc} within a soil layer that exceeds a critical excess head to produce artesian flow (h_A) to transport liquefied sediment to the ground surface during and after earthquake shaking. The thicker soil layer with longer $h_{exc} > h_A$ condition is sustained, the longer AFP exists, and the more sediment quantity that will be ejected. The duration aspect of the $h_{exc} > h_A$ condition is critical because it measures the accumulation of artesian pressure that must be dissipated. The AFP value tends to increase after the end of shaking, which suggests a higher potential of ejecta production after shaking stops.
- The EPI value is computed by integrating AFP time history over time (the area beneath the AFP time history curve). It is a single index number that quantifies the magnitude of artesian pressure to produce sediment ejecta by capturing the post-shaking hydraulic processes (upward seepage-induced

secondary liquefaction). The AFP time history for 150 sec is determined based on several case histories that indicate cracking of the nonliquefiable crust layer occurred 2 to 3 minutes after ground shaking initiated. The EPI accounts for the influence of these factors in evaluating the severity of sediment ejecta at liquefiable level-ground sites: (a) amount of h_{exc}; (b) potential of upward seepage-induced artesian flow; (c) duration of $h_{exc} > h_A$ (i.e., artesian flow condition); (d) hydraulic conductivity contrasts; (e) dynamic response of the soil system; and (f) advection process. The calculated EPI value is influenced by: (1) h_{exc} generated during shaking, which is predominantly determined by the location of z_{AFP} and GWL, soil density, and ground shaking intensity; (2) the earthquake input ground-motion characteristics and the resulting seismic site response, which depends on the properties of and impedance contrast between soil layers and whether liquefaction in Zone C reduces the seismic demand in shallower layers; and (3) the advection process, which is governed by the distribution of h_{exc} and the k_v profile of the deposit.

- Based on the 356 simulations results of 45 liquefaction case histories using multiple input ground motions, the computed median EPI values using the best-estimate site and earthquake parameters correlated well to the observed ejecta severity. The range median EPI values of the sites with None, Minor, Moderate, Severe, and Extreme ejecta severity are 0–1, 11–50, 43–113, 111–259, and 322–421, respectively.
- Two sites (i.e., Palinurus road and Cashmere High school) demonstrate how adjacent ground conditions at a site can produce contrasting ejecta amounts (None and Severe). Multiple 1D ESA using different CPT data and 2D cross-section drawings were used to evaluate the different responses. The analysis result shows that the area without ejecta had negligible EPI values and the area with severe ejecta had higher EPI values. The LSN values of the two areas are not capable of discerning the contrasting amounts of ejecta observed in close proximity with each other at these two sites.
- The key factors that control the occurrence and severity of sediment ejecta are: (1) depth of shaking-induced liquefaction and upward seepage-induced secondary liquefaction relative to z_{AFP}; (2) hydraulic continuity of Zones B and C liquefiable soil layers (i.e., k_v profile); and (3) the Zone A crust layer characteristics. Non-liquefiable, low k_v materials separate the zones B and C at the sites without ejecta. An overlying low k_v layer impedes the upward seepage flow from a deep liquefied layer; thus, h_{exc} remains low in Zone B, and secondary liquefaction is not triggered. The EPI value is negligible because h_{exc} never exceeds h_A or $h_{exc} > h_A$ occurs only for a moment. Consequently, there is not enough artesian water pressure to transport the liquefied sediment to the ground surface. The location and thickness of the low k_v layer contribute significantly to preventing the accumulation of the

artesian water pressure required to produce ejecta. At sites with observed ejecta manifestation, the liquefiable layers in Zones B or C are hydraulically connected without intermediate low k_v soil layers. Liquefaction of soil layers in Zones B and C produce high u_e and hence high h_{exc} that initiate excessive upward seepage, which increases the h_{exc} in shallow soil layers above z_{AFP}. For these cases, EPI is high. If the $h_{exc} > h_A$ condition lasts for a long time while accumulating high artesian water pressures, severe cases of ejecta can occur. The observed ejecta severity for sites with ejecta manifestations increase as the thickness of zone B and the duration of the $h_{exc}>h_A$ condition increase.

- Site k_v-profile, GWL location, and ground-motion intensity influence the computed EPI values. There are cases when EPI is sensitive to variables such as k_v and GWL. However, even when EPI was shown to be sensitive to variations in the input parameters, the resulting range of EPI values typically fell within a range of liquefaction ejecta severity categories that produced consistent assessments of ground performance. The EPI value of a site is limited to a peak value regardless of shaking intensity because there is a maximum thickness of the liquefied layer and the amount of generated h_{exc} (equivalent to the effective overburden stress). There are also cases when ESA results and EPI values are insensitive to variations in the input parameters. Importantly, the variation of k_v, GWL, and input ground motions do not change the calculated zero EPI value for highly stratified sites, thereby affirming that layer stratification is the primary reason why surficial ejecta were not produced at these sites for the Canterbury earthquakes.
- There are limitations to the nonlinear dynamic ESA performed in this research. The employed *u-p* formulation proposed by Zienkiewicz and Shiomi [1984] calculates fluid pore pressure, but it did not compute the displacement, velocity, and acceleration of the fluid phase that can evaluate where the fluid phase is transported. However, the *u-p* formulation is efficient and straightforward and produces reliable results. The ESA assumes the ground seepage will flow in the vertical direction during the advection stage; thus, the 1D assumption is employed. Two-dimensional post-shaking seepage analysis might be required to consider lateral seepage flow at sites with a variable subsurface condition or unlevel ground. However, multiple 1D analyses of closely spaced soil profiles representing a realistic 2D cross section can be used to evaluate the possibility of lateral flow. The ESA employed herein only estimate the hydraulic demand by considering the magnitude of artesian pressure represented by h_{exc}. The ESA did not consider the hydraulic fracturing process of non-liquefiable crust resistance because it is based on continuum finite-element analysis.

REFERENCES

Ambraseys N., Sarma S. (1969). Liquefaction of soils induced by earthquakes, *Bull. Seismol. Soc. Am.,* 59(2):651–664.

Ashford S., Boulanger R., Donahue J., Stewart J.P. (2011). Geotechnical Quick Report on the Kanto Plain Region during the March 11, 2011, Off Pacific Coast of Tohoku Earthquake, Japan. *GEER Report-025a,* doi:10.18118/G64S3W (Online video version: *https://youtu.be/GviJkVEMfwQ)*.

Bardet J.P., Kapuskar M. (1993). Liquefaction sand boils in San Francisco during 1989 Loma Prieta earthquake, ASCE, *J. Geotech. Eng*., 119(3):543–562.

Beaty M.H., Byrne P.M. (2011). UBCSAND constitutive model version 904ar. Itasca UDM Web Site, page 69.

Been K., Jefferies M.G. (1985). A state parameter for sands, *Géotechnique,* 35(2):99–112.

Bolton M.D. (1986). The strength and dilatancy of sands, *Géotechnique,* 36(1):65–78.

Bonilla L.F., Archuleta R., Lavallee D., Hysteretic and dilatant behavior of cohesionless soils and their effects on nonlinear site response: Field data observations and modeling, *Bull Seismol. Soc. Am*., 95(6):2373-2395, *https://doi.org/10.1785/012004012*.

Beyzaei C.Z., Bray J.D., Cubrinovski M., Riemer M., Stringer M. (2018a). Laboratory-based characterization of shallow silty soils in southwest Christchurch, *Soil Dyn. Earthq. Eng.,* 110:93–109, *https://doi.org/10.1016/j.soildyn.2018.01.046*.

Beyzaei C.Z., Bray J.D., van Ballegooy S., Cubrinovski M., Bastin S. (2018b). Depositional environment effects on observed liquefaction performance in silt swamps during the Canterbury earthquake sequence, *Soil Dyn. Earthq. Eng.,* 107:303–321, *https://doi.org/10.1016/j.soildyn.2018.01.035*.

Beyzaei C.Z., Bray J.D., Cubrinovski M., Bastin S., Stringer M., Jacka M., van Ballegooy S., Riemer M., Wentz R. (2020). Characterization of silty soil thin layering and groundwater conditions for liquefaction assessment, *Can. Geotech. J.*, 57(2), *https://doi.org/10.1139/cgj-2018-0287*.

Biot M.A. (1941). General theory of three-dimensional consolidation, *J. Appl. Phys*., 12:155–164, *https://doi.org/10.1063/1.1712886*.

Biot M.A. (1956). Theory of propagation of elastic waves in a fluid saturated porous solid. I. Low -frequency range, *J. Acoust. Soc. Am.*, 28:168–191, *https://doi.org/10.1121/1.1908239*.

Biot M.A. (1962a). Mechanics of deformation and acoustic propagation in porous media, *J. Appl. Phys.*, 33:1482–1498, *https://doi.org/10.1063/1.1728759*.

Biot M.A. (1962b). Generalized theory of acoustic propagation in porous dissipation media, *J. Acoust. Soc. Am.*, 34:1254–1264, *https://doi.org/10.1121/1.1918315*.

Boulanger R.W., DeJong J.T. (2018). Inverse filtering procedure to correct cone penetration data for thin-layer and transition effects, in: *Cone Penetration Testing 2018*, CRC Press, Boca Raton, FL.

Boulanger R.W., Idriss I.M. (2014). CPT and SPT based liquefaction triggering procedures, *Report No. UCD/CGM-14/01*, University of California, Davis, CA.

Boulanger R.W., Idriss I.M. (2016). CPT-based liquefaction triggering procedure, *J. Geotech. Geoenviron. Eng*., 142(2), *https://doi.org/10.1061/(ASCE)GT.1943-5606.0001388*.

Boulanger R.W., Khosravi M., Cox B., DeJong, J. (2018). Liquefaction evaluation for an interbedded soil deposit: St. Teresa's school, Christchurch, New Zealand, *Proceedings, IACGE 2018*, Chongqing, China.

Boulanger R.W., Meyers M.W., Mejia, L.H., Idriss I.M. (1998) Behavior of a fine-grained soil during the Loma Prieta earthquake, *Can. Geotech. J.,* 35:146–158, *https://doi.org/10.1139/t97-078*.

Boulanger R.W., Ziotopoulou K.A. (2017). PM4Sand (Version 3.1): a sand plasticity model for earthquake engineering applications, *UCD/CGM-17/01*, Center for Geotechnical Modeling, University of California, Davis, CA.

Boulanger R.W., Ziotopoulou K.A. (2018). PM4SILT (Version 1): a silt plasticity model for earthquake engineering applications, *UCD/CGM-18/01*, Center for Geotechnical Modeling, University of California, Davis, CA.

Bradley B.A. (2012). Strong ground motion characteristics observed in the 4 September 2010 Darfield, New Zealand earthquake, *Soil Dyn. Earthq. Eng.,* 42:32–46, *https://doi.org/10.1016/j.soildyn.2012.06.004.*

Bradley B.A. (2013). A New Zealand-specific pseudospectra acceleration ground-motion prediction equation for active shallow crustal earthquakes based on foreign models, *Bull. Seismol. Soc. Am.,* 103(3):1801–1822, *https://doi.org/10.1785/0120120021*.

Bradley B.A. (2016). Strong ground motion characteristics observed in the 13 June 2011 M_w6.0 Christchurch, New Zealand earthquake, *Soil Dyn. Earthq. Eng.,* 91:23–38, *https://doi.org/10.1016/j.soildyn.2016.09.006*.

Bradley B.A., Cubrinovski M. (2011). Near-source strong ground motions observed in the 22 February 2011 Christchurch earthquake, *Seismol. Res. Lett.*, 82(6):853–865, *https://doi.org/10.1785/gssrl.82.6.853*.

Bray J.D., Sancio R.B. (2006). Assessment of the liquefaction susceptibility of fine-grained soils, *J. Geotech. Geoenviron. Eng*., ASCE, 132(9), 1165–1177, *https://doi.org/10.1061/(ASCE)1090-0241(2006)132:9(1165)*.

Bray J.D., Cubrinovski M., Zupan J., Taylor M. (2014). Liquefaction effects on buildings in the central business district of Christchurch, *Earthq. Spectra,* 30(1):85–109, *https://doi.org/10.1193/022113EQS043M*.

Brown L.J. Weeber J.H. (1992). Geology of the Christchurch Urban Area, *GNS Science*, 104 pgs.

Cetin K.O., Tokimatsu K., Harder L.F., Moss R.E.S., Kayen R.E., Der Kiureghian A., Seed R.B. (2004). Standard penetration test-based probabilistic and deterministic assessment of seismic soil liquefaction potential, *J. Geotech. Geoenviron. Eng*., 130(12):1314-1340, *https//doi.org/10.1061/(asce)1090-0241(2004)130:12(1314)*.

Chen L. (2020). *Implementation, Verification, Validation, and Application of Two Constitutive Models for Earthquake Engineering Applications*, PhD Thesis, University of Washington, Seattle, WA.

Cubrinovski M., Green R.A., Wotherspoon, L (Eds.) (2011). Geotechnical reconnaissance of the 2011 Christchurch earthquake, Technical Report, *GEER Report-027, https://doi.org/10.18118/G68G65*.

Cubrinovski M., Ishihara K., Tanizawa F. (1996). Numerical simulation of the Kobe Port Island liquefaction, *Proceedings, 11th World Conference on Earthquake Engineering*, Paper No. 300, Acapulco, Mexico.

Cubrinovski M., Ishihara K. (1998). State concept and modified elastoplasticity for sand modelling, *Soils Found.,* 38 (4):213–225, *https://doi.org/10.3208/sandf.38.4_213*.

Cubrinovski M., Rhodes A., Ntritsos N., Van Ballegooy S. (2019). System response of liquefiable deposits, *Soil Dyn. Earthq. Eng.,* 124:212–229, *https://doi.org/10.1016/j.soildyn.2018.05.013*.

Dafalias, Y.F., Manzari M.T. (2004). Simple plasticity sand model accounting for fabric change effects, *J. Eng. Mech.*, 130(6):622–634, *https://doi.org/10.1061/(ASCE)0733-9399(2004)130:6(622)*.

Dahl K.R., DeJong J.T., Boulanger R.W., Pyke R., Wahl D. (2014). Characterization of an alluvial silt and clay deposit for monotonic, cyclic, and post-cyclic behavior, *Can. Geotech. J.*, 51(4):432–440, *https://doi.org/10.1139/cgj-2013-0057*.

Donahue J. (2007). *The Liquefaction Susceptibility, Resistance, and Response of Silty and Clayey Soils*, PhD Thesis, University of California, Berkeley, CA.

Elgamal A., Yang Z, Parra-Colmenares E.J. (2002). Computational modeling of cyclic mobility and post-liquefaction response, *Soil Dyn. Earthq. Eng.,* 22(4):259–271, *https://doi.org/10.1016/S0267-7261(02)00022-2.*

Elgamal A., Yang Z., Parra-Colmenares E.J., Ragheb A. (2003). Modeling of cyclic mobility in saturated cohesionless soils, *Int. J. Plasticity*, 19(6)883–905, *https://doi.org/10.1016/S0749-6419(02)00010-4*.

Elgamal A., Zeghal M., Parra E. (1996). Liquefaction of reclaimed island in Kobe, Japan, *J. Geotech. Eng*., 122(1):39–49, *https://doi.org/10.1061/(ASCE)0733-9410(1996)122:1(39)*.

Gao Z., Hu B., Chang D. (1983). Some geological considerations for the damage during the Tangshan earthquake, *North China Earthquake Science,* 1:64-72 (in Chinese).

Gingery J.R., Elgamal A.W., Bray, J.D. (2016). Response spectra at liquefaction sites during shallow crustal earthquakes, *Earthq. Spectra,* 31(4): 141208072728004, *http://dx.doi.org/10.1193/101813EQS272M*.

Green R.A., Cubrinovski M., Cox B., Wood C., Wotherspoon L., Bradley B., Maurer B. (2014). Select liquefaction case histories from the 2010-2011 Canterbury earthquake sequence, *Earthq. Spectra*, 30(1):131–153, *https://doi.org/10.1193/030713EQS066M*.

Holzer T.L., Bennett M.J., Noce T.E., Padovani A.C., Tinsley J.C., III. (2006). Liquefaction hazard mapping with LPI in the greater Oakland, California, area, *Earthq. Spectra*, 22(3):693–708, *https://doi.org/10.1193/1.2218591*.

Housner G.W. (1958). The mechanism of sandblows, *Bull. Seismol. Soc. Am.,* 48(2):155–161.

Huixian L., Housner G.W., Lili X., Duxin H. (2002). Report on the Great Tangshan earthquake of 1976, *EERL Report 2002-001,* California Institute of Technology, Pasadena, CA.

Hutabarat D., Bray J.D. (2019). Effective stress analysis of liquefiable site in Christchurch to discern the characteristics of sediment ejecta, *Proceedings, Earthquake Geotechnical Engineering for Protection and Development of Environment and Constructions,* AGI, Rome, Italy, pp. 2923–2931.

Huang M., Yue Z.-Q., Tham L.-G., Zienkiewicz O.C. (2004). On the stable finite element procedure for dynamic problems of saturated porous media, *J. Numer. Analy. Meth. Geomech.,* 61:1421–1450*, https://doi.org/10.1002/nme.1115*.

Iai S., Matsunaga Y., Kameoka T. (1992). Strain space plasticity model for cyclic mobility, *Soils Found.,* 32(2):1–15, *https://doi.org/10.3208/sandf1972.32.2_1*.

Idriss I.M., Boulanger R.W. (2008). *Soil Liquefaction during Earthquakes*, Earthquake Engineering Research Institute, Oakland, CA.

Idriss I.M., Boulanger R.W. (2010). SPT-based liquefaction triggering procedures, *Report No. UCD/CGM-10-02*, Center for Geotechnical Modeling, University of California, Davis, CA.

Ishihara K. (1985). Stability of natural deposits during earthquakes, *Proceedings, 11th International Conference on Soil Mechanics and Foundation Engineering*, San Francisco, CA, 1:321–376.

Iwasaki T., Tatsuoka F., Tokida K., Yasuda S. (1978). A practical method for assessing soil liquefaction potential based on case studies at various sites in Japan, *Proceedings, 2nd International Conference on Microzonation for Safer Construction Research and Application*, San Francisco, CA, pp. 885–896.

Iwasaki T., Tokida K., Tatsuoka F., Watanabe S., Yasuda S., Sato H. (1982). Microzonation for soil liquefaction potential using simplified methods, *Proceedings, 3rd International Conference on Microzonation*, Seattle, WA, 3:1319–1330.

Ishihara K., Yoshimine M. (1992). Evaluation of settlements in sand deposits following liquefaction during earthquakes, *Soils Found.*, 32(1):173–188, *https://doi.org/10.3208/sandf1972.32.173*.

Jamiolkowski M., Lo Presti D., Manassero M. (2001). Evaluation of relative density and shear strength of sands from CPT and flat DMT, (119):201–238, *https://doi.org/10.1061/40659(2003)7*.

Jeremic B., Cheng Z., Taiebat M., Dafalias T. (2008). Numerical simulation of fully saturated porous materials, *J. Numer. Analy. Meth. Geomech.,* 32(13):1635–1660*, https://doi.org/10.1002/nag.687*.

Joyner W.B., Chen A.T. (1975). Calculation of nonlinear ground response in earthquakes, *Bull. Seismol. Soc Am.,* 65(5):1315–1336.

Kawakami F. (1965). Studies on the dynamic properties of soils in Japan, Japan-U.S. Cooperative Science Program, *Proceedings, Soil Dynamics Conference*, Tokyo, July.

Kulhawy F.H., Mayne P.W. (1990). Manual on estimating soil properties for foundation design, *EPRI-EL-6800*, Cornell University, Ithaca, NY.

Kramer S.L., Arduino P. (1999). Constitutive modeling of cyclic mobility and implications for site response, *Proceedings, 2nd International Conference on Earthquake Geotechnical Engineering*, Lisbon, Portugal, pp. 1029–1034.

Kramer S.L., Greenfield M.W. (2019). The use of numerical analysis in the interpretation of liquefaction case histories, *Proceedings, 7th International Conference on Earthquake Geotechnical Engineering*, 4:173–188, Rome, Italy.

Kramer S.L., Sideras S.S., Greenfield M. (2016). The timing of liquefaction and its utility in liquefaction hazard evaluation, *Soil Dyn. Earthq. Eng*., 91(2), *https://doi.org/10.1016/j.soildyn.2016.07.025*.

Kwok A.O., Stewart J.P., Hashash Y.M., Matasovic N., Pyke R., Wang Z., Yang, Z. (2007). Use of exact solutions of wave propagation problems to guide implementation of nonlinear seismic ground response analysis procedures, *J. Geotech. Geoenviron. Eng*., 133(11):1385–1398, *https://doi.org/10.1061/(ASCE)1090-0241(2007)133:11(1385)*.

Li X.-S., Dafalias Y.F. (2004). A constitutive framework for anisotropic sand including non-proportional loading, *Geotéchnique,* 54(1):41–55, *https://doi.org/10.1680/geot.2004.54.1.41*.

Lowe D.R. (1975). Water escape structures in coarse-grained sediments, *Sedimentology*, 22(2):157–204, *https://doi.org/10.1111/j.1365-3091.1975.tb00290.x*.

Lysmer J., Kuhlemeyer R.L. (1969). Finite dynamic model for infinite media, *J. Eng. Mech. Div.,* 95(4), 859–878, *https://doi.org/10.1061/JMCEA3.0001144*.

Markham C.S. (2015). *Response of Liquefiable Sites in the Central Business District of Christchurch, New Zealand,* PhD thesis, University of California, Berkeley, CA.

Markham C.S., Bray J.D., Macedo J., Luque, R (2016). Evaluating nonlinear effective stress site response analyses using records from the Canterbury earthquake sequence, *Soil Dyn. Earthq. Eng*., 82:84–98, *https://doi.org/10.1016/j.soildyn.2015.12.007.*

Manzari M.T., Dafalias Y.F. (1997). A critical state two-surface plasticity model for sands, *Géotechnique* 47(2):255–272, *https://doi.org/10.1680/geot.1997.47.2.255*.

Maurer B.W., Green R.A., Cubrinovski M., Bradley B.A. (2014). Evaluation of the liquefaction potential index for assessing liquefaction hazard in Christchurch, New Zealand, *J. Geotech. Geoenviron. Eng*., 140(7), *https://doi.org/10.1061/(ASCE)GT.1943-5606.0001117*.

Maurer B.W., Green R.A., Oliver-Denzil S.T. (2015). Moving towards an improved index for assessing liquefaction hazard: Lessons from historical data, *Soils Found.,* 55(4):778–787, *https://doi.org/10.1016/j.sandf.2015.06.010*.

Maurer B.W., Green R.A., van Ballegooy S., Wotherspoon L. (2019). Development of region-specific soil behavior type index correlations for evaluating liquefaction hazard in Christchurch, New Zealand, *Soil Dyn. Earthq. Eng*., 117:96–105, *https://doi.org/10.1016/j.soildyn.2018.04.059*.

McGann C.R., Arduino P., Mackenzie-Helnwein P. (2012). Stabilized single-point 4-node quadrilateral element for dynamic analysis of fluid saturated porous media, *Acta Geotech.,* 7(4):297–311, *https://doi.org/10.1007/s11440-012-0168-5*.

McGann C.R., Bradley B.A., Taylor M.L., Wotherspoon L.M., Cubrinovski M. (2015). Development of an empirical correlation for predicting shear wave velocity of Christchurch soils from cone penetration test data, *Soil Dyn. Earthq. Eng*., 75:66–75, *https://doi.org/10.1016/j.soildyn.2015.03.023*.

McKenna F., Fenves G.L. (2000). An object-oriented software design for parallel structural analysis, *Proceedings, ASCE Structures Congress 2000*, Philadelphia, PA.

Mejia L., Dawson E. (2006). Earthquake deconvolution for FLAC, *Proceedings, 4th International FLAC Symposium on Numerical Modeling in Geomechanics*, Itasca Consulting Group, Minneapolis, MN.

Moss R.E.S., Seed R.B., Kayen R.E., Stewart J.P., Der Kiureghian A., Cetin K.O. (2006). CPT-based probabilistic and deterministic assessment of in situ seismic soil liquefaction potential, *J. Geotech. Geoenviron. Eng.*, 32(8):1032–1051, *https://doi.org/10.1061/(ASCE)1090-0241(2006)132:8(1032)*.

National Research Council (1985). *Liquefaction of Soil during Earthquakes*, Washington, D.C., The national Academies Press, *https://doi.org/10.17226/19275*.

National Academies of Sciences, Engineering, and Medicine (2016). State of the Art and Practice in the Assessment of Earthquake-Induced Soil Liquefaction and Its Consequences. Washington, DC: The National Academies Press, *https://doi.org/10.17226/23474*.

NZGD (2019). Investigation logs, Canterbury earthquake observations, collated investigation data, event specific groundwater surface elevations, New Zealand Geotechnical Database, available from *http://www.nzgd.org.nz/*.

Pastor M., Chan A.H.C., Mira P., Manzanal D., Fernandez-Merodo J.A., Blanc. T. (2011). Computational geomechanics: The heritage of Olek Zienkiewicz, *Numer. Analy. Meth. Geomech.,* 87(5):457–489*, https://doi.org/10.1002/nme.3192.*

Phoon K.-K., Fulhawy F.H. (1999). Characterization of geotechnical variability, *Can. Geotech. J*., 36(4), *https://doi.org/10.1139/t99-038*.

Polito C.P., Martin J.R. (2001). Effects of nonplastic fines on the liquefaction resistance of sands, *J. Geotech. Geoenviron. Eng.* 127(5):408–415, *https://doi.org/10.1061/(ASCE)1090-0241(2001)127:5(408)*.

Prevost J.H. (1985a). Wave propagation in fluid-saturated porous media: An efficient finite element procedure, *Soil Dyn. Earthq. Eng.*, 4(4):183–202, *https://doi.org/10.1016/0261-7277(85)90038-5*.

Prevost J.H. (1985b.) A simple plasticity theory for frictional cohesionless soils, *Soil Dyn. Earthq. Eng.*, 4(1):9–17, *https://doi.org/10.1016/0261-7277(85)90030-0*.

Price A.B., DeJong J.T., Boulanger R.W. (2017). Cyclic loading response of silt with multiple loading events, *J. Geotech. Geoenviron. Eng.,* 143(10):408–415, *https://doi.org/10.1061/(ASCE)GT.1943-5606.0001759*.

Robertson P.K. (2009). Interpretation of cone penetration tests—a unified approach, *Can. Geotech. J.,* 46(11), 1337–1355, *https://doi.org/10.1139/T09-065*.

Robertson P.K. (2016). CPT-based SBT classification system—an update, *Can. Geotech. J.,* 53(12):1910–1927, *https://doi.org/10.1139/cgj-2016-0044*.

Robertson P.K., Cabal K.L. (2015). *Guide to CPT for Geotechnical Engineering*, 6th ed., Gregg Drilling Testing, Inc. Signal Hill, CA.

Robertson P.K., Wride C.E. (1998). Evaluating cyclic liquefaction potential using the cone penetration test, *Can. Geotech. J*., 35(3):442–459, *https://doi.org/10.1139/t98-017*.

Roten D., Fah D., Bonilla L.F. (2014). Quantification of cyclic mobility parameters in liquefiable soils from inversion of vertical array records, *Bull. Seismol. Soc. Am.*, 104(6):3115–3138, *https://doi.org/ 10.1785/0120130329*.

Sancio R. (2003). *Ground Failure and Building Performance in Adapazari, Turkey*, PhD Thesis, University of California, Berkeley, CA.

Schneider J.A., Randolph M.F., Mayne P.W., Ramsey N.R. (2008). Analysis of factors influencing soil classification using normalized piezocone tip resistance and pore pressure parameters, *J. Geotech. Geoenviron. Eng*., 134(11):1569–1586, *https://doi.org/10.1061/(ASCE)1090-0241(2008)134:11(1569)*.

Seed H.B., Idriss I.M. (1971). Simplified procedure for evaluating soil liquefaction potential, *J. Soil Mech. Found. Div*., ASCE 97(9):1249–1273.

Seed H.B. (1979). Soil liquefaction and cyclic mobility evaluation for level ground during earthquakes. J. Geotech. Eng. Div., ASCE, 105(2):201–255.

Seed H.B., de Alba P. (1986). Use of SPT and CPT tests for evaluating the liquefaction resistance of sands. In: *Use of In Situ Tests in Geotechnical Engineering*. S.P. Clemence, Ed., ASCE, Geotechnical Special Publication 6, pp. 281–302.

Soga K. (1998). Soil liquefaction effects observed in the Kobe earthquake of 1995, *Proceedings, Institution of Civil Engineers, Geotech. Eng.*, 131(1):34–51, *https://doi.org/10.1680/igeng.1998.30004*.

Stark T.D., Olson S.M. (1995). Liquefaction resistance using CPT and field case histories, *J. Geotech. Eng.*, 121(12):856–869, *https://doi.org/10.1061/(ASCE)0733-9410(1995)121:12(856)*.

Sullivan W. (1979). Catastrophic Scope of 1976 China Earthquake is Revealed, *The New York Times, June 11, 1979.* New York, USA.

Suzuki Y., Tokimatsu K., Koyamada K., Taya Y., Kubota, Y. (1995). Field correlation of soil liquefaction based on CPT data, *Proceedings, International Symposium on Cone Penetration Testing, CPT '95,* Linkoping, Sweden. 2:583–588.

Taylor M. (2015). *The Geotechnical Characterization of Christchurch Sands for Advanced Soil Modelling*, Ph.D. Thesis, University of Canterbury, New Zealand,

Taiebat M., Dafalias Y.F. (2008). SANISAND: Simple anisotropic sand plasticity model, *J. Numer. Analy. Meth. Geomech.,* 32(8):945–948, *https://doi.org/10.1002/nag.651*.

Tokimatsu K., Yoshiaki Y. (1983). Empirical correlation of soil liquefaction based on SPT N-Value and fines content, *Soils Found*., 23(4):56–74, *https://doi.org/10.3208/sandf1972.23.4_56*.

Tonkin + Taylor, Ltd. (2013). *Liquefaction Vulnerability Study, Report to Earthquake Commission*, T and T ref. 52020.0200/v1.0, prepared by S. van Ballegooy and P. Malan, available at *https://canterburygeotechnicaldatabase.projectorbit.com*.

Toprak S., Holzer T.L. (2003). Liquefaction potential index: Field assessment, *J. Geotech. Geoenviron. Eng*., 4(315), 315 – 322, *https://10.1061/(ASCE)1090-0241 (2003)129*.

Towhata I., Ishihara K. (1985). Shear work and pore water pressure in undrained shear. *Soils Found.*, 25(3):73–84, *https://doi.org/10.3208/sandf1972.25.3_73*.

Towhata I., Yasuda S., Yoshida K., Motohashi A., Sato S., Arai M. (2016). Qualification of residential land from the viewpoint of liquefaction vulnerability, *Soils. Dyn. Earthq. Eng.,* 91:260–271, *https://doi.org/10.1016/j.soildyn.2016.09.030*.

Tsukamoto Y., Ishihara K., Nakazawa H., Kamada K., Huang Y.N. (2002). Resistance of partly saturated and to liquefaction with reference to longitudinal and shear wave velocities, *Soils Found.,* 42(6):93–104, *https://doi.org/10.3208/sandf.42.6_93*.

van Ballegooy S. (2018). *Personal Communication.*

van Ballegooy S., Green R.A., Lees J., Wentz F., Maurer B.W. (2015a). Assessment of various CPT based liquefaction severity index frameworks relative to the Ishihara (1985). H1–H2 boundary curves, *Soils Dyn. Earthq. Eng.,* 79:347–364, *https://doi.org/10.1016/j.soildyn.2015.08.015*.

van Ballegooy S., Malan P., Lacrosse V., Jacka M., Cubrinovski M., Bray J., O'Rourke T., Crawford S., Cowan H. (2014). Assessment of liquefaction-induced land damage for residential Christchurch, *Earthq. Spectra,* 30(1): 31–55, *https://doi.org/10.1193/031813EQS070M*.

van Ballegooy S., Wentz F., Boulanger R.W. (2015b). Evaluation of CPT-based liquefaction procedures at regional scale, *Soils. Dyn. Earthq. Eng.,* 79:315–334, *https://doi.org/10.1016/j.soildyn.2015.09.016*.

Wang R., Zhang J.M., Wang G. (2014). A unified plasticity model for large post-liquefaction shear deformation of sand, *Computer Geotechn.,* 59: 54–66, *https://doi.org/10.1016/j.compgeo.2014.02.008*.

Wotherspoon L.M., Orense R.P., Green R.A., Bradley B.A., Cox B.R., Wood C.M. (2015). Assessment of liquefaction evaluation procedures and severity index frameworks at Christchurch strong motion stations, *Soil Dyn. Earthq. Eng.,* 79(Part B): 335–346, *https://doi.org/10.1016/j.soildyn.2015.03.022*.

Yang Z., Elgamal A., Parra E. (2003). Computational model for cyclic mobility and associated shear deformation, ASCE, *J. Geotech. Geoenviron. Eng*., 129(12):1119–1127, *https://doi.org/10.1061/(ASCE)1090-0241(2003)129:12(1119)*.

Youd T.L., Idriss I.M., Andrus R.D., Arango G.C., Christian J.T., Dobry R., Finn W.D.L., Harder L.F., Jr., Hynes M.E., Ishihara K., Koester J.P., Liao S.-S.C., Marcuson W.F., III, Martin G.R., Mitchell J.K., Moriwaki Y., Power M.S.; Robertson P.K., Seed R.B., Stokoe K.H., II (2001). Liquefaction resistance of soils: Summary report from the 1996 NCEER and 1998 NCEER workshops on evaluation of liquefaction resistance of soils, *J. Geotech. Geoenviron. Eng*., 127(10): 817–833, *https//doi.org/10.1061/(ASCE)1090-0241(2001)127:10(817)*.

Zhang G., Robertson P., Brachman R.W. (2002). Estimating liquefaction-induced ground settlements from CPT for level ground, *Can. Geotech. J.*, 39(5): 1168–1180, *https://doi.org/10.1139/t02-047*.

Zhang J.M., Wang G. (2012). Large post-liquefaction deformation of sand, part I: Physical mechanism, constitutive description and numerical algorithm, *Acta Geotech.*, 7(2): 69–113, *https://doi.org/10.1007/s11440-011-0150-7.*

Zeghal M., Elgamal A.W. (1994). Analysis of site liquefaction using earthquake records, *J. Geotech. Eng*., 120(6), *https://doi.org/10.1061/(ASCE)0733-9410(1994)120:6(996)*.

Zienkiewicz O.C., Chan A.H.C., Pastor M., Schrefler B.A., Shiomi T. (1999). *Computational Geomechanics with Special Reference to Earthquake Engineering*, Chichester, UK: John Wiley & Sons, Inc.

Zienkiewicz O.C., Shiomi T. (1984). Dynamic behavior of saturated porous media; the generalized Biot formulation and its numerical solution, *J. Numer. Analy. Meth. Geomech.,* 8(1): 71–96, *https://doi.org/10.1002/nag.1610080106*.

Ziotopoulou K.A, Boulanger R.W., Kramer S.L. (2012). Site response analysis of liquefying sites, *Proceedings, GeoCongress 2012: State of the Art and Practice in Geotechnical Engineering*, 1799–1808, *https://doi.org/10.1061/9780784412121.185*.

APPENDIX A Post-Event Aerial Photographs and Summary of CPT-Based Liquefaction Triggering Analysis

This appendix section contains the following materials:

- Summary of CPT-based liquefaction triggering calculation results of 176 well-documented liquefaction field case histories.
- Aerial photographs for each liquefaction field case history and coordinate of the site taken after each Canterbury earthquake. The radius of white inner and outer circles on each page are 20 m and 50 m, respectively, which is measured from a CPT points as the center point.

APPENDIX B Summary of ESA Results of 45 Liquefaction Cases Histories

This appendix section contains electronic files from the numerical simulation performed in Chapter 5, including:

- AFP time histories of all 352 Christchurch and 4 Port Island simulation results.
- Input ground motions used in the analysis.

APPENDIX C EPI Sensitivity Analysis Results

This appendix section contains the following materials:

- Sensitivity analysis results of k_v, GWL, and ground-motion intensity parameters as presented in Chapter 5.
- Typical ESA results of adjacent sites with contrast soil layer stratification.

APPENDIX D PM4Sand and PM4Silt Parameters: Parametric Study

This appendix section contains the following materials:

- Effect of each PM4Sand primary and secondary parameters on the cyclic behavior.
- Effect of each PM4Silt primary and secondary parameters on the cyclic behavior.

Note:

Each plot represents a singular effect of each PM4Sand and PM4Silt parameters on the cyclic resistance vs. number of cycles to reach 3% single-amplitude shear strain, stress path, rate of pore pressure generation, cyclic shear stress vs. strain, and rate of shear strain accumulation.

The Pacifi c Earthquake Engineering Research Center (PEER) is a multi-institutional research and education center with headquarters at the University of California, Berkeley. Investigators from over 20 universities, several consulting companies, and researchers at various state and federal government agencies contribute to research programs focused on performance-based earthquake engineering.

These research programs aim to identify and reduce the risks from major earthquakes to life safety and to the economy by including research in a wide variety of disciplines including structural and geotechnical engineering, geology/seismology, lifelines, transportation, architecture, economics, risk management, and public policy.

PEER is supported by federal, state, local, and regional agencies, together with industry partners.

PEER Core Institutions

University of California, Berkeley (Lead Institution)
California Institute of Technology
Oregon State University
Stanford University
University of California, Davis
University of California, Irvine
University of California, Los Angeles
University of California, San Diego
University of Nevada, Reno
University of Southern California
University of Washington

PEER reports can be ordered at https://peer.berkeley.edu/peer-reports or by contacting

Pacific Earthquake Engineering Research Center
University of California, Berkeley
325 Davis Hall, Mail Code 1792
Berkeley, CA 94720-1792
Tel: 510-642-3437
Email: peer_center@berkeley.edu

ISSN 2770-8314
https://doi.org/10.55461/UCSE4741